UiT
THE ARCTIC UNIVERSITY OF NORWAY

Faculty of Science and Technology

Department of Geosciences

Geochemistry of the stratiform iron Dunderlandsdalen deposits, Nordland

Kristian Rolsted Lie

Master thesis in Geology, GEO-3900, May 2019

Abstract

The Dunderlandsdalen iron district, Northern Norway, hosts a world-class stratiform Fe-mineralization (total tonnage of ~500 Mt at 33% Fe). The iron ore units belong to the Dunderland Formation in the Ramnålia Nappe, which further belongs to the Rødingsfjellet Nappe of the Caledonian Uppermost Allochthon. Hematite and magnetite represent the principal ore minerals and are hosted by amphibolite grade dolomitic and calcitic marble units intercalated with various types of calcareous schists. Although having been described as a world-class iron deposit, it has not been a subject of detailed geochemical studies. In order to determine the controlling mechanisms of hematite and magnetite formation, the present study mainly focuses on investigating the geochemical characteristics of the mineralization and host rocks within a structural framework. In addition, the fluid inclusion study gives insight into the post-ore P-T-X evolution of the studied area.

Deformation processes, recrystallization of ore and gangue minerals as well as remobilization of metals during the Caledonian Orogeny affected the ore textures and mineral chemistry of the mineralization. Strain variations in ore bodies and host rocks, which are evident in both macro- and micro-scale, have given rise to different generations of Fe-oxides characterized by significantly different morphologies. The major element characteristics and REE patterns of mineralized samples indicate that the primary mineralizing events involved mixing of a low-temperature hydrothermal source of iron with a detrital component in a rift-related environment. $\delta^{13}C$ and $\delta^{18}O$ values of gangue carbonates support a deposition under the influence of hydrothermal fluids. Geochemical data, along with the age interval of host rock marble (800 to 730 Ma, Melezhik et al., 2015) have led the author to suggest that the Fe-mineralization of the Dunderland Formation accumulated in glacially and hydrothermally influenced passive margin rift-basins or back-arc basins. Fluid inclusion studies of recrystallized quartz witness a complex post-ore tectonic evolution during the Caledonian Orogeny.

Acknowledgements

This project was made possible by financial support from Rana Gruber and Mineralklynge Norge. The generous assistance from Rana Gruber during fieldwork is also highly appreciated.

I would like to express my deepest gratitude to my thesis advisor, Associate Professor Sabina Strmić Palinkaš, whose immense knowledge and enthusiasm have inspired me during my academic pursuit. Without her guidance, this thesis would not have been possible.

I am grateful to Professor Steffen G. Bergh for his guidance and invaluable suggestions which were enormously helpful during the writing of this thesis.

A special word of gratitude is due to my office partner and friend, Fredrik, who provided numerous stimulating discussions on our research topic but also innumerable laughs throughout the years.

I would like to thank the staff of the lab at the department, including Trine, Karina, Ingvild, and Matteus, for their generous support during my time in the lab. A special appreciation goes to Hanne, who was always available when I needed assistance. My thanks also go to Andrea at the University of Zagreb for the XRD analyses, and to Kai for the help during the EBSD mapping.

To my friends and fellow students: thank you for making these five years in Tromsø such a wonderful time. And to you Ørjan, my roommate of four years: our adventures in the heart of Tromsø will never be forgotten.

Last but not least, I would like to acknowledge the unwavering support and love of my family – my parents, Birgitte and Johan Inge and my sister, Else Maria – throughout all the years that have passed.

Kristian Rolsted Lie

Tromsø, May 2019

Table of Contents

1 Introduction

1.1 Context of the study

The Dunderlandsdalen iron district hosts a world-class stratiform Fe-mineralization with hematite and magnetite as the main ore minerals. The deposits represent a significant economic commodity located within the North-Central Scandinavian Caledonides, having been mined for nearly a century. Moreover, the reemergence of extensive Neoproterozoic iron formations (NIFs) worldwide represents a unique geological feature, interrupting an apparent 1.0 Ga hiatus as witnessed by the stratigraphic record (Cox et al., 2013). While incomparable in size to the more volumetrically significant Archean to Paleoproterozoic banded iron formations (BIFs), NIFs play an essential role in the Snowball Earth theory (Klein & Beukes, 1993; Hoffman et al., 1998). Most, if not all, NIFs have been linked with contemporaneous mafic volcanism. The Fe-deposits of Dunderlandsdalen share several features with other reported NIFs. However, the former display limited indicators of synchronous volcanic activity (Melezhik et al., 2015), and may thus represent a marked anomaly with respect to other reported NIFs.

The study is part of a project aimed at resolving structural, geochemical and environmental aspects related to the Dunderlandsdalen deposit. Although it is known as a world-class iron deposit, it has not been a subject of detailed geochemical studies. Understanding of the ore-forming processes responsible for the Fe-mineralization should increase the probability of discovering new ore bodies in the area. Additionally, results may have an important application to the environmental risk assessment of potential mining activities.

1.2 Purpose of the study

The primary goal of this study is to determine the controlling mechanisms of hematite and magnetite formation by obtaining the petrological, mineralogical and geochemical characteristics of host rocks, ore mineralization, and alteration products. To resolve these matters the study will combine data from optical microscopy, scanning electron microscope-energy-dispersive X-ray spectroscopy (SEM-EDS), electron backscatter diffraction (SEM-EBSD), X-ray powder diffraction (XRD), lithogeochemistry, and carbonate stable isotope analyses. Secondly, post-mineralizing P-T-X conditions are to be estimated through fluid inclusion studies. The mineralization is structurally controlled, and geochemical features will be investigated within a structural framework.

1.3 Mining history

The following summary of earlier mining activities has been compiled on the basis of Berg (1996) and Ellefmo (2005).

The stratiform iron deposits of Dunderlandsdalen have been known since the late 18th century. Rights to the iron ores were initially claimed in 1799 by Mostadsmarkens Iron Company in 1799. During the 1870s, Ole Tobias Olsen, who was responsible for the development of the Nordlandsbanen railroad, attained rights to 48 individual iron ore bodies. This was followed by the Swede Nils Persson's acquisition of rights to important ore findings during the 1880s. Known as the "Ore King of Northern Norway," Consul Persson teamed up with his compatriot and engineer Alfred Hasselbom, who performed extensive prospecting prior to early mining activity. In his report, Hasselbom claimed that "…there would be no exaggeration in saying that Dunderland is likely to become a second Bilbao" (Hasselbom, 1894, as cited in Berg, 1996, p. 11), knowing that Bilbao, at the time, was Europe's largest exporter of iron ore. Hasselbom estimated the iron deposits to a tonnage of approximately 840 million tons, however, the Norwegian geologist Johan Herman Lie Vogt presented a much more conservative estimate of tonnage to be 100 million tons.

In any case, the rights to ore and associated property, infrastructure, and preliminary ore prospecting results were sold to Edison Ore Milling Syndicate (EOMS) in 1899. The invention of the magnetic separator by Thomas Alva Edison made iron ore enrichment possible. EOMS continued the prospecting of iron ore until 1902, when the Dunderland Iron Ore Company, Limited (DIOC) and The Standard Construction Corporation, Limited (SCC) were established. SCC was established to carry out planning and development of the necessary infrastructure, such as a pier, briquette plant and power station in Gullsmedvika, along with a railroad connecting the Storforshei iron works and Gullsmedvika.

DIOC eventually commenced mining operations in 1906, but mining activities lasted only for two years due to difficulties attaining an economic surplus as a result of technical problems. Continued ore extraction was attempted with the incorporation of an alternate method of iron separation, though the commencing of WWI put a halt to continued production. The following financial and industrial depression further hindered the company from continuing mining activities during the years from 1920 to 1922. A second and third period of production lasted from 1928 to 1931 and from 1937 to 1939, respectively. Germany governed the company during WWII, and in 1947 the Norwegian State bought the rights to DIOC from the English shareholders.

Meanwhile, Rana Gruber AS was established by A/S Sydvaranger and Vereinigte Stahlwerke of Germany in 1937. The German shares of Sydvaranger A/S and Rana Gruber AS were eventually seized by the Norwegian State following the end of WWII, and by 1951 the latter was solemnly governed by

the State. During the 1950s steel production was commenced by Norsk Jernverk AS in Mo i Rana. By 1961, Rana Gruber AS was incorporated into Norsk Jernverk AS, with the former serving as the main provider of iron ore for steel production up until 1989. The closure of Norsk Jernverk AS the same year was followed by the privatization of Rana Gruber AS in 1991. In 2008, Rana Gruber AS was bought by Leonard Nilsen & Sønner AS, with current mining operations concentrated around the Kvannvatnet ore body through open pit mining and underground sub-level caving. Ore reserves have been estimated to 500 Mt at an ore grade of 33% iron.

1.4 Methods

1.4.1 Field sampling

Field-work took place in the mines of Rana Gruber, Mo i Rana, from the 22nd to the 23rd of August 2018, with the principal goal of collecting representative samples for further mineralogical and geochemical analyses. In total 27 samples were collected (Table 1), with 22 samples obtained from the Kvannvatnet open pit area and five samples coming from level 150 of the underground mine (U). The approximate sampling locations, including the eastern (E) and western (W) walls of the Kvannvatnet open pit area, are presented in Figure 15A.

1.4.2 Thin section preparation

Rock wafers of uniform thickness were made using a diamond-fitted rotary rock saw equipped with a parallel sliding stage. The rock slices were cut to appropriate sizes (approximately 1 x 2 x 3 cm) from 20 various samples and delivered to the geological lab at the Department of Geosciences, UiT-The Arctic University of Norway, for further preparation of thin sections.

1.4.3 Petrography

1.4.3.1 Optical microscopy

Petrographic observations were acquired from polished thin sections using a Leica DMLP petrographic microscope at the Department of Geosciences, UiT-The Arctic University of Norway. Transparent phases were identified by transmitted light microscopy, while opaque phases were identified by reflected light microscopy. Thin sections containing minerals of particular interest or unidentified phases were marked for further chemical analyses. Photomicrographs presenting descriptive observations of minerals and phase relationships were acquired using a Canon EOS 650D camera, mounted on top of the microscope, and the Leica Application Suite software.

1.4.3.2 SEM-EDS analyses

Elemental microanalysis, conducted in a Hitachi TM3030 scanning electron microscope (SEM) with energy-dispersive X-ray spectroscopy (EDS), was carried out at the Department of Geosciences, UiT-

The Arctic University of Norway. Imaging of un-coated polished sections was performed using a working distance of 8.5 mm, an accelerating voltage of 15kV and charge-up reduction mode. EDS data was further acquired and processed utilizing the Quantax 70 software provided by Bruker.

1.4.3.3 SEM-EBSD analyses

Scanning electron microscope-electron backscatter diffraction (SEM-EBSD) analysis was performed on two polished sections at the Faculty of Health Sciences, UiT-The Arctic University of Norway. Polished sections were carbon-coated (20 nm) using a Leica EM ACE600 sputter coater prior to analysis. BSE imaging and EBSD analysis were conducted on a Zeiss Merlin VP Compact electron microscope, equipped with a Nordlys EBSD detector. Data was collected using an accelerating voltage of 20,00 kV, with a hit rate of 83,2 %, step size of 2 µm, and field width and height of 1,36 and 1,02 mm, respectively. Specimens were tilted 70° prior to EBSD data collection, which was carried out using the refined accuracy indexing mode and an aperture opening of 240 µm, during which six bands were detected.

1.4.3.4 X-ray powder diffraction

X-ray powder diffraction (XRD) was conducted at the University of Zagreb on a Philips PW 3040/60 X'Pert PRO powder diffractometer (45 kV, 40 µA), with CuKα-monochromatized radiation (λ = 1.54056 Å) and θ-θ geometry. The area between 4 and 63° 2θ, with 0.02° steps, was measured with a 0.5° primary beam divergence. Compound identifications were based on a computer program X'Pert high score 1.0B and literature data.

1.4.4 Lithogeochemistry

Powder (5 g) of four selected mineralized samples, one gangue carbonate, and one host rock marble sample was prepared in an agate ball-mill and analyzed at Bureau Veritas Commodities Canada Ltd. (Vancouver, Canada) after lithium metaborate or tetraborate fusion using ICP-ES (Inductively Coupled Plasma - Emission Spectrometry) for the major elements and ICP-MS (Inductively Coupled Plasma - Mass Spectrometry) for the trace elements. Detection limits for all analyzed elements are listed in Appendix A.

1.4.5 Carbonate stable isotopes

Stable isotope analyses ($\delta^{13}C$ and $\delta^{18}O$) were performed on host as well as on different generations of gangue carbonates from the Dunderland Formation. The procedure was carried out at the Stable Isotope Laboratory at CAGE – Centre for Arctic Gas Hydrate, Environment and Climate located at UiT-The Arctic University of Norway, in Tromsø, Norway (http://site.uit.no/sil/). No pre-treatment was performed. Carbonate samples were placed in 4.5mL vials. The vials were flushed with He, and five drops of water free phosphoric acid (H_3PO_4) were added manually with a syringe. After equilibration >3h at T = 50°C, the samples were analyzed on a Gasbench II and Thermo Scientific MAT253 IRMS. The

normalization of results to VPDB was done by 2-3 in-house standards with a wide range of $\delta^{13}C$ and $\delta^{18}O$ values. The in-house standards have been normalized by several international standards. The instrument uncertainty for $\delta^{13}C$ and $\delta^{18}O$ was a standard deviation of ≤0.1‰ (ThermoScientific), whereas uncertainty in $\delta^{13}C$, $\delta^{18}O$ for heterogeneous/small samples may have been larger. A small correction factor was applied to the $\delta^{18}O$ values of non-calcite samples, using the following equations: $1000\ln\alpha_{CO2\text{-}calcite} = 3.89+5.61*10^5/T^2$ (Das Sharma et al., 2002); $1000\ln\alpha_{CO2\text{-}ankerite} = 4.15+6.68*10^5/T^2$ (Rosenbaum & Sheppard, 1986).

1.4.6 Fluid inclusion studies

1.4.6.1 Preparation of doubly polished thick sections

Preparation of doubly polished (0.1 to 0.3 mm) thick sections for fluid inclusion studies were carried out in accordance with the procedure recommended by Goldstein (2003), at the Department of Geosciences, UiT-The Arctic University of Norway. The procedure included: (1) cutting of rock samples using a liquid-cooled rotary diamond saw; (2) grinding, followed by polishing surface prior to mounting; (3) mounting of sample to glass with crystal balm; (4) sawing of samples; (5) coarse grinding of samples to appropriate size, followed by final polishing of surface.

1.4.6.2 Fluid inclusion petrography and microthermometry

Petrographic and microthermometric measurements of fluid inclusions within quartz were performed at UiT The Arctic University of Norway. Double polished, 0.1 to 0.3 mm-thick, transparent mineral wafers were studied. Measurements were carried out on Linkam THMS 600 stages mounted on an Olympus BX 2 microscope using 10× and 50× Olympus long-working distance objectives. Two synthetic fluid inclusion standards (SYN FLINC; pure H_2O and mixed H_2O-CO_2) were used to calibrate the equipment. The precision of the system was ±2.0°C for homogenization temperatures, and ±0.2°C in the temperature range between –60° and +10°C. Microthermometric measurements were made on carefully defined fluid inclusion assemblages, representing groups of inclusions that were trapped simultaneously. The fluid inclusion assemblages were identified based on petrography prior to heating and freezing. If all of the fluid inclusions within the assemblage showed similar homogenization temperature, the inclusions were assumed to have trapped the same fluid and to have not been modified by leakage or necking; these fluid inclusions would thus record the original trapping conditions (Goldstein & Reynolds, 1994; Goldstein, 2001; Bodnar, 2003a).

1.5 Samples

Table 1 - List of samples including sample locality (east – E; west – W; underground - U), structures/setting, main mineralogy (listed by decreasing relative abundance) and investigative methods. Mineral abbreviations are listed in Appendix B.

Sample name	Locality	Structures/setting	Mineralogy	Investigative methods
Rana 1	E	S_1, S_2, F_2, and L_1	Hem, Qz, Fsp, Grt, Cb, Bt, Mag, Ap	Mineralogy and microtextures
Rana 2	E	S_0/S_1	**Hem**, Qz	**Lithogeochemistry**
Rana 3	E	S_0/S_1	Qz, Fsp, Grt, *Cb*, Bt	Mineralogy, microtextures, SEM-EDS, and *stable isotopes*
FL 1 (a)	E	S_0/S_1	Qz, Grt, Bt, Ms, Hem	Mineralogy, microtextures, SEM-EDS
FL 1 (b)	E	S_0/S_1	Qz, Grt, Bt, Ms, Hem	Microtextures
FL 1 (c)	E	S_1	Qz, Grt, Bt, Ms, Hem	Microtextures
FL 2 (a)	E	S_1 and F_2	Qz, Hem, Cb, Bt, Fsp, Ep, Mag, Ms	Microtextures
FL 2 (b)	E	F_1 and F_2	Qz, Hem, Cb, Bt, Fsp, Ep, Mag, Ms	Microtextures
Rana 12	E	Host rock marble	***Cb***	**Lithogeochemistry** and *stable isotopes*
Rana 13	E	S_0/S_1-parallel vein	Qz, *Cb*, Fsp, Bt, Hem	Mineralogy, SEM-EDS, *stable isotopes,* and fluid inclusions
Rana 14	E	S_1/L_1 and S_2/F_2	Qz, ***Cb***, Hem, Grt, Hem, Amp, Ms	Mineralogy, SEM-EDS, **lithogeochemistry**, *stable isotopes,* and fluid inclusions
BF 2	E	F_2	Cb, Bt, Grt, Fsp, Qz, Hem	Microtextures
Rana 4 (a)	W	S_1 and F_2	Qz, Cb, Grt, Hem	Mineralogy and microtextures
Rana 4 (b)	W	-	Ep, Hem, Qz	Mineralogy and microtextures
Rana 5 (a)	W	S_1 and F_2	Qz, Fsp, Grt, Cb, Hem, Bt, Ap, Ms	Mineralogy and SEM-EDS
Rana 5 (b)	W	S_1 and F_2	Qz, *Cb*, Czo, Grt	Mineralogy and *stable isotopes*
Rana 7	W	S_0/S_1	-	-
Rana 8	W	-	-	-
Rana 6	W	-	Qz, Grt, *Cb*, Ky, Fsp, Amp, Bt	Mineralogy, SEM-EDS and *stable isotopes*
FL 3	W	F_2	Grt, Cb, Qz, Hem	Microtextures
FL 4	W	F_2	Grt, Cb, Qz, Hem, Bt	Microtextures
FL 5	W	F_2	Grt, Ep, *Cb*, Qz	Mineralogy, SEM-EDS and *stable isotopes*
Rana 11	W	F_1	Grt, Bt, Ms, Hbl, Qz, Hem	Mineralogy
FL 6	U	F_1 and F_2	*Cb*, Ep, Hem, Qz, Ap	Mineralogy, EBSD and *stable isotopes*
FL 7	U	F_1	**Mag**, Qz, Bt, Ep, Cb	Mineralogy, SEM-EDS and **lithogeochemistry**
FL 8	U	S_1/F_1 and F_2/L_2	Qz, Hem, Ep, Mag, Cb, Hbl, Fsp	Mineralogy, SEM-EDS and microtextures
SSP 3	U	S_1 and S_2	**Hem**, *Qz*, Mag, Cb, Ep	Mineralogy, SEM-EDS, **lithogeochemistry**, EBSD, and XRD
SSP 1	U	S_0/S_1	Qz, Hem, Cb, Bt, Ms, Fsp, Ep	Mineralogy
Rana 10	W	Post-D_2	Qz, *Cb*, Zo, Bt, Chl, Fsp, Py, Po, Ccp	Mineralogy, SEM-EDS, *stable isotopes* and fluid inclusions
Rana 9	W	Post-D_2	-	-

2 Geological setting

2.1 Geology of the Scandinavian Caledonides

2.1.1 The Caledonian Nappes

The initial breakup of Rodinia during the Neoproterozoic (750 to 725 Ma) was followed by redistribution of the long-lived supercontinent and opening of the Iapetus Ocean by the early Paleozoic (Torsvik et al., 1996, and references therein). Closure of the Iapetus Ocean initiated early stages of Pangean assembly, culminating in the collision between Laurentia and Baltica, known as the Caledonian Orogeny. Remnants of the Caledonian Orogeny reveal a complex and lengthy sequence of tectonic events involving rifting, oceanization, subduction, and continental collision (Stephens, 1988, as cited in Gee et al., 2008). Fragments of the mountain belt are made up of extensive thrust systems displaying several hundreds of kilometers displacement. In the Scandinavian Caledonides, these thrust systems are characterized by tectonic units stacked on top of each other, with the top units being the most far-displaced. Gee & Sturt (1985) assigned these units into the Lower, Middle, Upper, and Uppermost allochtons.

The Caledonian allochthons are underlain by autochthonous crystalline basement and thin metasedimentary sequences (Roberts et al., 2007). The Lower and Middle allochthons represent elements of Baltoscandian affinity and mainly consist of low- to medium grade metasedimentary rocks derived from the pre-collisional platform and margin setting (Roberts, 1988). Cambro-Silurian sequences, Caledonian high-grade complexes, and dolerite-intruded Neoproterozoic arkosic sandstones, along with tectonic windows of Precambrian crystalline nappes, characterize the two lowermost nappes (Gee et al., 2008). The Upper Allochthon represents Iapetus-derived terranes and is recognized by island-arc and back-arc basin assemblages, along with outboard ophiolites (Roberts, 2003). Roberts et al. (2007), among other authors, proposed a Laurentian ancestry for the elements of the Uppermost Allochthon, which is represented by schists, carbonates, granites, and volcanic rocks of foreign provenance.

2.1.2 Caledonian tectonic events

Regional tectonostratigraphic events in the Caledonian nappes have been recognized based on extensive fieldwork, and structural and isotopic studies, and notably, the presence of first-order unconformities (Sturt & Ramsay, 1999). Even though earlier tectonothermal events are recognized from the rock record, the Middle to Late Silurian Scandian Orogeny has been singled out as the main orogenic event responsible for the array of Caledonian nappes. Moreover, at least three other tectonothermal events have been identified, namely the Finnmarkian, Trondheim and Taconian events, in addition to the ensuing post-collisional orogenic collapse (Roberts, 2003). In the Uppermost

Allochthon, a pre-Scandian collisional event may be recognized from polydeformed carbonate formations of Neoproterozoic to Early Silurian age. These suspected shelf-successions have been "tectonically imbricated in nonstratigraphic order prior to final emplacement on Baltica" (Roberts et al., 2007, p. 362), with an early orogenic stage most likely represented by the Middle to Late Ordovician Taconian event. According to Roberts et al. (2001), early-stage NW-vergent folds and thrusts in higher nappes of North-Central Norway have been overprinted by later SE-vergent deformational structures during the Scandian event. Post-Caledonian orogenic collapse and extension ensued in the Devonian and involved reactivation of pre-existing detachments, followed by Devonian sedimentation (Fossen & Rykkelid, 1992). The present configuration of the Scandinavian Caledonides was resultantly highly influenced by the shift from a contractional to an extensional regime (Gee et al., 2008).

2.1.3 Geology of the Uppermost Allochthon

An almost continuous exposure of the Uppermost Allochthon extends from northern Trøndelag up to Troms over a length of more than 700 km, only interrupted by the Tysfjord tectonic window of northern Nordland (Roberts et al., 2007, Figure 1). The exotic terranes of the allochthon differ markedly from the subjacent nappes. Thus, early recognition of the various lithological assemblages of the allochthon has led researchers to propose a Laurentian ancestry or origin from an unknown microcontinent (Stephens & Gee, 1989). Grenne et al. (1999), for instance, note that these late Precambrian and early Paleozoic sequences are represented by a contemporary configuration of marble-schists, high-grade gneisses, and migmatites, along with lesser conglomerates and metasedimentary iron formations (IFs). The notion that the Uppermost Allochthon represents a slice of Laurentia has further been strengthened by chemostratigraphic carbon and strontium isotope studies (Melezhik et al., 2002), in addition to the observation of early stage NW-vergent folds and thrusts unique for the Caledonian nappes (Roberts et al., 2001).

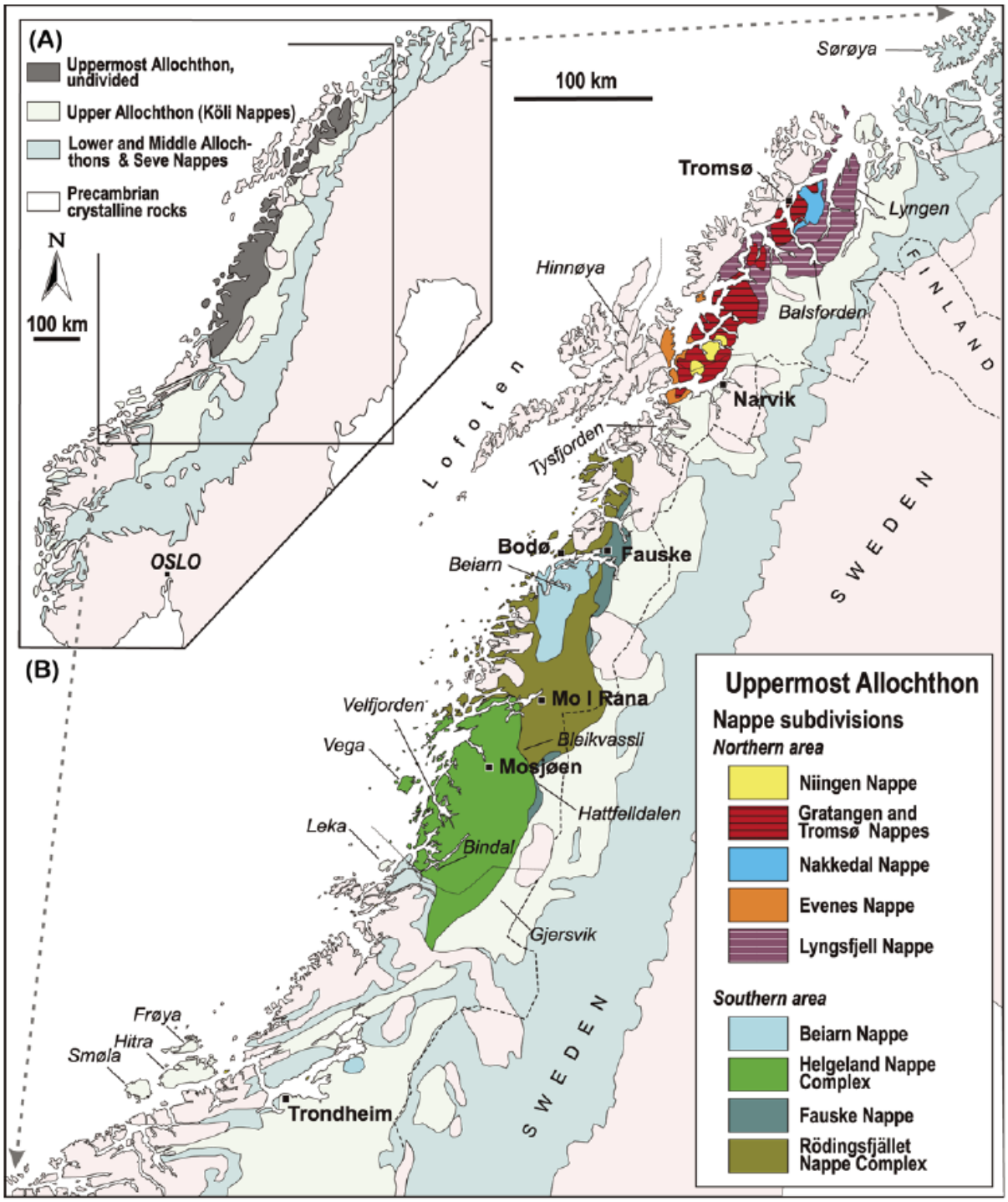

Figure 1 – (A) Geological map showing the main nappes of the Scandinavian Caledonides. Inset marks the area as illustrated in (B), which illustrates the extent of the Uppermost Allochthon and its main nappe subdivisions (reproduced from Roberts et al., 2007).

2.1.3.1 Uppermost Allochthon nappe subdivisions

Tectonostratigraphic subdivisions of the Uppermost Allochthon have been summarized by Roberts et al. (2007, Figure 1). The Helgeland and underlying Rødingsfjellet nappe complex are the main features of the region south of the Tysfjord tectonic window, further consisting of numerous thrust sheets made up of "diverse supracrustal rocks, basement gneisses, and a variety of intrusions" (Roberts et al., 2007, p. 360). Thrust-related mylonitic zones outline the basal contact between the Allochthon and the underlying Köli Nappes in the Upper Allochthon. Subjacent to the Helgeland Nappe Complex of North-Central Norway, such orogen-parallel shear zones have, according to (Osmundsen et al., 2003), been affected by late Scandian extensional shear movements.

The northernmost exposures of the Uppermost Allochthon are represented by the Lyngsfjell, Nakkedal and Tromsø nappes (Zwaan et al., 1998). In the Ofoten region, various tectonically imbricated marbles are found in the Narvik, Evenes, and Niingen nappe complexes (Melezhik et al., 2003). In addition, the marbles are found in association with iron ore-bearing schists, the Håfjellet iron formation (Melezhik et al., 2015). Chemostratigraphic studies have led the authors to suggest that deposition of the marbles and associated iron ores in the Ofoten-area was synchronous to those in the Rana region.

2.1.3.1.1 The Rødingsfjellet Nappe Complex

The Rødingsfjellet Nappe Complex, which covers nearly all of the Rana region, is further subdivided into the Beiarn, Dalselv, Slagfjellet, Plura, Ramnålia, Straumbotn, Tjørnrasta, and Snøfjellet nappes (Søvegjarto et al., 1988, Figure 2). These nappes are characterized by volcano-sedimentary sequences that are believed to derive from the Laurentian continental margin or an unknown microcontinent and were subsequently thrust upon land during the Caledonian Orogeny (Roberts et al., 2007). Lithological assemblages are highly dominated by medium to high-grade marble-schist successions, with iron ore-bearing sequences found in the Ramnålia and Plura nappes (Melezhik et al., 2015). The Ramnålia Nappe is further divided into three units including (from top to bottom) the Ørtfjellet Group, the Dunderland Formation, and the Kjerringfjellet Group (Figure 2), while the Plura Nappe solemnly consists of the Plurdalen Group (Gjelle et al., 1991).

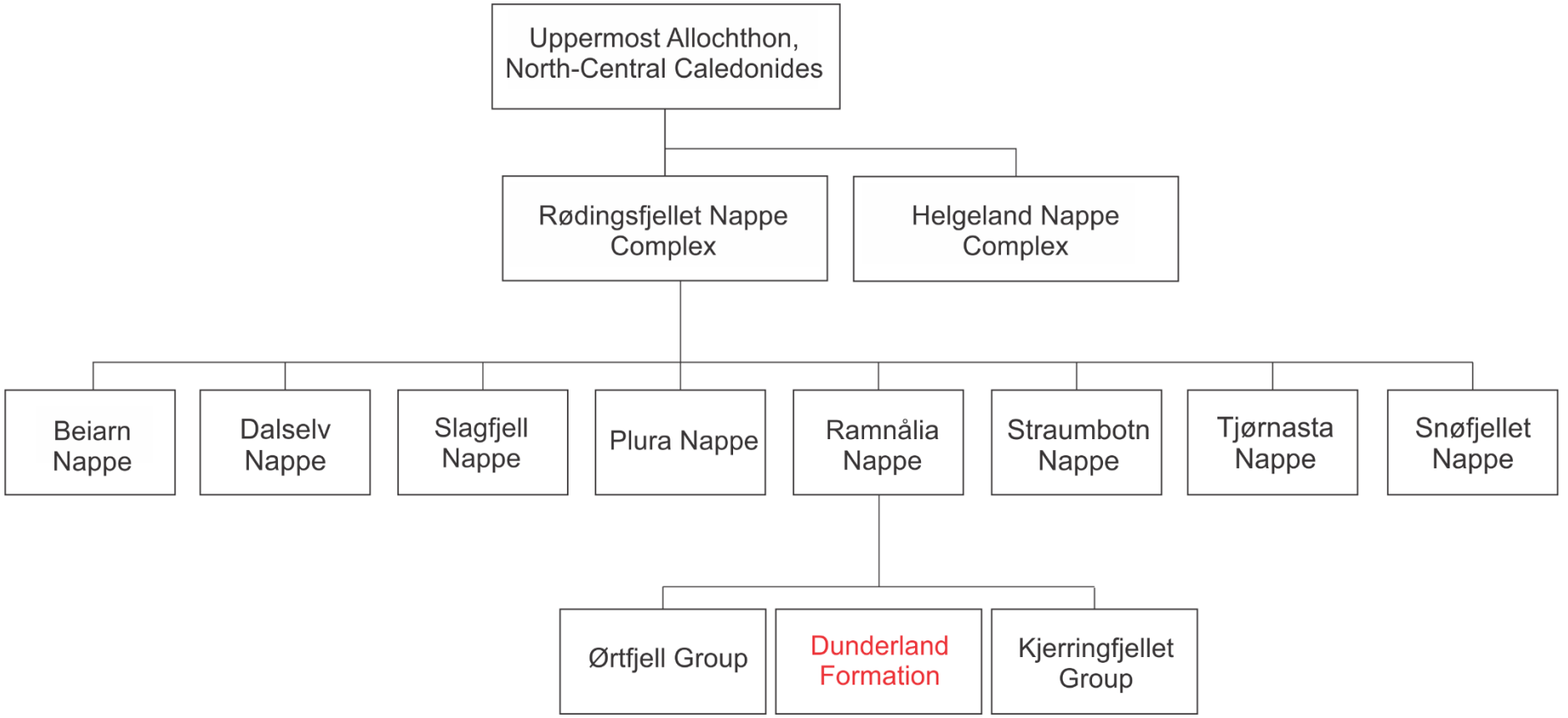

Figure 2 – Schematic illustration of the tectonostratigraphic subdivision of the Rødingsfjellet Nappe Complex, including a subdivision of the ore-bearing sequences of the Ramnålia Nappe (modified after Ellefmo, 2005). The subdivision of the Rødingsfjellet Nappe Complex is after Søvegjarto et al. (1988).

2.1.4 Geology of the Dunderland Formation

The iron mineralization studied within the framework of this project belongs to the Dunderland Formation (Figures 2; 3). As illustrated by Figure 4 (modified after Melezhik et al., 2015) the main ore-bearing lithologic units are dolomitic and calcitic marbles intercalated with various mica schists (Bugge, 1948). The formation has been folded and thrusted in a complex manner and makes up a sizeable antiformal structure (the Dunderland Antiform, Melezhik et al., 2015). Thus, the determination of relative stratigraphic ages has been deemed problematic.

The varieties of amphibolite facies schists in the Dunderland Formation include graphite-mica schists, quartz-oligoclase-mica schists, phosphorous-rich magnetite-hornblende schists, calcareous mica schists containing lenses of dolomite, and pyrrhotite-bearing quartz-garnet mica schists (Gjelle et al., 1991). In addition, numerous thin layers and veinlets of amphibolite, believed to be of intrusive origin, are found dispersed throughout the formation (Bugge, 1948). Although relatively comparable to the lithological assemblages of the Dunderland Formation, the Kjerringfjellet Group additionally contains para-gneisses intruded by post-Caledonian granites, as well as suspected metarhyolites. In the Ørtfjellet Group, a more substantial constituent of psammitic materials makes up barren schist and gneiss-sequences, along with minor marbles (Melezhik et al., 2015).

2.1.4.1 The stratiform iron mineralization of the Dunderland Formation

Iron mineralizations of the Dunderland Formation occur in close association with the aforementioned marble-schist sequences. In addition, the mineralization in the Ørtfjellet-Kvannvatnet mining area is found in contact with basal diamictites (Melezhik et al., 2015). Contacts between host rocks and ore-bodies are either tectonic or conformable. Conformable contacts are represented by thinly banded sequences of unmineralized manganese-rich marble-schists. The ore horizons have been tectonically deformed, and occur as closely associated and disjointed sections in either linear assemblies or isoclinal folds. The folded ore bodies may be "double to tripled in thickness in the hingezones" (Melezhik et al., 2015, p. 273).

The mineralization occurs within two main horizons, characterized by different iron, manganese, and phosphorous-contents (Melezhik et al., 2015, Figure 3). In the upper horizon, magnetite and specular hematite occur, and the P_2O_5 content ranges between 0.4 and 0.9 wt.%. The gangue mineralogy is dominated by quartz, calcite, epidote, and biotite. Local manganese-rich mineralogical assemblages, consisting of spessartine, grünerite, and quartz, are characterized with an MnO content between 5 and 20 wt.% and depletion in Fe_2O_3. The lower horizon is enriched in magnetite and apatite, with P_2O_5 contents exceeding 0.9 wt.%. Magnetite-bearing ores are accompanied by gangue minerals including

quartz, calcite, biotite, hornblende, and grünerite (Bugge, 1978, as cited in Melezhik et al., 2015). The MnO content is usually below 0,2 wt.%. Although the sulfur-

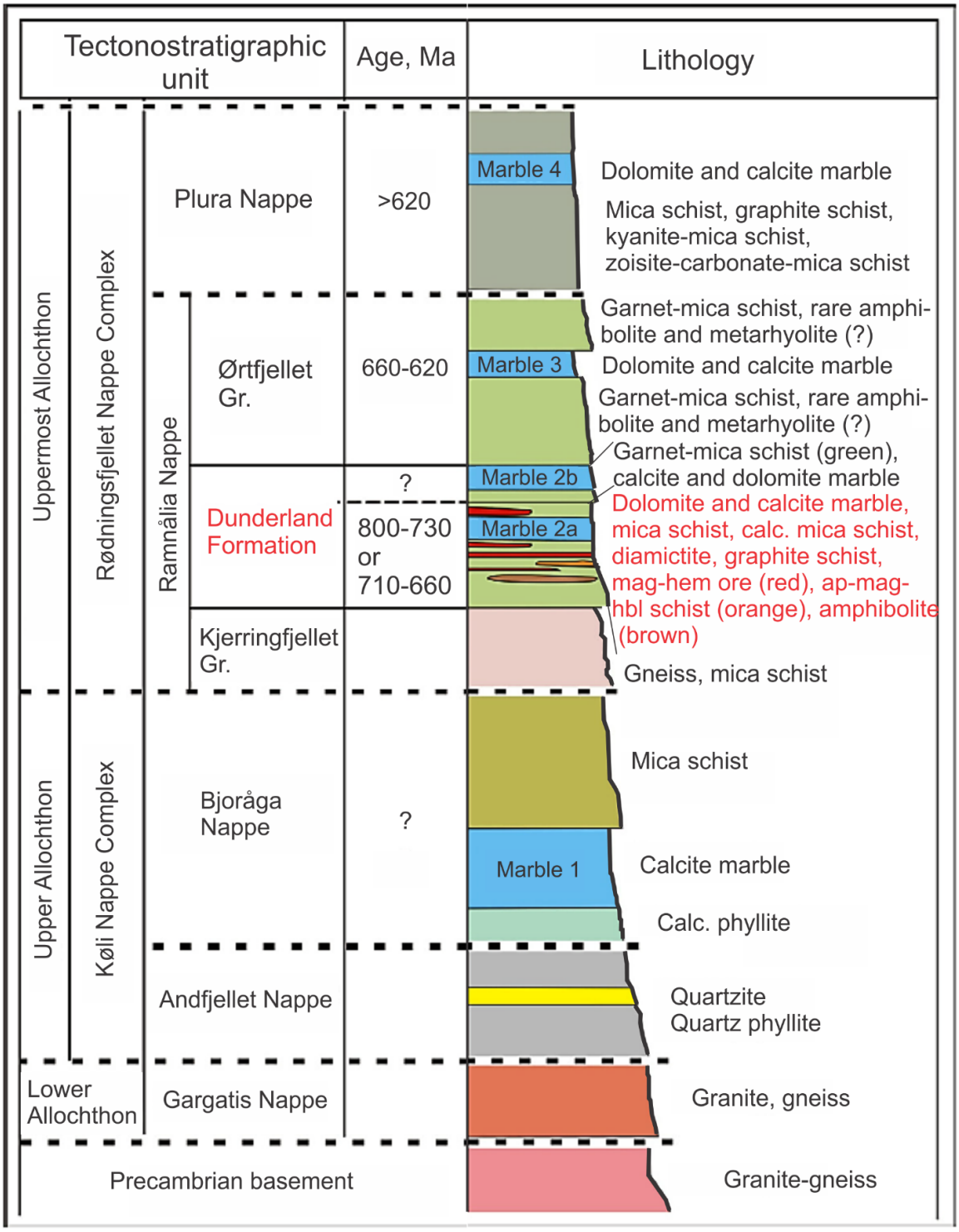

Figure 3 – Simplified tectonostratigraphic column of the Rana region (modified after Melezhik et al., 2015. The figure is based on the work of Søvegjarto et al., 1988, 1989; Gjelle et al., 1991; Marker et al., 2012) The depositional ages of the various marble units were determined by C and Sr isotope chemostratigraphy. The studied Dunderland Formation and its various lithologic units are marked in red.

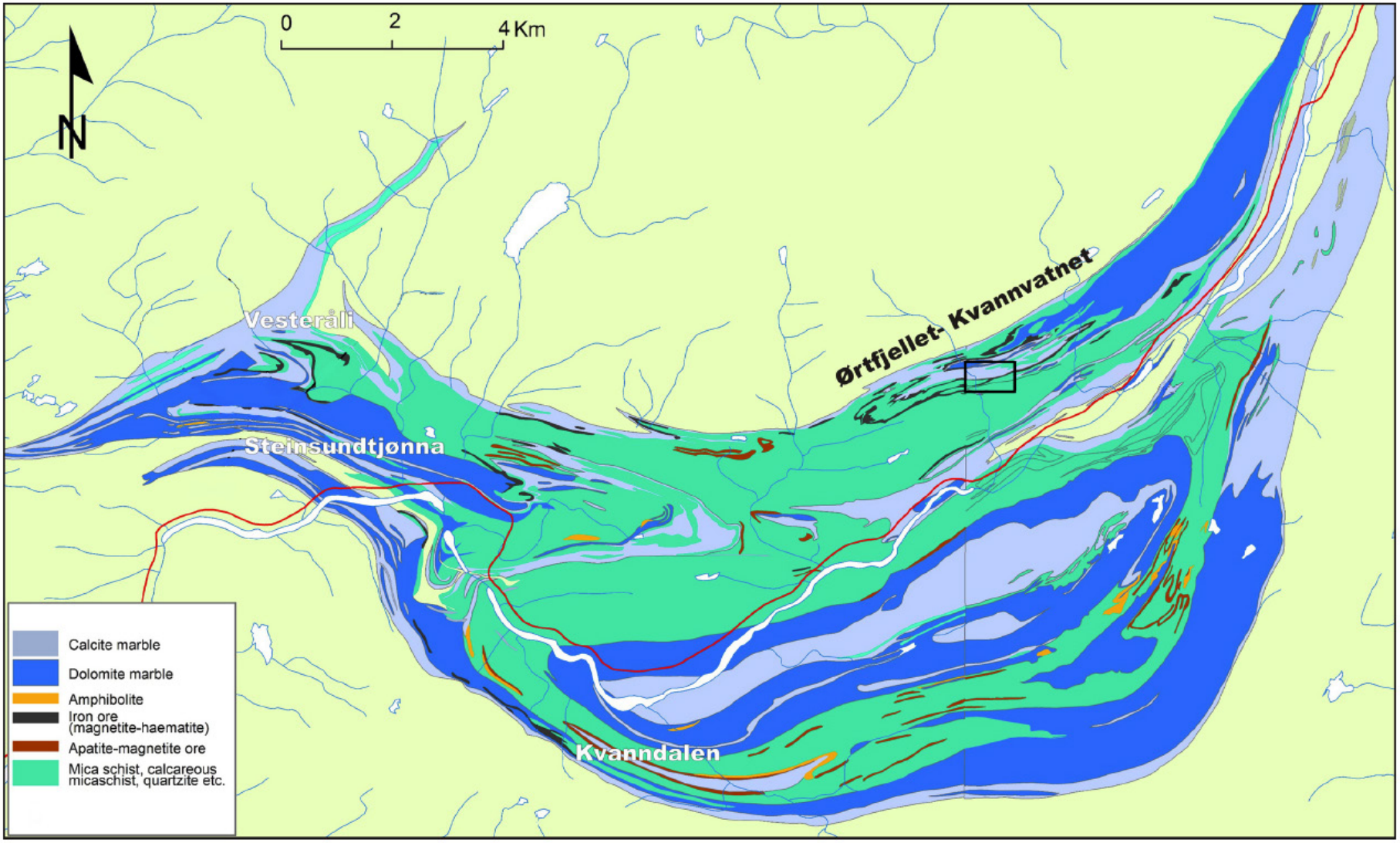

Figure 4 – Regional geological map of the Dunderland Antiform illustrating tectonostratigraphic relationships of iron ore and host rocks (modified after Melezhik et al., 2015). The original geological maps were from Søvegjarto et al. (1988, 1989) and Gjelle et al. (1991). Black rectangle marks the study area of this project.

contents of the iron ores are generally low, local occurrences of between 0.1 to 0.5-meter thick pyrrhotite bands and minor pyrite occur in mica-schists (Bugge, 1948).

Bugge (1948) suggested that the now disjointed and isoclinally folded iron mineralization in the Dunderland Formation belongs to the same stratigraphic horizon. The author argues that polyphase deformation led to the dismemberment of the originally coherent units. In contrary, Melezhik et al. (2015, p. 273) considered the mineralogical and chemical differences between the ore-horizons to represent a "deposition at several closely spaced levels in the original stratigraphy." However, as the authors note, the geological evidence is not unequivocal regarding this matter. While the tectonic deformation has erased any evidence of the original stratigraphic ordering of the units, a relative depositional time-ordering has been documented from the Salangen area, in which IFs rest on top of marble units. Assuming a contemporaneous deposition of the Salangen and Rana lithologic units, this would suggest a younger age of the IFs and diamictites relative to the marble units for the latter (Melezhik et al., 2018).

2.1.4.2 Age constraints

$^{87}Sr/^{86}Sr$ and $\delta^{13}C$ chemostratigraphic analyses of carbonate protoliths within the Upper and Uppermost Allochthons indicate deposition during the Neoproterozoic (800-730 Ma, Melezhik et al., 2018). This interval represents the maximum depositional age of the iron formations and diamictites associated with the mineralized sequences, and conform to other known Neoproterozoic iron formations, such as the Shilu iron deposit, China (Sun et al., 2018). Other marble units within the Uppermost Allochthon exhibit apparent depositional ages ranging from 685 to 600 Ma; however, these marbles lack any spatial association to iron formations (Melezhik et al., 2018).

3 Theoretical background

Iron has been an essential mineral commodity for humankind since the prehistoric Iron Age. The metal has been mined from different types of ore deposits, including banded iron formations (BIFs), Neoproterozoic iron formations (NIFs), sedimentary-exhalative (SEDEX) deposits, iron oxide copper gold (IOCG) deposits, and skarn deposits. The following subchapters will provide the reader with a theoretical background concerning BIFs and NIFs. An introduction to the principles of applied analytical methods is presented in section 3.2.

3.1 Banded iron formations (BIFs) and Neoproterozoic iron formations (NIFs)

James (1954, pp. 239-240) defined the term iron formation as "chemical sediment, typically thin-bedded or laminated, containing 15 percent or more iron of sedimentary origin, commonly but not necessarily containing layers of chert." However, the Archean to Paleoproterozoic (3.8 to 1.8 Ga)

banded iron formations (BIFs) are distinguished from the younger Neoproterozoic (0.85 to 0.7 Ga) iron formations (NIFs) based on several characteristic traits. Ilyin (2009), for instance, remarked that the NIFs are generally found in Phanerozoic orogenic belts, while the older BIFs reside within old platforms and shields. Further, a distinction between the volcanically associated Algoma-type and the sedimentary Lake Superior-type BIFs is made on the basis of the depositional environment (Gross, 1980). NIFs, in contrast, are generally denoted as the glacially associated Rapitan-type iron formations.

According to Konhauser et al. (2017), a subdivision of iron formations is made on the basis of textural characteristics. BIFs, typically of Eoarchaean to Paleoproterozoic ages, are characterized by a well-defined millimeter-scale banded texture. In contrast, iron formations of granular textures, referred to as GIFs, are typically of younger age. Although displaying a distinct granular texture, a banding on a larger scale may still be observed in the GIFs. The general belief is that BIFs were formed in a deep-water marine environment, while GIFs represent a shallow water deposition (Konhauser et al., 2017). NIFs, however, commonly lack the characteristic banding of the older iron formations (Cox et al., 2015). Further, the less abundant Phanerozoic ironstones are typified by ooidal textures and distinctly different mineralogy than that of the Precambrian mineralizations (Young, 1989).

BIFs and NIFs are highly dissimilar with regards to chemistry and mineralogy. Magnetite generally represents the principal iron-bearing phase in the Archean to Paleoproterozoic BIFs. Mineral associations of the BIFs are additionally characterized by substantial amounts of chert, hematite, carbonates, and various iron-silicates. According to Klein (2005), the BIFs show markedly low Al_2O_3 contents (between 0.09 and 1.8 wt.%), indicating an absence of detrital components in the ores. In contrast, the late Proterozoic ferruginous ores almost exclusively consist of quartz and hematite, with small amounts of carbonate (Klein & Beukes, 1993). Moreover, minor magnetite may be present in metamorphosed ores (Cox et al., 2015). Higher Al and Ti contents of NIFs, relative to BIFs, represent more significant detrital inputs (Cox et al., 2015). In addition, many NIFs are enriched in Mn, the latter often occurring in discrete manganese-rich beds (Klein & Ladeira, 2004).

3.1.1 Fundamental constraints

The cessation of BIF deposition at approximately 1,8 Ga marked the beginning of a prolonged stable period coined the "Boring Billion" (Holland, 2006). The reappearance of iron formations in the Neoproterozoic (Figure 5) and their close relation to glacial deposits represent important components of the Snowball Earth theory (Klein & Beukes, 1993). Although different models for these deposits have been suggested, a few fundamental premises still apply for the genesis of iron formations. These basic principles have been summarized by Cox et al. (2013) and include the prerequisite for anoxic and ferruginous basin waters, succeeded by oxidative conditions.

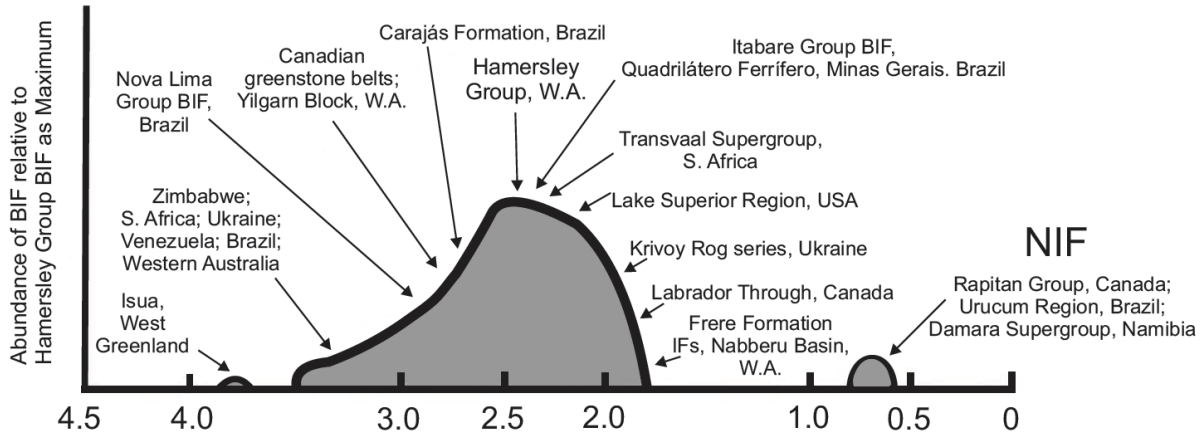

Figure 5 - Schematic diagram illustrating the relative abundance of Precambrian iron formations through time, using the Hamersley Group BIF as maximum (from Klein, 2005).

The preliminary build-up of iron in oceanic basins requires the deep oceanic waters to be anoxic. In such conditions, ferrous iron would accumulate in reservoirs. The accumulation of ferrous iron further necessitates relatively low sulfur activities, as pyrite would be precipitated in euxinic conditions ($H_2S/Fe^{2+} > 2$), which would result in decreased oceanic iron concentrations (Cox et al., 2015). In ferruginous basins ($H_2S/Fe^{2+} <2$), however, abundant ferrous iron would be present, and subsequent oxidation through oceanic circulation would lead to precipitation of insoluble ferric iron.

The mechanisms, by which iron would become oxidized, are not comprehensively understood. Although the different oxidizing mechanisms include both biological and abiotic pathways, the outcome would, in any case, be the precipitation of iron oxyhydroxide. Klein & Beukes (1993), for instance, studied the Neoproterozoic Rapitan IF, which is mostly made up of hematite and chert. Halverson et al. (2011) dismissed oxidative mechanisms that involve pathways associated with substantial biological material for the Rapitan IF and other coeval iron formations. The unlikeliness of biotic pathways is, according to the authors, witnessed by the relative lack of magnetite, which implies restricted accumulation of organic carbon and thereby the absence of dissimilatory iron reduction (Beukes & Gutzmer, 2008). Further, Cox et al. (2015) noted that the hematite of the Rapitan IF was formed through early stage diagenesis and dewatering of iron oxyhydroxides (i.e. goethite).

3.1.2 Models of Neoproterozoic iron formations

The issue of formational conditions for the Neoproterozoic iron formations is a subject of considerable discussion among scientists. Different models have been suggested for the depositional environment, including sedimentary exhalative rifting, Snowball Earth, anoxic sub-glacial outwash, sulfur limitation, continental resurfacing and silled basins (Cox et al., 2013). Based on geochemical data, Cox et al. (2013) argued that the iron formations formed through a combination of hydrothermal activity and detrital

iron source. The reappearance of ferruginous conditions in the Neoproterozoic may thus have been linked with an interplay between rifting, volcanism and glaciation. The various suggested models are presented in the following section.

3.1.2.1 Sedimentary exhalative (SEDEX) ore deposits

A metallogenic model involving rifting of continental crust during the breakup of Rodinia has been proposed by numerous authors (e.g. Breitkopf, 1988; Eyles & Januszczak, 2004; Volkert et al., 2010).

Being one of the two main types of base metal sediment-hosted ore deposits along with Mississippi Valley Type (Wilkinson, 2014), SEDEX deposits account for more than half of the global zinc and lead resources known (Robb, 2005). In addition, the deposits often carry an appreciable quantity of silver (Carne & Cathro, 1982). The principal ore minerals are typically sphalerite and galena, along with minor pyrite (Emsbo et al., 2016). Important Proterozoic occurrences of SEDEX deposits include Broken Hill, Mount Isa, and McArthur River in Australia (Meyer, 1985).

SEDEX deposits "form in sedimentary basins through submarine venting of hydrothermal fluids" (Lyons et al., 2006, p. 170). Their formation has commonly been associated with the extensional setting of intracontinental rifts, exemplified by today's Red Sea environment. In addition, SEDEX deposits of Phanerozoic age typically occur in the Atlantic-type passive margin setting (Wilkinson, 2014). Conversely, major Proterozoic SEDEX deposits, such as the Mount Isa and Broken Hill mineralizations of Australia, have been linked with intracontinental rifts or transtensional basins. Such deposits are characterized by relatively thick basinal sequences of sedimentary rocks and minor volcanics (Yang et al., 2006). The Paleozoic Red Dog Zn-Pb-Ag deposit of Alaska may exemplify stratiform base-metal mineralizations hosted in the passive-margin setting (Robb, 2005). Similar to the intracontinental rift-setting sequences, passive-margin hosted basins are made up of reduced rift-sediment packages underlain by "a basal clastic and/or volcanic-dominated succession" (Wilkinson, 2014, p. 221).

An essential control of SEDEX ore formation is syn-depositional growth faults (Figure 6), represented by geological phenomena such as debris flows and conglomerates. The fault-bounded sedimentary basins and mineralizations are purely associated with continental crust, in contrast to the related volcanogenic massive sulfides (VMS), which form in oceanic crust. Despite the notion of possible intermediate VMS-SEDEX styles of mineralizations, the two end-members are essentially believed to have formed at different points in time and tectonic settings through Earth's history.

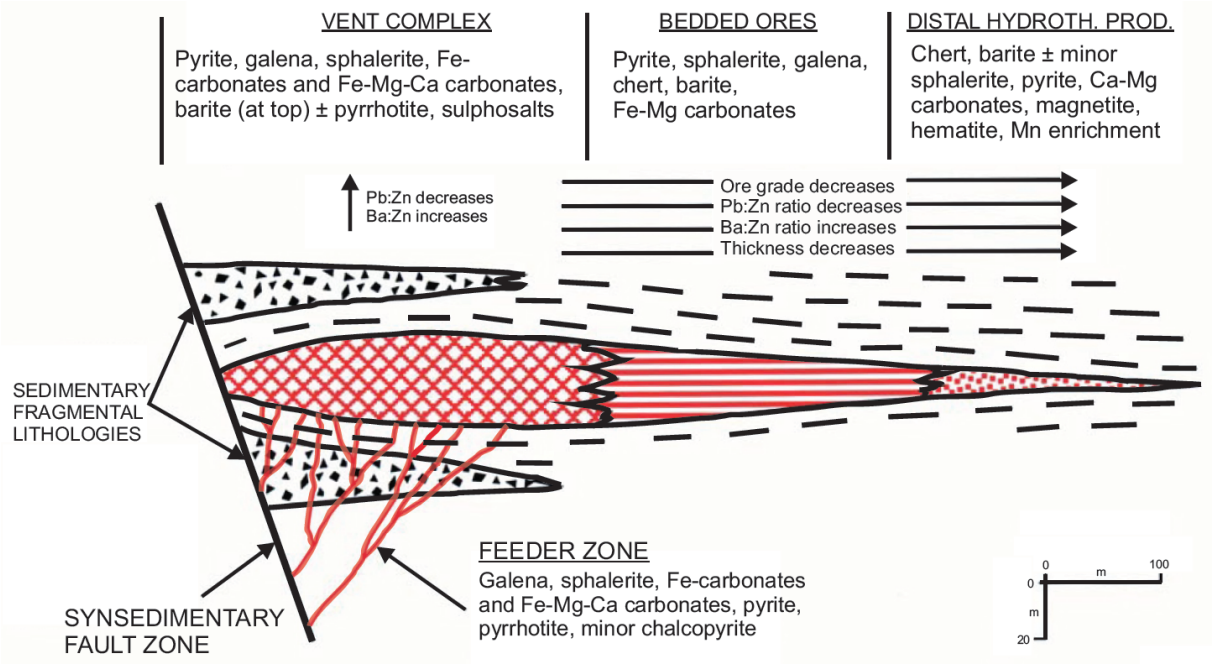

Figure 6 – Schematic diagram illustrating the features of an idealized SEDEX deposit (modified after Lydon, 1996).

SEDEX deposits form distant from volcanic centers (Robb, 2005), and thus the source of metals are solemnly sediments or basement rocks. Although SEDEX deposits generally lack direct links to synchronous volcanism, Cox et al. (2015, p. 246) noted that a "combination of hydrothermal activity, mafic volcanism and/or a preponderance of mafic crust to weather may be key pre-conditions for NIF deposition." As seawater percolates downwards through host rock, metals are dissolved and eventually transported along syn-sedimentary faults acting as conduits for warm metal-bearing hydrothermal fluids (Robb, 2005).

3.1.2.2 Snowball Earth

Similarly to the SEDEX model, a hydrothermal iron source is assumed to be responsible for deep ocean iron accumulation under global ice-house conditions (Cox et al., 2015). Extensive glaciation would have led to reduced oceanic sulfate concentrations (Kump & Seyfried, 2005). A eustatic sea-level fall and depressurization of hydrothermal systems would also add to the increased Fe to S ratio, leading to a buildup of dissolved oceanic iron. As noted by Swanson-Hysell et al. (2010), weathering of Rodinia followed by glacial erosion would also have enhanced the increased Fe to S ratio by an additional supply of Fe-rich sediments to the oceans, also known as the continental resurfacing model. Further, deposition of iron may have occurred due to the ensuing oxygenation of deep waters by oceanic circulation following glacial regression (Klein & Beukes, 1993). Though other authors have suggested alternative models, they all invoke a hydrothermal source of iron. Additionally, a model building upon the accumulation of iron due to the combined effects of decreased S and increased Fe supply to anoxic oceans, without the requisite of glaciation, has also been suggested (Canfield et al., 2008).

3.1.2.3 *Anoxic sub-glacial outwash systems*

Based on stable isotope analyses, Mikucki et al. (2009) suggested that the accumulation of deep oceanic iron may occur through sub-glacial outwash. Ancient, reducing and highly saline iron-bearing brines originating from beneath the East Antarctic Ice Sheet have led to precipitation of iron-hydroxide at the time of mingling with oxygenated fluids. Thus, the biogeochemical processes involved in brine-formation may, according to the authors, serve as a modern analog for Neoproterozoic iron formations. However, Cox et al. (2013) argued that the formation of vast Neoproterozoic iron formations by this mechanism seems improbable, considering the lack of other reported occurrences of ferrous sub-glacial brines.

3.1.2.4 *Restricted basins*

Baldwin et al. (2012) suggested a model which involves restricted or "silled" basins. The model was proposed on the basis of trace element data from the Rapitan IF and involved the buildup of iron in locally confined, anoxic, ice-covered basins. A glacially derived detrital, rather than a hydrothermal source for iron is proposed, with iron precipitating upon oxygenation during glacial regression. While comparable to the Snowball Earth model, the restricted basin model, however, does not require global ice-house conditions to explain the formation of Neoproterozoic iron formations.

3.2 Methodology

3.2.1 Scanning electron microscopy

Compared to visible light, electrons have wavelengths up to five orders of magnitude smaller (Science/AAAS, 2015). Hence, the use of electron microscopes allows for imaging with nm-scale resolution (Stevenson, 2003). Combined with various detectors the SEM technique allows for data acquisition pertaining to sample texture, chemistry, and crystal structure and orientation at an extraordinarily detailed level.

3.2.1.1 *Basic principles of the SEM technique*

The SEM technique utilizes a focused beam of primary electrons scanning across a sample surface, which produces various signals related to electron-sample interaction. The different signals are acquired by installing a variety of detectors, which produce 2D images by collation of point by point scanning. Figure 7 illustrates the SEM-detectable signals produced by the interaction between sample and electrons, which include secondary electrons, backscattered electrons, cathodoluminescence, X-rays, transmitted electrons and backscattered diffracted electrons (Science/AAAS, 2015).

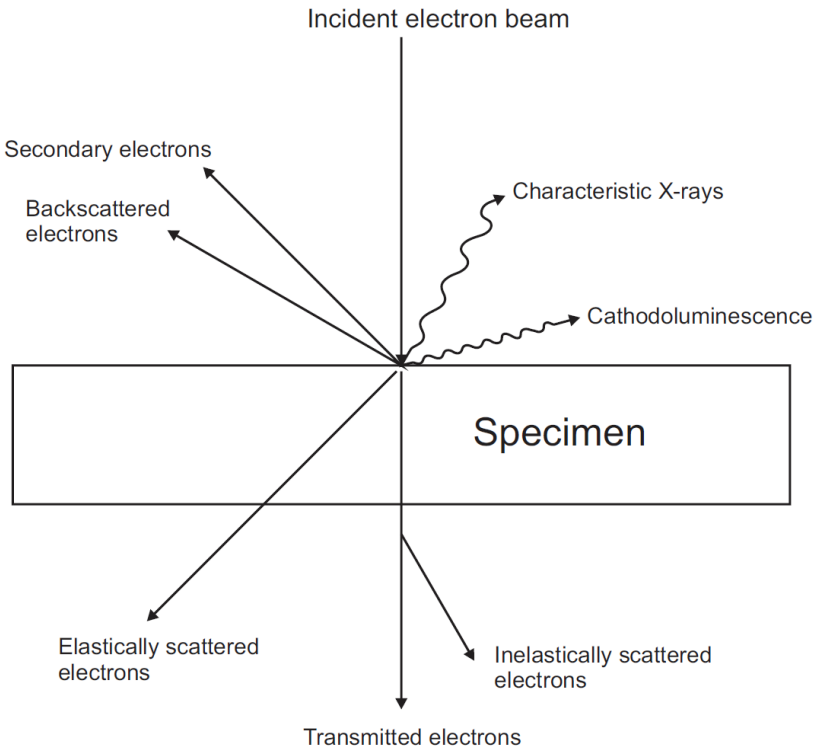

Figure 7 - Schematic diagram illustrating electron-sample interaction signals detectable in SEM (modified after Qureishy, 2012).

3.2.1.1.1 Secondary electrons and backscattered electrons

One of the essential applications of SEM is the study of solid sample surfaces (Collett, 1970). Secondary electrons (SE) are produced from an inelastic interplay between the incident (primary) electron beam and the sample surface and are commonly used to reveal the sample topography (Joy, 1991). The collected signal of the secondary electrons is further amplified to produce images. In contrast, the higher energy backscattered electrons (BSE) result from an elastic scattering and may provide valuable information on the chemical composition of the specimen (Joy, 1991). BSE images are commonly combined with EDS or WDS to obtain high-resolution element distribution maps (Newbury & Ritchie, 2013).

3.2.1.1.2 Cathodoluminescence

Cathodoluminescence (CL) detectors recognize emitted photons of characteristic wavelengths produced by the interaction of incident electrons and luminescent substances and may reveal sample composition, lattice structure and deformation mechanisms (Frelinger et al., 2015). The SEM-CL technique and resulting contrast images may, for instance, reveal textures in quartz that may relate to various precipitation events associated with the evolution of hydrothermal ore deposits (Rusk & Reed, 2002).

3.2.1.1.3 Transmission light microscopy

In relatively thin samples, transmitted electrons may be detected as both scattered and unscattered electrons once they pass through the sample material. Such signals are picked up by scanning transmission electron microscopy (STEM) systems to produce atomic-resolution images and chemical analyses (Browning et al., 1993).

3.2.1.1.4 Energy-dispersive spectroscopy and wavelength-dispersive spectroscopy

Based on the energy spectrum of various elements, X-rays may be detected either using energy-dispersive spectroscopy (EDS) or wavelength-dispersive spectroscopy (WDS) (Newbury & Ritchie, 2013). X-rays of characteristic wavelengths are, according to Egerton (2005), produced when electrons are knocked out of their orbitals and may provide useful information on the composition of the sample (Science/AAAS, 2015). EDS systems work by absorbing the energy of individual X-rays, which are further converted into electrical signals conforming to the X-ray characteristics of the various elements. The EDS technique is commonly put to use in the identification of unknown mineral phases through spot analysis, in addition to providing a semi-quantitative tool for analyzing mineral chemistry. In contrast, WDS utilizes X-ray wavelengths, rather than photon energy. The technique has the advantage of providing narrow X-ray peaks, allowing for accurate estimation of element distribution even at low concentrations (Egerton, 2005).

3.2.1.1.5 Backscatter diffracted electrons

Backscatter diffracted electrons (EBSD) occur as incident electrons are diffracted by the lattice structures of crystalline materials in accordance with Bragg's Law (Randle, 2009). According to Randle (2009), the resulting EBSD patterns project geometries of said lattice planes in Kikuchi diffraction patterns, which reveal information on the structure and crystallographic orientation of analyzed mineral. Combined with pre-existing data sets for the phases of interest and processing software, the EBSD technique allows for phase determination based on crystalline structure, along with the generation of crystal orientation maps (Randle, 2009).

3.2.2 X-ray powder diffraction

The X-ray powder diffraction (XRD) technique is commonly used to study the underlying details of crystallographic structures and atomic spacing (Bunaciu et al., 2015). XRD analysis is based on the interaction between primary monochromatic X-rays and crystalline sample, producing constructive interference according to Bragg's Law (Figure 8): $n\lambda = 2dsin\theta$, where n represents the integer number of wavelength, λ is the wavelength, d is interplanar spacing, and θ is the diffraction angle (Bunaciu et al., 2015).

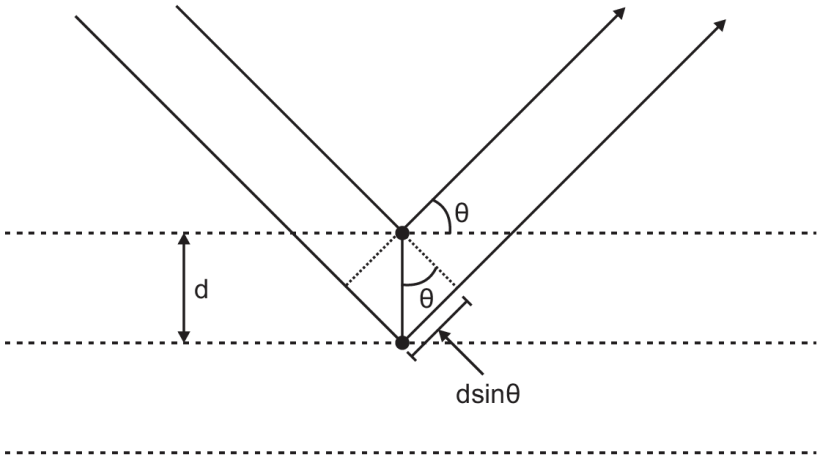

Figure 8 – Schematic representation of the relationship between interplanar spacing (d) and diffraction angle (θ) (modified after Baskaran, 2010).

Bragg's Law expresses the relationship between the wavelength of the electromagnetic radiation, interplanar lattice spacing, and diffraction angle, by scanning the powdered crystalline sample over a spectrum of 2θ, typically between 5 to 70° (Bunaciu et al., 2015). The X-rays diffraction through crystal structures is very much dependent on the arrangement of atoms in unit cells. Further, measured intensities of scattered X-rays are plotted against the range of 2θ-angles to produce XRD patterns that are unique for the phase analyzed.

As unique arrays of lattice spacing characterize different minerals, the XRD technique is most commonly put to use in phase determination of unknown crystalline solids. However, additional applications include determination of unit cell parameters, structural characterization of crystalline solids (i.e. crystallinity), identification of clay minerals and quantitative analysis of phases present (Bunaciu et al., 2015). Due to its wide array of applications, XRD is a valuable tool in mineral exploration.

3.2.3 Stable isotope geochemistry

Isotopes are atoms that have the same number of protons but different numbers of neutrons, and are divided into stable and unstable isotopes (Hoefs, 1980). Atomic species that spontaneously decompose into new elements by radioactive decay are termed radiogenic (unstable), while stable isotopes are species that do not disintegrate into new elements. Variations in isotopic signatures of substances result from physical and chemical processes and may serve as useful tools for investigating, among other subjects, geochemical processes and sources of elements in natural rock samples (O'Neil, 1986). The following section will present a brief description of the principles of stable isotope geochemistry and is largely based on the work of Hoefs (1980), O'Neil (1986) and Kendall & Caldwell (1998).

The isotopic composition of low atomic number elements, such as hydrogen, oxygen, and carbon, is usually reported as δ values, which are formulated by:

$$\delta = \left(\frac{R_x}{R_S} - 1\right) * 1000,$$

where δ is expressed in ‰ or per mille, and R_x/R_S represents heavy to light isotope ratio of the sample relative to a standard ratio value. The δ values may either be negative or positive, with negative values representing samples depleted in heavy isotopes compared to the standards, and vice versa for positive δ values. Depending on the isotopic species analyzed, a variety of standards are utilized to report δ values. For instance, $\delta^{18}O$ values are commonly reported relative to either Standard Mean Ocean Water (SMOW; Craig, 1961) or Vienna-SMOW (VSMOW; Coplen, 1995). $\delta^{13}C$ values are reported relative to either Pee Dee Belemnite (PDB; Craig, 1953) or Vienna-PDB (VPDB; Coplen, 1995).

3.2.3.1 Isotopic fractionation

According to Hoefs (1980, p. 55) "the properties of molecules differing only by isotopic substitution are qualitatively the same, but quantitatively different." Because the various isotopes of an element have different mass, they exhibit slightly different chemical and physical behavior. Stable isotope signatures are therefore mass-dependent, in contrast to nuclear isotope reactions, which are non-mass dependent (Kendall & Caldwell, 1998). Mass-contrasts in low atomic number elements may be of such magnitudes to result in fractionation or alteration of the distribution of various isotopes by a multitude of chemical, physical, and biological processes.

Stable isotope signatures occur as the expression of two principal fractionation mechanisms; isotope exchange reactions or equilibrium fractionation, and kinetic fractionation (O'Neil, 1986). Regardless of fractionation mechanism, mass-contrasts between isotopes result in different strength of chemical bonds for the various isotopic species. For instance, bonds between isotopically lighter isotopes are easier to break than between isotopically heavier equivalents. Thus, isotopic fractionation effects may arise from discrepancies in zero-point energies, which result in contrasting chemical reaction rates of the isotopic species (Kendall & Caldwell, 1998). At relatively low temperatures, such effects may be considerable but become less significant at higher temperatures.

3.2.3.2 Isotope exchange reactions

Isotope exchange reactions are, as according to Hoefs (1980), reactions that redistribute isotopic species among different compounds. Such reactions occur in closed systems at equilibrium (sensu stricto) and may be expressed by the generalized reaction: $aA_1 + bB_2 \rightleftharpoons aA_2 + bB_1$, where the heavy or light molecules (1 and 2) are contained within either compound A or B. The equilibrium constant (K) of this reaction is expressed by:

$$K = \frac{(\frac{A_2}{A_1})^a}{(\frac{B_2}{B_1})^b},$$

where bracketed letters represent molar ratios or concentrations of isotopic species within compound *A* and *B*. The isotope fractionation factor α between phases *A* and *B* expresses the ratio R of heavy to light isotopes between the two compounds in equilibrium systems and is defined by: $\alpha_{A-B} = R_A/R_B$, where R may, for instance, represent ($^{13}C/^{12}C$) or ($^{18}O/^{16}O$). Values of α usually do not diverge significantly from unity and are affected by factors such as temperature, pressure, composition, and crystal structure (Kendall & Caldwell, 1998). Moreover, α is related to the equilibrium constant *K* through the formula: $\alpha = K^{1/n}$, where n represents the total numbers of atoms exchanged in a reaction at equilibrium. The equilibrium constant is highly dependent on temperature, thus holding important implications for geological applications. At higher temperatures, fractionation factors approach 1 (Hoefs, 1980), resulting in smaller fractionation between heavy and light isotopes comparing to reactions at lower temperatures.

3.2.3.3 Kinetic effects

Deviations from the equilibrium isotopic exchange may manifest themselves as isotopic fractionations due to differing reaction rates of isotopic species. Such fractionation is governed by unidirectional kinetic reactions that commonly involve evaporation, dissolution or diffusion (Kendall & Caldwell, 1998). Moreover, the fractionation associated with evaporation or diffusion may, in numerous ways, result from differences in velocities of translational motion of the isotopic molecules passing through phases or phase boundaries (Kendall & Caldwell, 1998). For instance, evaporative isotopic fractionation may result in enrichment of heavy isotopes relative to lighter species due to the higher translational velocities of light molecules. Bonds of lighter isotopes are easier to break compared to those of heavier isotopes. Thus, in disequilibrium systems, the lighter molecules may react at a higher rate and become depleted in the residual reactants. Isotopic fractionation factors during kinetic processes are expressed by the equation: $\alpha = R_p/R_r$, where R_p/R_r represent the heavy to light isotope ratios of the product relative to the reactant.

3.2.3.4 The effect of chemical composition and crystal structure on isotopic signature

According to O'Neil (1977), the isotopic signatures of minerals are highly influenced by their chemical composition and, to some extent, crystal structure. Chemical composition, in particular, is essential due to its control of the nature of chemical bonding. As a rule of thumb, the heavy isotopes are preferentially incorporated into elements characterized by high ionic potentials and low atomic mass, due to their high vibrational energies. Clayton et al. (1972), for instance, stated that such equilibrium

fractionation allows for the application of mineral-pair isotope geothermometry, for example, the ^{18}O-fractionation between quartz and magnetite.

The effects of crystal structure on the isotopic signature are, in most cases, subordinate to the effects of chemical bonding. Nonetheless, heavy isotopes are preferentially incorporated into minerals of well-ordered or closely packed structures (O'Neil, 1977). For instance, one of the most significant isotope effects that arise from the nature of crystal structure may be seen in the contrasting isotope signatures of graphite, diamond and carbon dioxide. Bottinga (1968) has illustrated this effect and notes that diamond is always highly enriched in ^{13}C relative to graphite. In contrast, there is relatively little difference in the carbon isotope fractionation between mineral phases such as aragonite and calcite (Rubinson & Clayton, 1969).

In addition to temperature, chemical composition, and crystal structure, oxidation state and pressure are factors that may additionally affect the isotopic signatures of minerals. Heavy isotopes tend to become enriched in compounds of higher oxidation state; for instance, sulfates will be enriched in ^{34}S relative to sulfides (Kendall & Caldwell, 1998). Moreover, carbonates are commonly more enriched in ^{13}C than accompanying graphite and hydrocarbons. According to Joy & Libby (1960), the effects related to pressure may be observed at low temperatures for the ^{18}O-distribution in the $CaCO_3$-H_2O system, due to volume changes during fractionation. However, the effect of pressure on isotopic signatures has commonly been considered to be minuscule. Due to the seemingly insignificant effect of pressure on isotopic composition, equilibrium mineral-pairs are especially valuable as geothermometers in the cases where there is a lack of knowledge on pressure gradients.

3.2.4 Principles of mass spectrometry

As according to Hoefs (1980), stable isotope compositions are commonly acquired using mass spectrometric methods. The applications of mass spectrometry also extend to a wide variety of analytical issues, including the determination of elemental composition and structural elucidation of molecules and complex mixtures (Kind & Fiehn, 2010). Such analyses are performed by ionization of analyte and generation of accelerated gaseous ions that are separated based on mass-to-charge ratios (m/z).

The components of mass spectrometers are essentially comprised of four different parts (Figure 9). Small amounts of sample are introduced into the *inlet system*, where the components are converted into gaseous ions. The ions are generally produced thermally (i.e. ICP-MS) or by electron bombardment by the *ion source*, and are accelerated to maintain equal kinetic energy. Confined to narrow beams in a high vacuum (10^{-4} to 10^{-6} Torr), the ions are further deflected by a magnetic field and separated by the *mass analyzer*. The extent of deflection is a function of both mass and charge (m/z), in which the

highly charged and low ionic mass species are deflected more compared to low charge and high atomic number ions. Once the ions pass through the magnetic field, they are collected by the *ion detector*, which converts the signals into electrical impulses. These signals are further amplified and recorded by a signal processor.

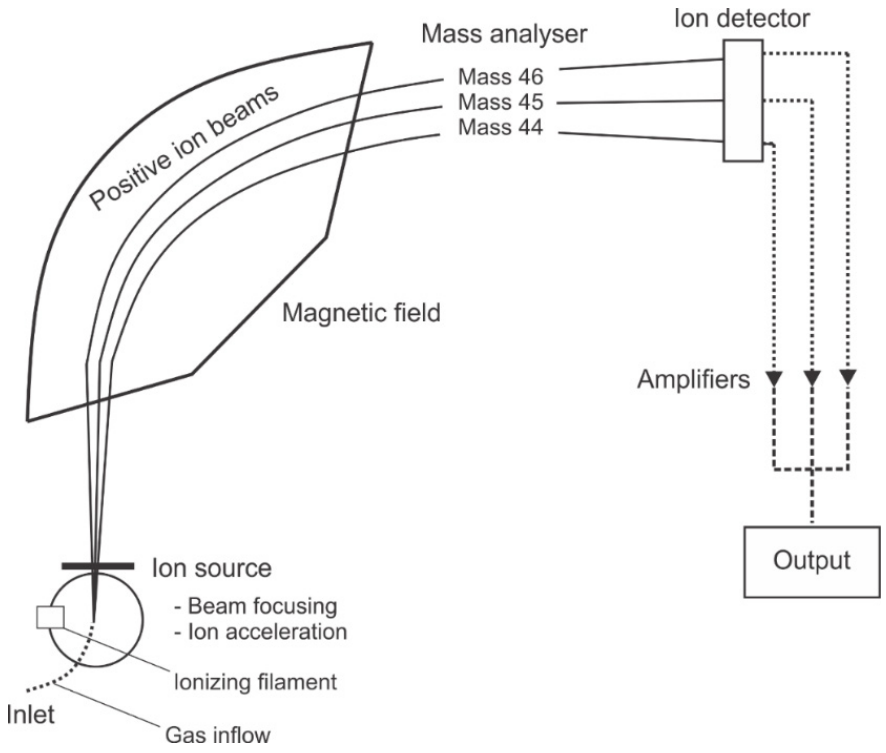

Figure 9 - Schematic diagram illustrating the components of mass spectrometry systems (modified after Coplen et al., 2006).

3.2.5 Fluid inclusion studies

Fluid inclusions (FIs) are naturally occurring droplets of fluids trapped within crystals. As minerals often form in the presence of a liquid or aqueous medium, microscopic samples may become trapped within 3D defects in the crystal lattice during mineral growth or in healed microfractures (Bodnar et al., 2014). Such entrapped fluids may consist of liquid, gas or supercritical fluids of different compositions, including "essentially pure water, brines of various salinity, gas or gas-bearing liquids, and silicate, sulfide or carbonate melts, among others" (Bodnar, 2003a, p. 11). Bodnar (2003a) also extended the term fluid inclusion to comprise any trapped phase that was fluid during the initial temperature and pressure conditions of formation, without concerns for the inclusion properties observed under standard conditions. Resultantly, the term fluid inclusion includes trapped components such as crystallized melt and solid carbon dioxide inclusions.

When conducted appropriately, fluid inclusion studies may provide information about different stages pertaining to rock evolution (Kerkhof & Hein, 2001). Fluid inclusions bring, as according to Fall et al. (2011), one of the most important tools for determining pressure and temperature conditions during

the development of enclosing minerals. In addition, FIs may provide direct insights into the chemical composition and origin of fluids from which host minerals crystallized. In the field of ore geology, for instance, FI studies are particularly applicable in the determination of formation temperature of hydrothermal ore deposits (Bodnar et al., 2014).

3.2.5.1 Fluid inclusion petrography

Microthermometric analysis is the most common technique for analyzing the P-T-X properties of FIs. However, before microthermometric measurements can be performed on representative samples, FIs need to be characterized on the basis of petrographic observations (Kerkhof & Hein, 2001). Goldstein (2003) stated that the most fundamental goal of fluid inclusion studies is to constrain the order of fluid entrapment relative to the host mineral's crystal growth. As such, a distinction between primary, secondary, and pseudosecondary fluid inclusions are made based on textural evidence (Figure 10A). Primary fluid inclusions form during crystal growth and are most notably observed in discrete growth zones. Fluid inclusions, which have formed in fractures after crystal growth has come to a halt, are termed secondary. Secondary inclusions appear in trails or planar arrays that completely crosscut the growth zonation. Lastly, fluid inclusions formed in healed microcracks during actual crystal growth are termed pseudosecondary. From a petrographic point of view, pseudosecondary and secondary inclusions fluid may appear very much alike, though the former is ensued by continued crystal growth. Fluid inclusions in which origin cannot be determined with confidence are said to be indeterminable (Goldstein, 2003). In these cases, applying a fluid inclusion assemblage approach, rather than the primary-secondary terms, is favorable (see section 3.2.5.1.1).

Textural criteria for determination of fluid inclusion origin was proposed by Roedder (1984). Petrographic characterization of fluid inclusions includes several descriptive optical parameters. As illustrated by Figure 10B (modified after Shepherd et al., 1985), one of the most common criterions pertaining to FI petrography is the "the number and types of phases present at room temperature" (Kerkhof & Hein, 2001, p. 30). Alongside vapor (V) and liquid-phases (L), fluid inclusions may contain solids, such as daughter solids, crystalline, and glasseous solids in melt inclusions and solid phases trapped by accident (Goldstein, 2003).

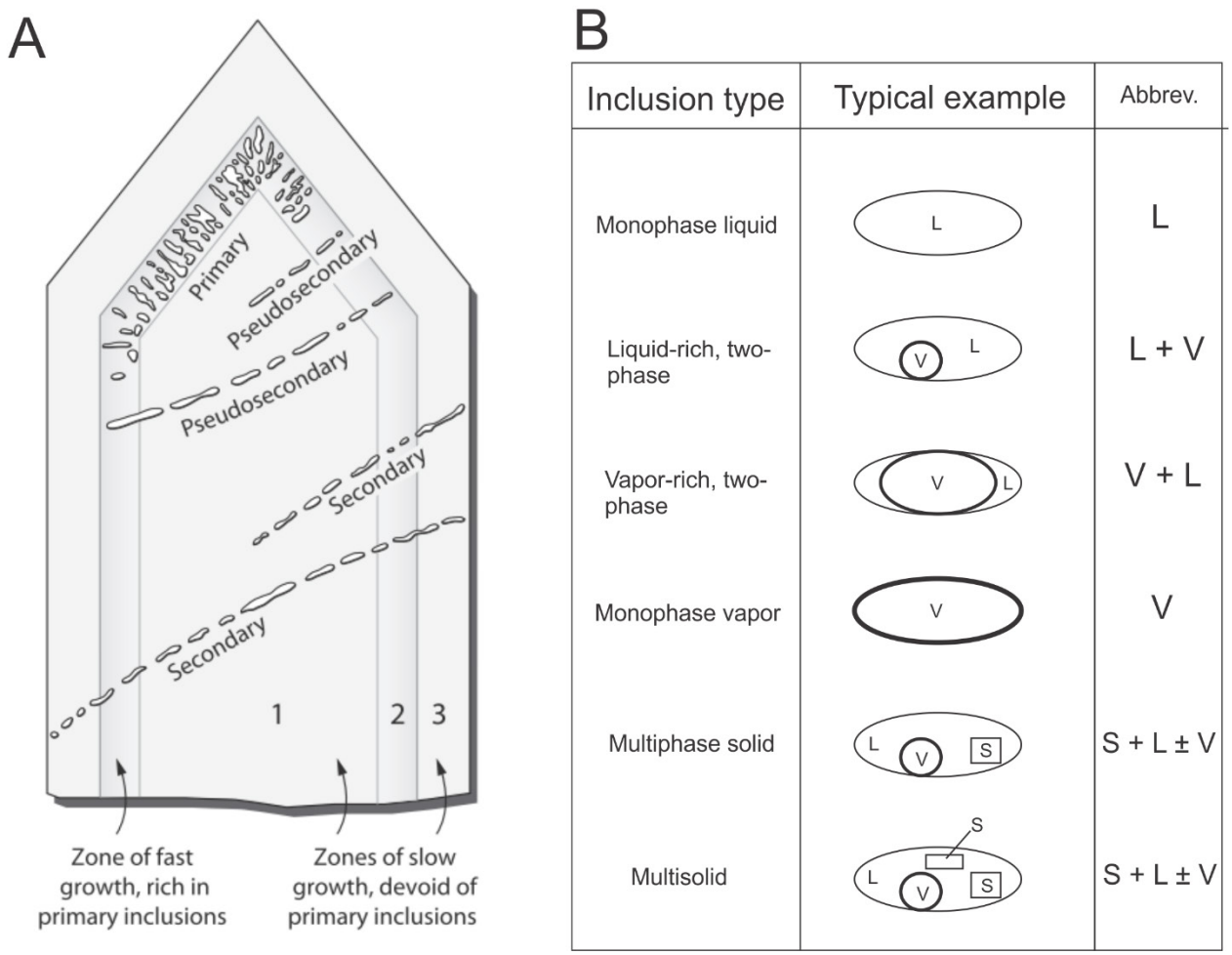

Figure 10 – (A) Schematic diagram illustrating the genetic relationship of primary, secondary and pseudosecondary FIs in quartz displaying concentric growth zonation (reproduced after Lambrecht & Diamond, 2014). (B) Illustration depicting different types of fluid inclusions at room temperature conditions (modified after Shepherd et al., 1985). The textural features of immiscible liquids and glasseous FIs are not shown.

3.2.5.1.1 Fluid inclusion assemblages

Use of the primary-secondary term for genetic classification of fluid inclusions (Figure 10A) in deformed rocks may be difficult to apply, as the term is generally used for non-deformed euhedral crystals (Kerkhof & Hein, 2001). Goldstein & Reynolds (1994, as cited in Bodnar, 2003a, p. 55) introduced the concept of fluid inclusion assemblage (FIA) and defined them as "a group of fluid inclusions that were all trapped at the same time." An FIA thus represents a single fluid event. In defining an FIA, one assumes that inclusions were trapped at the same pressure and temperature conditions, in addition to having relatively similar compositions during entrapment. Such determination is done based on petrographic observations described earlier. Inclusions distributed in a trail that crosscuts the entire crystal, may, for instance, represent an FIA as inclusions were trapped at the same time during fracture healing. As stated by Bodnar (2003a), fluid inclusions distributed randomly within the core of a crystal may, on the other hand, provide less compelling evidence for representing an FIA.

3.2.5.1.2 Roedder's Rules

Fluid inclusion assemblages can be used to investigate the evolution of temperature, pressure, and chemistry of geologic systems through time. For the inclusions to be representative of the entrapped fluid during formation, one has to be confident that post-entrapment re-equilibration has not occurred. For this to be achieved, petrographic and microthermometric observations must conform to "Roedder's Rules", stating that: (1) inclusions were trapped as a homogenous phase; (2) inclusions represent an isochoric system (i.e. inclusion has not changed its volume since it has been entrapped); and (3) no post-entrapment removal from, or addition to, the fluid inclusions has occurred since the inclusion has been entrapped (Bodnar, 2003a). If fluid inclusions display similar phase proportions under room temperature conditions and similar microthermometric behavior, then the fluid inclusions probably adhere to Roedder's Rules. It is also worth noting that fluid inclusion 'type' is not equivalent to the concept of fluid inclusion assemblage. Fluid inclusion type pertains to the numbers and relative ratios of phases in a fluid inclusion under room temperature conditions, e.g. liquid-rich, CO_2-bearing, halite-bearing, and multiphase (Bodnar, lecture, 23.4.2018).

3.2.5.2 Recrystallization and fluid inclusions

As noted above, difficulties often arise during attempts of applying the primary-secondary terms to deformed rocks, because primarily grown phases frequently are not observed. Therefore, the terms 'early' and 'late' may, in many cases, be more suitable to describe the paragenetic sequence of different fluid inclusion generations. As noted by Goldstein (2003), entrapment of fluids often occurs during recrystallization, resulting in an appearance similar to inclusions trapped under normal mineral growth. In these cases, the entrapment of fluids would be primary relative to the recrystallization, and the characterization of fluid inclusions would rightfully be primary. Recognition of recrystallized phases is therefore critical when establishing a paragenetic sequence of fluid inclusions in rock samples. Microcrystalline quartz or amorphous silica, for instance, are often subject to recrystallization during deformation.

3.2.5.3 Fluid inclusion microthermometry

As stated by Roedder (1984, p. 66), "fluid inclusions provide a rich source of small but valuable clues for unraveling past geologic processes." They are most often the only representatives of fluids that circulated and from which rocks crystallized. Thus, fluid inclusions may reveal valuable information on the temperature, pressure, composition, and density (P-T-X) evolution of fluids through geological history. In the study of ore deposits, in particular, fluid inclusions have shown to be an important tool for understanding principal ore-forming processes, and not least in the prospecting of natural mineral resources (Bodnar, 2003b).

3.2.5.4 Basic principles of fluid inclusion microthermometry

In compliance with petrographical observations, microthermometric analyses are frequently applied in the study of fluid inclusions. Microthermometric analyses build upon observations of phase changes in FIs during controlled changes of temperatures (Figure 11), i.e. throughout freezing and heating runs (Shepherd et al., 1985).

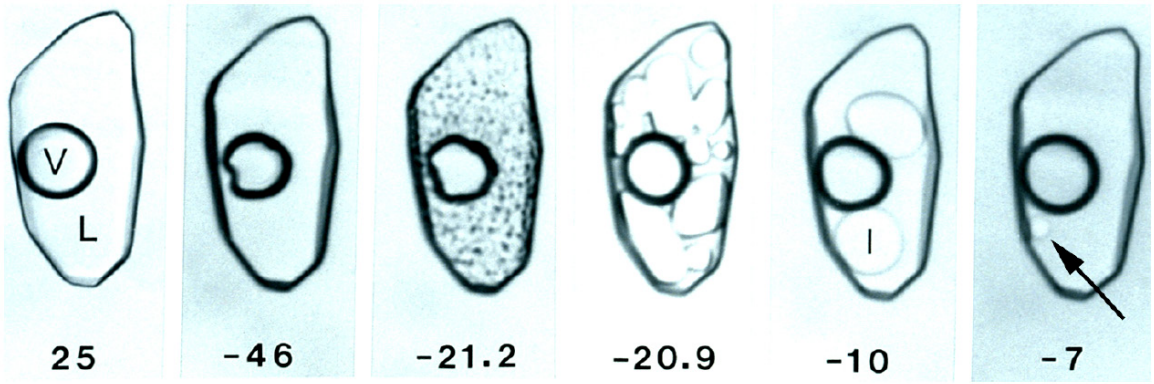

Figure 11 – Phase changes in "an H_2O-NaCl fluid inclusion with a salinity of 10 wt.% during heating from low temperature" (from Bodnar, 2003b, p. 84, I - ice).

3.2.5.4.1 The H_2O-NaCl system

Natural electrolyte systems of various geologic environments commonly contain significant amounts of NaCl, KCl, $CaCl_2$, $MgCl_2$, and LiCl. However, the composition of fluid inclusions is in many cases difficult to determine, and thus salinities are customarily reported as NaCl wt.% equivalents (Shepherd et al., 1985). Moreover, the binary H_2O-NaCl system has been studied extensively, and, as noted by Bodnar (2003b), there is a scarcity of pressure-temperature-composition data for other aqueous electrolyte systems. Therefore, the H_2O-NaCl system is frequently utilized in the interpretation of microthermometric data from fluid systems containing components other than NaCl or KCl.

The solubility curve of the H_2O-NaCl system is presented in Figure 12. The critical curve extends continuously between the critical points of the two end-member components and does not intersect the solubility curve (Morey, 1957). The shaded region represents the complete P-T range where immiscibility, being the co-existence of "higher salinity liquid and lower salinity vapor, is possible" (Bodnar, 2003b, p. 81). The relative size of this region is highly dependent on the salinity, in that higher salinity yields a broader immiscibility region. Whether or not a fluid exists in the immiscibility region depends upon the pressure and temperature conditions of formation, along with fluid composition. A description of how to determine the composition of aqueous fluid inclusion through microthermometry is presented below.

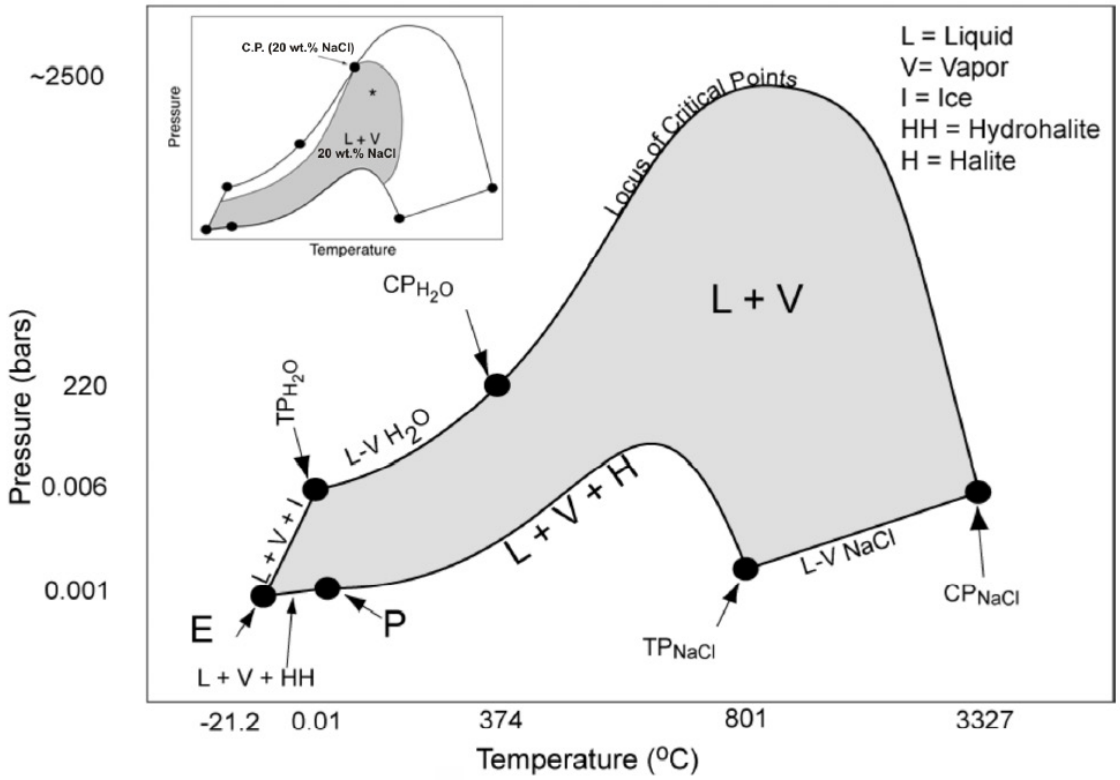

Figure 12 - Pressure-temperature projection of the binary H_2O-NaCl system (from Bodnar, 2003b). The shaded region (of the inset) represents the two-phase field (immiscibility) for fluids with a salinity of 20 wt.% NaCl. A higher salinity would yield a larger immiscibility region.

3.2.5.4.2 Composition, salinity and density of aqueous FIs

In order to interpret microthermometric data, one must be able to estimate the chemical composition of the fluid system, so that one may utilize PVTX-data of the suitable chemical system (Bodnar, 2003b). Composition of FIs directly influence the melting behavior during freezing/heating runs, and may, therefore be used in the estimation of the fluid composition. Temperatures at which the first melting of completely frozen fluid inclusion content occurs, i.e. eutectic temperatures (Shepherd et al., 1985), are direct functions of the chemical constituents present. For instance, the first melting temperature for the binary NaCl-H_2O system occurs at -21.2 °C whereas the three-component $CaCl_2$-NaCl-H_2O system has its eutectic at -55.0 °C.

Final ice-melting temperatures are directly proportional to salinity (for FIs with wt.% NaCl < 23.2%; Figure 13), and the experimental data of Bodnar (1993) may be used to exploit freezing point depressions in salinity estimation. For FIs with salinities in the interval between the eutectic and peritectic composition, i.e. between 23.2 and 26.3 wt. % NaCl, hydrohalite also forms. In these cases, salinity-estimation is performed by utilizing the known relationship between final hydrohalite-melting temperature and concentration of wt.% NaCl equivalents (Sterner et al., 1988). Though, according to Roedder (1984), these phase changes are commonly much slower in comparison to ice melting due to

the metastability of hydrohalite. Salinity-estimation of solid-bearing FIs (>26.3 wt. % NaCl) is done by exploiting the known relationship between halite-melting temperature and salinity, which will be discussed in more detail in section 3.2.5.4.3.

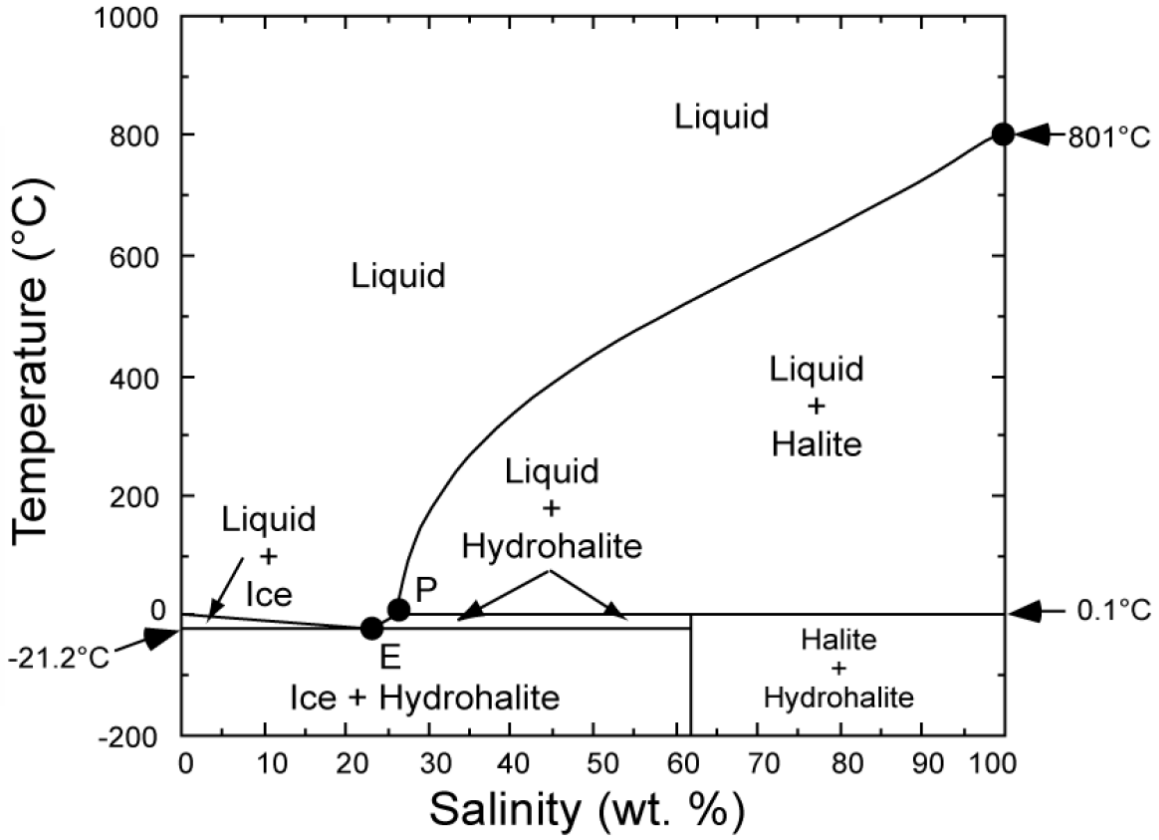

Figure 13 - Temperature-salinity projection of a vapor-saturated H_2O-NaCl system constructed by Bodnar (2003b) based on data from Hall et al. (1988), Sterner et al. (1988) and Bodnar et al. (1989).

Temperatures of homogenization are observed as phase changes during heating runs, which may happen by three different modes of homogenization (Shepherd et al., 1985). FIs that homogenize into liquid (L+V→L) are termed liquid-rich, while those that homogenize to vapor (L+V→V) are termed vapor-rich. Homogenization by critical behavior occurs by gradual disappearance "of the liquid-vapor meniscus (L+V → supercritical fluid)" (Shepherd et al., 1985, p. 64). The mode by which FIs homogenize and the temperature of homogenization itself is directly dependent on the density of fluid or degree of fill.

3.2.5.4.3 Composition, salinity, and density of halite-bearing FIs

In solid-bearing FIs, salinities are obtained by measuring the temperature of daughter mineral dissolution. For instance, Shepherd et al. (1985, pp. 67-68) stated that in "a saturated NaCl-H_2O system the final solution temperature for the halite (Ts_{NaCl}) is directly proportional to the wt.% NaCl in solution." The dissolution temperatures of daughter minerals also depend on the rate of dissolution in liquid and is inherently related to the chemical species that define the system. For example, a halite

crystal will dissolve at higher temperatures in comparison to a sylvite crystal of equal mass (Shepherd et al., 1985).

Salinities may be calculated by the formula provided by Sterner et al. (1988):

$$Wt.\,\%\,NaCl = 26{,}242 + 0{,}4928x + 1{,}42x^2 - 0{,}223x^3 + 0{,}04129x^4 + 0{,}006295x^5 - 0{,}001967x^6 + 0{,}0001112x^7, \quad (1)$$

where x = Ts_{NaCl} (0,1°≤T°C≤770°C). However, this equation is only valid for FIs where halite dissolution and liquid-vapor homogenization occurs at the same temperature, i.e. the homogenization occurs at the halite-liquidus. Though, the equation may be used to approximate salinity, provided that the temperature of homogenization is considerably higher than that of the halite melting (Chou, 1987).

3.2.5.4.4 The H_2O-CO_2-NaCl system

Fluid inclusions represented by the H_2O-CO_2-NaCl system occur in various geological settings, including metamorphic terranes (Roedder, 1984). In contrast to aqueous FIs, the salinity of such FIs cannot be determined from the final ice-melting temperatures, due to the formation of clathrates (CO_2 x $2H_2O$) during freezing runs. As these gas-hydrates incorporate water into their structure, thereby increasing the salinity of residual aqueous phase, the apparent salinity of aqueous phase attained from last ice-melting temperatures will be overestimated (Fall et al., 2011). Fall et al. (2011) noted that the stability of clathrate in FIs approximated by the H_2O-CO_2-NaCl system is determined by temperature, pressure, and salinity (Figure 14).

Calculation of salinities based on clathrate melting temperatures may be carried out using the equation provided by Chen (1972b, as cited in Darling, 1991):

$$Wt.\,\%\,NaCl = 0{,}00098241(10 - T)(T^2 + 45{,}385T + 1588{,}75),$$

where T = final melting temperature of clathrate (-10 to 10°C). A prerequisite for calculating the salinities based on this equation is the known pressure inside an FI during clathrate melting. Thus, the equation is only valid for the FIs in which clathrate melting occurs in the presence of both liquid and vapor CO_2 (Fall et al., 2011), represented by the invariant Q_2 point (Figure 14).

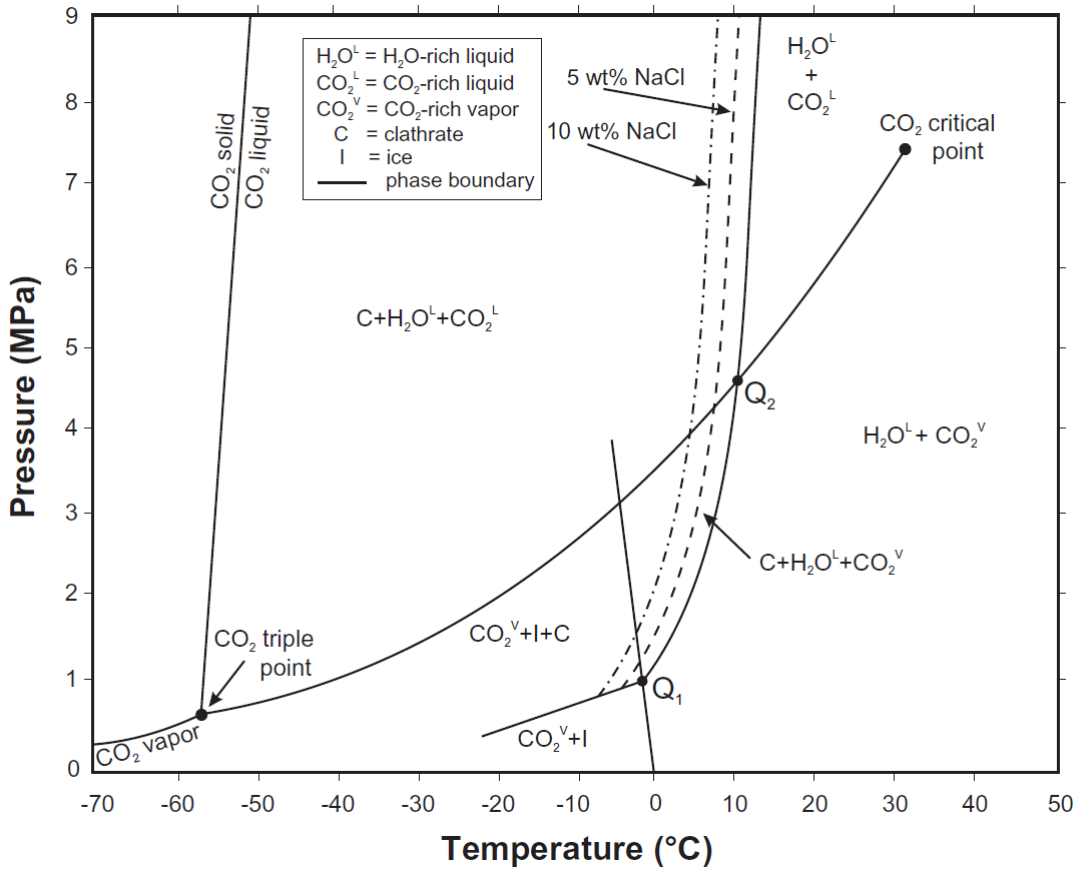

Figure 14 - Pressure-temperature phase diagram of the H_2O-CO_2-NaCl system constructed by Fall et al. (2011) based on data from Chen (1972) and Larsson (1995).

3.2.5.4.5 Calculation of isochores

When there are no indicators of post-entrapment modification and entrapment of FIs in the two-phase field is evident, the temperature of homogenization represents the temperature of entrapment (Bodnar, 2003b). Such FIs are embodied by co-existing vapor and liquid aqueous inclusions representing boiling or immiscible fluid systems, in which the vapor pressure is equal to that of the trapping pressure. However, most FIs are trapped in the single-phase field (Shepherd et al., 1985), and in these cases, the temperature of homogenization represents the minimum temperature of formation. To obtain the actual trapping temperatures, a pressure correction must be made. Such corrections are commonly done by determining the slope of isochores, which represent lines of constant fluid density (Bodnar, 2003b). The starting points of isochores correspond to the measured temperatures of homogenization.

The temperature of homogenization of FIs is a direct indicator of density. Thus, density calculation may be carried out by combining the obtained temperature of homogenization and composition of the representative fluid system (for example H_2O-NaCl) with thermodynamic density data of liquid-vapor curves (Archer, 1992). Given the assumption that the volume of an FI has remained constant, its

density is also directly related to the pressure conditions during entrapment. This relationship could be explained by rewriting the ideal gas law for density (ρ):

$$P = \frac{\rho}{\mu} RT, \qquad (2)$$

where P is pressure, μ is molar mass, R is the ideal gas constant, and T is temperature.

Once fluid density has been calculated, different equations of state for isochore calculation may be utilized depending on the approximation which represents the fluid system, e.g. pure H_2O, H_2O-NaCl or any gas mixture + NaCl. For instance, Bodnar & Vityk (1994) provided an equation to determine the slope of isochores by relating the temperature of homogenization, salinity, and entrapment temperature and pressure for the H_2O-NaCl system:

$$\frac{dP}{dT} = a_s + b_s * Th + c_s * Th^2,$$

where $\frac{dP}{dT}$ (bar/°C) represents the slope of the isochore and a_s, b_s, and c_s are fitting parameters based on salinity, and Th represents the temperature of homogenization.

For FIs approximated by the NaCl-KCl-$CaCl_2$-H_2O system, Zhang & Frantz (1987) relate the molality (m), pressure and temperature of formation to temperature of homogenization (Th) by the equation:

$P = A_1 + A_2 T$, with $A_1 = 6{,}100 * 10^{-3} + (2{,}385 * 10^{-1} - a_1)Th - (2{,}855 * 10^{-3} + a_2)Th^2 - (a_3 Th + a_4 Th^2)m$ and $A_2 = a_1 + a_2 Th + 9{,}888 * 10^{-6} Th^2 + (a_3 + a_4 Th)m$,

where $a_1, a_2, a_3\ and\ a_4$ represent constants of the respective fluid systems. Applying equations, such as the those mentioned, in the determination of isochores allows for valuable investigations on the paragenesis of minerals and their pressure-temperature paths through time.

4 Results

As noted by Bugge (1948), the deposits of the Dunderland Formation have been folded in a complex manner during the Caledonian Orogeny. The structural framework is essential in order to resolve the geochemical characteristics and genetic relations between the Fe-mineralization and its host rocks. The following section will present a brief introduction to the main structural elements observed in the Kvannvatnet mining area, followed by a petrographic description of the various hand specimens sampled (4.2). The ensuing sections present findings from thin section studies (4.3), lithogeochemical analyses (4.4) and carbonate stable isotope geochemistry (4.5). Data from fluid inclusion studies are presented in the final section of this chapter (4.6).

4.1 Introduction to main structural elements and deformation

The main lithologic units and structural features of the investigated Kvannvatnet mining area are presented in the geological map and schematic cross-section below (Figures 15A and 15B, respectively).

The main foliation (S_1) of the study area is characterized by a steeply dipping orientation (Figures 15B; 16A), along with isoclinal folds containing axial surfaces parallel to the main foliation (in accordance with Lindberg, 2014). These macro- to meso- and microscale folds presumably relate to E-W trending shear folding (F_1) of the original banding (S_0) and may represent the main thrusting stage (D_1) during the Caledonian Orogeny (Roberts et al., 2007). Parallel to the F_1-fold axial surface, L_1-stretching lineations have been observed. In addition, this event probably gave rise to complex transposed fold hinges and shear fabrics (Figure 16B).

The main foliation and associated structures are truncated by asymmetric F_2-folds (Figure 16C). These mesoscale E-W trending folds are characterized by north-dipping axial surfaces, along with axial-surface-parallel crenulation cleavage/lineations (S_2/L_2, Lindberg, 2014). The D_2 event probably resulted in the tilting of the entire ore-bearing metasedimentary sequences.

The regional-scale Dunderland Antiform, as illustrated by the geological map of Melezhik et al. (2015, Figure 4), is interpreted to originate from refolding during a late-stage regional-scale NNE-SSW-directed ductile event (D_3), in accordance with Lindberg (2014).

Additionally, a suspected post-D_2 sulfide-mineralized quartz-carbonate vein affected the ore-bearing metasedimentary sequences and was presumably related to late-stage Caledonian uplift and exhumation or extensional collapse (Figure 22). The vein is neither indicated by the geological map nor cross-section below as it was located further east.

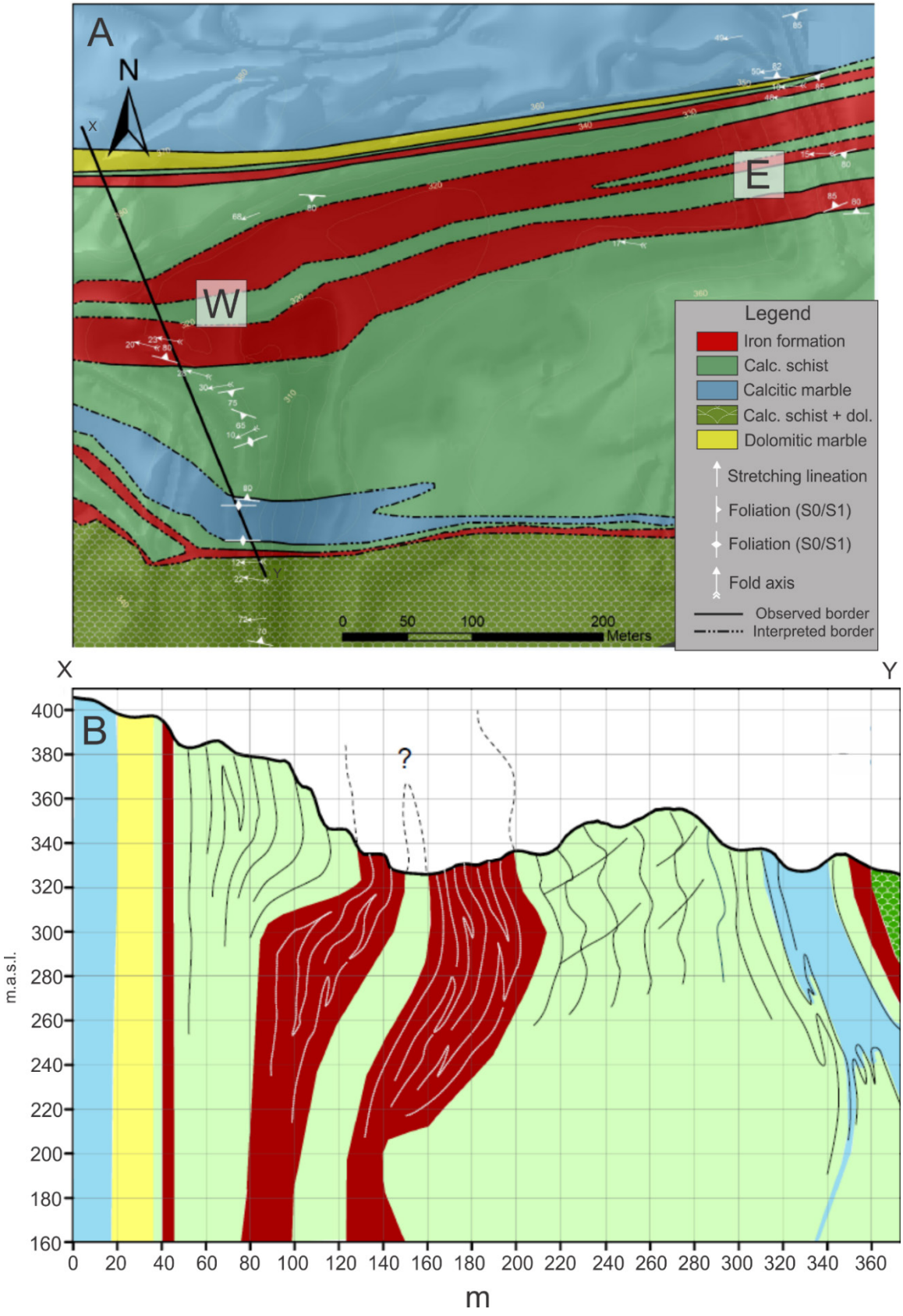

Figure 15 - (A) Geological map of the Kvannvatnet open pit mining area (modified after Søvegjarto, 1973). The main lithologies include iron formations, various types of calcareous schists, and calcitic and dolomitic marbles, in addition to calcareous schists containing lenses of dolomite. (B) Schematic cross-section (line X-Y) displaying the geometry of the ore bodies and host rock lithologic units. The profile was produced based on field observations and data provided by Rana Gruber. Note the presence of isoclinal folds (F_1) with axial surfaces oriented parallel to the steeply dipping main foliation, along with asymmetric F_2-folds typified by N-dipping axial planar surfaces.

Figure 16 – Photographs from the Kvannvatnet open pit mining area illustrating the main structural features of the ore-bearing Dunderland Formation. (A) Eastern wall of the open pit exposing the steeply dipping main (S_0/S_1) foliation of the various rock types, including dolomitic and calcitic marble, calcareous schists and iron formations (IF). (B) An isoclinally sheared dolomitic marble unit typified by steeply south-dipping axial planar (S_1) surfaces (scale of photo is c. 4 m in height). (C) East-facing wall exposing asymmetric, open F_2-folds with N-dipping axial planar surfaces (S_2) in an Mn-enriched zone.

4.2 Sample introduction

The studied samples of the Dunderland Formation (Figure 3) predominantly included various schists exhibiting internal strain variations. Based on hand specimen descriptions these have been subdivided into Mn-rich metapelites, calc-silicate hematite (±magnetite) schists, quartz-hematite schists, and garnet-mica schists. Additionally, calcitic host rock marble and the quartz-carbonate vein of presumed post-D_2 origin were sampled. A more detailed description of the respective hand specimens, including their structural features, is given in the following paragraphs.

4.2.1 Mn-rich metapelites

Fine to medium-grained Mn-rich metapelites were sampled from a discrete zone of Mn-enrichment in the Kvannvatnet open pit area (Figure 17). The samples are commonly characterized by rhythmic bands of fine-grained grey to yellowish brown silicate-carbonate layers in alternation with minor bands of hematite typified by the S_0/S_1 foliation (Figure 17B). The former are predominantly made up of fine-grained garnets and carbonate minerals (± quartz). More coarse-grained ribbons or veinlets of quartz (± carbonate) are aligned in parallel orientation to the main foliation, while late-stage quartz veins cutting across the foliation also occur. In addition to the rhythmical banding, the Mn-rich samples commonly display open asymmetric F_2-folds (Figures 17A; 17C). Additionally, an S_0/S_1-parallel quartz-vein found in close association with calc-silicate schists and a thick unit of calcitic marble was sampled (Figure 18), with the main purpose of obtaining fluid inclusion data.

4.2.2 Calc-silicate hematite (±magnetite) schists

Hematite-rich calc-silicate schists, collected from the open pit and underground mine, are characterized by dark hematite bands in alternation with carbonate-silicate layers oriented along the S_0/S_1 and S_1-foliation (Figure 19). Magnetite is occasionally present in domains parallel to the main foliation in samples (for example sample Rana 1), where the relict banding has been affected by the F_2-event (S_2-axial planar surfaces, Figure 19A). However, magnetite is always a minor component relative to hematite.

Other varieties of sampled calc-silicate hematite schists include fine to medium-grained schistose rocks predominantly composed of intercalated epidote and carbonate-rich layers (±quartz) in alternation with bands of "mirror-like" specular hematite. In such samples, polyphase deformation is witnessed by the presence of refolded isoclinal folds (F_1/F_2, Figure 19D), in which F_1-fold hinges may contain significant amounts of carbonate minerals.

4.2.3 Quartz-hematite schists

Medium-grained, hematite-rich quartzite schists were sampled from the underground mine in the Kvannvatnet mining area. This type of schists displays distinctly foliated textures (S_1), defined by bands of the specular hematite variety (hereby specularite) in alternation with quartzitic layers (Figure 20). The highly abundant specularite give these rocks a silvery or metallic luster. Some of the quartz-hematite schists also contain locally abundant magnetite, though hematite is always the main Fe-bearing phase. The S_1-foliation is occasionally truncated by S_2/L_2-crenulation cleavage/lineations (Figure 20B). Additionally, at least two generations of hematite were observed from hand specimens (Figure 20D), oriented along the S_1- and S_2-foliation, respectively.

4.2.4 Garnet-mica schists and calcitic marble

A garnet-mica schist was sampled from the Kvannvatnet open pit area, characterized by pink garnet porphyroblasts in a medium-grained, dark-grey matrix of quartz and mica (Figures 21A; 21B). The size of the garnet porphyroblasts is commonly around 3-4 mm. Quartz is distributed in thin ribbons parallel to the S_1-foliation in alternation with darker bands of biotite (± muscovite). Presence of highly abundant micas gives the rocks a shiny luster. The garnet-mica schist is found in contact with a dolomitic marble, presumed to be tectonic due to its non-gradational appearance (see Melezhik et al., 2015).

Calcitic marble of the Dunderland Formation, characterized by pale grey colors, coarse grain size, and a massive texture punctuated by millimeter-thick dark bands, was also sampled from the Kvannvatnet open pit area (Figure 21C). The calcitic marble was sampled from a thick, isoclinally folded, marble unit exhibiting rhythmic banding with alternating pale grey and dark grey layers parallel to the steeply dipping main foliation (Marble 2a, Figure 3).

4.2.5 Post-D_2 quartz-carbonate vein

A quartz-carbonate vein/lens truncating the main foliation was sampled from an eastern locality in the Kvannvatnet open pit area (Figure 22A). The sample is characterized by a coarse-grained texture and contains relatively abundant sulfide minerals (such as pyrite) visible to the naked eye (Figures 22B; 22C). It presumably post-dates the D_1 and D_2 events and was formed during a semi-ductile/brittle late Caledonian event. The sampling was predominantly carried out with the purpose of obtaining fluid inclusion data, in addition to determining its mineralogical and geochemical makeup (Figure 22C).

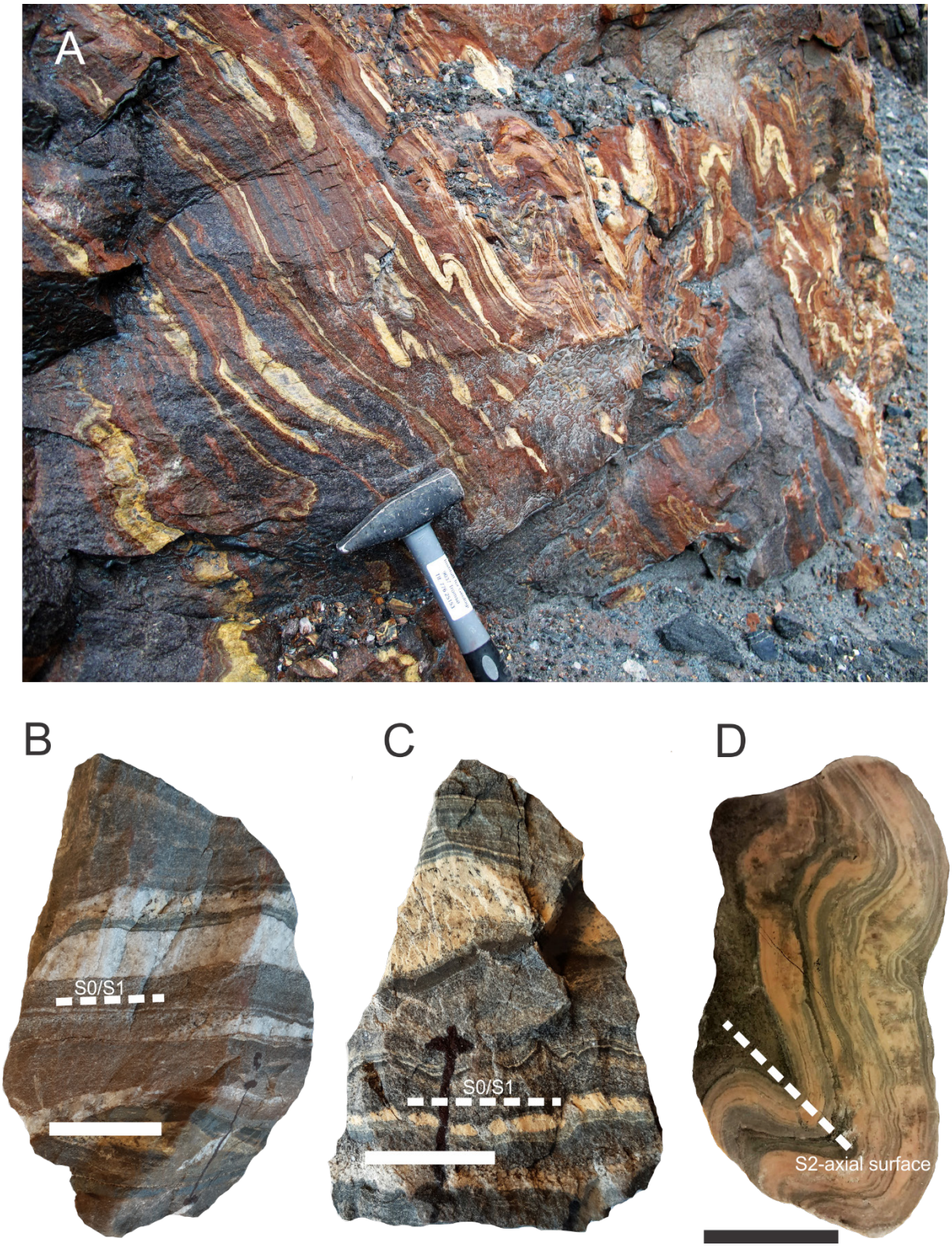

Figure 17 – Representative metapelite samples of the Kvannvatnet open pit mining area. Scale bars in hand specimen photographs are 5 cm. (A) Zone of Mn-enrichment from the western wall, exhibiting parasitic F_2-folds. (B) Mn-rich schist (sample Rana 3) exhibiting fine-grained rhythmic bands of carbonate-silicate admixtures, along with more coarse-grained ribbons of pure quartz parallel to the S_0/S_1 foliation. (C) Mn-rich metapelite with minor bands of hematite (sample Rana 5b). The yellow bands are predominantly composed of fine-grained Mn-bearing garnets along with carbonate minerals. (D) Mn-rich metapelite (sample Rana 4a) displaying open, asymmetric parasitic folds representing larger macroscale F_2-folds in (A).

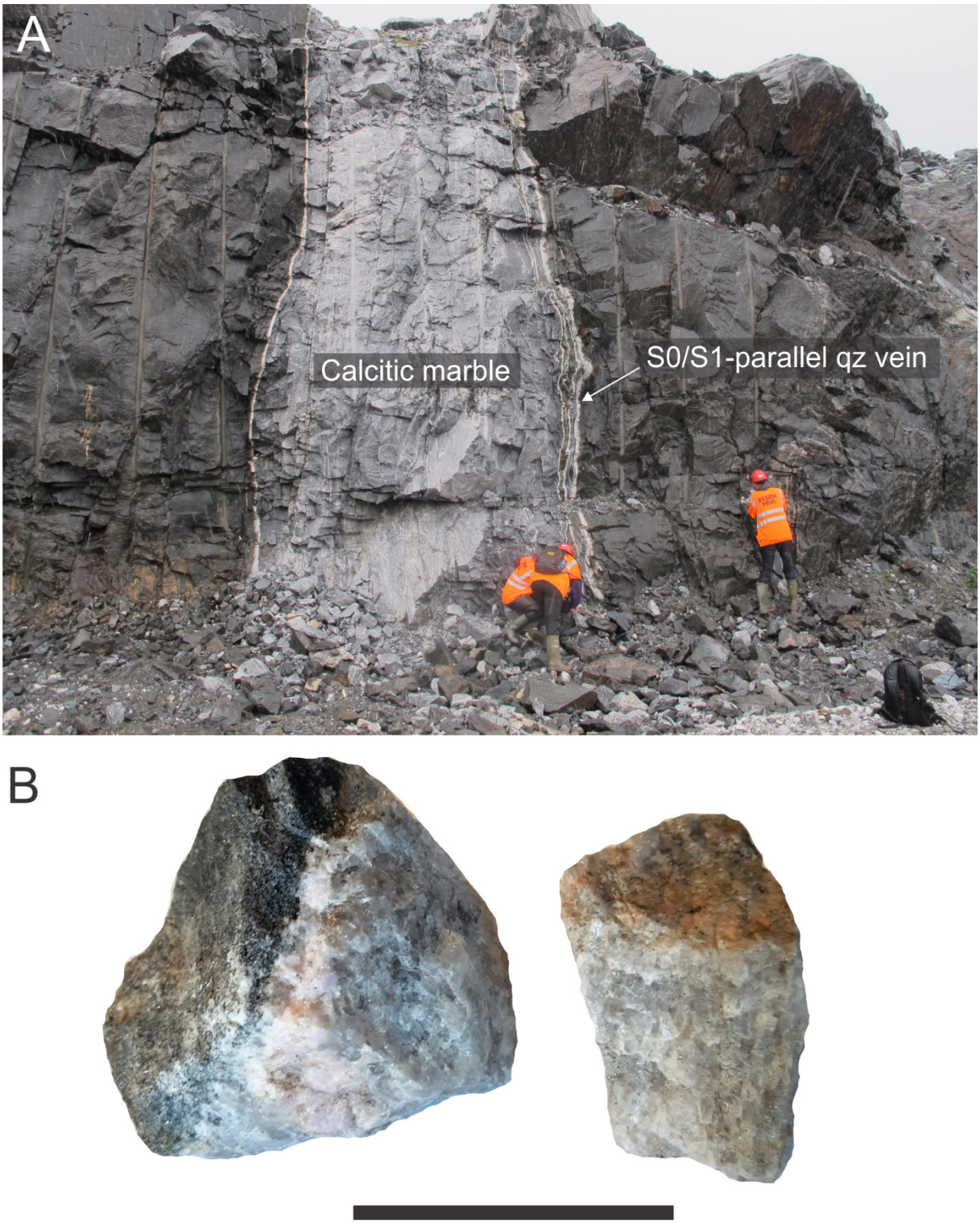

Figure 18 – (A) Photograph of an eastern wall of the Kvannvatnet open pit mining area illustrating the sampling location of an S_0/S_1-parallel quartz vein and (B) sampled hand specimens. (A) The quartz vein is found in close association with a relatively thick, steeply dipping unit of grey-colored calcitic marble oriented parallel to the main foliation (S_0/S_1). (B) Coarse-grained vein quartz hand specimens (sample Rana 13) sampled with the objective of obtaining fluid inclusion data. The scale bar is 5 cm.

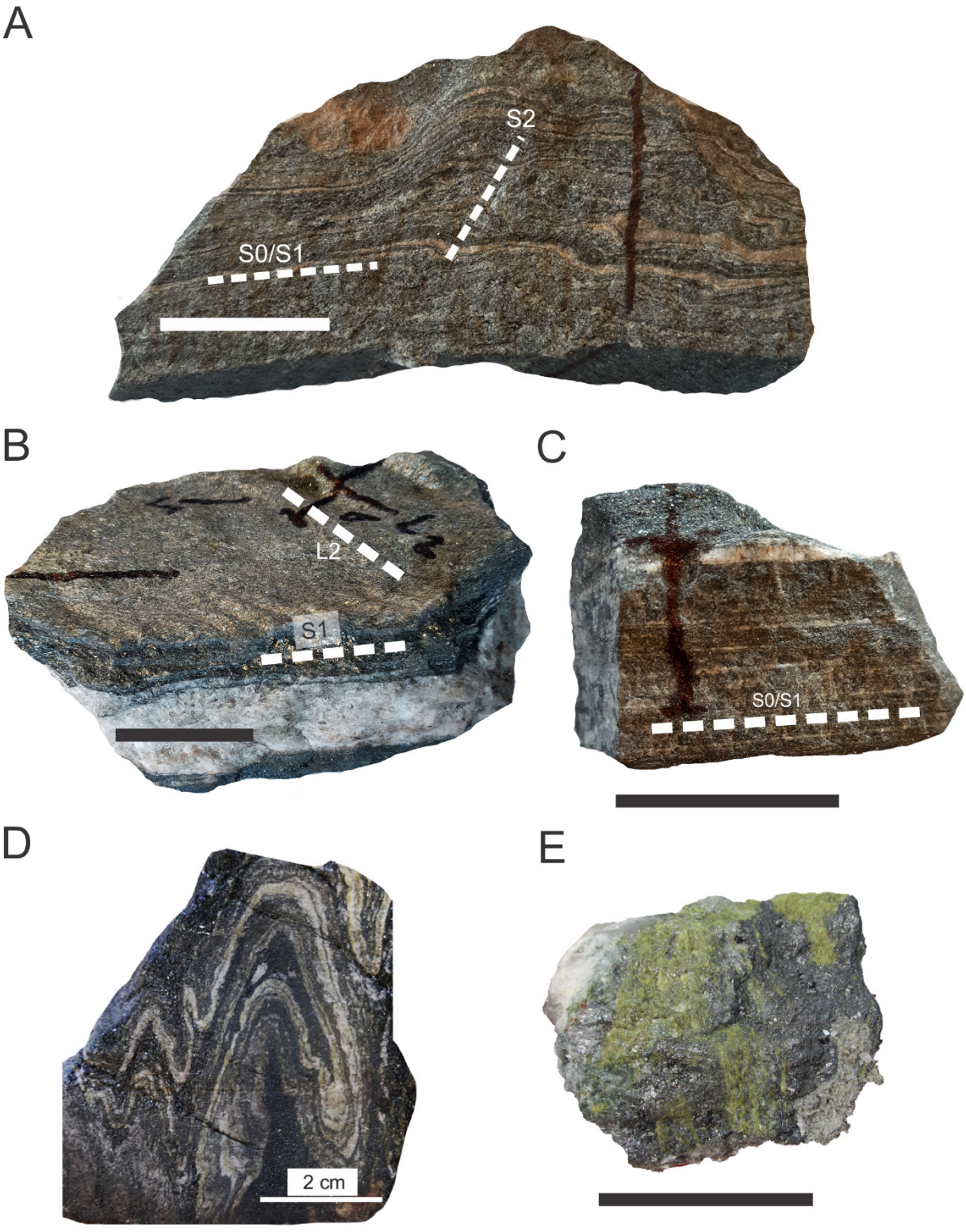

Figure 19 – Various calc-silicate hematite schists sampled from the Kvannvatnet open pit area (scale bars are 5 cm unless otherwise is specified). (A) Medium-grained magnetite-hematite-rich calc-silicate schist (sample Rana 1) characterized by alternating bands of Fe-oxides and silicate-carbonate admixtures oriented parallel to the main foliation (S_0/S_1), along with relatively minuscule F_2-folds (S_2-axial planar surface). (B) Calc-silicate hematite schist (sample Rana 14) comprised of cm-thick bands of tabular hematite alternating with coarse-grained quartz-carbonate layers oriented along the S_0/S_1 foliation. The sample also exhibits L_2-lineations. (C) Calc-silicate schist (sample Rana 2) containing fine-grained hematite, as shown in the top part of the sample. (D) Calc-silicate hematite schist (sample FL 6) exhibiting polyphase deformation and refolding of isoclinal folds (F_1/F_2). Significant amounts of carbonate is present in the F_1-fold hinge. (E) Epidote- and hematite-rich schist (sample Rana 4b) representing a less common, local variety of hematite-bearing rock types from the study area.

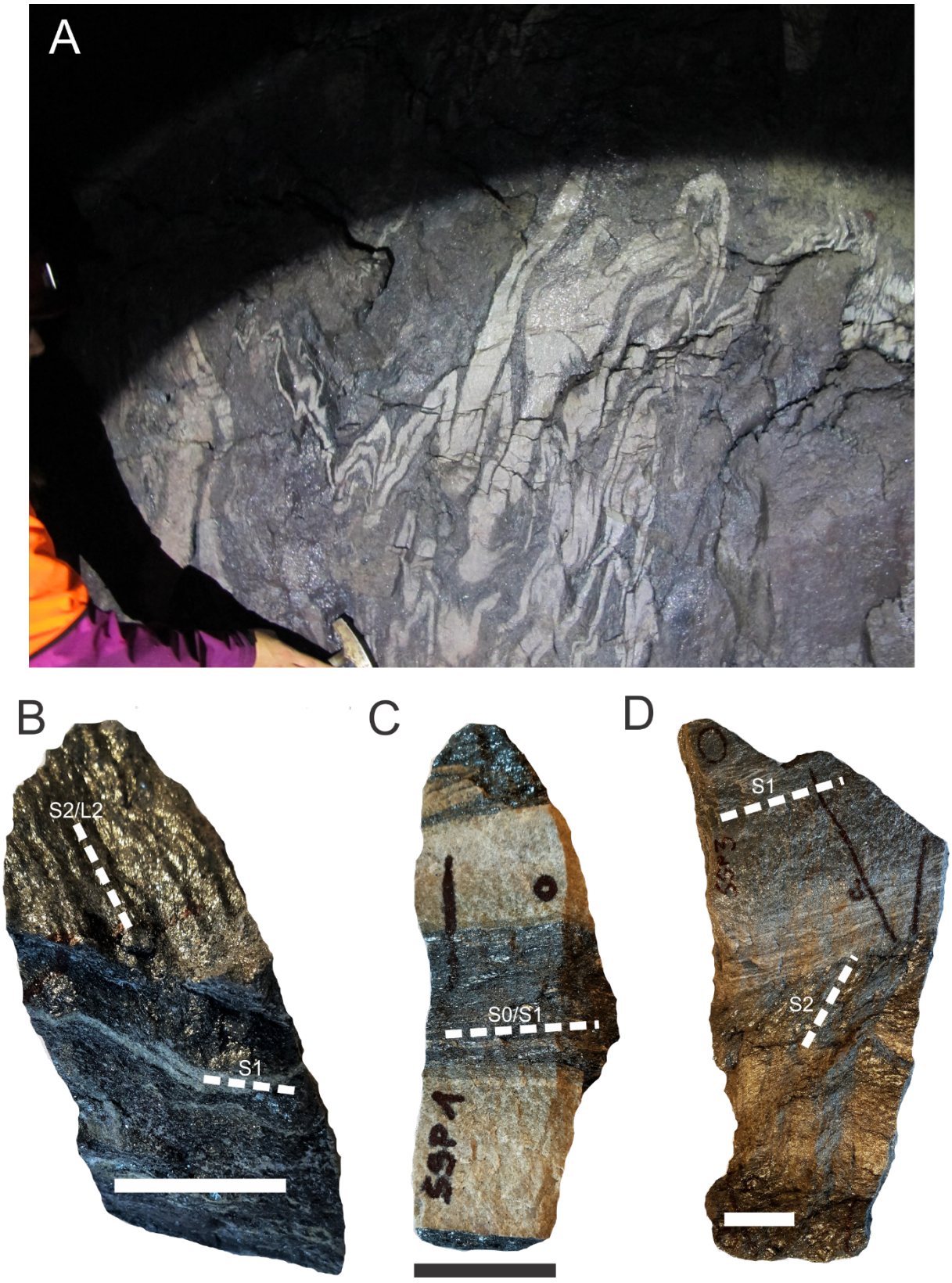

Figure 20 – (A) Photograph of underground outcrop (level 150) illustrating a complex deformational pattern and (B; C; D) representative quartz-hematite schists sampled from the underground mine. Scale bars of the respective hand specimen photographs are 5 cm. (B) Quartz-hematite schist (sample FL 8) displaying S_1-foliation, as illustrated by isoclinal folds of quartz, along with crenulation cleavage/lineations (S_2/L_2, seen in the top part of the sample). (C) Quartz-hematite schist (sample SSP1) characterized by alternations of fine-grained quartz and bands of specularite aligned along the main foliation. (D) Quartz-hematite schist (sample SSP3) displaying two different types of hematite, aligned along the S_1- and S_2-foliation, respectively.

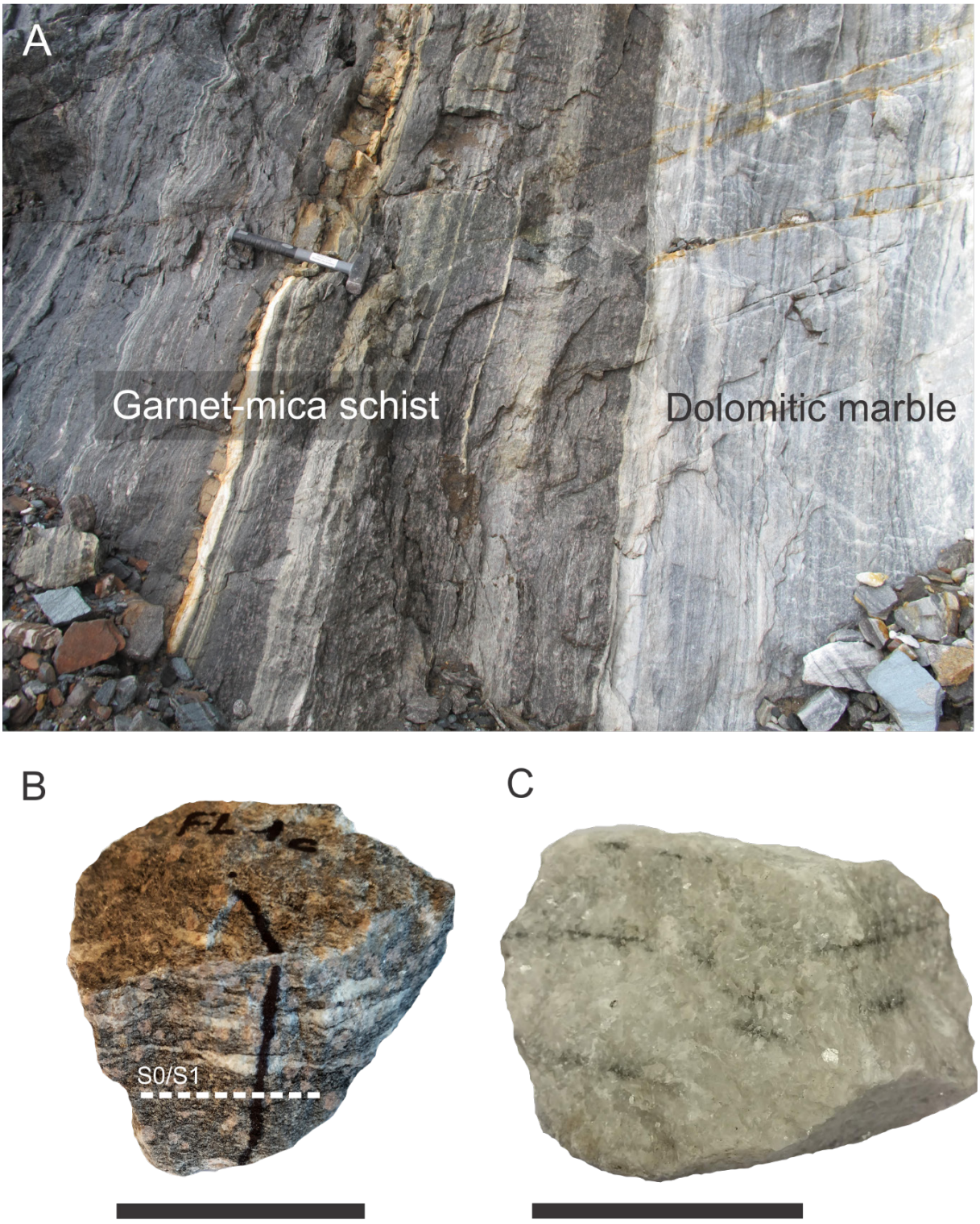

Figure 21 – Photographs illustrating (A) the sharp contact between the garnet-mica schist and dolomitic marble in the Kvannvatnet open pit area, and (B; C) hand specimen of a garnet-mica schist and calcitic marble, respectively (Scale bars are 5 cm). (A) The contact has been presumed to be tectonic rather than depositional due its non-gradational nature. (B) Garnet-mica schist (sample FL 1c) displaying large garnet porphyroblasts in a fine-grained matrix of quartz and biotite (±muscovite) defining the S_0/S_1 foliation. (C) Calcitic host rock marble (sample Rana 12) characterized by coarse grains and a pale grey color, along with thin bands of dark minerals distributed parallel to the main foliation (S_0/S_1). Please note that the sampled marble is not the same as the dolomitic marble illustrated in (A).

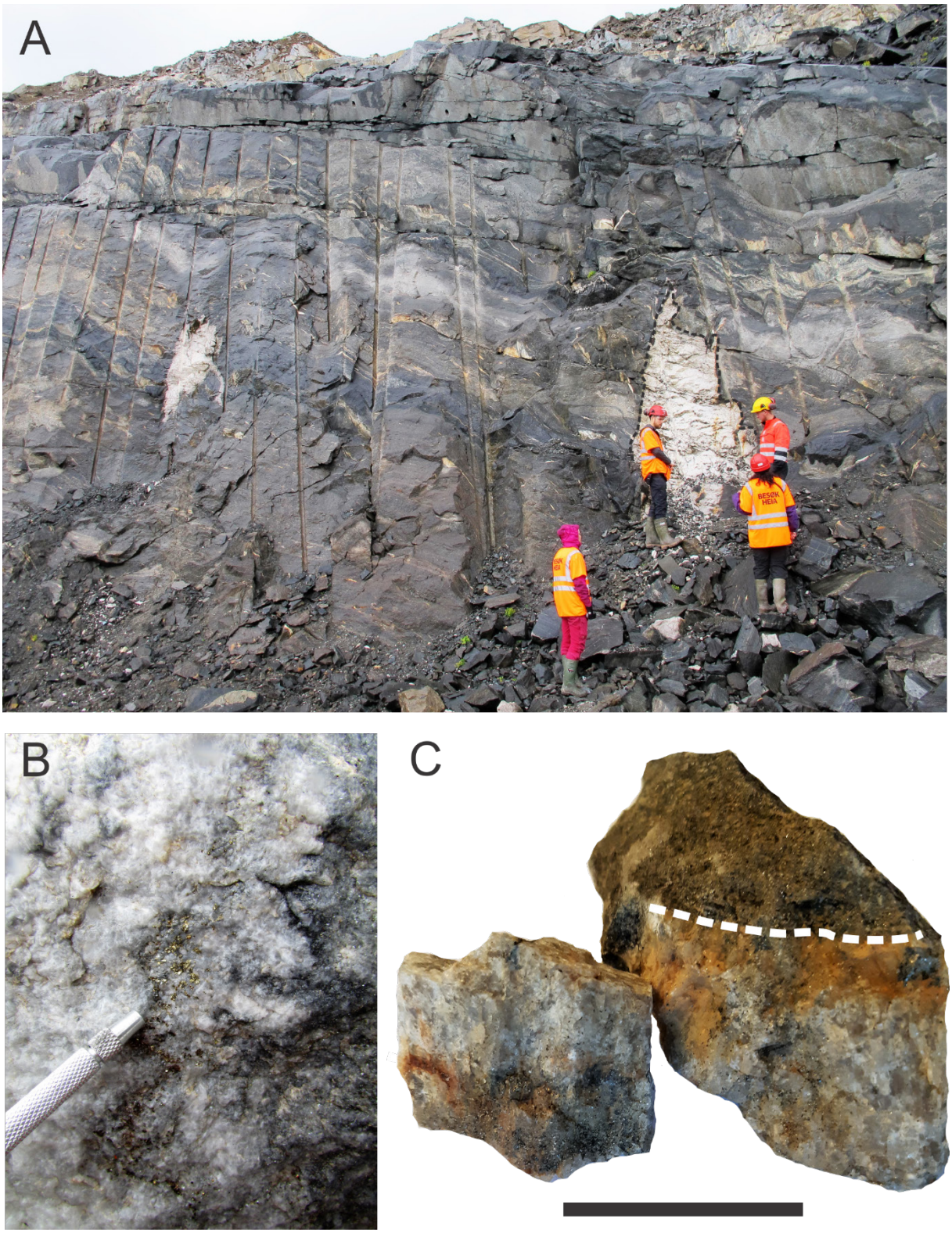

Figure 22 – Photographs presenting the sampled post-D_2 quartz-carbonate vein. (A) The quartz-carbonate vein/lens (outlined by stippled lines) cuts across the foliation and thus believed to be of post-D_2 origin. (B) Close-up of quartz-carbonate vein displaying abundant sulfide mineralizations (e.g. pyrite, chalcopyrite). (C) Sample from the vein (sample Rana 10) characterized by the presence of coarse-grained quartz and carbonate minerals (scale bar is 5 cm). The stippled line represents the contact between the vein and the surrounding schist.

4.3 Mineralogical description

The following mineralogical description is based on observations from transmitted and reflected light microscopy, and data from SEM-EDS, SEM-EBSD and XRD analyses. The description of the gangue mineralogy is initially given with respect to the main lithologic units introduced in the preceding paragraphs. Further, internal strain variations in the ore body have given rise to various texturally distinct Fe-oxides. The mineralogical description of the ore mineralogy is presented within a structural framework which includes S_0/S_1, F_1/S_1, and F_2/S_2 domains. A summary of the main mineralogical features is given in Table 2 below. Mineral abbreviations are presented in Appendix B.

Table 2 – Summary of mineralogical assemblages for the various lithologic units.

Lithology	Major phases	Accessory phases
Mn-rich metapelite	Grt, Cb, Qz, Fsp, Bt, ±Ep, **Hem**	Ms, Ap, Czo, Rho, Amp,
Calc-silicate hematite schist	Qz, Cb, Ep, Hbl, Bt, Fsp, **Hem**, **Mag**	Py, Cpp, Cct
Quartz-hematite schist	Qz, **Hem**	Cb, Bt, Ms, Ep
Garnet-mica schist	Bt, Qz, Grt, Cb	Fsp, Ms, Czo, Py
Post-D_2 quartz-carbonate vein	Qz, Cb	Bt, Chl, Czo, Fsp, Py, Po, Ccp, Rt

4.3.1 Gangue mineralogy

4.3.1.1 Mn-rich metapelites

Common gangue minerals in the Mn-rich metapelite samples include garnet, carbonate, quartz, feldspar, and biotite, along with varying amounts of epidote. Apatite, clinozoisite, rhodonite, and amphibole represent accessory phases. In addition, small occurrences of C-rich infillings may represent organic matter (Figure 23C).

A predominance of garnet (≥50 vol.%) and carbonate (~20 vol.%) is evident in the Mn-rich metapelite samples (Figure 23). Garnets occur as fine-grained, brown-colored aggregates of cubic grains, while carbonate is present as subhedral to anhedral interstitial grains in S_0/S_1-parallel garnet bands. While generally exhibiting creamy white interference colors, the carbonates are distinguished by their pastel-colored grain edges in cross-polarized light (XPL). The grain size of individual garnets and carbonate minerals generally ranges from less than 10 µm up to 25 µm in rhythmically banded samples (Figure 23A). However, in Mn-rich metapelite typified by F_2-domains, the grain size of the garnets is more massive and generally ranges from 50 to 100 µm. Moreover, in some sections euhedral to subhedral garnets up to 600 µm occur in polymineralic domains, in close association with epidote, carbonate, and quartz (Figure 23B). Minor amounts of apatite have also been observed in close proximity to these garnets. SEM-EDS elemental analyses could indicate that the composition of garnet, observed in spatial association with Ca-Mn carbonates, could approximate that of spessartine ($Mn_3Al_2Si_3O_{12}$, Figures 23C; 23D; Appendix C).

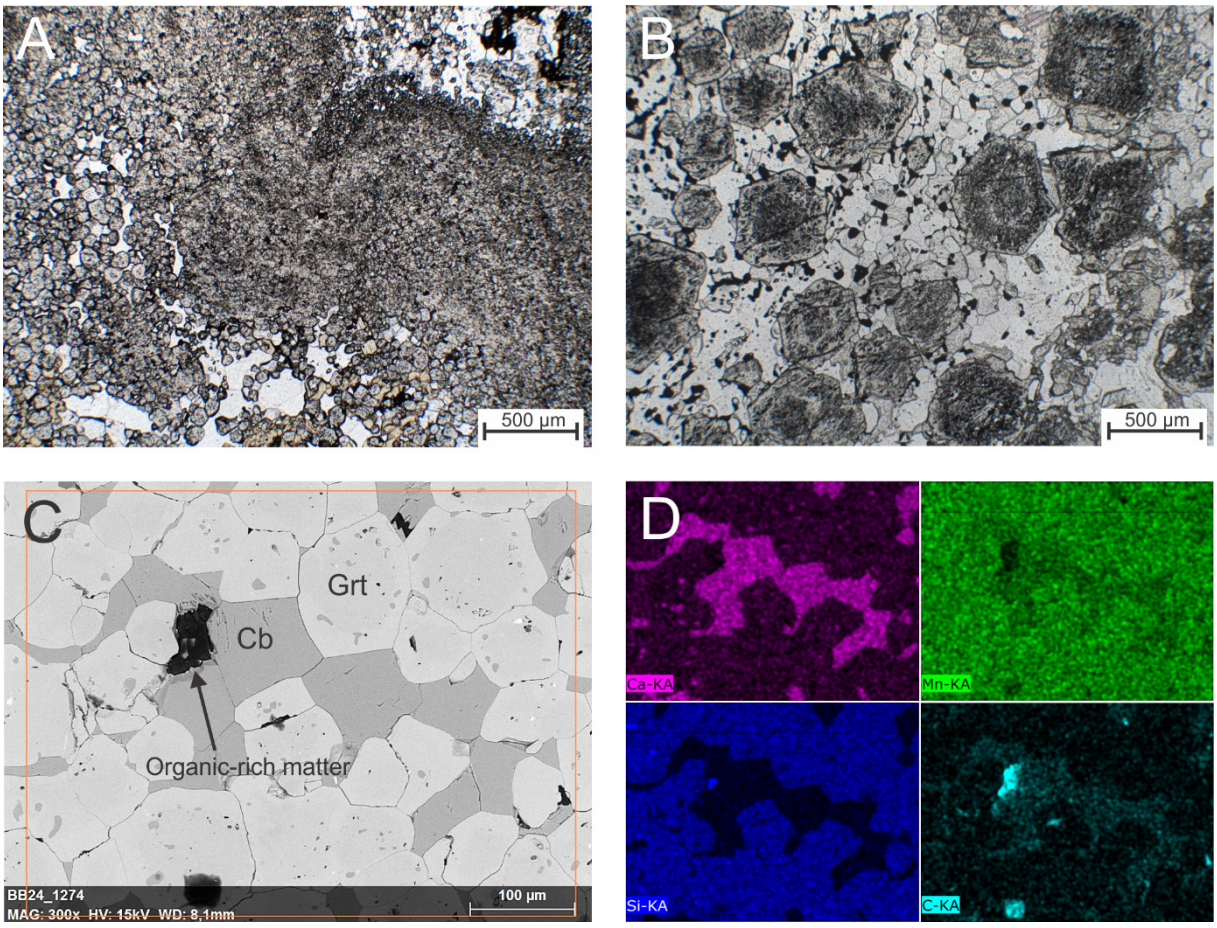

Figure 23 – Microphotographs illustrating the variable appearance of garnet in Mn-rich metapelitic rocks (A; B), along with BSE image (C) and associated elemental distribution maps of selected atomic species (D). (A) Microphotograph showing a fine-grained aggregate of garnets along with minor pale yellow epidote (lower part), as seen in plane polarized light (PPL, thin section FL 5). (B) Relatively large euhedral to subhedral garnets (thin section Rana 6, PPL). (C) BSE image showing garnet in close association with carbonate. The inset marks the area of SEM-EDS elemental distribution in (D), which showed a relative Mn-enrichment of garnet and carbonate. Dark infillings suspectedly represented organic-rich matter.

Relatively fine-grained, euhedral to subhedral quartz (~10 to 20 vol.%) is commonly observed in polymineralic domains along with feldspar, garnet, carbonate, and biotite (Figures 24A; 24B). More coarse-grained quartz also occurs in monomineralic domains, along with varying amounts of carbonate, and is distributed in ribbons along the S_0/S_1 foliation. The grain size ranges between 50 to 200 µm and 100 µm to 1 mm for the fine-grained and coarse-grained quartz, respectively. Furthermore, the latter is commonly characterized by subhedral to anhedral grains displaying undulose extinction, subgrains, and lobate grain boundaries. A significant proportion of the quartz in monomineralic domains exhibits 120° triple junctions, suggestive of post-deformational annealing. Quartz also occurs along with carbonate (±clinozoisite) in fractures that cut across the S_0/S_1 foliation.

Locally abundant, subhedral to anhedral plagioclase feldspar (~5 to 10 vol.%) is present as poikiloblasts in close association with biotite and hematite (Figure 25C). The poikiloblasts are riddled with fine-grained inclusions of fine-grained hematite, garnet, and mica, while occasionally exhibiting multiple twinning. The size of the individual poikiloblasts commonly ranges from 500 to 700 µm. The SEM-EDS

spot analysis revealed a high Na and low plagioclase composition, suggesting the presence of albite (Appendix C). Furthermore, feldspar grains of smaller size (~100 to 200 μm) also display tartan twinning (Figure 24B), indicative of microcline. These grains are generally observed in random distributions along with quartz, carbonate, biotite, and garnet.

Pale brown biotite (~5 vol.%) occurs in an anticlustered, often random distribution (Figure 24A). Its elongate sections commonly vary between 200 to 800 μm. The SEM-EDS analysis indicated that the biotite composition may be approximated by the Mg-endmember, i.e. phlogopite (Figures 24C; Appendix C). Accessory apatite (<5 vol.%) is characterized by subhedral rod-shaped grains (Figure 24A). Similarly, epidote, represented by minuscule anhedral grains, is present in relatively small amounts (<5 vol.%) in the rhythmically banded schists (Figures 24A; 24B). In contrast, abundant epidote (~20 vol.%) has been observed as uniformly distributed, pale yellow, subhedral ellipsoidal to prismatic grains (100 μm) aligned along the S_2-axial surfaces. A close relation between epidote and hematite has also been noted.

A rare subhedral and colorless mineral characterized by approximately 90° cleavage and dull interference colors is found in elongate aggregates and was determined to be rhodonite ($MnSiO_3$) by the SEM-EDS analysis (Figures 24D; 24E; Appendix C). Also, accessory amphibole is present as pale yellow, weakly pleochroic, euhedral to subhedral mineral grains commonly exhibiting a 120° cleavage. The SEM-EDS spot analysis of amphibole revealed its Fe-Mg-Mn-rich composition and suggests cummingtonite-grünerite mineralogy (Appendix C).

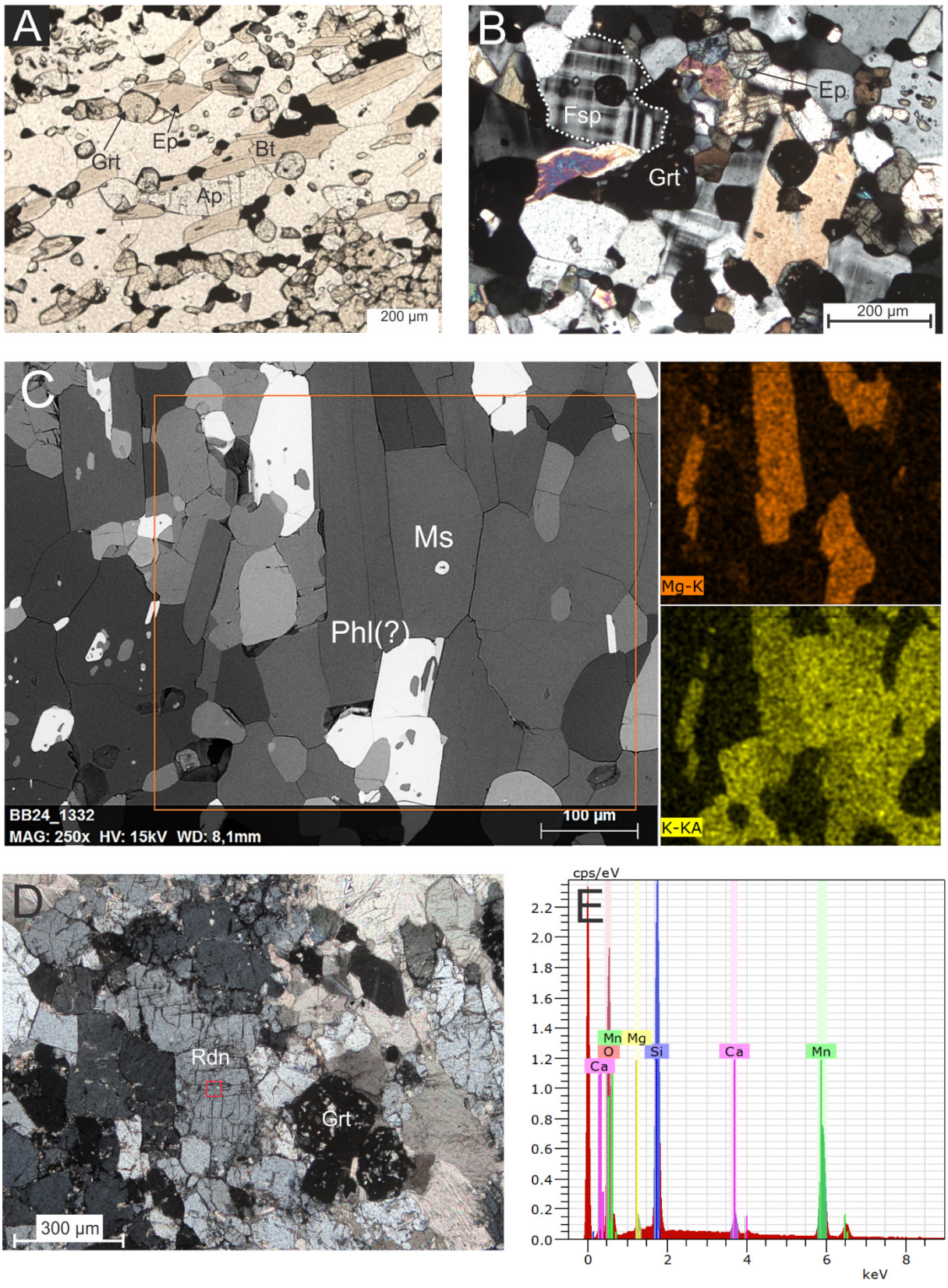

Figure 24 – Microphotographs illustrating the gangue mineralogy of various Mn-rich metapelitic rocks. (A) Polymineralic domain containing co-existing garnet, epidote, biotite, feldspar, and apatite (+quartz), as observed in PPL (thin section Rana 3a). (B) Note the presence of tartan twinning (outlined grain), indicative of microcline feldspar. (C) BSE image of Mn-rich schist (thin section Rana 3a) and associated elemental distribution maps of selected atomic species, with biotite (phl) showing relative enrichment of Mg. Inset marks the area of SEM-EDS analysis. (D) Elongate aggregate of rhodonite closely associated with garnet, with the former exhibiting dull interference colors under crossed polars (thin section Rana 6). Red inset marks the area of SEM-EDS spot analysis, with resulting EDS spectrum illustrated by (E).

4.3.1.2 Calc-silicate hematite schists

The gangue mineralogy of hematite-rich (±magnetite) schists is made up of varying amounts of quartz, carbonate, hornblende, epidote, mica, and feldspar. Garnets are virtually non-existent in these samples (<1 vol.%).

The abundance of quartz is highly variable between samples (<5 to 20 vol.%). The grain size ranges from approximately 100 up to 500 µm, with quartz homogenously distributed in polymineralic domains containing carbonate, epidote, mica, and feldspar. Undulose extinction and diffuse grain boundaries are common features of the quartz mineral grains. Carbonate (~10 to 30 vol.%) is present as randomly distributed subhedral to anhedral grains, and it is characterized by a uniform grain size distribution within an approximated range of 250 to 500 µm. Subhedral grains often exhibit 120° grain boundaries and polysynthetic twinning (Figure 25D). The SEM-EDS analysis revealed the Ca-rich composition and variable amounts of Fe-, Mg- and Mn (Appendix C). In addition, large carbonate grains (up to 4 mm across) have been observed in cm-thick S_1-parallel quartz ribbons which, as indicated by the SEM-EDS analysis, are rich in Mg, Ca, and Mn (Appendix C).

Epidote (~30 vol.%) occurs as pale yellow, weakly pleochroic and subhedral to anhedral elongated sections oriented parallel to the S_1-foliation in polymineralic domains, but also as interstitial grains in foliation-parallel hematite bands. In general, the length of elongate sections ranges from approximately 100 to 300 µm. However, a local variety of epidote-rich schist (Figure 19E) displays euhedral prismatic and lath-shaped grains with long axes ranging from 0,5 to 2 mm (Figure 25B). The prismatic grains produce a weakly defined linear fabric, while the lath-shaped grains show no preferred orientation. Moreover, epidote consistently truncates tabular hematite.

Hornblende is observed both as euhedral hexagonal and anhedral mineral grains in close association with epidote, the former exhibiting a strongly pleochroic green color (Figure 25A). Hexagonal crystals (~5 vol.%) up to 500 µm appear in close relation to hematite bands. However, hornblende is more commonly found in spatial association with varying amounts of magnetite, in line with Bugge (1948). The SEM-EDS analysis revealed a Ca-Mg-Fe-rich composition, which could suggest the presence of magnesiohastingsite (Appendix C).

Additionally, the magnetite-rich hematite schists commonly display poikiloblastic feldspar (~5 to 10 vol.%), which contains fine-grained inclusions of mica, hematite, and lesser amounts of garnet (Figure 25C). The feldspar is observed in close association with biotite, quartz, and hematite. The size of individual poikiloblasts is generally around 600µm, though larger grains have been observed.

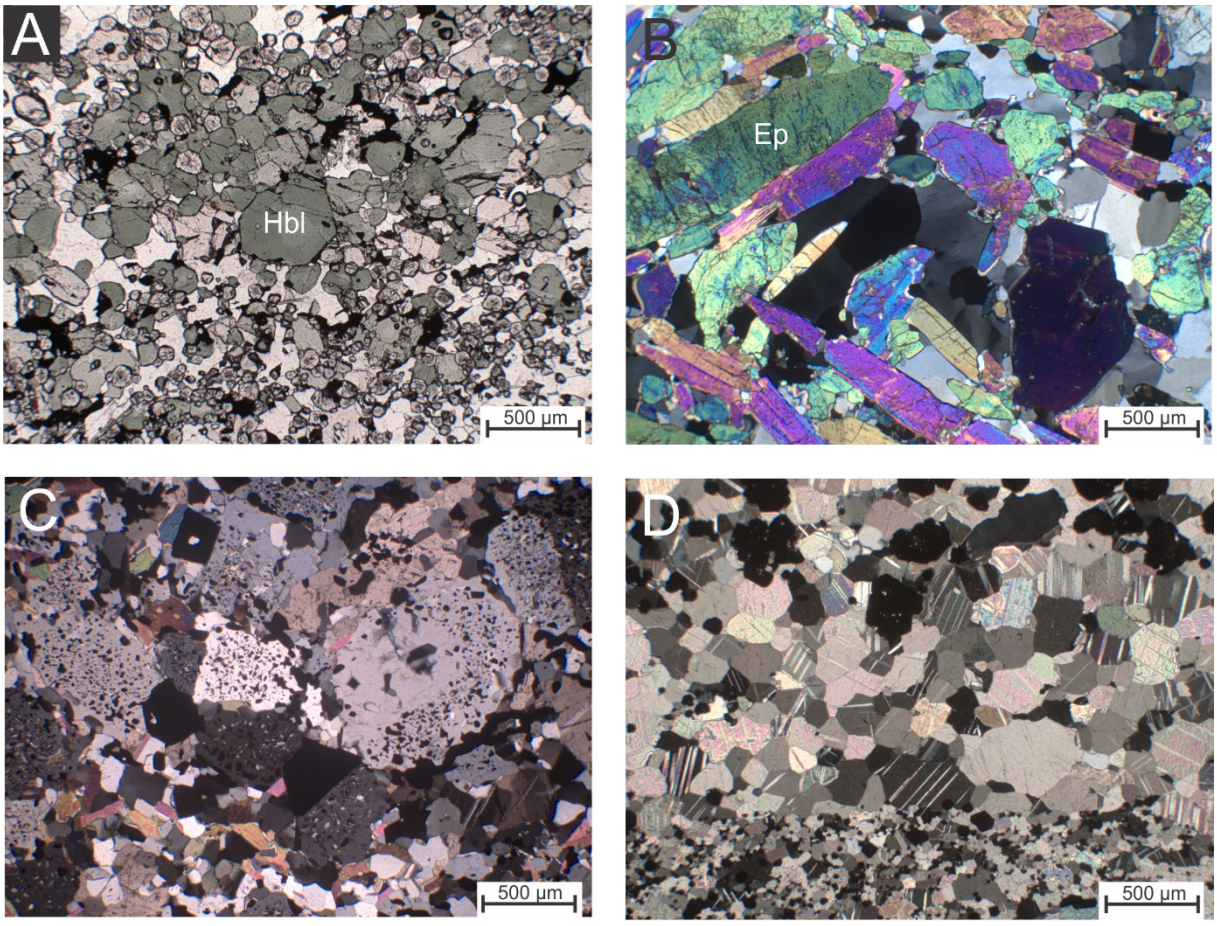

Figure 25 – Microphotographs illustrating the gangue mineralogy of studied calc-silicate hematite schists. (A) Euhedral to subhedral hornblende in assocation with more fine-grained, homogeneously distributed garnet and opaque hematite, as seen in PPL (thin section Rana 11a). (B) Epidote-rich schist exhibiting relatively large grains of euhedral prismatic to lath-shaped epidote making up a nematoblastic fabric (thin section Rana 4b, XPL). (C) Poikiloblastic feldspar containing fine-grained inclusions of hematite (thin section Rana 1, XPL). (D) Carbonate-rich domain, in which the carbonate grains display polysynthetic twinning (thin section Rana 14a, XPL).

4.3.1.3 Quartz-hematite schists

The quartz-hematite schists show relatively simple mineralogical assemblages. Quartz (up to 60 vol.%) occurs in monomineralic bands oriented along the S_1-foliation and frequently exhibits granoblastic textures containing 120° triple junctions (Figure 26A). The quartz also commonly pins small, tabular hematite grains (<100 µm), while the grain size of the former ranges from 150 to 500 µm. More fine-grained fractions have been observed in polymineralic associations with carbonate and minute quantities of epidote and biotite.

Carbonate appears as anhedral grains in relatively low amounts (~5 to 10 vol.%) which are randomly distributed throughout. With similar grain sizes to those of quartz, carbonate exhibits polysynthetic twinning and occur in spatial association with disseminations of elongated epidote (<5 vol.%) aligned along the S_1-foliation. Accessory amounts of fine-grained muscovite and biotite (≤50 µm) have also been observed in close relation to tabular hematite.

4.3.1.4 Garnet-mica schists

The garnet-mica schists are predominantly made up of quartz, biotite, garnet, and carbonate, along with minute quantities of feldspar, muscovite, and clinozoisite (Figure 26B). Quartz (~25 to 30 vol.%) occurs in foliation-parallel ribbons and as widely dispersed grains, with grain sizes ranging from around 50 µm up to 2 mm (longest axis). Individual quartz grains are commonly elongated along the S_1-foliation together with subhedral carbonate (~15 vol.%). Strongly pleochroic green biotite (~20 vol.%) delineates a well-defined S_1-foliation and is in general homogenously distributed throughout polished sections. The SEM-EDS analyses revealed an iron-rich biotite (Appendix C).

Garnets (~10 to 15 vol.%) appear as anhedral, fractured grains (Figure 26A) overgrowing the mineral phases described in the preceding paragraph. These are elongated along the S_1-foliation, but also commonly display fractures oriented perpendicular to the foliation. Although highly fractured in polished sections, individual garnets have been noted to be up to 5mm in diameter in hand specimens. In accordance with Bugge (1948), the SEM-EDS analysis revealed an iron-rich composition approximated to that of the almandine variety ($Fe_3Al_2Si_3O_{12}$, Appendix C).

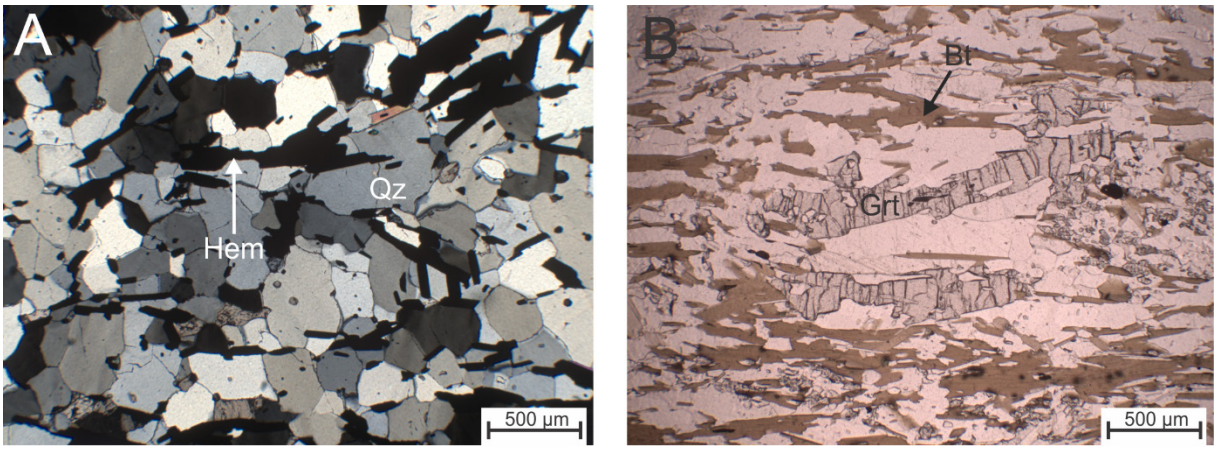

Figure 26 – Microphotographs illustrating the gangue mineralogy of (A) quartz-hematite schists and (B) garnet-mica schists. (A) Relatively randomly oriented and scattered tabular hematite (opaque) in association with quartz aggregates exhibiting granoblastic textures (thin section SSP3a, XPL). (B) Biotite making up a distinct S_1-foliation along with an elongate, anhedral grain of fractured garnet (thin section FL 1c, PPL).

4.3.1.5 Post-D_2 quartz-carbonate vein

Petrographic analysis of the post-D_2 quartz-carbonate vein revealed the presence of biotite, zoisite, chlorite, feldspar, and rutile, in addition to the highly abundant quartz and carbonate. The vein sample also contains minor amounts of sulfides (Figure 27).

Quartz exhibits undulose extinction and lobate/irregular grain boundaries and is found in close association with anhedral carbonate grains (Figure 28A). Carbonate often displays polysynthetic twinning and vivid pastel-colored interference colors. The grain sizes of quartz and carbonate are generally around 2 mm. However, more fine-grained carbonate and quartz (<500µm) are found in close

proximity to biotite, zoisite, and feldspar in polymineralic domains. The biotite (~10 vol.%) is characterized by a pale brown pleochroic appearance in plane polarized light.

Alteration of biotite to chlorite (<5 vol.%) has been observed, with the latter exhibiting anomalous brown interference colors, indicative of a high-Mg variety (Figure 28B). Zoisite (~5 vol.%) is recognized by euhedral prismatic to lath-shaped sections, though anhedral zoisite has also been observed. The zoisite grains exhibit characteristic anomalous grey-blue to yellow interference colors (Figure 28C). Furthermore, the presence of lamellar twinning distinguishes closely associated plagioclase feldspar (<5 vol.%).

Various sulfides are present in accessory amounts as disseminations in the coarse-grained carbonate and quartz, and include pyrite, pyrrhotite, and chalcopyrite (Figures 27; 28D; 28E; 28F). Pyrrhotite and pyrite commonly exist as anhedral intergrowths along with V-enriched rutile (Figures 28A; 28B). Lesser amounts of chalcopyrite are found in close relation with pyrite. In addition, rare zircon was observed by the occurrence of high intensity rounded grains during the SEM-EDS analyses.

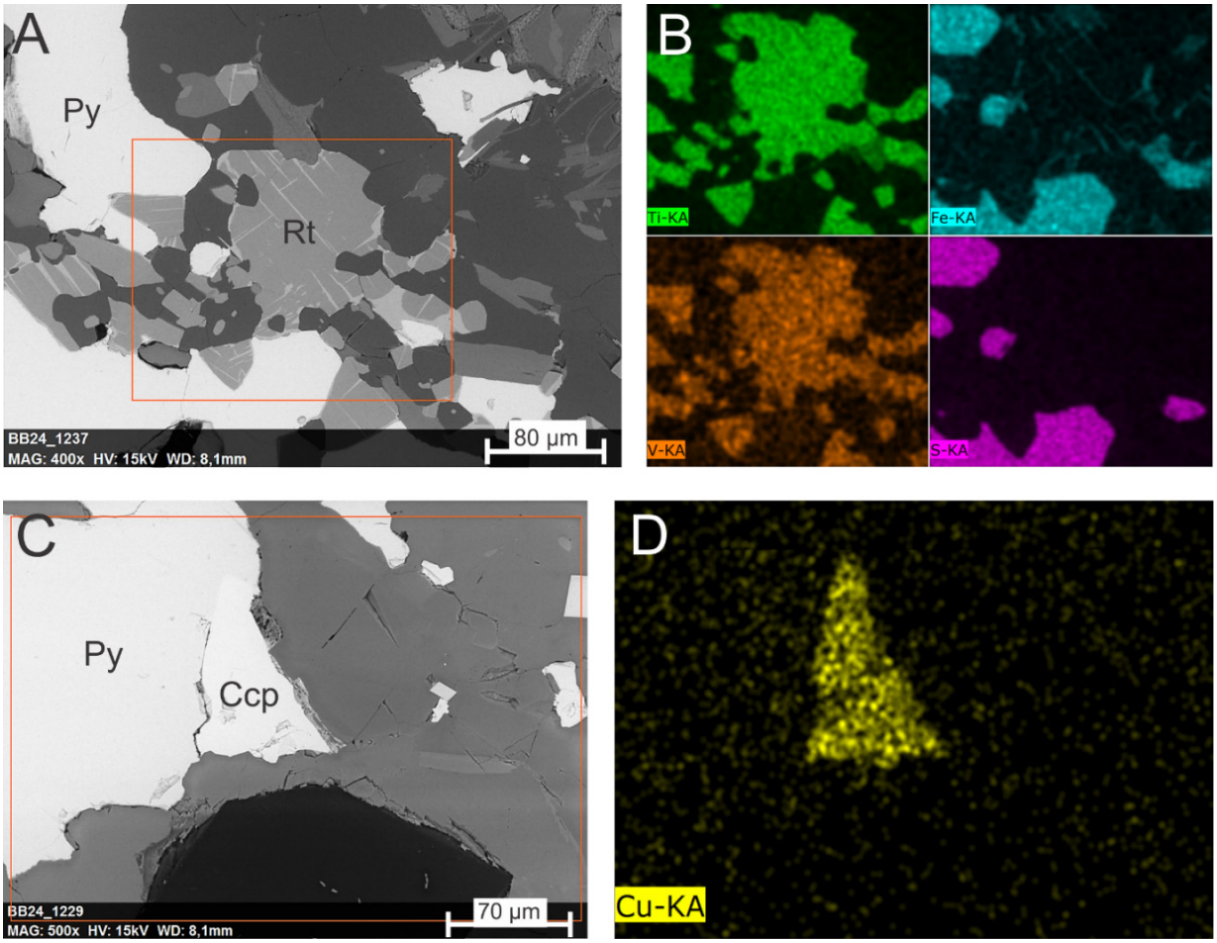

Figure 27 – BSE images and associated elemental distribution maps of selected atomic species from the post-D_2 quartz-carbonate vein. Red insets mark the areas of SEM-EDS analysis. (A) Anhedral intergrowth of rutile and pyrite, with the former exhibiting V-enrichment and Fe-rich laminas, as illustrated in (B). (C) Pyrite and chalcopyrite intergrowth, with chalcopyrite identified by its positive Cu signal, as seen in (D).

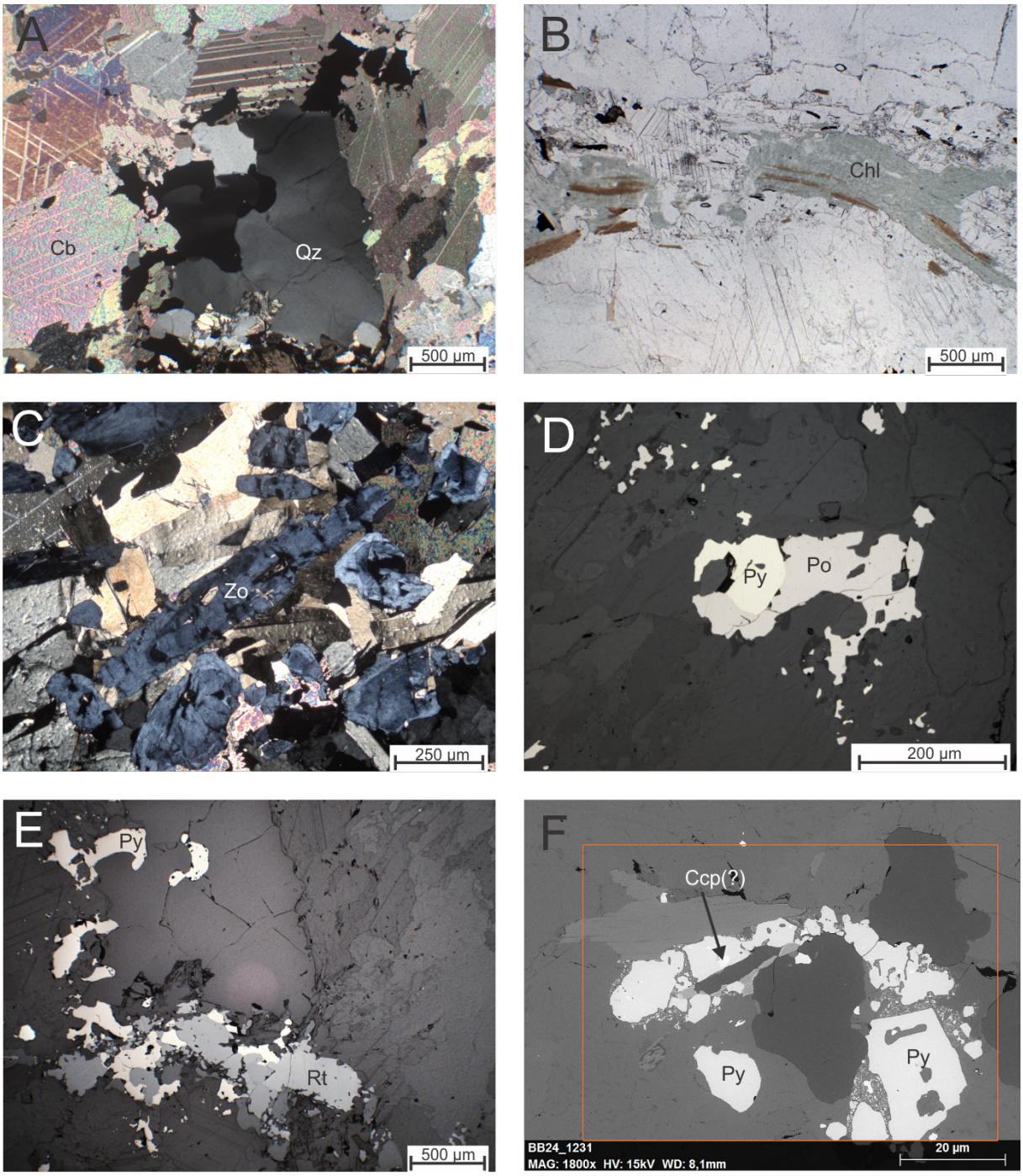

Figure 28 - Microphotographs illustrating the mineralogy of the suspected post-D_2 quartz-carbonate vein. All microphotographs were taken from thin section Rana 10a. (A) Quartz exhibiting undulose extinction and lobate/irregular grain boundaries in contact with relatively large grains of carbonate, with the latter exhibiting abundant polysynthetic twinning in XPL. (B) Hydrothermal alteration of biotite to chlorite represented by pale-green colors consuming unaltered brown biotite. (C) Euhedral lath-shaped (middle) to anhedral zoisite (Zo) grains exhibiting anomalous grey-blue interference colors in close association with abundant biotite. (D) Anhedral intergrowth of pyrite (Py) and pyrrhotite (Po), which are distinguished on the basis of reflective color; whitish yellow for pyrite and brownish to pinkish tint for pyrrhotite (as observed in PPL). (E) Anhedral pyrite (Py) and Rutile intergrowth (Rt) on the grain boundary of quartz and carbonate. (F) BSE image illustrating pyrite (Py) containing small stains of suspected chalcopyrite.

4.3.2 Ore mineralogy

In the studied samples, hematite invariably represents the principal ore constituents, whereas magnetite occurs less frequently. Furthermore, internal strain variations, observed within ore bodies and host rocks, have given rise to various generations of Fe-oxides. In order to establish a paragenetic sequence, the description of these texturally distinct Fe-oxides is given with respect to the various structural features observed both on the macro- and micro-scale. These structural domains include S_0/S_1, F_1/S_1, and F_2/S_2, and will accordingly be depicted in this order.

4.3.2.1 S_0/S_1-domains

In the rhythmically banded rock samples, hematite is present in fine-grained bands parallel to the S_0/S_1-foliation (Figure 29). Hematite is commonly found in alternation with fine-grained bands of spessartine in the Mn-enriched zones. The size of hematite grains is commonly equivalent to that of the individual garnets and ranges from 15 to 30 µm, though grains up to 100 µm also occur. The former is generally characterized by subhedral granular grains. Also, fine-grained, ellipsoidal hematite is found as inclusions within poikiloblastic plagioclase, though euhedral tabular and prismatic grains occasionally occur. Local spots of Ti-enrichment were detected by the SEM-EDS analysis (Figure 30). Under crossed polars, the fine-grained hematite exhibits a relatively weak anisotropy and little intracrystalline polysynthetic twinning. No magnetite has been observed in the samples represented by S_0/S_1 domains.

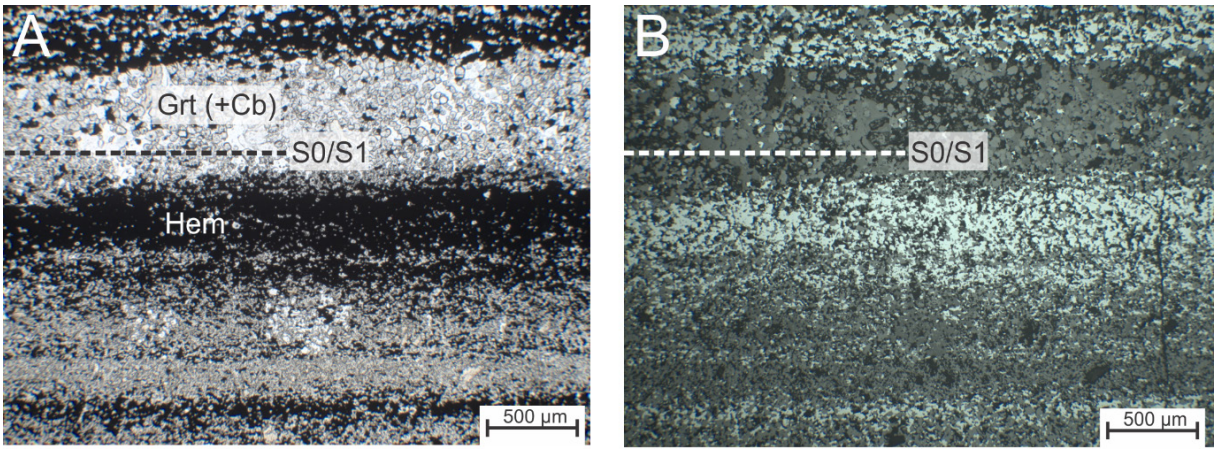

Figure 29 – Microphotographs of an Mn-rich metapelite (thin section Rana 5b) illustrating S_0/S_1-parallel, rhythmically alternating bands of hematite and garnet (+carbonate), as observed under (A) transmitted and (B) reflected PPL.

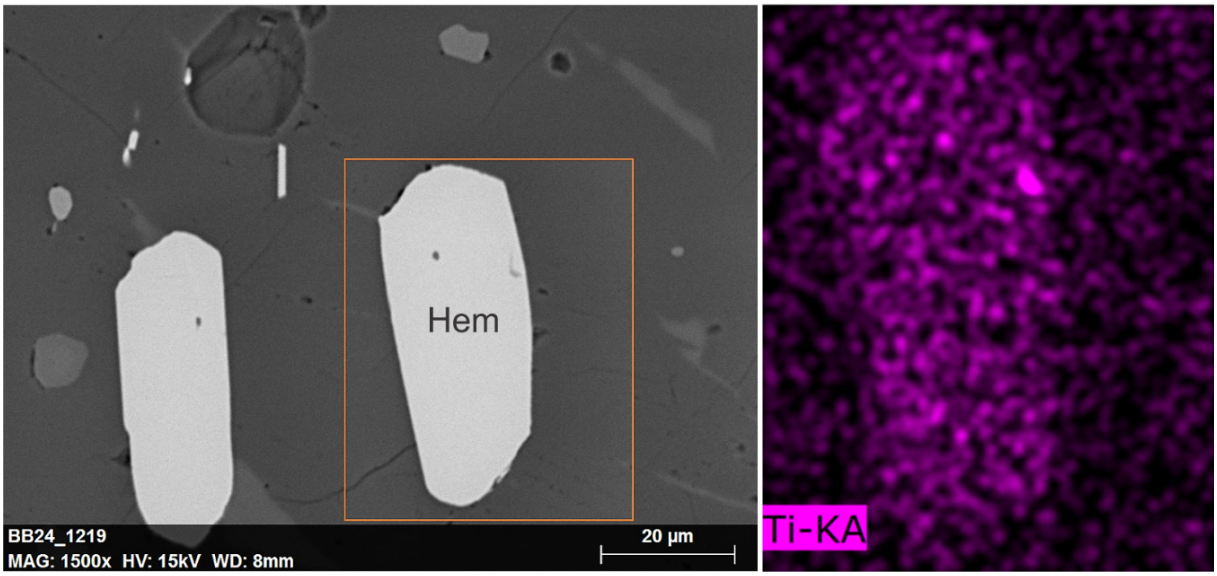

Figure 30 – BSE image and associated distribution map of Ti, showing local spot of Ti-enrichment in an elongate, small hematite grain within an Mn-rich metapelite (thin section Rana 5a). Inset marks the area of SEM-EDS analysis.

4.3.2.2 F_1/S_1-domains

Reflective light microscopy revealed at least two different types of hematite in the quartz-hematite schists and calc-silicate hematite schists. Euhedral specularite is typically characterized by a strong crystallographic orientation in folded bands along the S_1-foliation (Figures 31A; through 31F), and it is common in the quartz-hematite schists. The specularite is characterized by a grey-white bluish tinted reflective color in plane polarized light and a distinct grey to yellow anisotropy under crossed polars. The length of the elongate sections commonly exceeds 500 µm. Moreover, the specularite is occasionally associated with elongated subhedral magnetite grains. Magnetite is distinguished by brown-tinted reflective colors in air and isotropy in XPL and consistently overgrows specularite in F_1-fold hinges (Figure 31F).

Euhedral to subhedral equidimensional and tabular hematite also overgrows the S_1-parallel specularite (Figures 31A; through 31E). The former is characterized by a larger grain size than the specularite, though it is substantially less common in abundance. However, similar to the behavior of S_1-parallel specularite, the larger hematite grains regularly display intracrystalline twinning and strong anisotropy under crossed polars, suspectedly relating to deformation processes. The inverse pole figure coloring map, obtained by EBSD analysis, illustrates the different crystallographic orientations of the two types of hematite (Figure 31C).

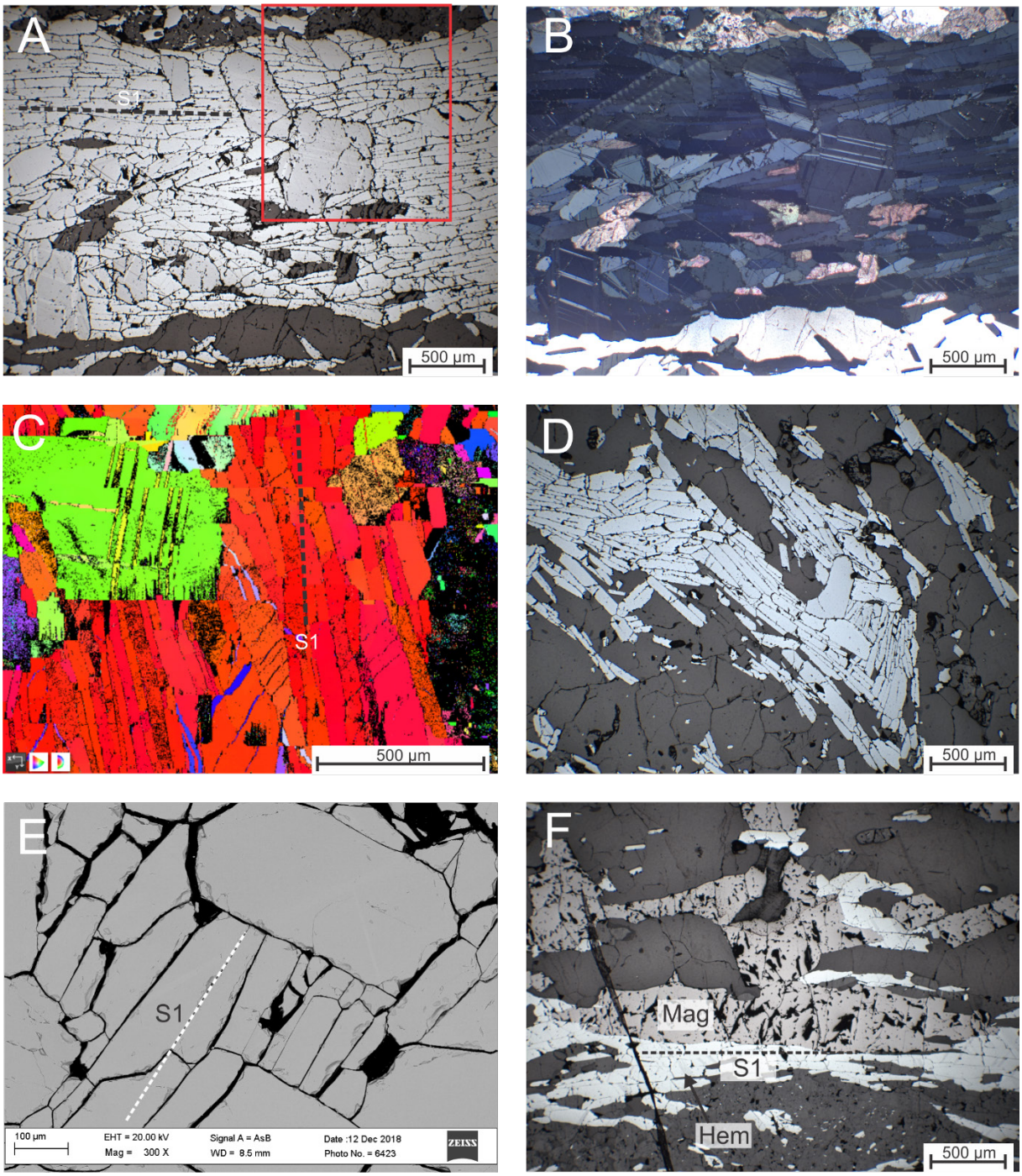

Figure 31 – Microphotographs illustrating the principal ore constituents in F_1/S_1-domains. (A) S_1-parallel euhedral specularite truncated by more massive subhedral hematite in a calc-silicate hematite schist, as observed in reflected PPL (thin section FL 6). The red inset outlines area illustrated by (C). (B) Equivalent area as shown by (A) under crossed. Notice the presence of intracrystalline twinning in hematite and its highly anisotropic nature. (C) Inverse pole figure coloring map (for reference direction X). Red color represents hematite where the [001] crystallographic direction is oriented parallel to the reference direction, while green color represents hematite in which [120] is oriented parallel to the reference direction. (D) Folded layer of hematite in a quartz-hematite schist (thin section SSP3a), in which specularite is truncated by larger hematite along the suspected S_2-foliation. (E) BSE image from a calc-silicate hematite schist illustrating S_1-parallel hematite overgrown by more massive hematite at right angles to the foliation (thin section FL 6). (F) Bands of specularite truncated by elongated magnetite grains along the S_1-foliation in an F_1-fold hinge, as observed in a quartz-hematite schist (thin section FL 7).

4.3.2.3 F_2/S_2-domains

In samples representing F_2/S_2-domains, hematite occurs as fine-grained inclusions within poikiloblastic feldspar (Figure 32A) and closely resembles the hematite in S_0/S_1-domains. More coarse-grained granular hematite (100 to 150 µm) has been observed as interstitial grains between individual poikiloblasts. However, hematite more commonly occurs as subhedral equigranular to elongate grains in bands oriented along the main S_0/S_1-foliation (Figure 32B). The individual grains are regularly oriented parallel to the S_2-axial surfaces and display insignificant to no intracrystalline twinning.

The hematite bands are further overgrown by anhedral grains of magnetite (Figure 32B), though euhedral spinel-shaped magnetite is also present in polymineralic domains (Figure 32A). The grain size of the former is approximately 500 µm, while the euhedral magnetite crystals display grain sizes ranging from 250 to 400 µm. Notably, no magnetite has been observed as inclusions in feldspar poikiloblasts.

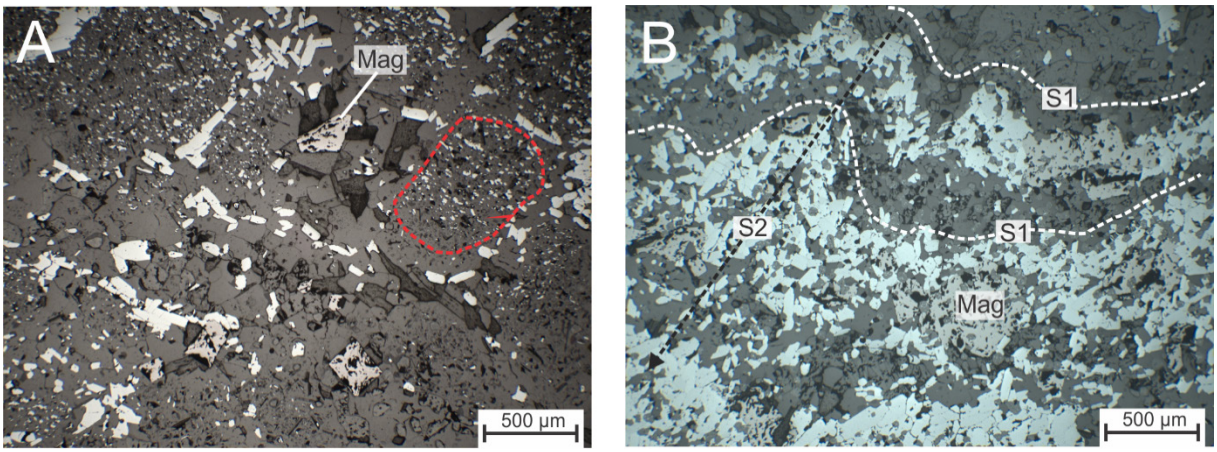

Figure 32 – Microphotographs of a magnetite-bearing calc-silicate hematite schist (thin section Rana 1) in reflected PPL. (A) Polymineralic domain principally consisting of poikiloblastic plagioclase (red outline) with fine-grained hematite inclusions, along with more coarse-grained interstitial hematite and spinel-shaped magnetite. (B) Bands of hematite along the S_0/S_1-foliation, further overgrown by anhedral magnetite. The individual hematite grains are commonly oriented parallel to the S_2-axial surface.

4.3.2.4 XRD patterns of S_1 and S_2-parallel hematite

Due to the finely intergrown nature of the hematite and gangue minerals the degree of crystallinity could not be resolved for the two hematite types, as initially intended for the XRD analyses. However, the results did reveal the presence of additional mineral phases along with hematite. The XRD pattern of S_1-parallel hematite only revealed intergrowth with quartz (Figure 33A), whereas the XRD pattern of S_2-oriented hematite showed the co-existence of clinochlore, phlogopite biotite along with Fe-oxide (Figure 33B). The obtained diffraction values and corresponding compounds are listed in Appendix D. Due to the finely intergrown nature of the hematite and gangue minerals the degree of crystallinity could not be resolved for the two hematite types as initially intended.

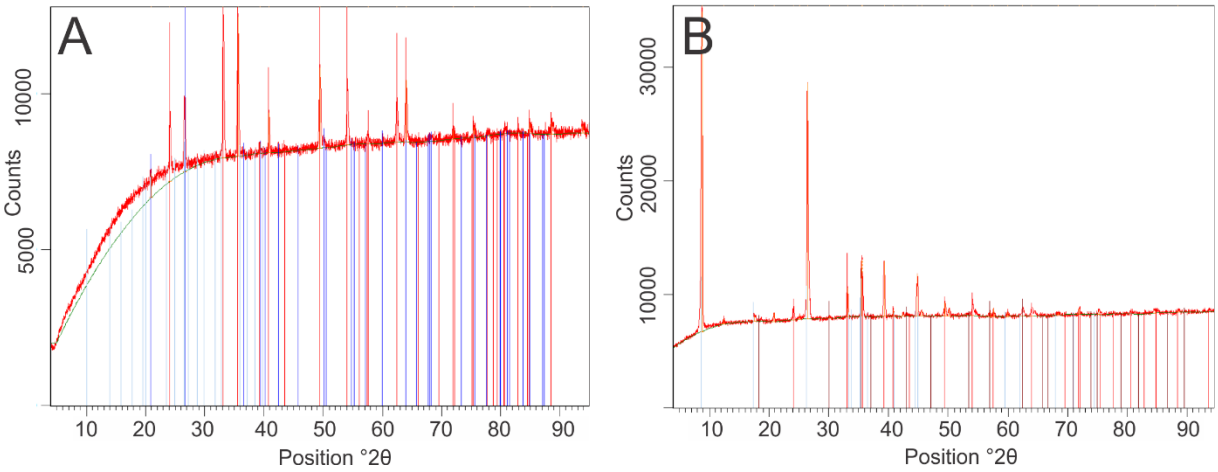

Figure 33 - X-ray differaction (XRD) patterns of two different types of hematite from quartz-hematite schist (sample SSP3): (A) S_1-parallel hematite and (B) S_2-parallel hematite. The respective compound tables are presented in Appendix D.

4.3.2.5 Accessory opaque phases

Accessory sulfides have been detected by SEM-EDS analyses (Figure 35; Appendix C). Subhedral pyrite has been observed in S_1-parallel quartz veins, and often in close association with chalcopyrite. Mg-Fe-Ca carbonates enclosed in an S_1-parallel quartz ribbon also contained chalcopyrite inclusions, while the latter occasionally replaces magnetite (Figures 35C; 35D). In addition, individual grains of suspected chalcocite (Cu_2S) sporadically occur in close association with hematite (Figures 35E; 35F). Bugge (1948) noted that enrichment of pyrrhotite often occurs in the hinge zones of ore bodies. However, no relation between microscopic structures and sulfide mineralizations has otherwise been observed. Additionally, an individual grain of an unidentified phase containing discernable amounts of P, Ag, Ce, and Th was detected by the SEM-EDS analysis of an Mn-rich metapelite (Figure 34, Appendix C).

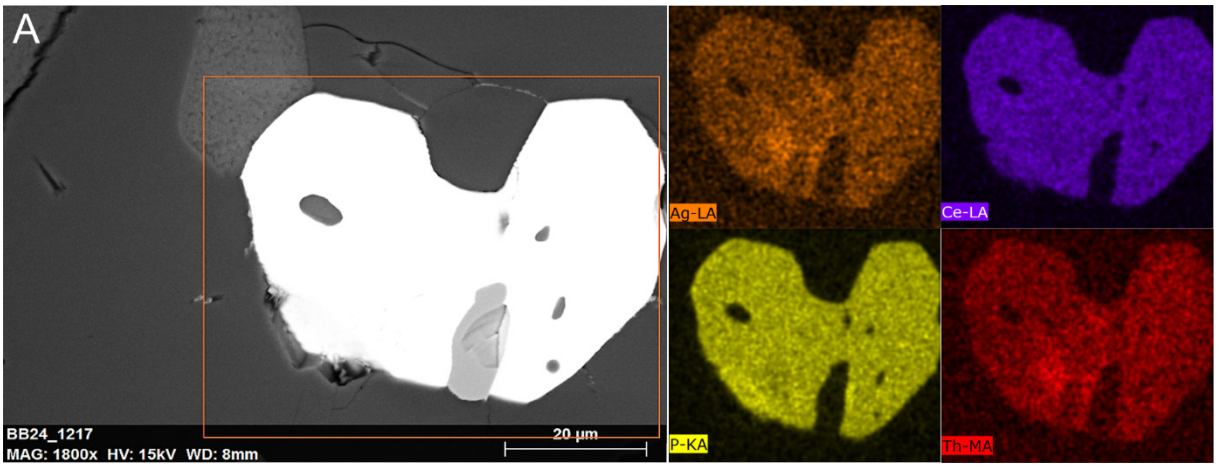

Figure 34 – BSE image and associated elemental distribution maps of selected atomic species of an unidentified P-Ag-Ce-Th-bearing mineral in an Mn-rich metapelite (thin section Rana 5a).

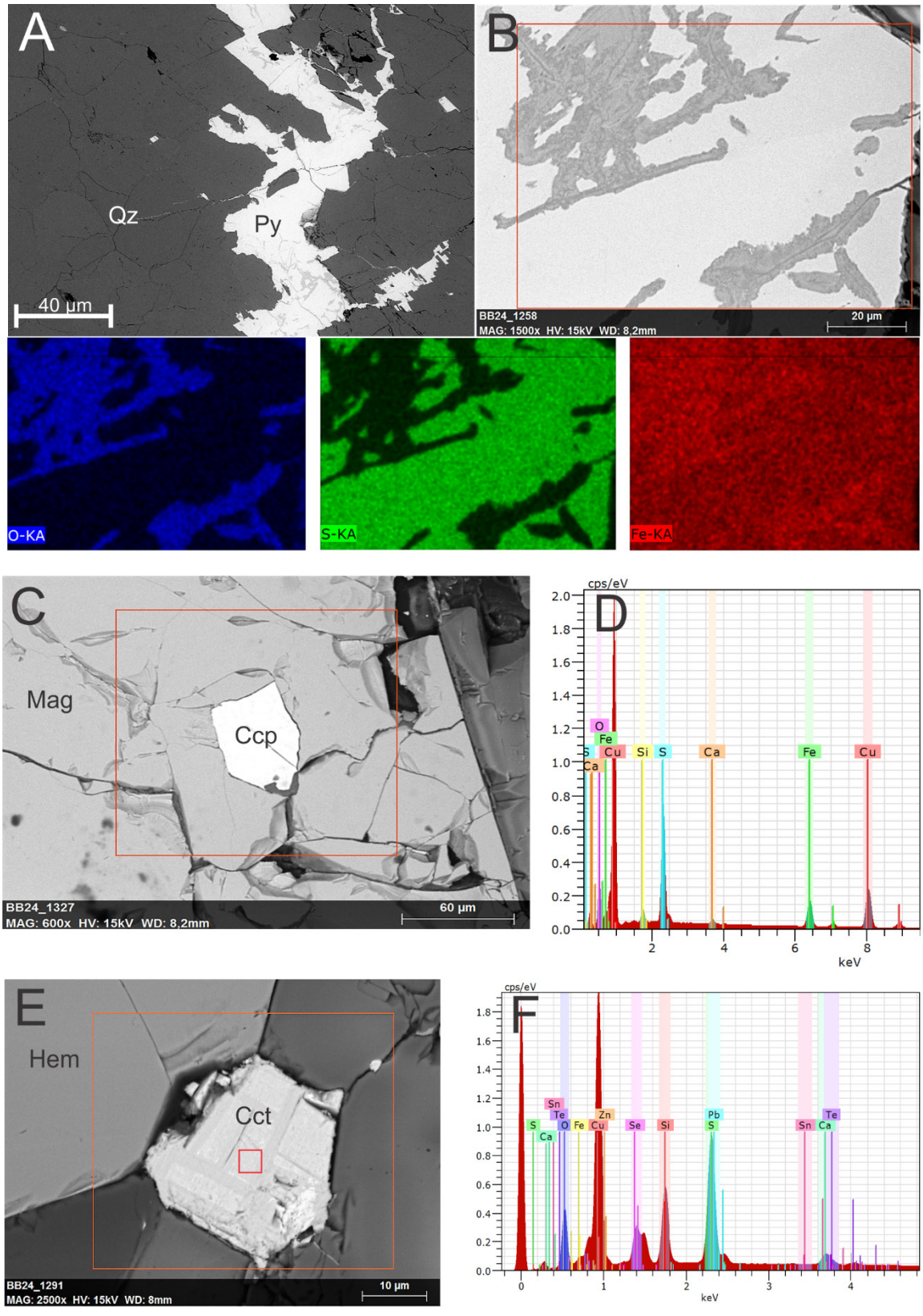

Figure 35 – BSE images, associated elemental distribution maps and EDS spectrums of various accessory opaques of the studied samples. (A) Anhedral pyrite contained in an S_1-foliation parallel quartz-vein (thin section Rana 13c). (B) BSE image at higher magnification revealing surface textures in pyrite. Inset marks area of SEM-EDS elemental analysis for the associated elemental distribution maps, revealing a patchwork of O-enrichment. (C) Grain of chalcopyrite enclosed within magnetite (thin section FL 8), with associated EDS spectrum represented by (D). (E) Suspected chalcocite in close association with hematite (thin section FL 8), the former exhibiting elevated values of Se in associated EDS spectrum in (F).

4.4 Major and trace element composition

Major element compositions and trace element contents, including rare earth elements (REEs), of six individual mineral and rock samples from the study area were analyzed. The various samples are represented by different structural settings or lithologic units, which are compiled in Table 3 below.

Table 3 – List of samples analyzed for major and trace element contents, including representative the structural/lithological framework of respective samples.

Sample	Mineralogy	Setting
Rana 2-Hm-LG	Hematite	S_0/S_1-parallel hematite
Rana 12-Cb-LG	Carbonate	Host rock marble
Rana 14-Rds-LG	Ca-Mg-Mn-carbonate	S_1-parallel quartz-carbonate vein
FL 7-Mt-LG	Magnetite	F_1-fold hinge magnetite
SSP3-Hm-LG1	Hematite	S_2-parallel hematite
SSP3-Hm-LG2	Hematite	S_1-parallel hematite

4.4.1 Major element oxides

Major element oxide contents of the individual samples are presented in Table 4. Al_2O_3-normalized major element oxide patterns are illustrated in Figure 36, which also includes values of typical marine shales and Mn-nodules for comparison (Appendix E). The various samples displayed enrichment of Fe, Mn, and P relative to typical marine shales. Carbonate samples showed significant enrichment of Ca and Mg. On the other hand, the values for Ti, Mg, Na, and K of the different types of Fe-oxides exhibited similar values to the marine shale. The characteristic Mn-nodules were enriched in Mn, Fe and Ca, but showed rather low SiO_2/Al_2O_3 in comparison with the various samples studied. Mn/Fe values for the various types of Fe-oxides were low, ranging from ~0.002 to 0.007.

A negative correlation was observed between Al_2O_3 and Fe_2O_3 (Figure 37). No correlation was observed between the Al_2O_3, SiO_2 or P_2O_4 contents (Figures 38; 39). In contrast, a strong correlation was evident between the contents of Al_2O_3 and TiO_2 (Figure 40). Compositional values of three bulk rock samples from the Dunderland Formation have been added to the various correlation plots presented by this thesis, along with one sample from the SEDEX deposit of Vareš, Bosnia, for comparison. The respective bulk rock compositions are presented in Appendix F.

Loss on ignition (LOI) is presented in Table 4, with high LOI values for Ca-Mg-Mn carbonate and host rock marble, 28.7 and 43.7% respectively. The various types of hematite showed low LOI (from 0.2 to 1.1 %), while the analyzed magnetite showed a negative LOI value (-3.0 wt.%).

Table 4 - Major element oxide composition (wt. %) of samples from the Dunderlandsdalen deposits.

Sample	SiO_2	Al_2O_3	Fe_2O_3	MgO	CaO	Na_2O	K_2O	TiO_2	P_2O_5	MnO	Cr_2O_3	LOI	Total	TOT/C	TOT/S
Rana 2-Hm-LG	8.27	0.69	85.98	0.21	2.15	0.01	0.06	0.1	1.0	0.55	0.004	0.9	99.02	0.16	n.d.
Rana 12-Cb-LG	0.54	0.07	0.26	1.13	54.13	n.d.	0.02	n.d.	0.02	0.03	n.d.	43.7	99.9	11.95	0.04
Rana 14-Rds-LG	33.4	0.13	2.1	9.63	19.57	n.d.	n.d.	n.d.	n.d.	6.22	n.d.	28.7	99.75	7.85	n.d.
FL 7-Mt-LG	5.65	0.4	96.16	0.09	0.2	0.02	0.04	0.02	n.d.	0.34	0.004	-3.0	99.92	0.04	n.d.
SSP3-Hm-LG1	12.13	2.27	81.62	1.85	0.4	0.02	0.96	0.12	0.15	0.15	0.005	0.2	99.86	0.05	n.d.
SSP3-Hm-LG2	27.04	0.18	69.95	0.2	1.13	n.d.	n.d.	0.02	0.23	0.15	0.004	1.1	100.004	0.24	n.d.

n.d. = not detected

Table 5 – Trace element composition (in ppm) of samples from the Dunderlandsdalen deposits.

Sample	Be	Sc	V	Co	Ni	Cu	Zn	Ga	As	Se	Rb	Sr	Y	Zr	Nb	Mo
Rana 2-Hm-LG	n.d.	6.0	44.0	17.6	21.3	0.9	4.0	1.8	21.6	n.d.	2.1	123.5	42.9	18.1	0.6	n.d.
Rana 12-Cb-LG	n.d.	n.d.	n.d.	n.d.	1.2	0.3	n.d.	n.d.	n.d.	n.d.	0.6	520.3	1.2	2.7	n.d.	n.d.
Rana 14-Rds-LG	n.d.	n.d.	n.d.	140.9	44.4	22.4	71.0	3.4	0.5	n.d.	0.9	423.8	0.9	0.6	n.d.	0.3
FL 7-Mt-LG	n.d.	2.0	104.0	14.6	5.1	23.6	18.0	9.8	0.5	n.d.	0.9	11.1	2.3	15.3	1.0	n.d.
SSP3-Hm-LG1	1,00	6.0	90.0	21.6	10.5	25.3	55.0	6.7	n.d.	0,8	41.2	10.8	4.3	92.2	12.6	n.d.
SSP3-Hm-LG2	n.d.	2.0	26.0	1.9	5.7	0.9	n.d.	n.d.	0.6	n.d.	0.2	36.4	21.7	3.6	n.d.	0.9

Table 6 – Trace element composition (in ppm) of samples from the Dunderlandsdalen deposits.

Sample	Ag	Cd	Sn	Sb	Cs	Ba	Hf	Ta	W	Au	Hg	Tl	Pb	Bi	Th	U
Rana 2-Hm-LG	n.d.	n.d.	n.d.	n.d.	n.d.	8.0	0.3	n.d.	n.d.	1.5	n.d.	n.d.	1.0	0.1	1.3	0.2
Rana 12-Cb-LG	n.d.	n.d.	n.d.	n.d.	n.d.	112.0	n.d.	n.d.	0.6	n.d.	n.d.	n.d.	0.5	n.d.	n.d.	0.3
Rana 14-Rds-LG	n.d.	0.2	n.d.	n.d.	n.d.	3.0	n.d.	n.d.	n.d.	1.2	n.d.	n.d.	3.6	n.d.	n.d.	n.d.
FL 7-Mt-LG	n.d.	n.d.	n.d.	n.d.	n.d.	14.0	0.2	n.d.	n.d.	0.6	n.d.	n.d.	n.d.	n.d.	n.d.	n.d.
SSP3-Hm-LG1	n.d.	n.d.	1.0	n.d.	2.0	134.0	1.2	0.5	n.d.	2.7	n.d.	0.3	0.4	n.d.	0.4	0.2
SSP3-Hm-LG2	n.d.	n.d.	n.d.	n.d.	n.d.	n.d.	n.d.	n.d.	n.d.	0.8	n.d.	n.d.	0.4	n.d.	n.d.	0.2

Table 7 - Rare earth element content (in ppm) of samples from the Dunderlandsdalen deposits.

Sample	La	Ce	Pr	Nd	Sm	Eu	Gd	Tb	Dy	Ho	Er	Tm	Yb	Lu	∑REEs
Rana 2-Hm-LG	13.3	25.9	3.52	15.3	3.28	0.88	4.25	0.71	4.95	1.21	3.75	0.53	3.52	0.59	81.69
Rana 12-Cb-LG	1.0	1.5	0.2	0.5	0.13	0.02	0.14	0.02	0.13	0.02	0.09	n.d.	0.06	n.d.	3.81
Rana 14-Rds-LG	1.1	1.4	0.15	0.6	0.19	0.05	0.23	0.04	0.19	0.03	0.08	0.01	0.1	n.d.	4.17
FL 7-Mt-LG	1.9	2.7	0.39	1.5	0.29	0.06	0.38	0.04	0.33	0.07	0.2	0.03	0.19	0.03	8.11
SSP3-Hm-LG1	3.0	4.5	0.48	1.8	0.26	0.08	0.36	0.07	0.43	0.11	0.51	0.09	0.83	0.18	12.7
SSP3-Hm-LG2	2.3	4.4	0.62	3.1	0.71	0.22	1.26	0.22	2.09	0.56	2.05	0.29	1.94	0.33	20.09

Table 8 - Rare earth element content from the Dunderlandsdalen deposits normalized to post-Archean Australian shale (Taylor & McLennan, 1985).

Sample	La	Ce	Pr	Nd	Sm	Eu	Gd	Tb	Dy	Ho	Er	Tm	Yb	Lu	Ce/Ce*	Eu/Eu*
Rana 2-Hm-LG	0.35	0.32	0.4	0.48	0.59	0.8	0.9	0.92	1.13	1.21	1.29	1.325	1.26	1.37	0.870161	1.099263
Rana 12-Cb-LG	0.03	0.02	0.02	0.02	0.02	0.02	0.03	0.03	0.03	0.02	0.03	n.d.	0.02	n.d	0.771033	0.691424
Rana 14-Rds-LG	0.03	0.02	0.02	0.02	0.03	0.05	0.05	0.05	0.04	0.03	0.03	0.03	0.04	n.d	0.792288	1.115526
FL 7-Mt-LG	0.05	0.03	0.04	0.05	0.05	0.05	0.08	0.05	0.08	0.07	0.07	0.08	0.07	0.07	0.721027	0.842967
SSP3-Hm-LG1	0.08	0.06	0.05	0.06	0.05	0.07	0.08	0.09	0.1	0.11	0.18	0.23	0.30	0.42	0.862041	1.219558
SSP3-Hm-LG2	0.06	0.06	0.07	0.10	0.13	0.2	0.27	0.29	0.48	0.56	0.71	0.73	0.69	0.77	0.847012	1.084822

Table 9 - Rare earth element content from the Dunderlandsdalen deposits normalized to chondrite (Taylor & McLennan, 1985).

Sample	La	Ce	Pr	Nd	Sm	Eu	Gd	Tb	Dy	Ho	Er	Tm	Yb	Lu	Ce/Ce*	Eu/Eu*
Rana 2-Hm-LG	56.12	42.25	37.9	33.48	22.16	15.6	21.4	19.7	20.1	22.16	23.4	21.46	21.86	23.98	0.915778	0.718456
Rana 12-Cb-LG	4.22	2.48	2.16	1.1	0.88	036	0.7	0.55	0.53	0.37	0.56	n.d.	0.37	n.d.	0.811454	0.451901
Rana 14-Rds-LG	4.64	2.28	1.62	1.31	1.28	0.89	1.16	1.11	0.77	0.55	0.5	0.40	0.62	n.d.	0.833823	0.729085
FL 7-Mt-LG	8.02	4.41	4.2	3.28	1.96	1.07	1.91	1.11	1.34	1.28	1.25	1.21	1.18	1.22	0.758826	0.550947
SSP3-Hm-LG1	12.66	7.34	5.17	3.94	1.76	1.42	1.81	1.94	1.75	2.015	3.19	3.64	5.16	7.32	0.907233	0.797078
SSP3-Hm-LG2	9.71	7.18	6.68	6.78	4.80	3.91	6.33	6.09	8.5	10.26	12.8	11.74	12.05	13.41	0.891416	0.709018

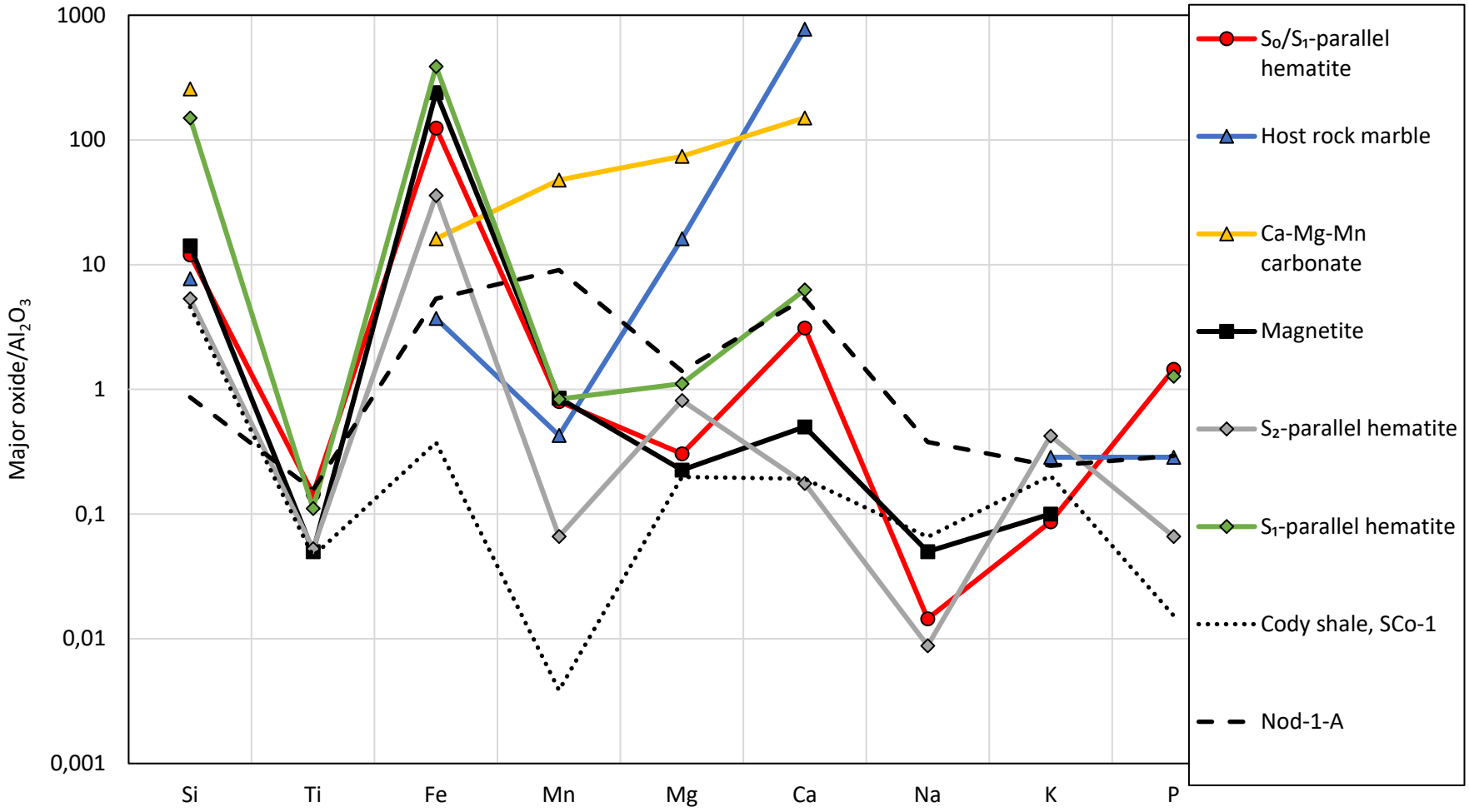

Figure 36 - Major elemental enrichment of selected samples relative to Al_2O_3. Dotted black line represents characteristic enrichment of typical marine shale (from Smith, 1995), while stippled black line represents enrichment of Mn-nodules (from Flanagan & Gottfried, 1980). Reference values are listed in Appendix E.

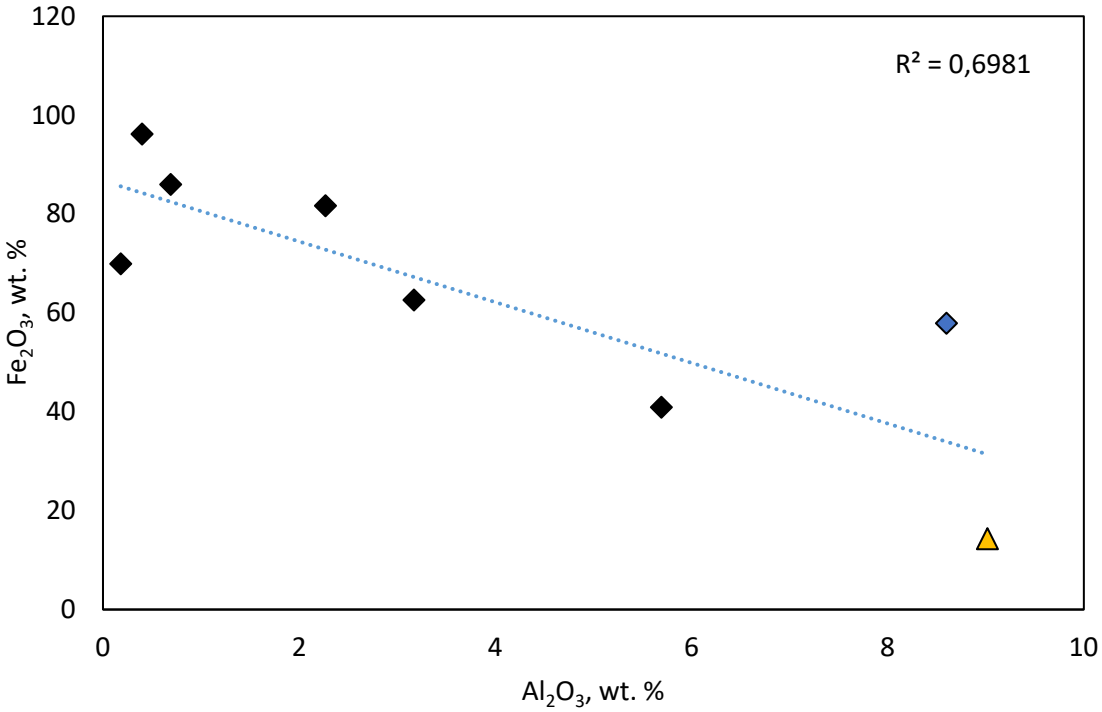

Figure 37 – Plot of Al_2O_3 against Fe_2O_3 (wt. %) showing a negative statistical correlation between the two components (black squares – Fe-oxides; blue square – bulk rock sample from the SEDEX deposit of Vareš, Bosnia; yellow triangle – Ca-Mg-Mn carbonate). Results of bulk rock samples have been included and are listed in Appendix F.

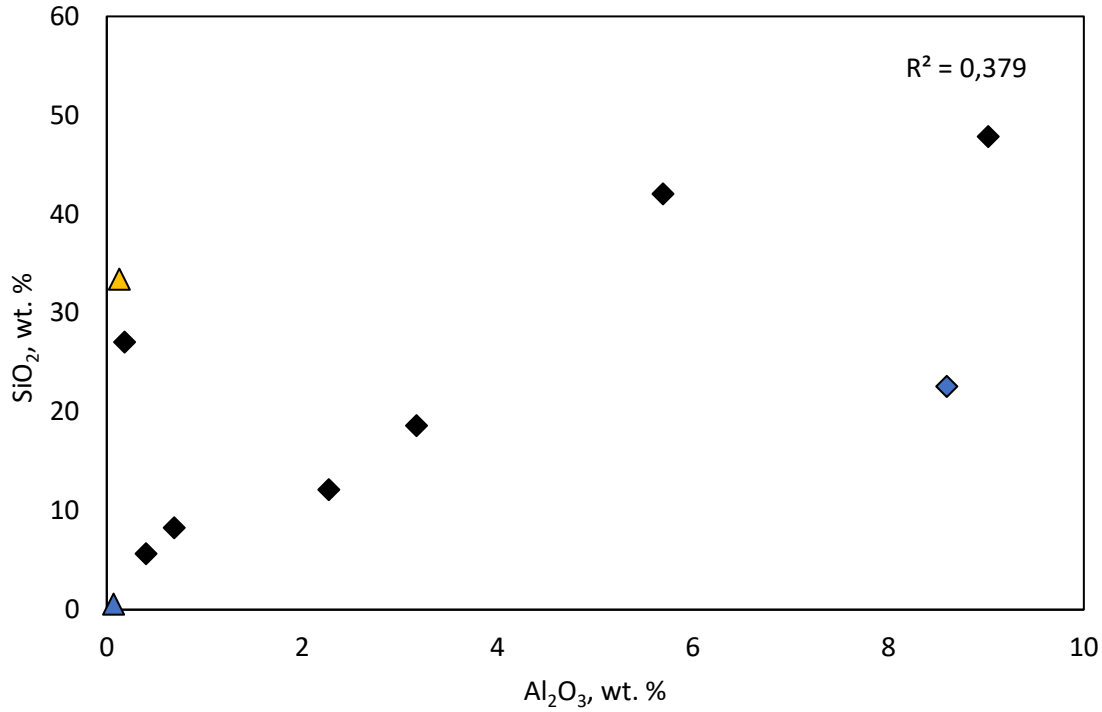

Figure 38 – Plot of Al_2O_3 against SiO_2 (wt. %) showing no statistical correlation between the two components (black squares – Fe-oxides; blue square – Vareš, Bosnia; yellow triangle – Ca-Mg-Mn carbonate; blue triangle – host rock marble).

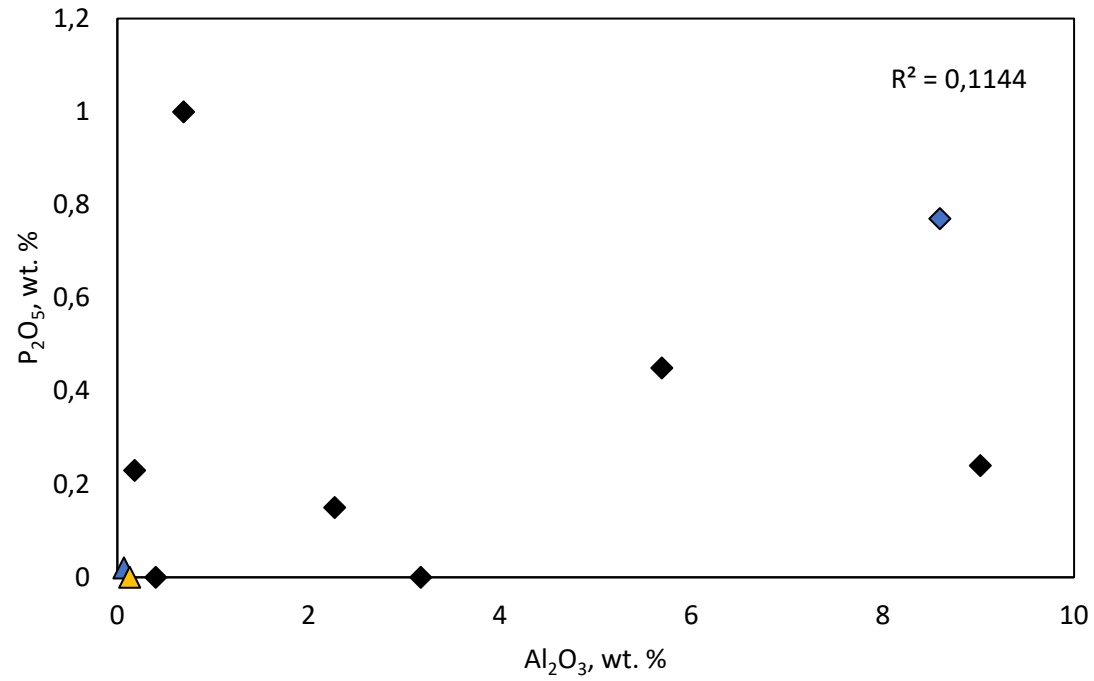

Figure 39 – Plot of Al_2O_3 against P_2O_5 (wt. %) displaying no statistical correlation between the two components.

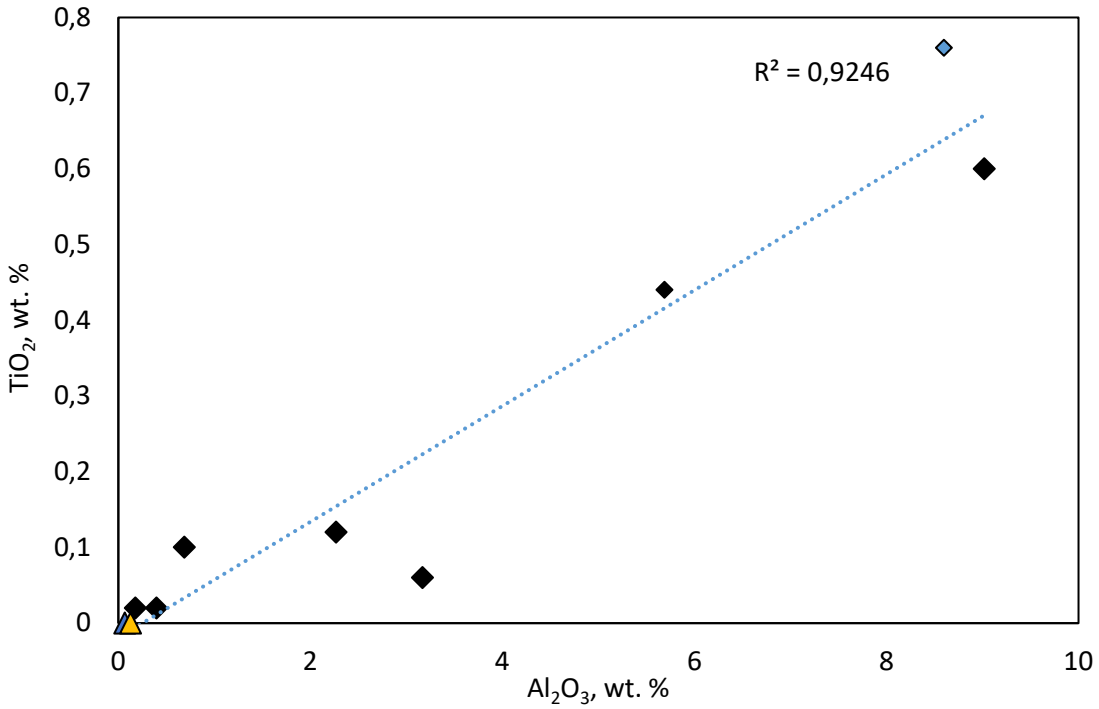

Figure 40 - Plot of Al_2O_3 against TiO_2 (wt. %) showing a strong positive correlation between the two components.

4.4.2 Trace elements

The trace element contents are presented in Table 5 and Table 6. In general, the analyzed samples were characterized by low trace element contents and undetectable total S. The distribution of trace elements in the various samples is presented in Figure 41. The content of Fe_2O_3 showed a weak negative correlation with Sr (Figure 42). In contrast, CaO positively correlated with Sr, while Zr correlated with Al_2O_3 (Figures 43 and 44, respectively).

Host rock marble displayed enrichment of Ba (112 ppm) and Sr (520.3 ppm), but otherwise low to undetectable trace element contents. Sr contents were also elevated within S_0/S_1-parallel hematite and gangue Ca-Mg-Mn carbonate (123.5 and 423.8 ppm, respectively). The latter further exhibited a relative enrichment in Co (140.9 ppm), Ni (44.4 ppm) and Cu (22.4 ppm).

S_2-parallel hematite displayed a relative enrichment in Zn, Rb, Ba, and Zr (55, 41, 134, and 92,2 ppm respectively). Zn-contents in Ca-Mg-Mn carbonate were also elevated (71 ppm). As-contents were slightly elevated in the S_0/S_1-parallel hematite (21.6 ppm) when compared to the other analyzed samples.

The contents of Cr in the various types of Fe-oxides were in the uniform range of 13.7 to 17.1 ppm. V contents showed a higher variability, with magnetite and S_2-parallel hematite exhibiting elevated contents of V (104 and 90 ppm, respectively) when compared to S_0/S_1 and S_1-parallel hematite (44 and 26 ppm, respectively).

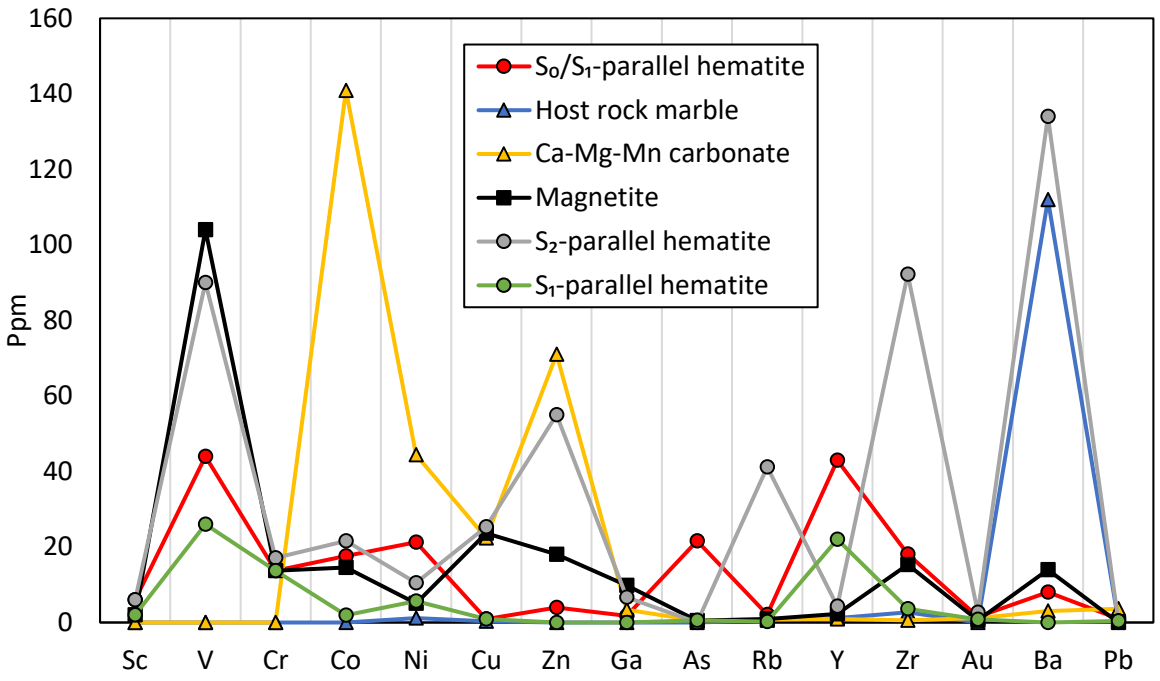

Figure 41 - Trace element composition of the various Fe-oxides, along with host rock marble, and gangue Ca-Mg-Mn carbonate. The Ti and Sr contents have been omitted to better illustrate the distribution of less abundant trace elements.

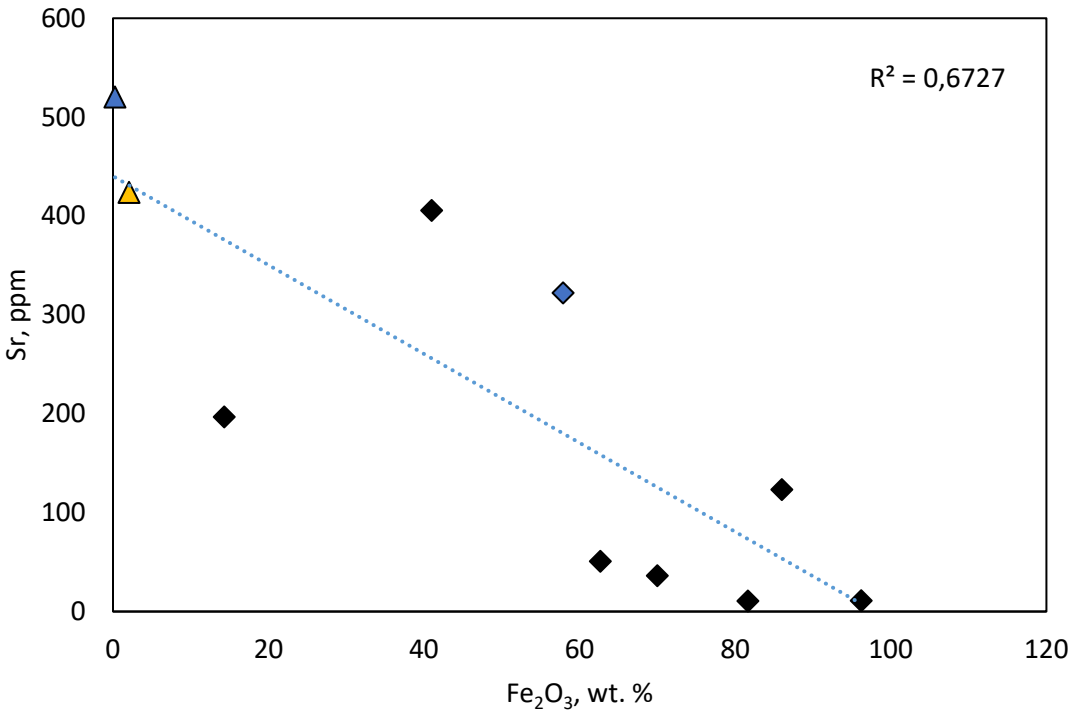

Figure 42 - Plot of Fe_2O_3 (wt. %) against Sr (ppm) showing a weak negative statistical correlations between the Fe_2O_3 and Sr contents of the analyzed samples (black squares – Fe-oxides; blue square – Vareš, Bosnia; yellow triangle – Ca-Mg-Mn carbonate; blue triangle – host rock marble).

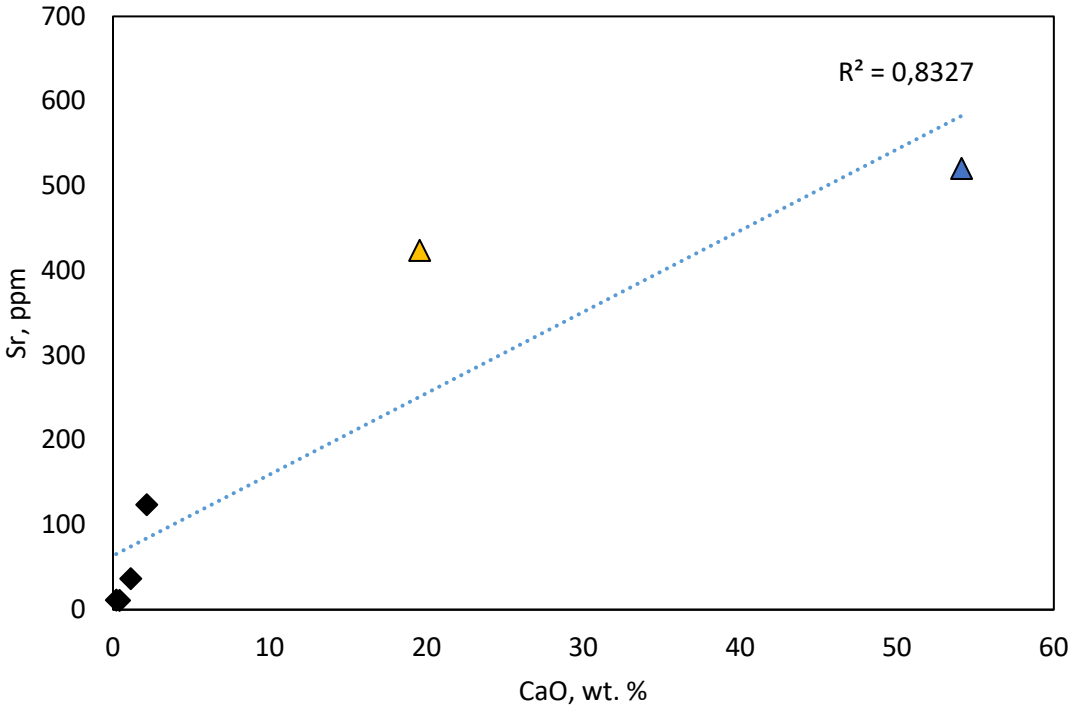

Figure 43 - Plot of CaO (wt. %) against Sr (ppm) showing a positive statistical correlation between the CaO and Sr contents of the analyzed samples.

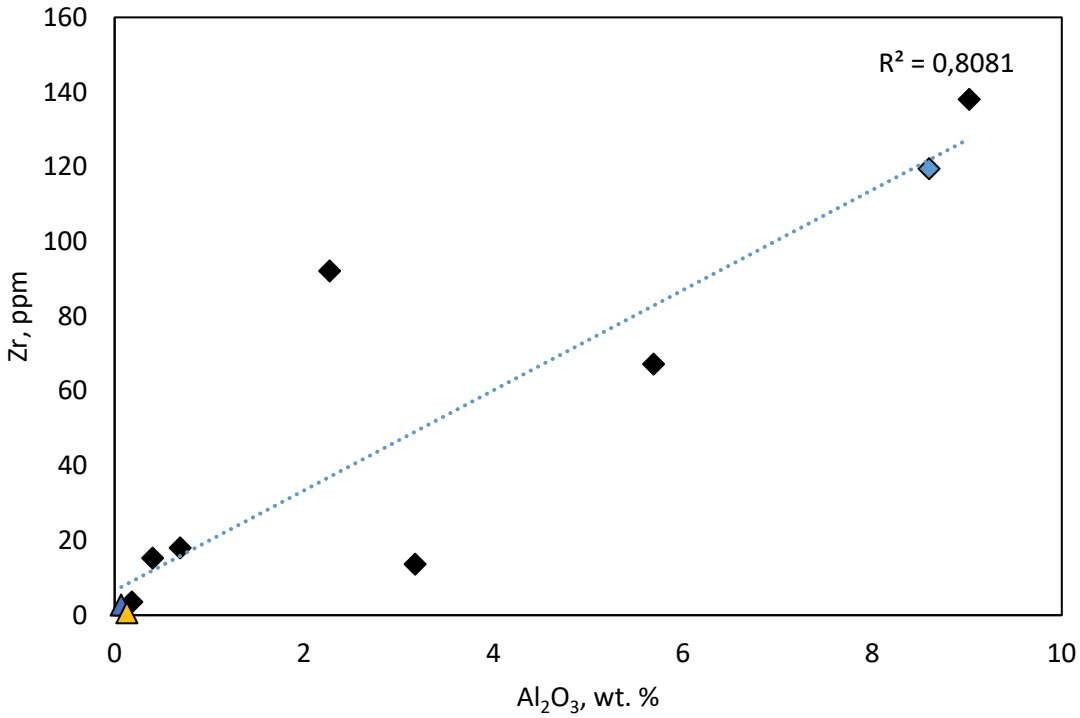

Figure 44 – Plot of Zr (ppm) against Al_2O_3 (wt. %) showing a positive correlation between the Zr and Al_2O_3 contents of the samples analyzed.

4.4.3 Rare earth elements

The rare earth element (REE) content is presented in Table 7. Table 8 and Table 9 bring normalized REE values relative to post-Archean Australian shale (PAAS) and chondrite (after Taylor & McLennan, 1985, Appendix D), further illustrated by Figures 45 and 46, respectively.

The total REE content (∑REEs) displayed a positive correlation with Al_2O_3 (Figure 47). ∑REEs progressively decreased between the various types of Fe-oxides in the following order: S_0/S_1-parallel hematite (81.7 ppm), S_1-parallel hematite (20.1 ppm), S_2-parallel hematite (12.7 ppm) and magnetite (8.11 ppm). Both host rock marble and Ca-Mg-Mn carbonate exhibited low ∑REEs values of 3.2 and 4.2 ppm, respectively.

When normalized to PAAS, REE patterns of the various Fe-oxides, except for magnetite, displayed a light rare earth element (LREE) depletion relative to the heavy rare earth elements (HREE) enrichment (Figure 45). Magnetite, host rock marble, and Ca-Mg-Mn carbonate exhibited relatively flat REE patterns, with the latter characterized by an apparent MREE enrichment.

Ce anomalies, defined as $\frac{Ce}{Ce^*} = Ce_N/[(La_N) * (\mathrm{Pr}_N)]^{1/2}$, were always negative, whether normalized with to chondrite or PAA. Further, chondrite normalization illustrated depleted Eu values, with Eu anomalies defined as $\frac{Eu}{Eu^*} = Eu_N/[(Sm_N) * (\mathrm{Gd}_N)]^{1/2}$. Shale-normalized Eu anomalies were slightly

positive for the different types of hematite and Ca-Mg-Mn carbonate (in the range of 1.08 to 1.22), while magnetite and host rock marble displayed negative values (0.84 and 0.69, respectively).

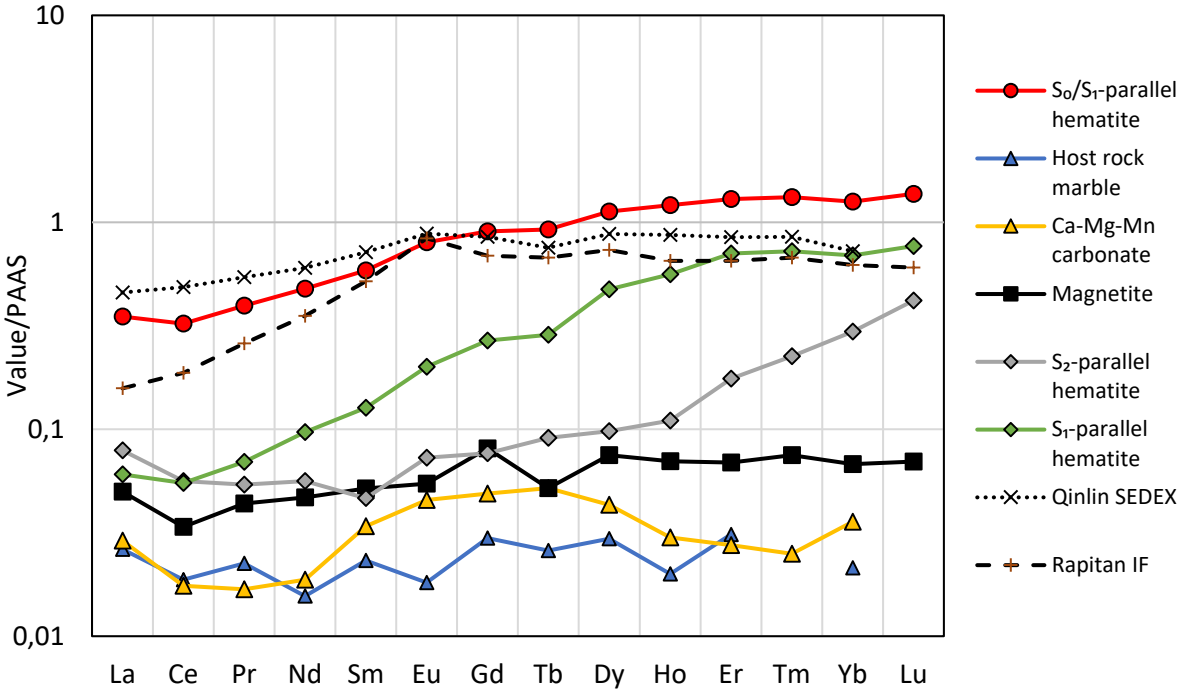

Figure 45 - REE content of selected samples normalized to PAAS (Taylor & McLennan, 1985). REE patterns of the Qinling-type SEDEX deposit (Xuexin et al., 1997) and the Rapitan IF (Halverson et al., 2011) have been added for comparison.

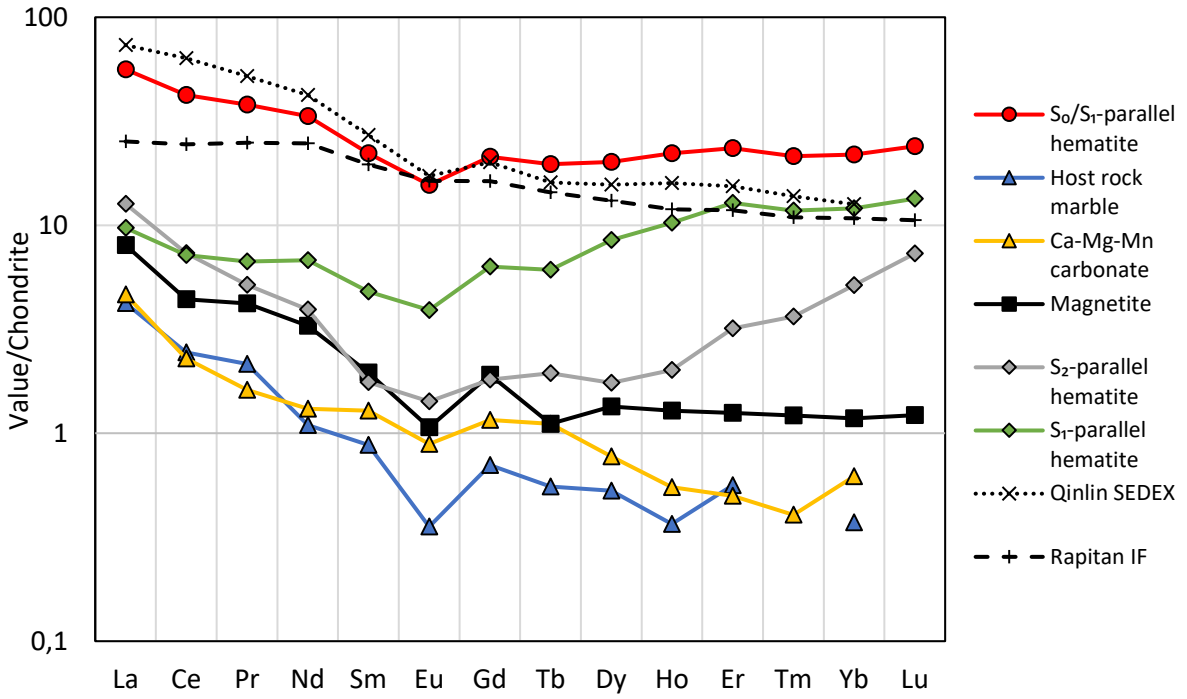

Figure 46 - REE content of selected samples normalized to chondrite (Taylor & McLennan, 1985). REE patterns of the Qinling-type SEDEX deposit (Xuexin et al., 1997) and the Rapitan IF (Halverson et al., 2011) have been added for comparison.

As illustrated by Figure 48, results indicate a strong positive correlation between Y and Ho, while no correlation has been observed between Y/Ho and Al_2O_3 (Figure 49). The Y/Ho values ranged between 32.9 and 39.1 for the various Fe-oxides and Ca-Mg-Mn carbonate, while host rock marble showed an elevated Y/Ho value of 60.

4.4.3.1 REEs correlation plots

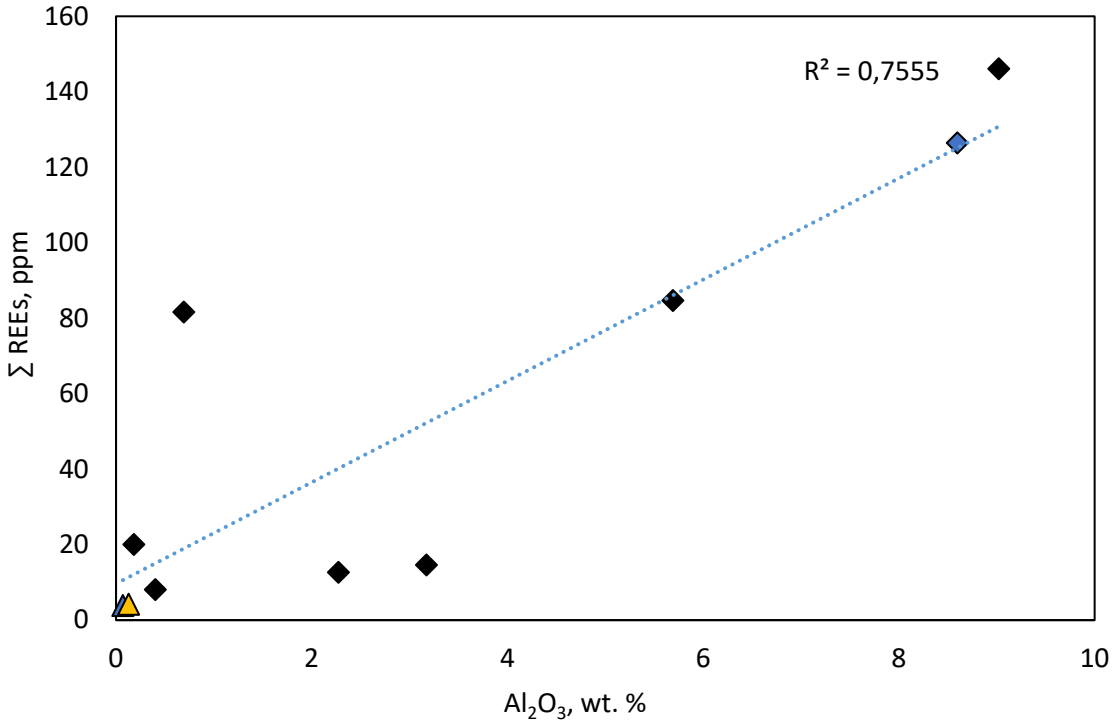

Figure 47 - Plot of Al_2O_3 against ∑REEs showing a positive correlation between the ∑REEs and Al_2O_3 contents of the samples analyzed (black squares – Fe-oxides; blue square – Vareš, Bosnia; yellow triangle – Ca-Mg-Mn carbonate; blue triangle – host rock marble).

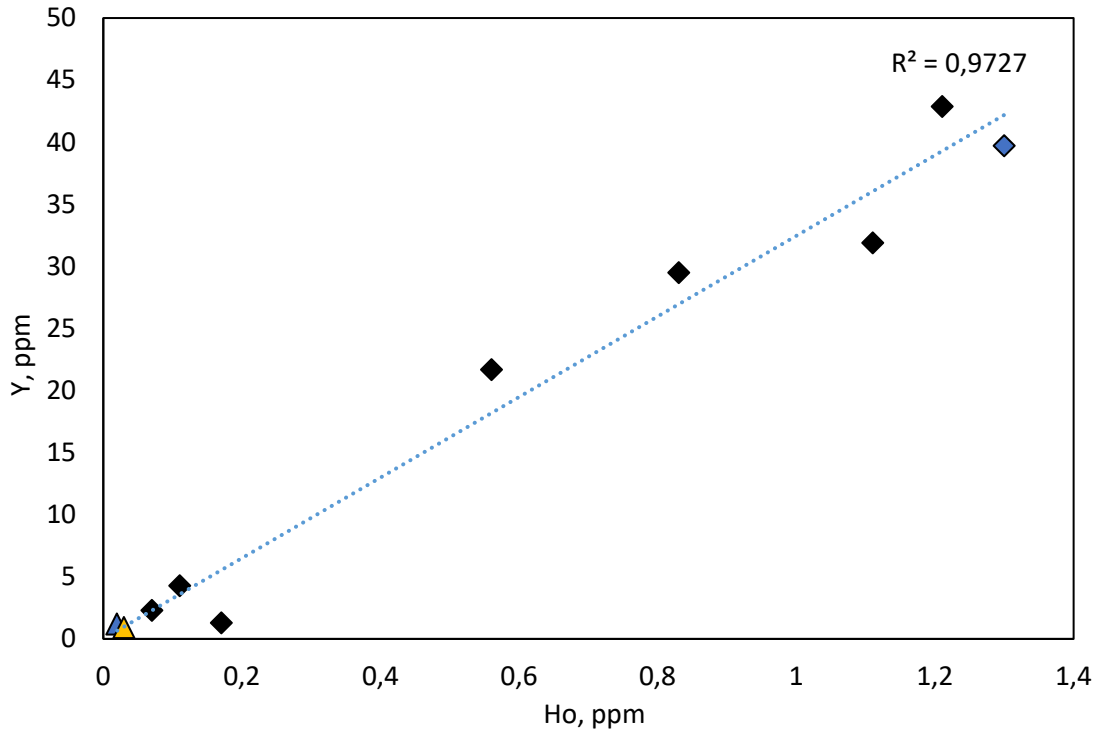

Figure 48 - Plot of Ho against Y (ppm) showing a strong positive correlation between the two elements.

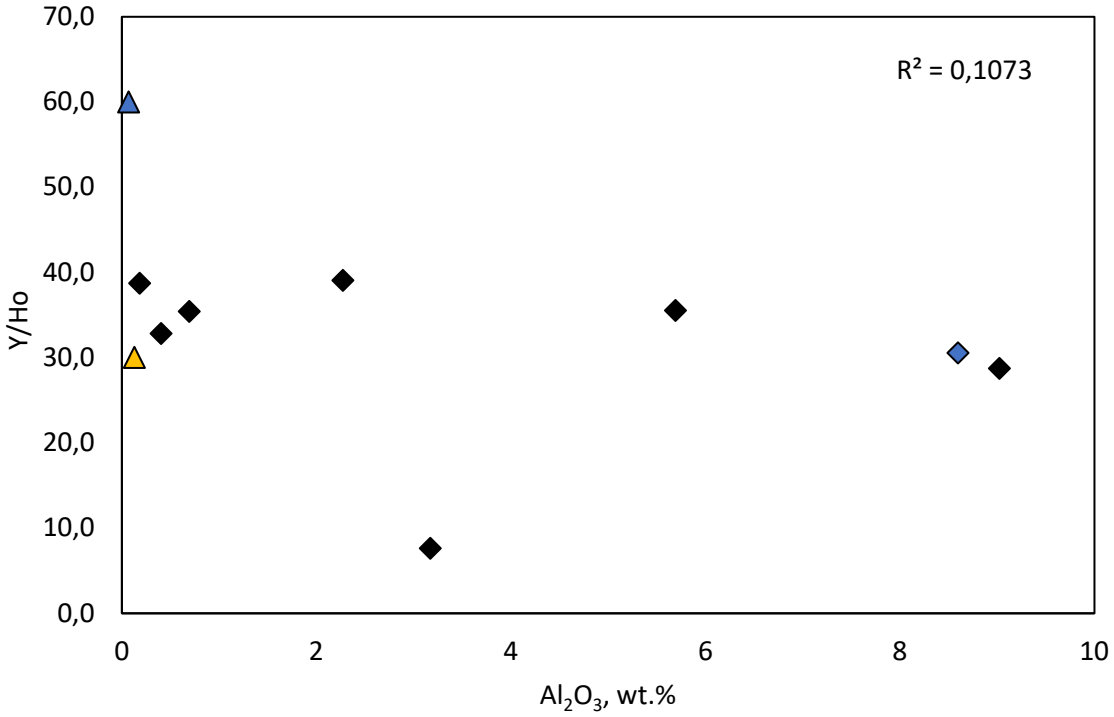

Figure 49 – Plot of Al_2O_3 (wt. %) against Y/Ho values showing no statistical correlation between these.

4.5 Carbonate stable isotopes

Stable isotope analyses ($\delta^{13}C$ and $\delta^{18}O$) were performed on host rock marble and various generations of gangue carbonates from the Kvannvatnet mining area. The $\delta^{13}C$ and $\delta^{18}O$ values are listed in Table 10 and illustrated in Figure 50. Slightly enriched barren calcitic host rock marble (Figure 18A) exhibited $\delta^{13}C$ and $\delta^{18}O$ values between 4.5 to 4.7‰ and 25.7 to 25.9‰, respectively. Various generations of S_0/S_1-parallel carbonate associated with the iron mineralization displayed $\delta^{13}C$ values in the range of -2.8 to -0.3‰ and $\delta^{18}O$ values varying between 15.2 to 19.4‰. Isotopic compositions of Ca-Mn-carbonate from F_1-fold limbs overlapped with the values of foliation-parallel carbonate and showed $\delta^{13}C$ and $\delta^{18}O$ values ranging between -2.4 to -2.3‰ and 16.8 to 17.0‰, respectively. Carbonates of an F_1-fold hinge (Figure 19D) showed significant depletion of ^{13}C ($\delta^{13}C$ values vary between -6.6 to -8.2‰), while $\delta^{18}O$ values ranged from 17.3 to 17.7‰. In addition, carbonate from the sampled post-D_2 quartz-carbonate vein (Figure 22) exhibited a mixed isotopic composition with $\delta^{13}C$ values varying from -1.1 and -0.9‰ and $\delta^{18}O$ values of 20.5‰.

Table 10 – Carbon and oxygen isotope composition ($\delta^{13}C$ and $\delta^{18}O$) of host rock marble and various types of gangue carbonates from the ore-bearing Dunderland Formation.

Sample name	Sample type	Mineralogy	$\delta^{13}C$ VPDB [‰]	$\delta^{18}O$ VPDB [‰]	$\delta^{18}O$ SMOW [‰]
Rana 12 #1	Host rock marble	Cal	4.5	-5.0	25.7
Rana 12 #3	Host rock marble	Cal	4.7	-4.8	25.9
Rana 12 #2	Host rock marble	Cal	4.5	-5.0	25.7
Rana 5b	S_0/S_1-parallel	Ca-Mn-Cb+Sps	-2.0	-12.2	17.0
Rana 14 #1	S_0/S_1-parallel	Ca-Mg-Mn Cb	-2.8	-13.8	15.3
Rana 14 #2	S_0/S_1-parallel	Ca-Mg-Mn Cb	-2.3	-14.0	15.2
Rana 13 #1	S_0/S_1-parallel	Cal+Qz	-1.9	-11.3	19.2
Rana 13 #2	S_0/S_1-parallel	Cal+Qz	-0.3	-11.1	19.4
Rana 6	S_0/S_1-parallel	Ca-Mn-Cb	-2.0	-11.7	17.6
Rana 6	S_0/S_1-parallel	Ca-Mn-Cb	-1.8	-11.7	17.6
FL5 #1	F_1-fold limb	Ca-Mn-Cb+Sps	-2.3	-12.4	16.8
FL5 #2	F_1-fold limb	Ca-Mn-Cb+Sps	-2.4	-12.2	17.0
FL5 #3	F_1-fold limb	Ca-Mn-Cb+Sps	-2.4	-12.4	16.8
FL6 #1	F_1-fold hinge	Cal+Qz+Ep	-6.6	-12.8	17.7
FL6 #2	F_1-fold hinge	Cal+Qz+Ep	-8.2	-13.1	17.3
Rana 10 #1	Post-D_2 Qz-Cb vein	Cal+Qz+Ep	-1.1	-10.0	20.5
Rana 10 #2	Post-D_2 Qz-Cb vein	Cal+Qz+Ep	-0.9	-10.1	20.5

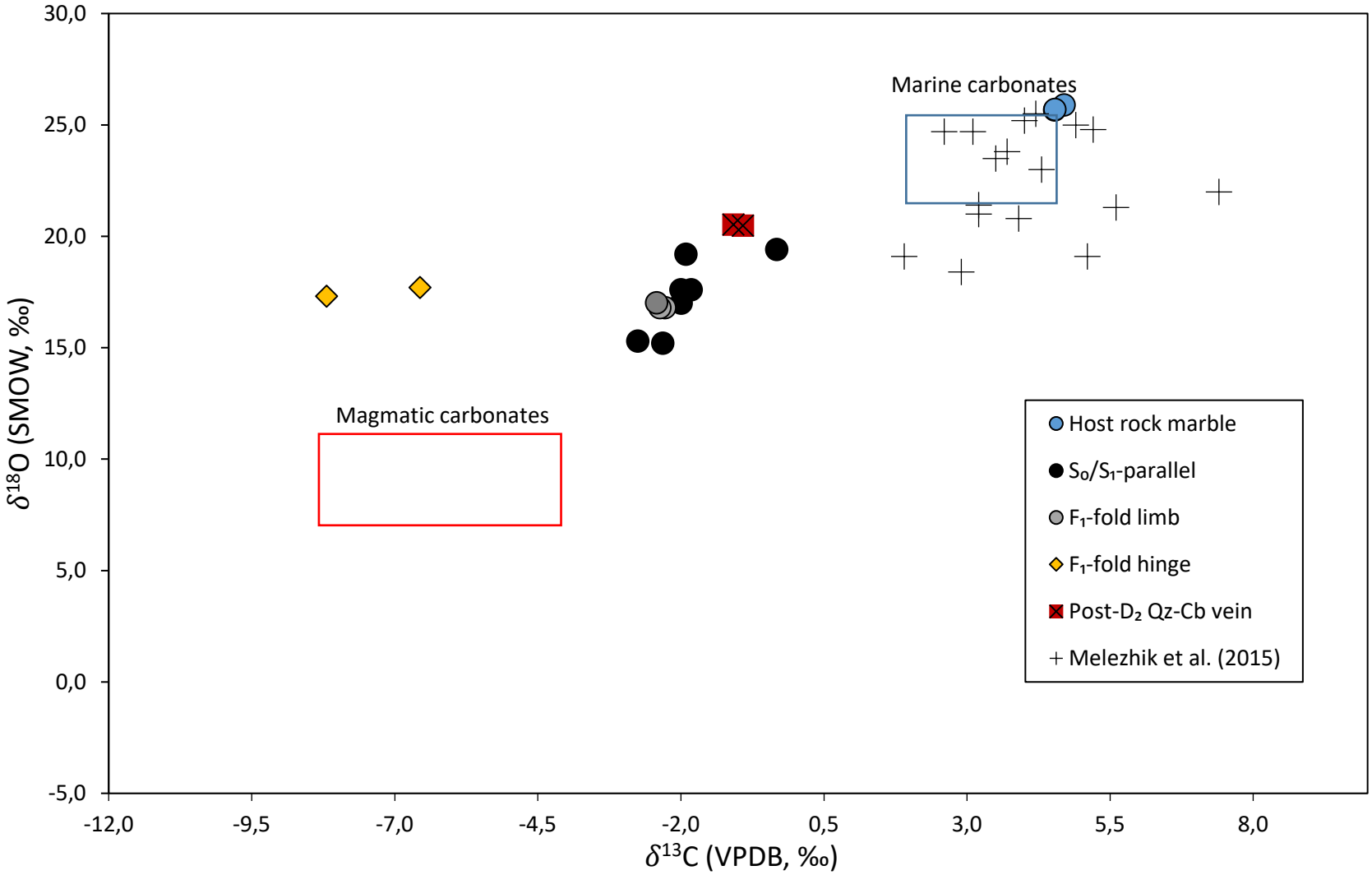

Figure 50 – Plot of $\delta^{13}C$ vs. $\delta^{18}O$ values (relative to PDB and SMOW, respectively) of the different generations of carbonates from the ore-bearing sequences of the Dunderland Formation. The reference values of marine and magmatic carbonates are from Veizer & Hoefs (1976) and Taylor et al. (1967), respectively. Isotopic compositions of host rock marbles from the Dunderland Formation obtained by Melezhik et al. (2015) have been included (marked by +).

4.6 Fluid inclusion petrography and microthermometry

In general, five different fluid inclusion types have been recognized according to their petrographical features: Type 1 - aqueous two-phase (L+V) liquid-rich (Figures 51A; 51B); Type 2 - aqueous two-phase (L+V) vapor-rich (Figures 51C; 51D); Type 3 - CO_2-bearing (Figures 51E; 51F); Type 4 - late aqueous two-phase (L+V) liquid rich (Figures 52A; 52B); and Type 5 - halite-bearing (L+V+S) aqueous inclusions (Figures 52C; 52D). All fluid inclusions were observed in anhedral quartz displaying no observable crystal zoning under the transmissive light microscope. As no focal points could aid in the genetic classification of the various FI types, classification of the FIs with regards to the primary-secondary terminology was generally problematic. Hence, the FI assemblage approach has been applied instead. FIs in the post-D_2 quartz-carbonate vein do, in any case, represent late-stage fluids with respect to the Type 1, 2 and 3 FIs observed in S_0/S_1-parallel quartz veins. The obtained petrographic and microthermometric data are summarized in Table 11 below.

Table 11 – Summary of fluid inclusion data obtained from quartz samples of the Kvannvatnet open pit mining area (L – liquid phase; V – vapor phase; Th – temperature of homogenization).

Setting	S_0/S_1-parallel quartz			Post-D_2 quartz	
Fluid inclusion type	1	2	3	4	5
Genetic classification	(?)	(?)	Primary	(?)	(?)
Phases (at 25°C)	L+V	L+V	L+V	L+V	L+V+S
Degree of fill (at 25°C)	0.7-0.8	0.4-0.6	-	0.6 to 0.9	0.8-0.9
Composition	NaCl-$CaCl_2$-H_2O	NaCl-$CaCl_2$-H_2O	NaCl-$CaCl_2$-CO_2-H_2O	NaCl-$CaCl_2$-H_2O	NaCl-H_2O
Salinity (wt% NaCl eq.)	2.9-8.1	3.7-7.8	2.0-2.6	3.4-6.0 (16.0)	32.9-34.1
Th (°C)	360-435	380-430	340-365	140-420	360
Density (g/cm^3)	0.399-0.760	0.403-0.456	0.854-0.870	0.619-0.828	0.977-0.983

4.6.1 S_0/S_1-parallel quartz veins

4.6.1.1 Type 1 – two-phase liquid-rich FIs

Type 1 FIs are two-phase (L+V) liquid-rich inclusions distributed in parallel to subparallel intragranular trails and planar arrays (Figure 51A) in S_0/S_1-parallel veins composed of recrystallized quartz (Figure 19B). These FIs are suspected to be of a pseudosecondary origin, as the trails apparently do not cross-cut quartz grain boundaries. The aqueous inclusions generally exhibit a relatively uniform degree of fill of 0.7 to 0.8. The size of the inclusions varies between 5 to 15 µm and are characterized by elongate to distorted spherical morphologies (Figure 51B).

During microthermometric experiments eutectic temperatures were difficult to observe, with a first ice-melting temperature of approximately -55°C obtained only once, indicating the presence of $CaCl_2$ in the system. Salinities (8.1 to 2.9 wt.% NaCl eq., Figure 53) were determined using the last ice-melting temperatures (-5.2 to -1.7°C) and experimental data of Bodnar (2003b). Type 1 FIs homogenized to

liquid at temperatures in the range between 360 to 435°C, but most commonly between 380 to 390°C (Figure 54). Calculated end-member bulk densities ranged from 0.399 to 0.760 g/cm^3.

4.6.1.2 Type 2 – two-phase vapor-rich FIs

Type 2 FIs were two-phase (L+V) vapor-rich inclusions observed in the same foliation-parallel quartz vein as the Type 1 FIs mentioned above. They are, however, less prevalent compared to the type 1 FIs and occur in planar arrays and trails (Figure 51C). Although, the genetic classification purely based on petrographic observations were problematic, the Type 1 and Type 2 FIs occur in individual FI assemblages. Further, the vapor-rich inclusions regularly exhibit spherical to equant shapes with varying degrees of fill (0.3 to 0.6, Figure 51D). The sizes of Type 2 FIs are similar to those of Type 1 FIs and vary between 5 to 10 µm.

Eutectic temperatures were indeterminable, barring two occasions that yielded first ice-melting temperatures of approximately -60°C. Such temperatures indicate the presence of Ca^{2+} and/or other divalent ions in solution. Last ice-melting temperatures ranged between -4.8 and -2.2°C, yielding salinities in the range from 3.7 to 7.8 wt.% NaCl eq. (Figure 53). Temperatures of homogenization were obtained in the interval between 380 and 430°C (Figure 54), while bulk densities ranged from 0.403 to 0.456 g/cm^3.

4.6.1.3 Type 3 – CO_2-bearing FIs

CO_2-bearing FIs have been observed in S_0/S_1-parallel quartz veins closely associated with a thick, steeply dipping calcitic marble unit (Figure 18). Although no crystal zonation could be observed, these inclusions occur in distinctly isolated clusters (Figure 51E), thereby signifying a primary origin relative to the crystallization/recrystallization of the host quartz. The size of the inclusions ranges from a few microns up to approximately 20 µm, with equant to distorted spherical morphologies commonly observed (Figure 51F). The percentage of CO_2-free phase was estimated to approximately 20%.

The CO_2-bearing inclusions are similar in appearance to the aforementioned aqueous inclusions under room-temperature. However, a distinct double bubble behavior occurred during microthermometric cooling runs (Figure 51F), suggesting the presence of a volatile component in the system. Further, eutectic temperatures indicate the presence of Ca^{2+} and/or other divalent cations in the system, commonly observed at approximately -60°C. Salinities were calculated based on the temperatures of final clathrate melting (8.8 to 9.0°C) and lied in the uniform range of 2.0 to 2.6 wt.% NaCl eq. (Figure 53). Temperatures, at which CO_2-homogenization occurred after clathrate melting, ranged from 14.0 to 16.4°C and were obtained in order to calculate the densities of CO_2-phases. Temperatures of total homogenization, meanwhile, were generally problematic to obtain as the CO_2-bearing inclusions often decrepitated before homogenization. However, total homogenization temperatures were observed on

three occasions and ranged between 340 to 365°C (Figure 54). The temperatures of CO_2 homogenization were used to calculate the density of the CO_2-phase. Bulk densities lied in the range between 0.854 and 0.870 g/cm^3.

4.6.2 Post-D_2 quartz-carbonate vein

4.6.2.1 Type 4 – post-D_2 two-phase liquid-rich FIs

Abundant two-phase liquid-rich FIs in post-D_2 quartz (Figure 22) represent fluids observed in random distributions and planar arrays. Type 4 FIs are irregularly shaped (Figure 52B), with elongate morphologies commonly oriented in parallel trails (Figure 52A) and display heterogeneous degrees of fill. The size of the inclusions ranges between 5 up to 20 µm, though the FIs are generally smaller than 10 µm.

Similarly to Type 1 and Type 2 inclusions described earlier, eutectic temperatures were difficult to obtain. Though, a first ice-melting temperature of -60°C was recorded at one occasion, pointing to the presence of Ca^{2+} in the system. Final ice-melting temperatures (-3.7 to -2.0) correspond to salinities in the range of 3.4 to 6.0 wt.% NaCl eq. (Figure 53). In addition, final ice-melting temperatures of -12°C for three individual inclusions correspond to a salinity of 16 wt.% NaCl eq. Type 4 FIs were typified by scattered temperatures of homogenization, ranging from 140 to 420°C (Figure 54). Calculations of bulk densities from end-member homogenization temperatures yielded values between 0.619 and 0.828 g/cm^3.

4.6.2.2 Type 5 – post-D_2 halite-bearing FIs

Halite-bearing multiphase (L+V+S) FIs have been observed in numerous densely spaced, irregular trails (Figure 52C). The largest inclusions (approx. 10 µm) are often irregularly shaped (Figure 52D), though distorted spherical morphologies commonly typify smaller inclusions. Moreover, the inclusions are characterized by uniform degrees of fill in the range of 0.8 to 0.9, where the cubic halite crystals generally make up less than 30% of the inclusion volumes.

Eutectic temperatures of halite-bearing inclusions were obtained within the range of -25 to -20°C and indicate the presence of NaCl in solution. Salinity calculations were based on halite-dissolution temperatures (1), ranging from 220 to 240°C and yielding salinities ranging from 32.9 to 34.1 wt.%. Dissolution of solid phases occurred before homogenization to liquid took place. The latter temperatures were, however, problematic to obtain as nearly all halite-bearing FIs decrepitated before homogenization. Nevertheless, a homogenization temperature of 360°C was documented on two occasions (Figure 54). Bulk densities lied in the range from 0.977 to 0.983 g/cm^3, which were calculated using the temperatures of halite dissolution and liquid-vapor homogenization.

4.6.2.3 *Vapor-rich and decrepitated FIs*

Rare and homogenously distributed vapor-rich FIs containing minuscule amounts of liquid along the rims (seldom observable by microscopy) commonly display negative crystal shapes (Figure 52E). However, performing microthermometric measurements on these was not viable, and they will thus not be considered further. Additionally, abundant dark masses containing ample offshoots represent post-D_2 FIs that have undergone decrepitation (Figure 52F).

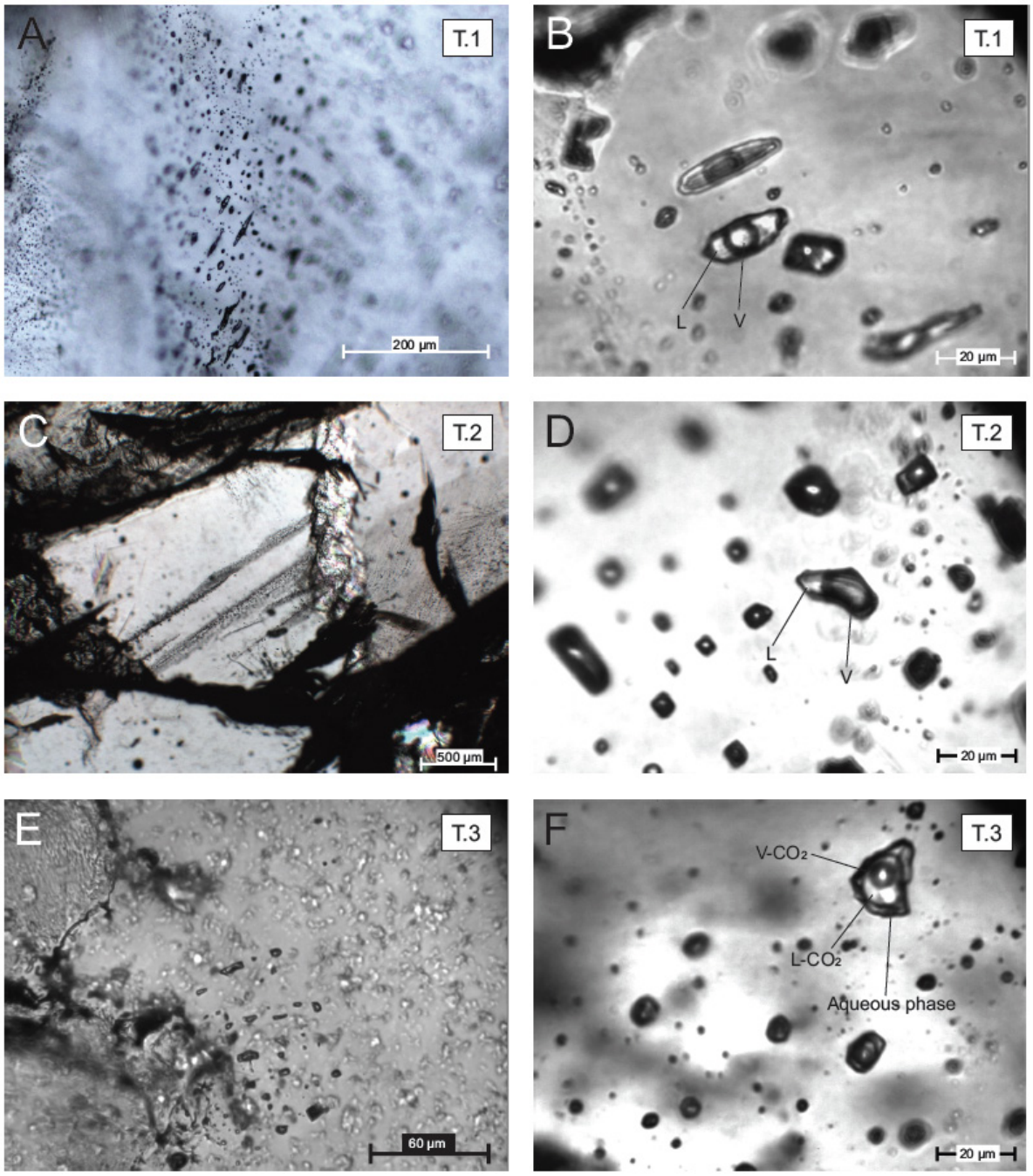

Figure 51 – Microphotographs illustrating Type 1, 2, and 3 FIs in S_0/S_1-parallel quartz-veins. (A) Suspected secondary or pseudosecondary Type 1 FIs distributed in planar arrays (sample Rana 14). (B) Type 1 FIs were aqueous two-phase (L+V) liquid-rich inclusions characterized by highly filled elongated to sub-spherical or equant inclusions. (C) Trails of suspected pseudosecondary (i.e. do not cross grain boundaries) Type 2 FIs in quartz (sample Rana 14). (D) Type 2

(Figure 51 cont.) FIs were aqueous two-phase (L+V) vapor-rich inclusions characterized by equant to distorted spherical inclusion morphologies and relatively low degrees of fill. (E) CO_2-bearing (Type 3) inclusions found in distinctly isolated clusters, indicating a primary origin relative to the recrystallization of host quartz. (F) Presence of CO_2-bearing phases was inferred from the distinct double bubble behavior occurring as inclusions were cooled during microthermometric experiments.

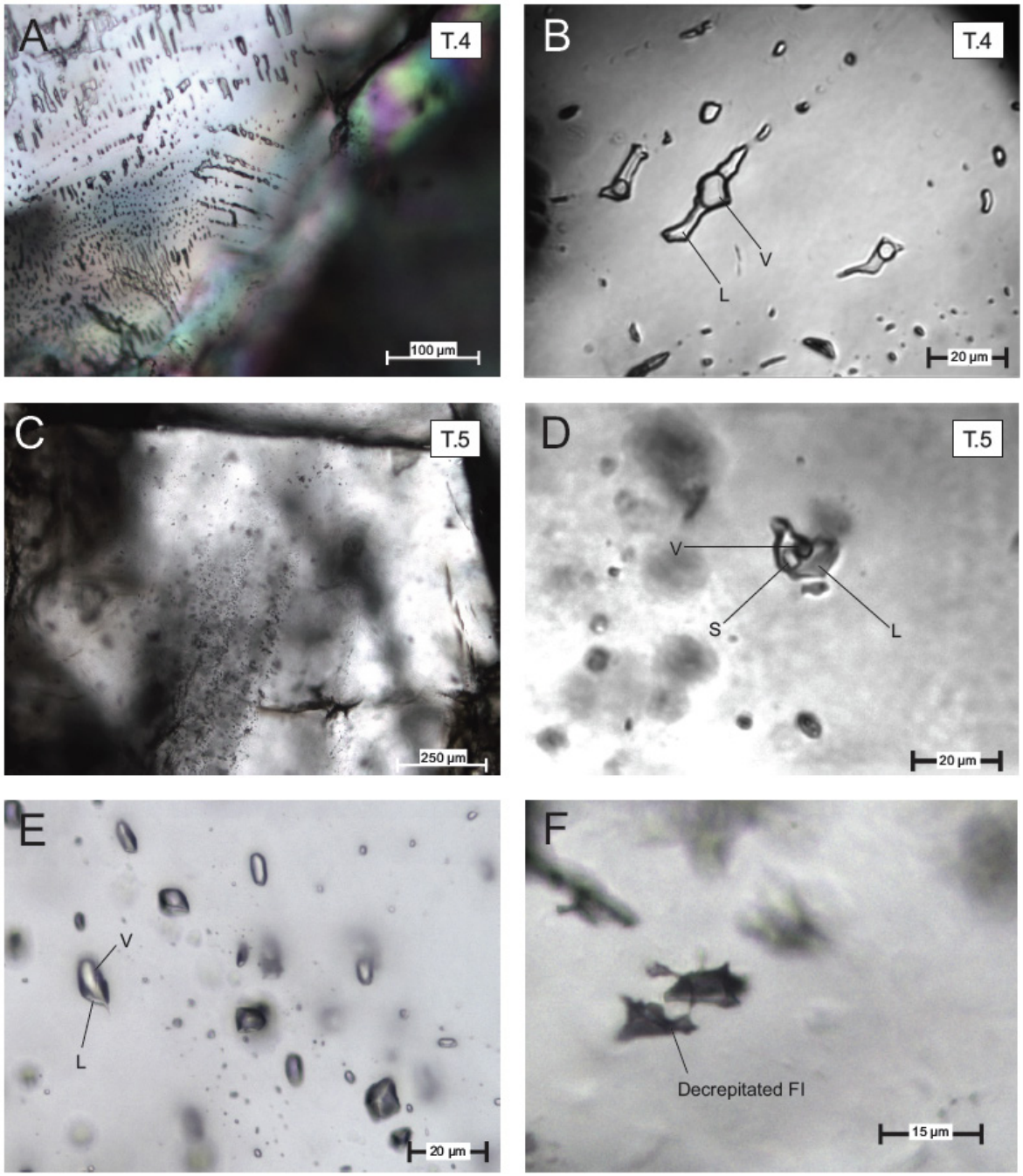

Figure 52 – Microphotographs illustrating Type 4 and Type 5 FIs observed within post-D_2 quartz (sample Rana 10), in addition to vapor-rich and decrepitated FIs. (A) Type 1 FIs were commonly observed in planar arrays where elongated inclusions aligned in parallel orientations. (B) Type 1 FIs were aqueous two-phase (L+V) liquid-rich inclusions characterized by irregular, elongate shapes and heterogeneous degrees of fill. (C) Halite-bearing inclusions (Type 5) were distributed in numerous densely spaced traced, irregular trails. (D) The halite-bearing FIs were commonly irregularly shaped and were characterized by uniform phase ratios and large degrees of fill. (E) Additionally, two-phase (L+V) vapor-rich FIs were observed within post-D2 quartz, containing minuscule amounts of liquid phase on the rims of the inclusions (barely visible under microscope). These FIs, often exhibiting negative crystal shapes, were not deemed viable for microthermometric analyses. (F) Abundant dark masses exhibiting ample offshoots were also observed along with the aforementioned inclusions and represented FIs which had undergone decrepitation (fluid loss).

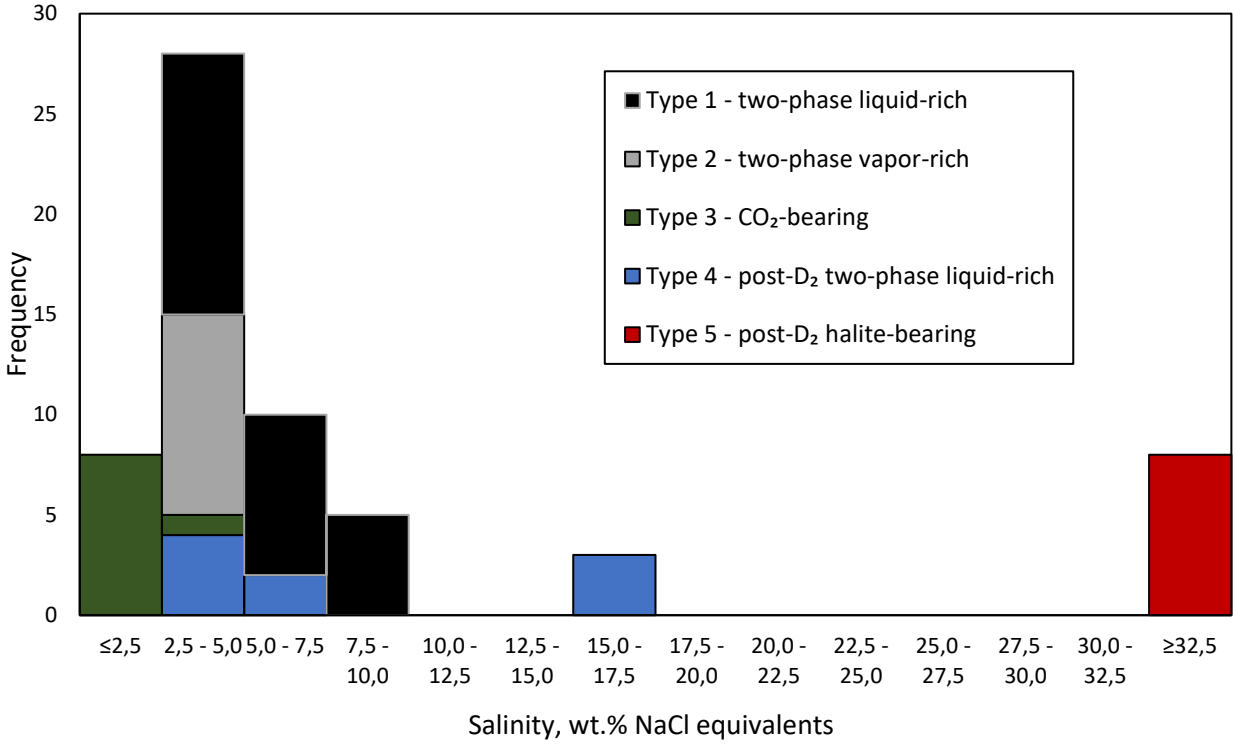

Figure 53 – Calculated salinities (in wt.% NaCl equivalents) of the different FI types observed within the studied samples. The FIs were generally portrayed by low salinity fluids representing a unimodal distribution in the histogram. Three individual Type 4 inclusions recorded salinities of 16 wt.% NaCl equivalents. In contrast, halite-bearing inclusions represented highly saline fluids in the range of 32.9 to 34.1 wt.% NaCl equivalents.

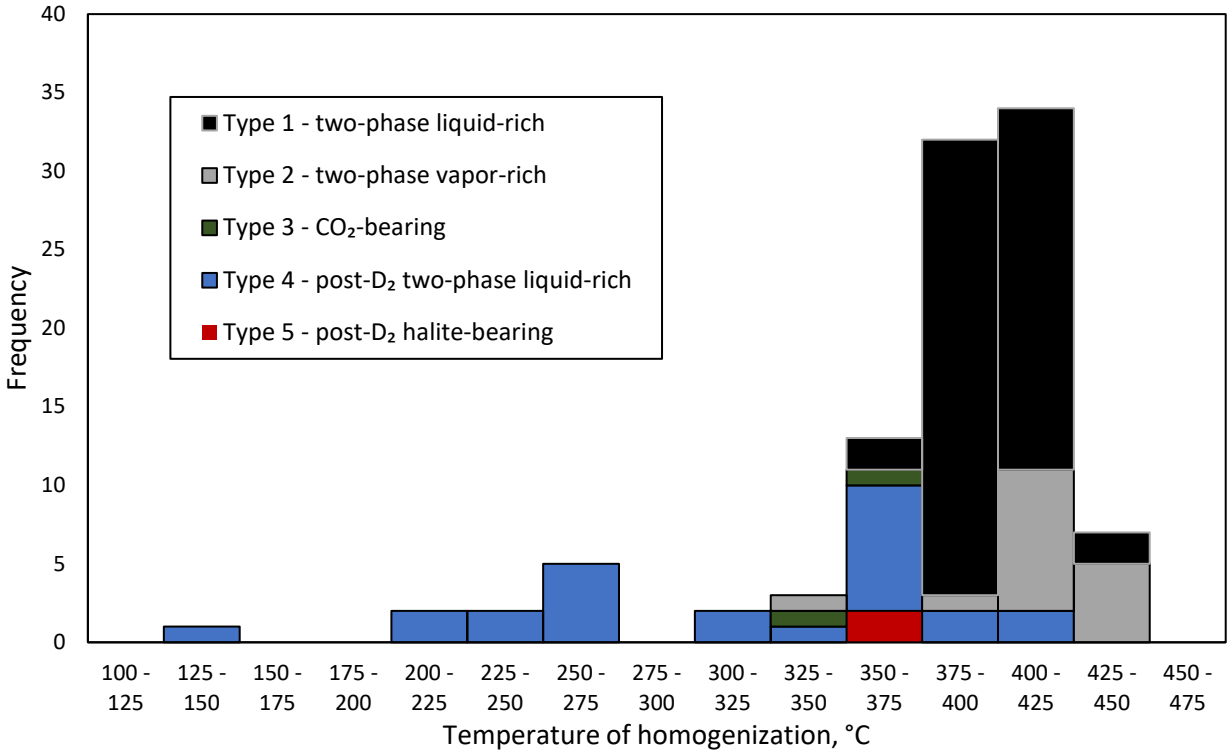

Figure 54 – Obtained temperatures of homogenization of the different FI types from the studied samples. Type 1, 2 and 3 FIs exhibited a relatively unimodal distribution of homogenization temperatures. In contrast, the homogenization temperatures of late-stage aqueous (Type 4, blue) FIs were typified by a widely scattered distribution.

5 Discussion

In order to determine the controlling mechanisms of Fe-oxide formation, an emphasis has been placed on investigating the geochemical characteristics of host rocks and ore mineralization within a structural framework. The following subchapters reflect upon the findings from petrographic analyses (5.1), lithogeochemistry (5.2), and carbonate stable isotope analyses (5.3). The obtained fluid inclusion data and its implications for the tectonic evolution of the studied area are discussed in section 5.4. Whereas section 5.5 presents a comparison of the Dunderland IFs with banded iron formations and Neoproterozoic iron formations, section 5.6 brings a comparison between the studied mineralization and classic SEDEX deposits. The final section (5.7) of this chapter addresses the matters relating to hematite and magnetite formation as inferred from the obtained experimental data.

5.1 Mineral paragenesis and strain variations

Based on the results of petrographic analyses, a paragenetic sequence for the various studied lithologic units has been suggested (Figure 55). Furthermore, strain variations in ore bodies and host rocks, which were evident in both macro- and micro-scale, have given rise to different generations of Fe-oxides characterized by significantly different morphologies. The observed strain variations may be explained by differences in the competence of lithologic units or a heterogeneous strain distribution, but will not be further expanded upon in the following paragraphs.

Following the primary mineralizing events and diagenesis, the Dunderland IFs were subjected to different stages of metamorphism and deformation during the Caledonian Orogeny. Similar to reports from other Precambrian BIFs, such as the high-grade Fe-ores in Quadrilátero Ferrífero of Brazil (Ramos de Oliveira et al., 2015), enrichment of the Dunderland Fe-ores has occurred through multiple stages.

Where rhythmic layering is believed to be preserved, hematite is found as equigranular to sub-spherical, small and randomly oriented grains in bands parallel to the S_0/S_1-foliation (Figure 29). These grains also exhibit a relatively weak anisotropy and limited polysynthetic twinning. Twin lamellas are generally believed to result from mechanical deformation, although growth lamellas are not uncommon (Ramdohr, 1969). The aforementioned textural observations, along with randomly oriented biotite, are suggestive of a diagenetic origin for the hematite preserved in low strain (S_0/S_1) domains. However, due to the relatively homogeneous grain size of these samples, the possibility that the hematite was recrystallized to smaller grains may not be ruled out (Ramdohr, 1969). Paragenetically early hematite, similar to the hematite in S_0/S_1-parallel bands, is also present as inclusions within poikiloblastic feldspars (Figure 32A). More coarse-grained euhedral to subhedral hematite grains were observed is interstitial grains in between the feldspar poikiloblasts (Figure 32A), and are thus believed to have formed at a later stage.

A syn-deformational Fe-enrichment is evident from samples characterized by higher degrees of strain. During the main thrusting-stage (D_1) of the Caledonian Orogeny, the original bedding was strongly sheared, resulting in the formation of isoclinal F_1-folds. Consequently, samples from high strain domains are characterized by euhedral specular hematite with a strong crystallographic orientation along the S_1-axial surfaces (Figure 31A). The development of distinctly foliated fabrics was accompanied by an increase in the grains size of hematite: In the low strain domains, grain size typically ranges from 15 to 30 µm, while the longest axes of the specularite commonly exceed 500 µm. Specularite bands have also been overprinted, often at right angles to the foliation, by lesser amounts of more equigranular elongated hematite crystals. The latter could have originated from the reworking of hematite during the D_1/D_2 events (Figure 55).

Paragenetically late hematite is characterized by less well-developed tabular grains that are oriented along the crenulation surfaces (S_2) of F_2-folds (Figure 32B) but is also present in the thickened hinge zones of F_2-folds (Figure 31D). The late stage hematite has a similar textural character to hematite found as interstitial grains in between poikiloblastic feldspars and exhibit little to no polysynthetic twinning. These observations suggest that the hematite recrystallized from pristine hematite (or Fe-oxyhydroxides) during the early stages of the D_2-event. Furthermore, the hematite is consistently overgrown by lower amounts of elongated magnetite grains (Figure 32B). The latter may thus have formed at a late stage by the replacement of hematite during the D_2-event. Spinel-shaped magnetite was also observed in the hinge zones of F_1/F_2-folds (Figure 32A), which could suggest that magnetite is preserved in zones of low strain. Additionally, the late-stage sulfide-bearing quartz-carbonate vein is suggested to represent a post-D_2 semi-ductile/brittle event associated with late Caledonian Orogeny, which is further discussed in section 5.4.3.

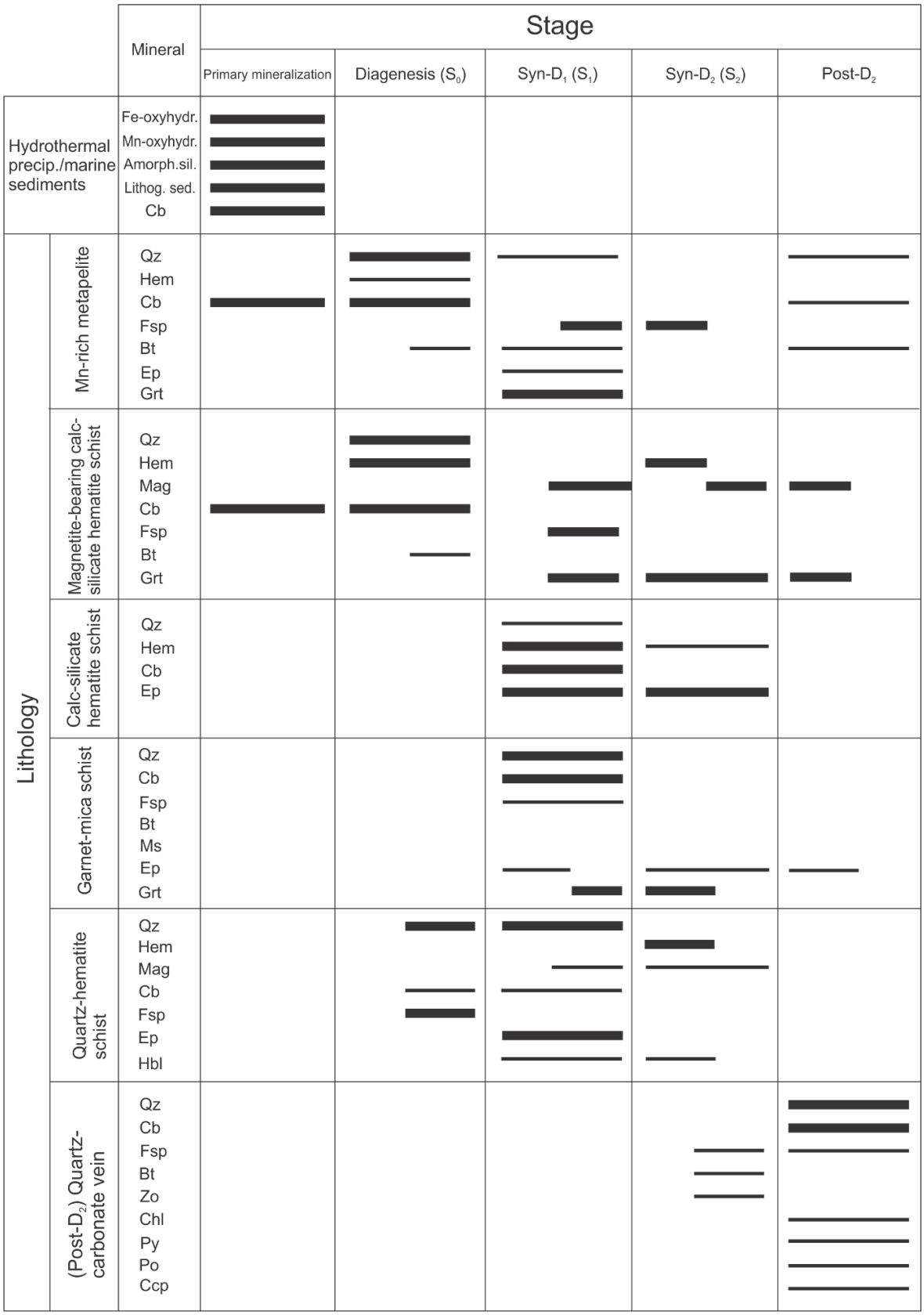

Figure 55 – Suggested mineral paragenetic sequence of the principal lithologic units studied. Except for the primary mineralizing stage, the relative time-ordering of ore mineralization and its genetic relations to host rocks have been inferred from petrographic observations. For discussion on primary mineralizing events the reader is referred to sections 5.2 and 5.7. The subsequent stages included diagenesis, metamorphism and deformation during the Caledonian Orogeny (D_1 and D_2), and a post-D_2 semi-ductile/brittle event. Note that a major part of the recrystallization occurred during the D_1-event.

5.2 Major and trace element composition

In the following section, the results of the lithogeochemical analyses and their implications will be discussed in more details. Notably, the dataset represents a relatively small number of samples from limited sections of the ore bodies; hence any local or regional geochemical variations are not revealed. However, the obtained data reflects the chemistry of the various generations of Fe-oxides as inferred from their particular textural features and structural association (section 5.1).

5.2.1 Sources of major elements

The major element composition of the mineralized samples was characterized by enrichment of Si, Fe, Mn, and P, while values for Ti, Mg, Na, and K from hematite and magnetite were similar to those of typical marine shales (Cody Shale, Figure 36). In comparison to Mn-nodules, analyzed samples showed high SiO_2/Al_2O_3 values, which, according to Gurvich (2006), could reflect a hydrothermal source of Si. Enrichment of Si could arise from quartz inclusions, or alternatively, co-precipitated silica intergrowths. No correlation was observed between Al_2O_3 and SiO_2 contents, suggesting that the source of the Al and Si was not the same. MnO and MgO contents, although low when compared to that of SiO_2, were likely bonded in the carbonate component of mineralized samples.

High Fe_2O_3/Al_2O_3 values reflect the original enrichment in Fe compared to Al, and may, according to Cox et al. (2013), indicate a hydrothermal source of Fe. Although the dataset is limited, the positive correlation between TiO_2 and Al_2O_3 suggests that Al was delivered as a detrital component. A somewhat negative correlation between Fe_2O_3 and Al_2O_3 may, according to Cox et al. (2013), indicate in situ precipitation of Fe, i.e. orthochemical precipitation.

No correlation was observed between P_2O_5 and Al_2O_3, suggesting that P-enrichment did not occur due to the addition of a detrital component. A correlation was also lacking between P_2O_5 and Fe_2O_3, indicating that P was delivered by some other mechanism than Fe was. For instance, Planavsky et al. (2010) related high amounts of dissolved oceanic phosphorous during the Neoproterozoic to increased post-glacial phosphate fluxes following snowball Earth conditions.

The analyzed carbonate samples displayed high values of LOI, reflecting the devolatilization of carbonate during inductive heating, through the loss of CO_2 via the generalized reaction: $CaCO_3 \rightleftharpoons CaO + CO_2$ (g). The different generations of hematite displayed, as expected, low values of LOI. The negative LOI of magnetite would suggest the addition of mass upon heating. A negative LOI was, in this case, a result of oxidation of Fe^{2+} to Fe^{3+} in iron and formation of Fe_2O_3, represented by the reaction: $4Fe_3O_4 + O_2 \longrightarrow 6Fe_2O_3$.

5.2.1.1 Behavior of Mn

As noted by Lepp (1968), the distribution of Mn in IFs may serve as a valuable indicator of the physicochemical conditions during primary mineralizing events and post-depositional processes. The geochemical behavior of Mn and Fe is relatively similar, as mobility is highly dependent on redox conditions (Murray, 1994). However, separation of the elements may occur due to differential mobility at various redox potentials. For instance, Fe may precipitate as oxides or oxyhydroxides under lower redox potentials than Mn at any given pH (Figure 56), i.e. $Fe(OH)_3$ is less mobile and more readily precipitates in the seawater environment, in comparison to Mn-oxides. Alternatively, Fe and Mn may co-precipitate by incomplete oxidation as carbonates or sulfides. Further separation of the two elements may occur by post-depositional processes, such as diagenesis, metamorphism, and weathering.

The Mn/Fe values of the various generations of Fe-oxides (from 0.002 to 0.007) are low in comparison to the Mn/Fe value of bulk continental crust (0.015, after Rudnick & Gao, 2003), bulk oceanic crust (0.013, after White & Klein, 2014), marine shales (0.011, after Smith, 1995) and typical Mn-nodules (1.70, after Flanagan & Gottfried, 1980). Taking into account that the analyzed Fe-oxides do not represent primary mineralizations, the low Mn/Fe values of mineralized samples suggest that Mn was relatively mobile during diagenetic and metamorphic processes. Such mobilization could take place under reducing conditions, as Mn^{2+} is easily mobilized in comparison to the highly immobile behavior of Mn^{3+} and Mn^{4+} (Figures 56C; 56D). Alternatively, the low Mn/Fe value of diagenetic hematite relative to bulk crustal composition could reflect differential dissolution during fluid/host rock interaction rather than preferential precipitation (Kimberley, 1989). However, whether or not this separation took place during the primary mineralizing events or post-depositional processes is difficult to ascertain purely based on the preceding paragraph. See section 5.7.1.2 for a closer discussion on the genetic relationship between the IF and Mn-enriched zone.

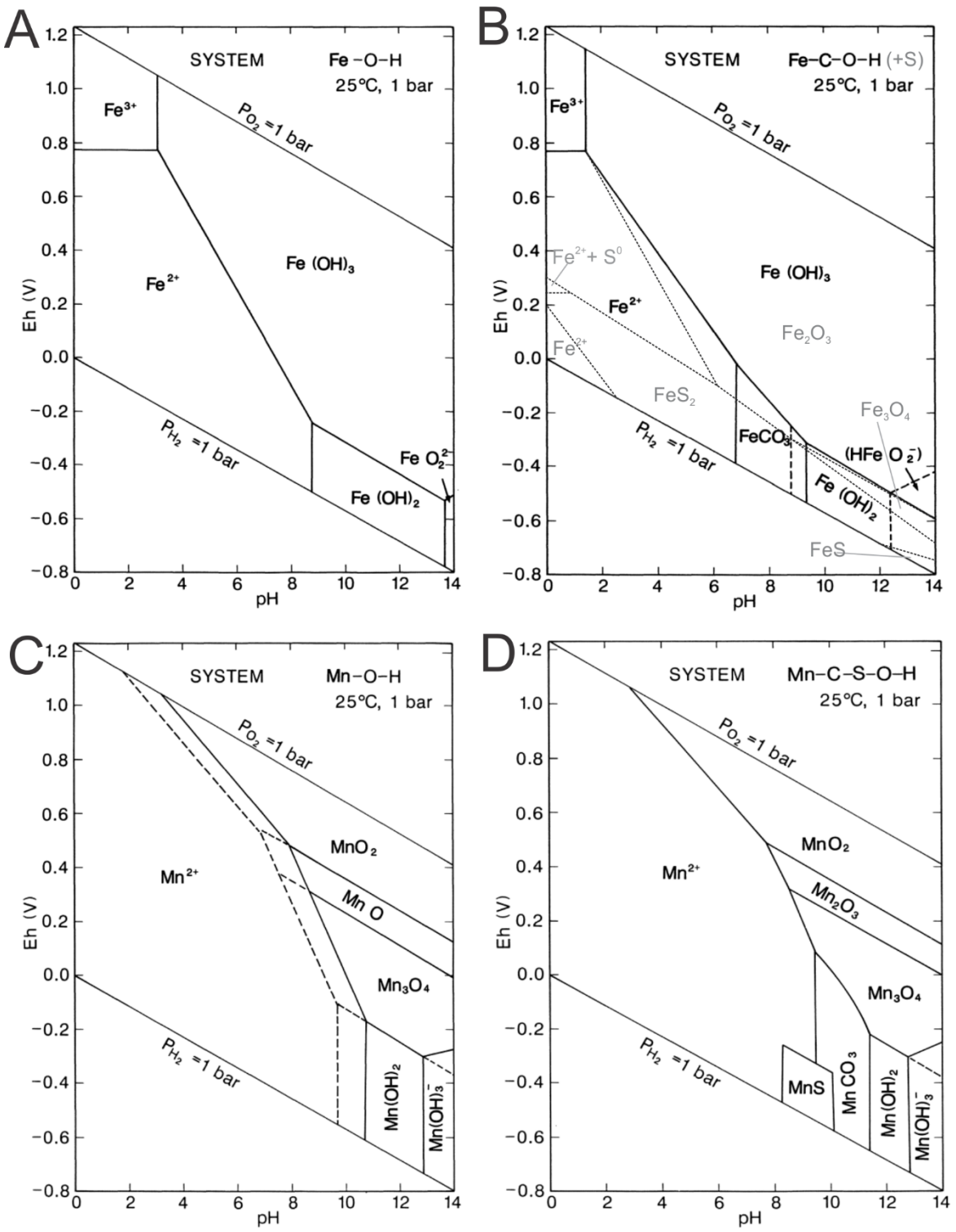

Figure 56 – Eh-pH diagrams of selected Fe and Mn systems (reproduced from Brookins, 1988). (A) Eh-pH diagram of the Fe-O-H system assuming $Fe(OH)_3$ as the stable Fe(III) phase and an Fe-activity of 10^{-6}. (B) Eh-pH diagram for the Fe-C-O-H system assuming $Fe(OH)_3$ as the stable Fe(III) phase and Fe- and C-activities of 10^{-6} and 10^{-3}, respectively. The Fe-S-O-H system has been included and is indicated by stippled lines, where Fe_2O_3 is assumed to be the stable Fe(III) phase and Fe- and S-activities of 10^{-6} and 10^{-3}, respectively. (C) Eh-pH diagram of the Mn-O-H system assuming an Mn-activity of 10^{-6}. (D) Eh-pH diagram of the Mn-C-S-O-H system assuming Mn-, C-, and S-activities of 10^{-6}, 10^{-3} and 10^{-3}, respectively.

5.2.2 Mobility of trace elements

The obtained trace element contents of the analyzed samples were generally low, a feature typically shared by other voluminous IFs (Kimberley, 1989). Figures 57 and 58 illustrate the trace element compositions of the various generations of Fe-oxides and gangue Ca-Mg-Mn carbonate normalized to bulk continental and oceanic crust, respectively. Notably, the syn-D_1 specularite exhibited the lowest amount of trace elements, except for Y. On the other hand, syn-D_2 hematite showed enrichment of nearly all trace elements relative to diagenetic hematite (Figure 41).

5.2.2.1 Mobile elements

The elements Sr, Zn, As, Rb, Ba, and Pb are mobile in the presence of aqueous solutions. Sr contents were elevated within diagenetic hematite and gangue Ca-Mg-Mn carbonate, and a positive correlation between CaO and Sr suggests that Sr is favorably incorporated into carbonate minerals. Along with a negative correlation between Fe_2O_3 and Sr, these results suggest that the Sr contents in hematite and magnetite reflect the presence of co-precipitated/remobilized carbonate intergrowths. Syn-D_2 hematite displayed enrichment of Zn, Rb, and Ba relative to older generations of hematite. The Rb and Ba contents were also elevated relative to bulk oceanic crust (Figure 58). This enrichment probably reflects the mobile behavior of these elements during metamorphism. Additionally, enrichment of As in diagenetic hematite (Figure 57) could suggest that the element remained mobile during the formation of later generations of Fe-oxides.

5.2.2.2 Immobile elements

Ti, Cr, and V are lithophile elements and readily substitute for Fe^{2+} and Fe^{3+} in magnetite and hematite. The various generations of Fe-oxides showed little variability in the Cr contents, suggesting that Cr has remained immobile during the formation of paragenetically late hematite and magnetite. In contrast, the samples exhibited relatively large variability in the amounts of Ti and V. Magnetite and syn-D_2 hematite displayed elevated contents of V in comparison to diagenetic and syn-D_1 hematite. Although usually immobile during metasomatic processes, the variability in Ti and V contents indicates a relatively mobile behavior of these. Alternatively, a variable Ti content could represent differing detrital loads in the analyzed samples, as reflected by the positive correlation between Al and Ti.

Syn-D_2 hematite exhibited a relative enrichment of Zr. A positive correlation between Al_2O_3 and Zr indicates that the Zr was derived from a detrital source. Ca-Mg-Mn gangue carbonate was enriched in Co relative to other samples. Similar Co enrichment in Mn-rich samples has been reported by Klein & Ladeira (2004) from the Urucum District NIFs. Elevated amounts of Co relative to bulk continental and oceanic crust (Figures 57 and 58, respectively) could indicate precipitation of Mn in oxides, due to their high base metal scavenging capacities (Dillard et al., 1982).

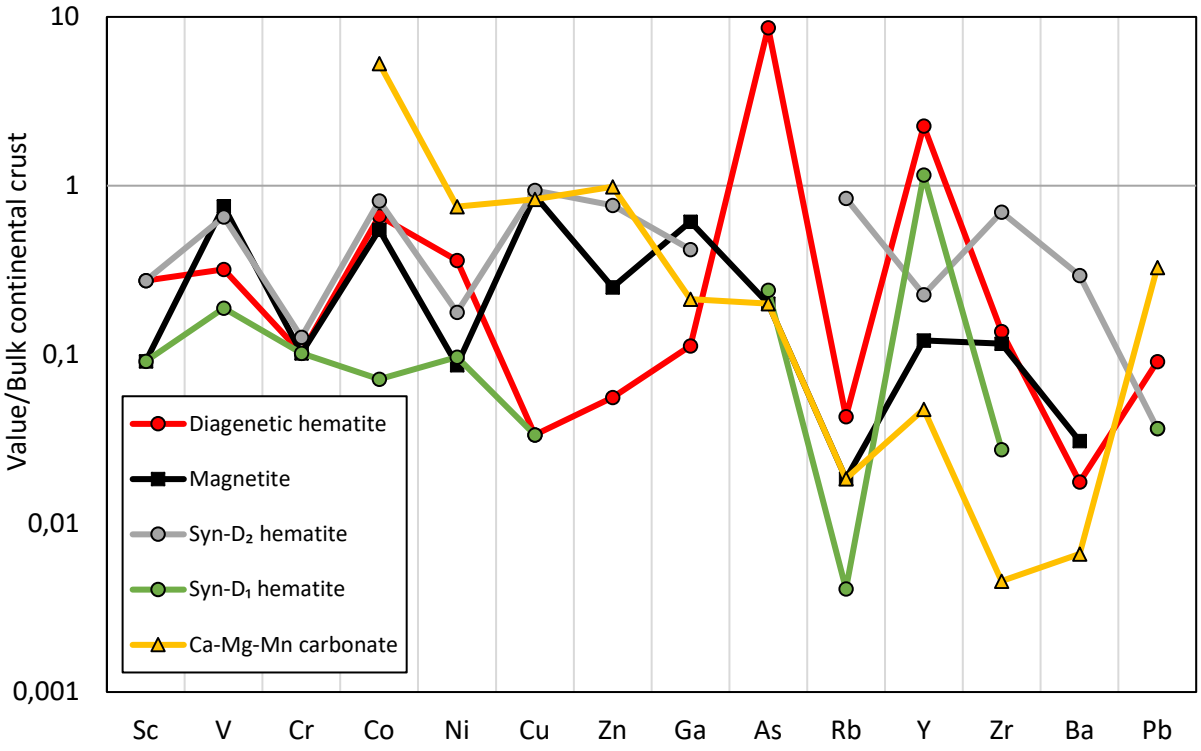

Figure 57 – Trace element composition of the various generations of Fe-oxides and gangue Ca-Mg-Mn carbonate normalized to the composition of bulk continental crust (from Rudnick & Gao, 2003). Reference values are presented in Appendix E.

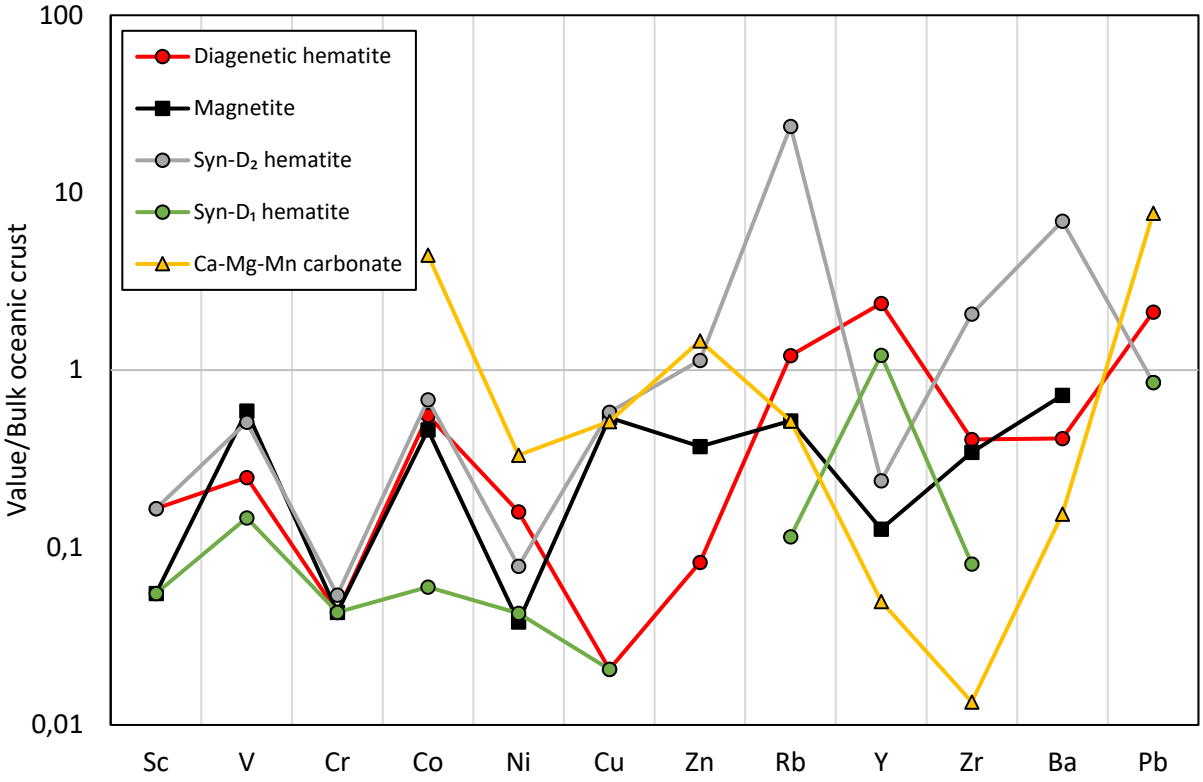

Figure 58 – Trace element composition of the various generations of Fe-oxides normalized to the composition of bulk oceanic crust (from White & Klein, 2014). Values for Ga and As were missing. Reference values are presented in Appendix E.

5.2.3 Trace elements as proxies for IF

The chemistry of Fe-oxides is "a function of the thermodynamic conditions during crystallization" (Dupuis & Beaudoin, 2011, p. 45). Dare et al. (2014) noted that the trace element composition of magnetite reflects the physicochemical properties and composition of melt or fluid, from which the magnetite crystallized. Further, the chemistry of magnetite crystallizing from high-temperature magmatic fluids and low-temperature hydrothermal fluids are typified by distinctly different geochemical features.

For instance, magnetite from hydrothermal systems is typically depleted in the immobile trace elements, such as Al, Ti, Sc, and Zr. Due to the immobile behavior of these elements during hydrothermal alteration, they are resultingly depleted in the hydrothermal fluids (Van Baalen, 1993). According to Dare et al. (2014), discrimination between magnetite from magmatic and hydrothermal settings may be done by plotting Ti versus Ni/Cr, as depicted by Figure 59. The different generations of hematite and magnetite from Dunderland Formation plot within the hydrothermal field, with the assumption that the plot is valid for hematite as well. Further, magnetite formed from high-temperature magmatic-hydrothermal fluids commonly exhibits elevated values of elements such as Ni, V, and Co (Dare et al., 2014). However, the various analyzed samples exhibited depletion of these elements relative to the composition of bulk continental crust (Figure 57).

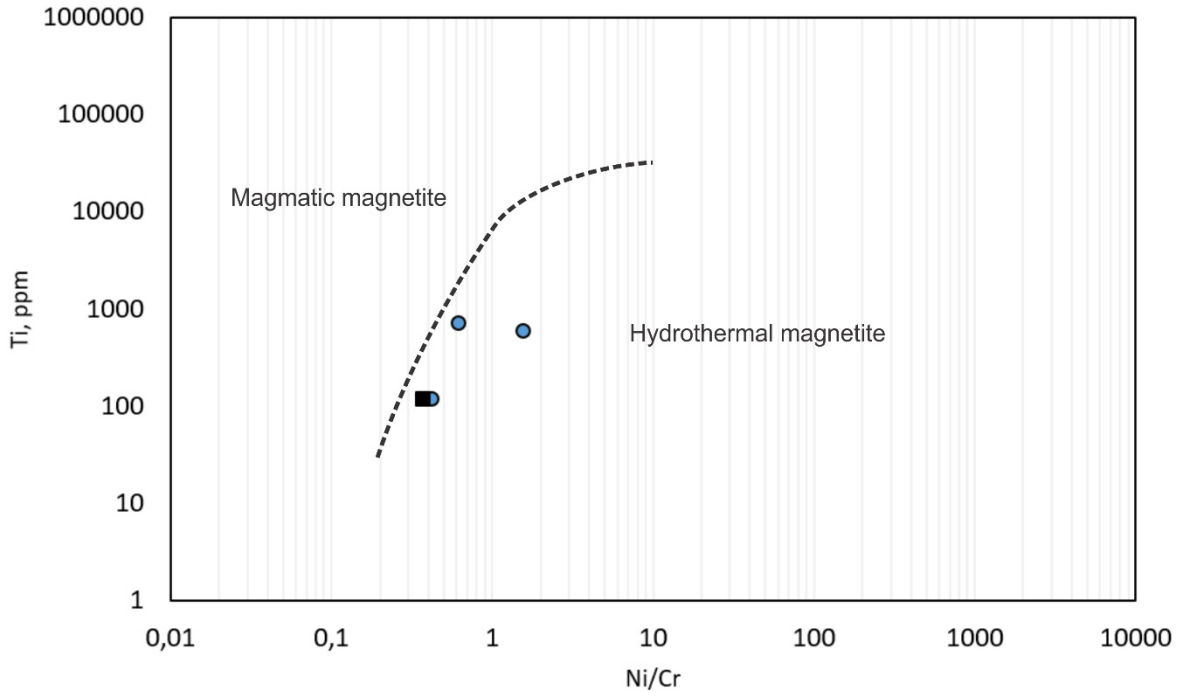

Figure 59 – Plot of Ni/Cr against Ti (ppm) for discriminating between magmatic and hydrothermal magnetite (after Dare et al., 2014). The diagram is assumed to be valid for hematite (blue circles) as well.

Based on the average Fe-oxide compositions from a diverse array of deposits, Dupuis & Beaudoin (2011) constructed a string of discriminant diagrams that may be used in the identification of various deposit types. The discriminant diagram illustrated by Figure 60 discriminates volcanogenic massive sulfide (VMS) deposits from other types of mineralizations, with the exception of Ni-Cu deposits (Dupuis & Beaudoin, 2011). Magnetite of typical VMS deposits exhibit high Si, Ca and Zn, and low Al contents, the latter due to a limited supply of detrital matter. Figure 61 depicts the function of Ti+V and Ca+Al+Mn for various types of deposits, including BIF, skarn, iron-oxide copper gold (IOCG), Fe-Ti(+V) and Kiruna type Fe-deposits.

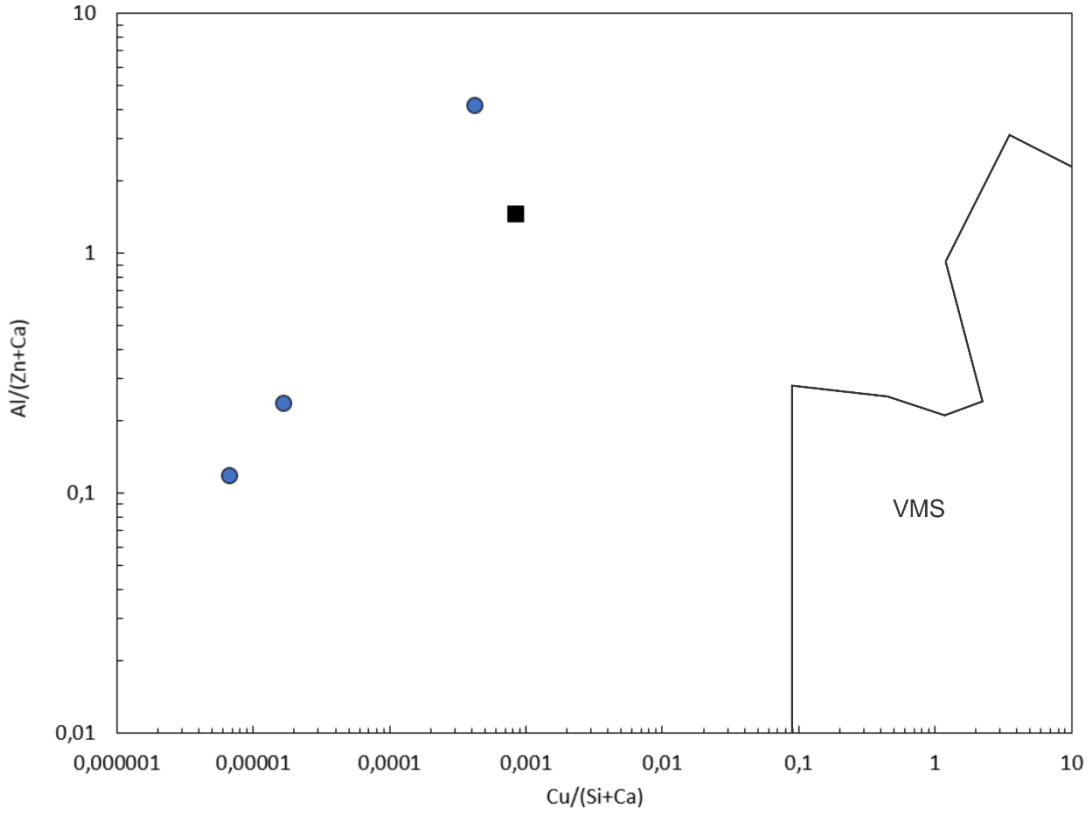

Figure 60 - Cu/(Si+Ca) vs Al/(Zn+Ca) (wt. %) discriminant diagram for identifying VMS deposits from other mineralizations (modified after Dupuis & Beaudoin, 2011). Blue circles – hematite; black square – magnetite.

The compositions of the different Fe-oxide generations plot within the typical field of skarn deposits, with the latter typified by low Ti+V and relatively high Ca+Al+Mn (Figure 61). Similarly, the trace element compositions lie within the skarn field when plotted for Ti+V against Ni/(Cr+Mn) (Figure 62). However, no features are otherwise suggestive of a skarn deposit origin for the Fe-mineralization of the Dunderland Formation. There are few indicators of significant contemporaneous magmatism within the latter. Moreover, it is possible that the observed trace element signatures do not represent those of the primary mineralizing events because the compositions of the Fe-oxides do not correspond to the apparent deposit types based on these diagrams. Instead, the hematite and magnetite compositions suspectedly reflect the influence of the post-depositional metamorphism. It may also be

questioned whether or not the diagrams illustrated by Figures 61 and 62 are applicable to Neoproterozoic iron formations.

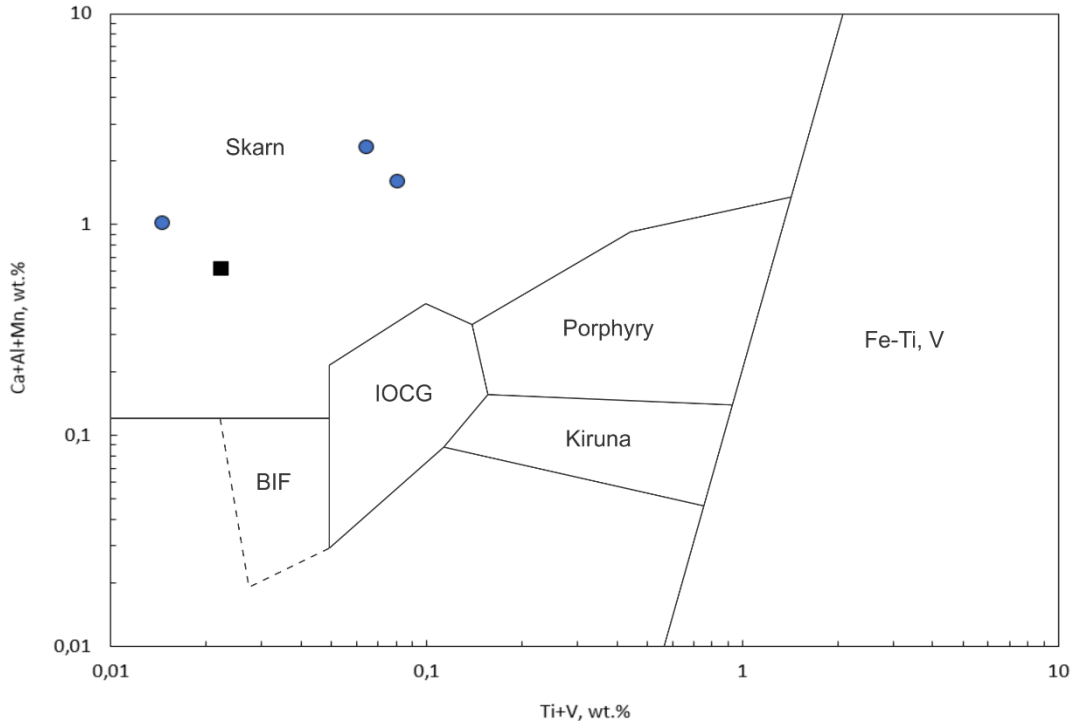

Figure 61 – Ti+V vs Ca+Al+Mn (wt.%) discriminant diagram for fingerprinting Fe-oxides from various types of deposits (modified after Dupuis & Beaudoin, 2011). Blue circles – hematite; black square – magnetite.

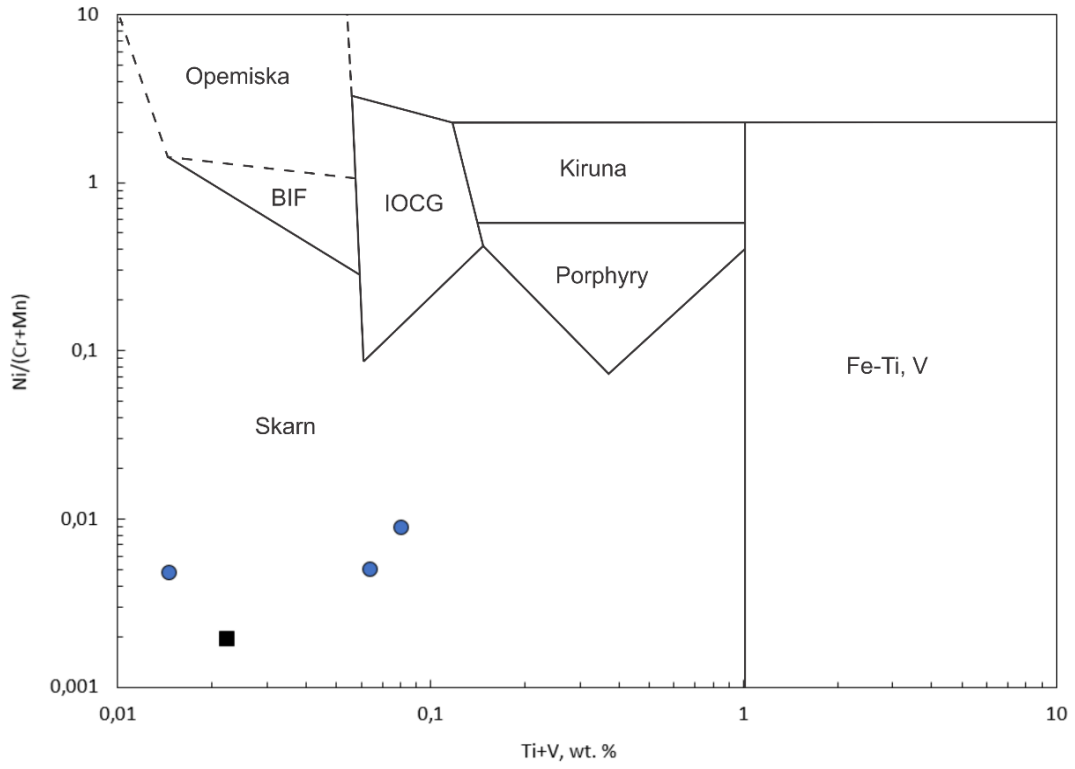

Figure 62 – Ti+V vs Ni/(Cr+Mn) (wt.%) discriminant diagram for fingerprinting Fe-oxides from various types of deposits (modified after Dupuis & Beaudoin, 2011). Blue circles – hematite; black square – magnetite.

5.2.4 Rare earth elements and Y behavior

The total REE contents (∑REEs) of the different generations of minerals displayed a positive correlation with Al_2O_3 (Figure 47). This relationship indicates that a significant proportion of the REE content was contributed through detrital aluminosilicates components, such as clay minerals. Further, this correlation could render the use of REE patterns as proxies for iron formation problematic. Alternatively, apatite may have contributed to some proportions of the REEs (Laajoki, 1975).

5.2.4.1 ∑REEs

A systematic trend with regards to the REE patterns of the different generations of Fe-oxides was evident. Early stage, diagenetic hematite exhibited the highest ∑REEs, while the younger generations of Fe-oxides showed a progressive decrease in the total REE content (Figures 45; 46; Table 7). The progressive depletion in the ∑REEs of early to late hematite suggests that extensive fluid-rock interaction could have resulted in the removal of REEs during metamorphism and recrystallization. Alternatively, recrystallization could have resulted in a refinement of the crystal lattice and removal of REEs. However, Michard & Albarède (1986) studied the geochemistry of submarine and continental hydrothermal systems and noted that REEs are highly immobile during hydrothermal alteration. Similarly, Gu et al. (2007) noted a comparable REE distribution between altered and unaltered metasediments, indicating that the primary REE patterns are preserved following primary deposition.

Taking into account the relatively immobile behavior of REEs and the observation of high ∑REEs in early stage hematite, the difference between the REE compositions of Fe-oxides and carbonates could be accounted for by the high REE scavenging capacity of Fe-oxyhydroxides from solution (Olivarez & Owen, 1989). Moreover, this could indirectly suggest that the primary mineralizing events were characterized by the precipitation of an Fe-rich colloidal suspension of Fe-oxyhydroxides.

5.2.4.2 REE patterns and Ce anomalies

The REE patterns of various generations of hematite were characterized by a depletion of LREEs relative to HREEs when normalized to PAAS (see Figures 45 and 46 for respective PAAS and chondrite-normalized REE patterns). Along with negative Ce/Ce* anomalies, LREE depletion could represent the composition of seawater (Elderfield & Greaves, 1982). The obtained REE patterns showed relatively similar slopes compared to the Qinling-type SEDEX in China (Xuexin et al., 1997). However, a lack of pronounced negative Ce anomalies sets the exhalites apart from the studied Dunderland Formation. The negative Ce anomalies of the latter could suggest that the primary mineralization was not associated with oxidation of Ce^{3+} to Ce^{4+}, i.e. the ore-forming fluids were not significantly oxidized.

Nonetheless, Toth (1980) noted that hydrothermally derived Fe-Mn-deposits may exhibit large negative Ce anomalies, depending on the proximity to the venting site and the temperature of the

hydrothermal solutions. For instance, the more proximal and higher temperature hydrothermal solutions would yield more negative Ce anomalies in ferromanganese crusts. However, the obtained Ce anomalies were only slightly negative and are perhaps more likely to record the REE composition of seawater or detrital components, the latter supported by the positive correlation between Al_2O_3 and ∑REEs. Alternatively, slightly negative Ce anomalies could reflect mixing of Fe, derived from a dilute hydrothermal source, with minute quantities of hydrogenetic Fe-Mn-oxyhydroxides (Hein et al., 1994).

5.2.4.3 Eu anomalies

When normalized to chondrite, the different samples exhibited pronounced negative Eu anomalies (Eu/ Eu* from 0.45 to 0.80, Table 9), which are consistent with reports from other Neoproterozoic iron formations (Cox et al., 2013). Such values differ from those of typical hydrothermal fluids, which commonly exhibit marked positive Eu anomalies resulting from the albitization of plagioclase feldspar during hydrothermal alteration (Klinkhammer et al., 1994). However, a lack of positive Eu anomalies relative to chondrite does not preclude the possibility of a significant hydrothermal component, due to the possibility of mixing of hydrothermal fluid with seawater during upflow or addition of detrital material (Douville et al., 1999). BIFs older than 2.5 Ga generally display positive Eu anomalies, and according to Danielson et al. (1992), the apparent disappearance of such REE patterns indicates a transition from hot to predominantly low-temperature hydrothermal fluid systems during the Proterozoic. While pronounced positive Eu anomalies would record the hydrothermal component in sediments, the lack of such values is also not inherently unexpected, due to the low plagioclase content of the analyzed samples.

In contrast, mineralized samples normalized to PAAS showed weakly positive Eu anomalies (Table 8). Typical low-temperature hydrothermal fluids commonly display weak or no Eu anomalies (Michard et al., 1993; Basta et al., 2011), hence; the weakly positive Eu anomalies could indicate the presence of low-temperature hydrothermal fluids. Alternatively, the Eu anomalies may have been inherited by the interaction between hydrothermal fluids and seawater or by "contamination" from detrital material (Douville et al., 1999). Ti, K, and Na values similar to those of typical marine shale (Figure 36) could, in any case, indicate that the amount of detrital material supplied was not insignificant.

5.2.4.4 Y/Ho values

Although not regarded as an REE, Y behaves in a similar physicochemical manner to Ho due to a similar charge, radius, and oxidation state. This behavior is supported by the observation of a strong positive correlation between Y and Ho (Figure 48). The Y/Ho value of host rock marble (60.0) exceeded that of typical chondrite (Y/Ho ~ 28) and is consistent with the superchondritic composition of seawater (Bau

& Dulski, 1999). Chondritic values are, in contrast, common for igneous rocks and shales. Elevated Y/Ho values could arise due to selective scavenging and depletion of the more surface reactive Ho (compared to Y) from seawater (Bau et al., 1996). However, the near-chondritic Y/Ho values (30.0 to 39.09) observed in the different generations of hematite, magnetite and gangue carbonate could indicate interaction with hydrothermal fluids (Bau & Dulski, 1999). The Y/Ho values progressively increased from early diagenetic hematite to late-stage syn-D_2 hematite, possibly reflecting the influence of metamorphogenic fluids. There was no correlation between Y/Ho and Al_2O_3, suggesting that Y/Ho values do not reflect variability in the aluminosilicates contents (Figure 49).

5.2.5 Implications for iron formation

Lithogeochemical data present no direct indicators of depositional mechanism. Hence, it is difficult to reveal whether the primary mineralization occurred by precipitation of Fe-oxyhydroxides or some other mechanism. Konhauser et al. (2007) suggested that the co-precipitation of SiO_2 decreases the absorption of P by oxyhydroxides, which would result in a weak negative correlation between the Si and P contents. However, no correlation between the two elements was noted from the analyzed samples. Nonetheless, there is a common notion that oxide facies IFs reflect the precipitation of Fe-oxyhydroxide precursor minerals (e.g. Konhauser et al., 2002; Webb et al., 2003; Cox et al., 2013).

In any case, the near-chondritic Y/Ho values of iron-bearing phases could support a low-temperature hydrothermal source of Fe and Si. On the other hand, negative Ce anomalies, LREE depletion and HREE enrichment record the chemical signature of seawater. The overall REE patterns of other SEDEX-type ore deposits, such as the Qinling deposit, are similar to those of the diagenetic hematite of the Dunderland Formation. It is also highly probable that trace element compositions of the various generations of hematite and magnetite have been altered, quite possibly as a result of the deformational events related to the Caledonian Orogeny. Additionally, there seems to be a crystallographic control on the REE patterns obtained, with hematite typically exhibiting LREE-depletion, a feature shared by other reported NIFs.

The contrasting character of Eu anomalies of the mineralized samples on PAAS- and chondrite-normalized plots has not been commonly reported. However, Bhatia (1985) reported a similar Eu behavior from greywackes associated with continental island arcs. Bhatia (1983, p. 613) stated that arcs "of this tectonic setting are continental fragments, detached from the mainland." According to the author, sedimentation would occur adjacent to continental island arcs in inter-arc, fore-arc or back-arc basins on continental crust. The author of this thesis thus suggests that the contrasting character of Eu anomalies could indicate that the mineralization received its original REE signature in a rifting-related environment.

5.3 Carbonate stable isotopes

Different generations of gangue carbonates from the Dunderland Formation exhibited isotopic depletion relative to the paragenetically early host rock marble (Figure 50). Although represented by a relatively limited dataset, the $\delta^{13}C$ and $\delta^{18}O$ values of S_0/S_1-parallel and F_1-fold limb carbonates, along with Post-D_2 carbonates displayed a positive correlation (r = 0.85, Figure 63).

5.3.1 Host rock marble

Isotopic compositions of barren calcitic host rock marble (sample Rana 12) overlapped with $\delta^{13}C$ and $\delta^{18}O$ values of typical marine carbonates (Figure 50). Although slightly enriched in the heavy isotopes, the isotopic compositions correspond to the least-altered marble isotopic values reported by Melezhik et al. (2015), indicating that the isotopic signal was not significantly affected by recrystallization processes. Since metamorphic processes, such as devolatilization, are known to result in depletion of the heavy isotopes (Hoefs, 1980), these cannot account for the apparent isotopic enrichment of the host rock marble. Instead, the observed $\delta^{13}C$ enrichment corresponds to the global trend of highly elevated $\delta^{13}C$ values of carbonates deposited during the Neoproterozoic. Knoll et al. (1986) attributed this to enhanced rates of organic carbon burial, initially linked with increased atmospheric oxygen. Also, according to Melezhik et al. (2015), $\delta^{13}C$ and $\delta^{18}O$ enrichment indicates low degrees of post-depositional dolomitization of host rock marble, which is further supported by a relatively low MgO/CaO value (0.021). Low-Mg calcites are stable over a wide range of conditions, implying that the isotopic signature of the host rock marble reflects the original conditions of deposition (Hassan, 2011).

5.3.2 S_0/S_1-parallel and F_1-fold limb carbonates

The isotopic signatures of different generations of carbonates associated with S_0/S_1-parallel quartz veins as well as carbonate from F_1-fold limbs were depleted in ^{13}C and ^{18}O relative to host rock marble (Figure 63). While the exact timing of their formation is uncertain, the gangue carbonates presumably represent the main mineralizing stage, displaying a relatively narrow range of $\delta^{13}C$ and $\delta^{18}O$ values from -2.8 to -0.3 ‰ and 15.2 to 19.4 ‰, respectively. The isotopic values plotted in a narrow field between magmatic and marine carbonates, which could suggest deposition under the influence of hydrothermal fluids. A positive correlation of $\delta^{13}C$ vs. $\delta^{18}O$ could be interpreted as the effects of mixing of fluids of dissimilar isotopic signatures (Zheng & Hoefs, 1992), i.e. extensive mixing of hydrothermal fluids and seawater.

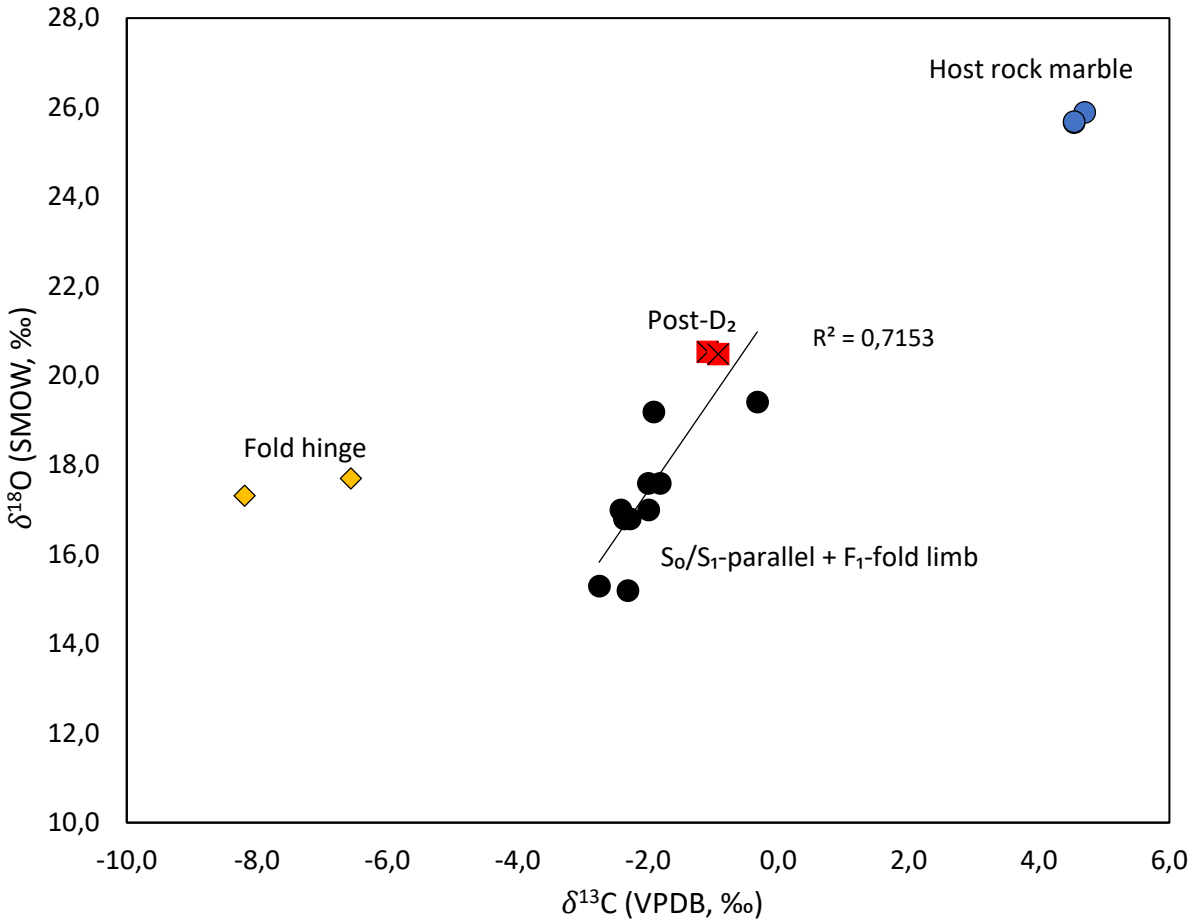

Figure 63 – Plot of $\delta^{13}C$ vs. $\delta^{18}O$ values of the different generations of carbonates, with S_0/S_1-parallel, F_1-fold limb, and post-D_2 carbonates showing a positive correlation between the $\delta^{13}C$ and $\delta^{18}O$ compositions.

The presumed syn-ore carbonates displayed $\delta^{13}C$ values slightly lower than zero, and according to Hoefs (1980), this could indicate that hydrothermal carbon was initially sourced from marine carbonates, in contrast to a deep-seated source. The difference between host rock marble and gangue carbonate isotope compositions suggests that the syn-ore carbonate is not a relic of the host carbonates. Further, these may have been affected by prograde devolatilization, resulting in a shift to depleted $\delta^{13}C$ isotopic signatures. The lack of strongly negative $\delta^{13}C$ values (≤-20‰) rules out the possibility of an organic carbon source from sedimentary rocks (Hoefs, 1980). Lowering of the $\delta^{18}O$ values relative to those of the host rock marble may also be linked to isotopic exchange with of H_2O-rich fluids liberated from silicate rocks by prograde dehydration (Pitcairn et al., 2010).

The isotopic compositions of the syn-ore carbonates resemble those of the calcites associated with the stratiform iron oxide ores of the New Jersey Highlands (Johnson & Skinner, 2003). Johnson & Skinner (2003) argued that the $\delta^{13}C$ and $\delta^{18}O$ values of -5±1‰ relative to PDB and 11 to 20‰ relative to VSMOW were consistent with a seafloor (or sub-seafloor) hydrothermal origin. These isotopic values were also consistent with the values reported from the carbonates associated with Superior-type BIFs,

such as the Transvaal basin IFs of South Africa (Kaufman et al., 1990). Kaufman et al. (1990) interpreted the isotopic depletion of the latter as the result of hydrothermal activity.

5.3.2.1 Glacial isotopic signals?

As mentioned above, the isotopic signatures of syn-ore carbonates correspond to those of other reported hydrothermal carbonates (Zheng & Hoefs, 1992). However, similar isotopic intervals of $\delta^{13}C$ values (-3.37 to -0.83‰) have been reported from the carbonates of the Rapitan iron formation (Klein & Beukes, 1993). According to Klein & Beukes (1993), this isotopic range illustrated the presence of glacially derived diamictites and dropstones. Whether or not the low $\delta^{13}C$ record the effects of glacial terminations (Spero & Lea, 2002) or hydrothermal activity is difficult to ascertain purely based on the C-isotope values themselves. Coupled with the observation of diamictites closely related to the iron deposits of the Dunderland Formation (Melezhik et al., 2015), a glaciogenic impact on the isotopic signal cannot be ruled out.

5.3.3 F_1-fold hinge and post-D_2 carbonates

Carbonate from F_1-fold hinges was isotopically light with $\delta^{13}C$ values ranging from -6.6 to -8.8‰ (Figure 63). Significant depletion of the ^{13}C isotope may be related to decarbonation during the liberation of metamorphic fluids (Valley, 1986). However, the depletion may be too large to be explained simply by closed system devolatilization processes. Instead, the isotopic values may reflect the influence of low $\delta^{13}C$ extraneous fluids, and a structurally channelized fluid flow and remobilization/precipitation of paragenetically late carbonates during the D_1/D_2 events.

The mixed isotopic composition of the post-D_2 vein quartz-carbonate vein corresponds to those of the syn-ore carbonates and could also represent remobilization of pre-existing carbonates in the area. However, the dataset is limited; thus it is difficult to conclude by anything as of yet confidently. Alternatively, low isotopic values may arise from the oxidation of organic matter by iron oxides, though this seems unlikely in the case of the late quartz-carbonate veins.

5.4 Fluid inclusion studies

The studied fluid inclusions represent post-mineralizing fluids entrapped during deformation events related to the Caledonian Orogeny. Presumably, the initial gangue minerals were too fine-grained to yield any useful FI observations; hence the FI data does not provide an index of the temperature, pressure or composition of the primary ore-bearing fluids. Nonetheless, the studied FIs present valuable insights into the post-ore P-T-X evolution of the study area.

Based on the data obtained from FI microthermometry isochores were calculated for the various FI types (Figure 64). Isochores represent lines of constant volume (or density) and mark the possible P-T

space where the respective fluids could have been entrapped. In general, the chronological relationship between different generations of FIs and host mineral has been indeterminable purely based on petrographic observations. However, FIs observed in S_0/S_1-parallel quartz veins are, in any case, of earlier origin compared to the inclusions in post-D_2 quartz. Furthermore, the different densities calculated for the various FI types represent different stages of formation for the respective inclusions.

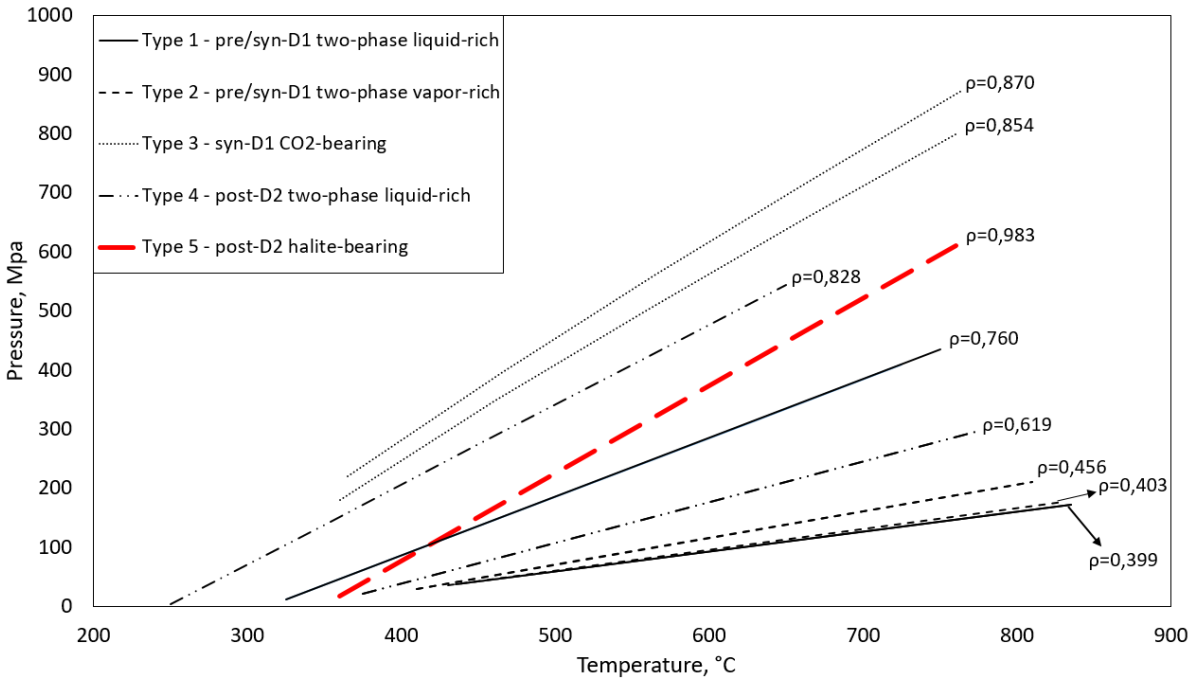

Figure 64 – Calculated isochores of the various FI types and bulk densities (ρ, in g/cm³) of end-member inclusions (based on lowest and highest homogenization temperatures of the respective FI types). Isochores represent lines of constant density and mark the P-T space where each end-member FI could have been entrapped. CO_2-bearing (Type 3) FIs represent high density fluids entrapped during the D_1-event. The genetic relationship of low density Type 1 and Type 2 (aqueous two-phase) FIs relative to host mineral is more difficult to construe, but these probably formed prior to or during early stages of the D_1-event. Isochores and densities of late-stage aqueous FIs (Type 4) are probably dubious due to the highly scattered range of homogenization temperatures these represent. The halite-bearing (Type 5) inclusions represent late-stage high density and highly saline fluids post-dating the D_1 and D_2-events.

5.4.1 Pre/syn-D_1 aqueous FIs

Type 1 and Type 2 FIs were found in S_0/S_1-parallel quartz veins and were approximated by the H_2O-NaCl-$CaCl_2$ system. As noted by Bodnar (2003b), such fluids are commonly found in various geological settings, including medium to high-grade metamorphic rocks. Type 1 FIs represent low-density aqueous fluids that, presumably, were entrapped during early phases (pre/syn-D_1) of the main Caledonian thrusting stage. Type 2 FIs were vapor-rich inclusions found in relatively close association with Type 1 inclusions. The co-existence of liquid and vapor-rich inclusions is, in some cases, indicative of fluid immiscibility. However, this would not be the case for the aqueous inclusions observed, because the two FI types showed overlapping salinities. If boiling or fluid immiscibility would have been the case, then the fluids would have been entrapped in the two-phase field, and the liquid-rich inclusions would have been characterized by higher salinities than the vapor-rich (Bodnar, 2003b), as

NaCl prefers to go into liquid-phase. The lack of any high salinity fluids in S_0/S_1-parallel quartz thus argues against boiling or fluid immiscibility. Instead, the presence of liquid and vapor-rich inclusions together may represent different fluid events relating to varying pressure conditions, as explained by the ideal gas law (2). Therefore, low-density V-rich inclusions may correspond to a drop in pressure following entrapment of early liquid-rich inclusions, or vice versa.

5.4.2 Syn-D_1 CO_2-bearing inclusions

CO_2-bearing FIs were observed in a sampled S_0/S_1-parallel quartz vein found in close association with a calcitic marble unit. They were distributed in distinctly isolated clusters, signifying a primary origin. Microthermometric measurements yielded uniform results, suggesting that Type 3 FIs could be regarded as part of the same FI assemblage (i.e. represent one particular fluid event). Their relatively high densities (from 0.854 to 0.870 g/cm^3) correspond to entrapment during a high-pressure stage and could represent fluids formed during the main thrusting stage (D_1). The liberation of CO_2-rich fluids could have come from the prograde devolatilization of local carbonates, as suggested by Sisson & Hollister (1990). Although no independent proxies for the trapping temperature exist, the high-density CO_2-rich inclusions may represent devolatilization at peak metamorphic conditions, following influx and entrapment of aqueous fluids during early stage deformation. Also, the absence of aqueous FIs in close association with CO_2-bearing inclusions demonstrates "different mechanisms for fluid transport for infiltrating vs. locally derived fluids" (Sisson & Hollister, 1990, p. 68).

5.4.3 Post-D_2 FIs

Late-stage fluids are represented by Type 4 and Type 5 FIs found in the sampled post-D_2 quartz-carbonate vein. Type 4 FIs were similar in composition to the earlier trapped aqueous two-phase inclusions, with eutectic temperatures indicating the presence of Ca^{2+} and/or other divalent ions in the system. However, these inclusions were commonly typified by elongated irregular morphologies and highly variable phase ratios, along with a widely scattered distribution of homogenization temperatures (from 140 to 420°C). These observations are suggestive of post-entrapment modification through necking and partial leakage, occurring as a result of changes in pressure-temperature conditions through time (Bodnar, 2003c). Thus, the compositional data of Type 4 inclusions is probably unreliable, and the associated isochores of these are thereby dubious.

5.4.3.1 Petrographic evidence of post-D_2 hydrothermal activity

The late-stage sulfide-bearing quartz-carbonate vein is suggested to represent a post-D_2 semi-ductile/brittle event associated with late Caledonian Orogeny (Figure 22). Various sulfide-minerals, including pyrite, chalcopyrite, and pyrrhotite, are disseminated throughout coarse-grained carbonate. In addition, pyrite and pyrrhotite were commonly observed as anhedral intergrowths with rutile. Rutile

may, in this case, represent the residual product from hydrothermal alteration, by the reaction of Ti-bearing silicates with sulfur-bearing fluids (Rabbia & Hernández, 2012).

5.4.3.2 Halite-bearing FIs

The halite-bearing (Type 5) FIs represent late, salt-saturated, high-density fluids approximated by the NaCl-H_2O system. The absence of low salinity, vapor-rich FIs in close association with halite-bearing inclusions suggests that fluid immiscibility was not responsible for the generation of highly saline fluids. Other possibilities could include an influence of magmatic fluids or dissolution of evaporites. However, there were no indications or field suggestions that pointed to either being the case. Instead, the formation may be associated with late orogenic retrograde metamorphic reactions involving rehydration of pre-existing metamorphic assemblages (Bennett & Barker, 1992). The halite-bearing FIs correspond the observations made by Bennett & Barker (1992), who noted the presence of high salinity FIs in quartz veins related to late Caledonian Orogeny. According to the authors, retrograde rehydration reactions resulted in abundant chlorite and sericite formation. The recognition of abundant chloritization of biotite from petrographic analyses hence support formation involving retrograde rehydration. The source of the fluids is unclear but may be related to surface waters migrating through pre-existing thrust zones, or devolatilization reactions and fluid migration from deeper to shallower parts of the crust (Bennett & Barker, 1992).

5.4.3.3 Decrepitated inclusions

The post-D_2 quartz also contained abundant dark cavities displaying ample offshoots. These suspectedly embody early post-D_2 FIs that have undergone decrepitation. Although these fluid-free (or low-density fluid) enclaves could not provide any data during microthermometric analyses, they hold valuable information on the tectonic evolution of the study area. Their presence suggests that the internal FI pressures were initially high, and that eventual rapid uplift and exhumation may have led to fluid leakage due to overpressure. Such fluid leakage could occur in the cases where the uplift path diverges from that of the isochore, i.e. during isothermal uplift (Kerkhof & Hein, 2001).

5.4.4 Tectonic history of the study area

As far as the author can tell no earlier studies on the metamorphic evolution of the Dunderland Formation have been carried out. Bucher-Nurminen (1988) investigated the metamorphic mineralogical assemblages of ultramafic rocks (amphibolites) in the Central Scandinavian Caledonides. The study included characterization of metaharzburgites of the Tjørnrasta and Straumbotn Nappe of the Rødingsfjellet Nappe Complex at Altermark (c. 20 km west of Mo i Rana). The mineralogical assemblage indicated metamorphic conditions of approximately 480 to 520°C and 4 to 6 kbars. Cook (1993) examined the metamorphic development of the Bleikvassli Zn-Pb-(Cu) deposit, which is located

within the Rødingsfjellet Nappe Complex as well. Peak metamorphic conditions were found to range from 540 to 570°C and 7.5 to 8.5 kbars. However, as Cook (1993) notes; such conditions are not incontrovertibly valid for nearby rock assemblages, due to the great geologic complexity of the Rødingsfjellet Nappe Complex.

Although there exist no independent proxies for the trapping temperatures of the respective FI types, the Dunderland Formation is, according to Bugge (1948), typified by amphibolite facies sequences. Figure 65 illustrates a proposed P-T path of the Dunderland Formation, based on the FI data obtained. The CO_2-bearing FIs could represent the prograde devolatilization of carbonates in the study area during the main Caledonian thrusting stage (D_1). In any case, the high densities of these (compared to other syn-D_1 FIs) correspond to a high-pressure stage following the P-T path indicated in Figure 65. By what means the P-T fields of the pre/syn-D_1 aqueous FIs (Type 1 and 2) fit in with the tectonic evolution is a little more unclear. Though, these FIs may represent fluid influx during early stages of the Caledonian Orogeny. The composition of Type 5 inclusions corresponds to the highly saline FIs reported from other late Caledonian quartz veins, and suspectedly represent retrograde rehydration of the pre-existing mineral assemblages during late-stage Caledonian exhumation/extension. Such highly saline fluids have considerable potentials of remobilization of metals by transport in chloride complexes. Their presence could explain the low trace element contents within the iron deposits; however, more evidence would be needed to back up such a claim.

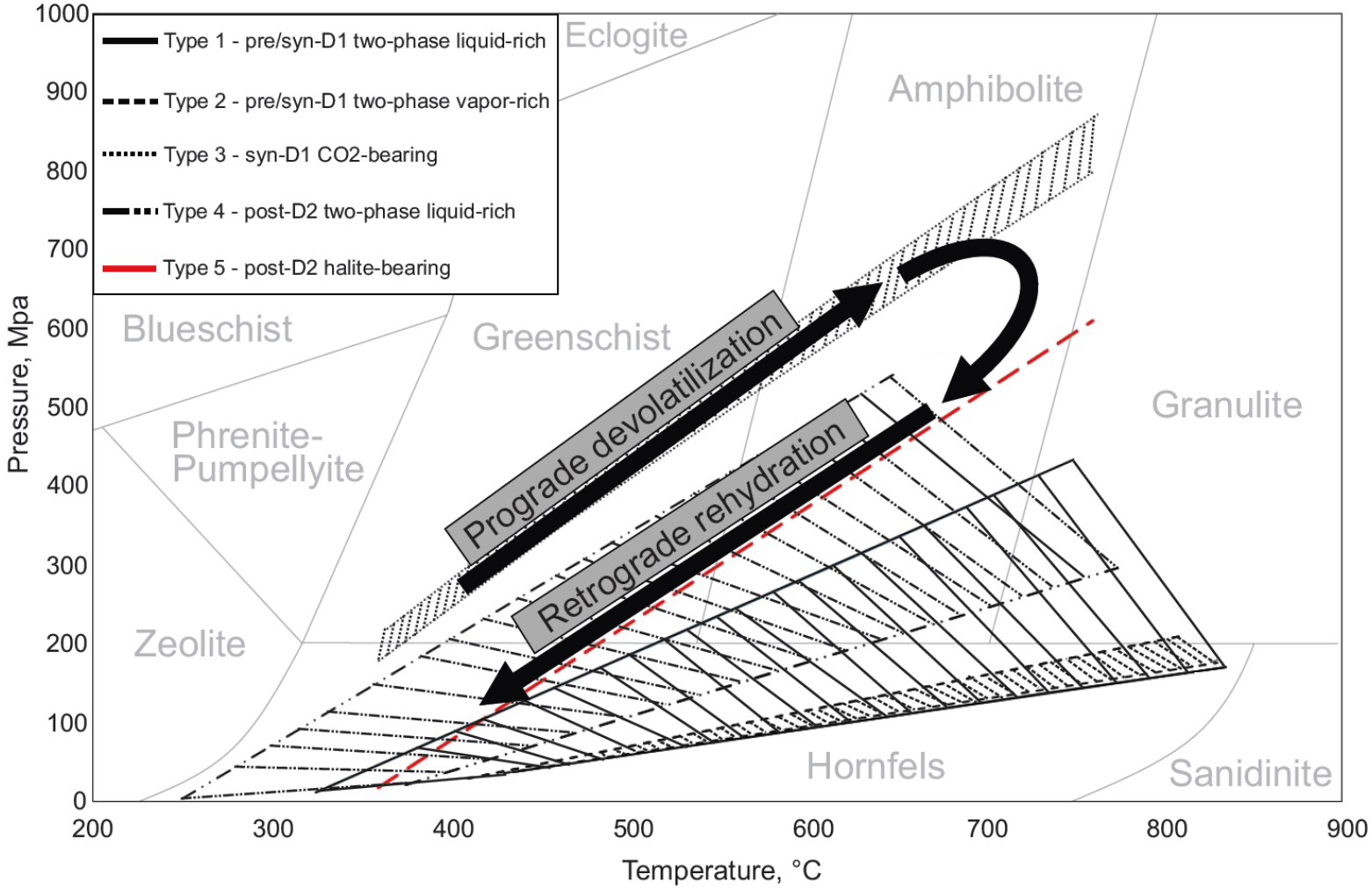

Figure 65 – Constructed isochores of studied FIs combined with a simplified representation of metamorphic facies (grey lines). The shaded areas mark the possible P-T spaces where the respective FI types may have been entrapped. Arrows illustrate a possible P-T path of the studied area during the Caledonian Orogeny. The proposed tectonic evolution involves the liberation of CO_2-rich fluids through the prograde devolatilization of carbonates during the main thrusting stage (D_1). Retrograde rehydration and generation of highly saline (Type 5 FIs) probably relates to late-stage Caledonian Orogeny through exhumation/extension. Note that the large P-T space occupied by Type 4 FIs is probably unreliable, due to suspected post-entrapment modification.

5.5 Comparison to BIF and NIF

5.5.1 Paleotectonic environment

The iron deposits of the Dunderland Formation share several characteristic traits with coeval Neoproterozoic iron formations (NIFs). On a global tectonic scale, the Archean to Paleoproterozoic banded iron formations (BIFs) are located within old platforms and shields, while the NIFs reside within Phanerozoic orogenic belts (Ilyin, 2009). In this respect, the Dunderlandsdalen deposits, located within the Caledonian orogenic belt, are similar to other NIFs.

The age interval of the host rock marble formation, from 800 to 730 Ma (Melezhik et al., 2015), marks the minimum age of the iron formation and corresponds to the rifting stage of Rodinia, which culminated with the formation of the Iapetus ocean. Similarly, paleogeographic reconstruction and distribution of other NIFs indicate deposition in intracontinental basins or rift-basins related to the breakup of Rodinia (Jefferson et al., 1979). Melezhik et al. (2015) suggest that the sedimentological and geochemical characteristics of the sediment-hosted IFs within the Uppermost Allochthon indicate deposition in an open marine environment. However, there have been no prior reports of NIFs forming in such environments. Moreover, the contrasting behavior of Eu anomalies of mineralized samples, when normalized to chondrite and PAAS, suggests that the Dunderland IFs formed in a rift-related environment (see section 5.2.4).

As noted by Melezhik et al. (2015), the studied deposits are found in close association with diamictites and dropstones, thus resembling the exclusively Neoproterozoic Rapitan-type IFs believed to have formed under glacially influenced conditions (Klein & Beukes, 1993). Other NIFs, such as the Jucurutu Formation in Brazil (Nascimento et al., 2007), display no glacial features and are instead associated with volcanic rocks (Algoma type). Although commonly neglected, the NIFs that are associated with neither volcanic rocks nor glacial deposits and occur within carbonate-shale passive margin sequences are labeled as the Lake Superior-type, such as the Shilu Fe-ore deposit of South China (Xu et al., 2013). According to Cox et al. (2013), NIFs are generally believed to have formed in close association with mafic volcanics. However, there are only minor amounts of amphibolite lenses suspected to be of intrusive origin within the Dunderland Formation (Bugge, 1948).

5.5.2 Age constraints

No NIFs have currently been directly dated, and definite age determinations are thus scarce. However, general age constraints of NIFs are in good agreement with the general notion that most NIFs were formed during the Cryogenian glaciation (Cox et al., 2013). For instance, the formation of the Chuos-Damara IF in Namibia has been constrained to the age interval between 746±2 Ma (Hoffmann & Prave, 1996) and 635.5±1,2 Ma (Hoffmann et al., 2004). Significantly older NIFs, such as the IFs of Wadi Karim

and Un Anab in Egypt (Basta et al., 2011) are, however, not believed to have formed under glacially influenced conditions. The age constraints of host rock marble (800 to 730 Ma) and the association with diamictites suggests that the Dunderlandsdalen iron deposits formed during the Cryogenian, in accordance with Cox et al. (2013).

5.5.3 Texture and mineralogy

From a textural point of view, the profound deformation and recrystallization make it difficult to assess whether or not a granular texture typified the original mineralization. The Dunderland IFs do, nevertheless, exhibit a micro- to mesoscale banding represented by granular layers in low strain zones and discontinuous specularite bands in more highly strained domains. The textural heterogeneity observed stands in contrast to other NIFs, which are generally characterized by poorly defined to non-existent banding (Cox et al., 2013). On the other hand, BIFs older than approximately 2,0 Ga generally display micro-banded textures, while the younger granular IFs (GIFs) of the Superior type typically display cm-scale banding.

The mineralogical assemblages of IFs usually reflect post-depositional processes, such as diagenesis and metamorphism. The Archean to Paleoproterozoic IFs are generally, but not entirely, characterized by assemblages predominantly composed of chert and magnetite, with lesser amounts of hematite (Konhauser et al., 2017). Magnetite commonly occurs in low-grade mineral assemblages containing iron-silicates, e.g. greenalite, minnesotaite, and stilpnomelane, but also siderite, ankerite, and pyrite. With increasing metamorphic grades, Fe-bearing amphibole, pyroxene, and olivine may also occur. The composition of NIFs thus differs from earlier IFs by being predominantly composed of hematite and chert, along with minor quantities of carbonate (Cox et al., 2013). Similarly, in the studied specimens of the Dunderland Formation, hematite is always the principal Fe-oxide, though carbonate is present in significant amounts within the calcareous schists. Magnetite is a minor component relative to hematite, similar to other metamorphosed NIFs.

The extensive Fe-deposits of the Dunderland Formation also locally occur in close association with a discrete zone of Mn-enrichment. Such occurrences have frequently been reported from multiple IFs throughout the world, such as the c. 900 Ma Fe-mineralization of the Urucum District, Brazil (Klein & Ladeira, 2004). The IFs of the Damara Supergroup (720-590 Ma) are also interbedded with substantial Mn-deposits (Roy, 1988). Contrarily, a similar association has not been reported from the perhaps most characteristic of the late Proterozoic Fe-mineralizations, the Rapitan Group IFs (Baldwin et al., 2012). The Fe-Mn-association is further discussed in section 5.7.1.2.

5.5.4 REE patterns

Although generally assigned to the Rapitan type, numerous NIFs lack the feature of a glacial association and may instead be denoted as Algoma or Superior type IFs. In any case, REE distribution patterns represent valuable tools for solving the origin of BIFs. Neoproterozoic IFs typically display LREE-depleted patterns when normalized to PAAS, an exception being the LREE-enriched Jacadigo Group Fe-mineralization (Graf et al., 1994).

Reported values of Eu and Ce anomalies, however, vary between different types of NIFs. The absent Ce and Eu anomalies of the Rapitan IF have, for instance, been judged to reflect a dilute hydrothermal signal (Klein & Beukes, 1993). In contrast, Baldwin et al. (2012) argued that such anomalies depict a glacial source of Fe. The Algoma type NIFs, such as the volcanically associated Jucurutu Formation IFs in Brazil, typically display positive Eu anomalies and negative Ce anomalies (mean values of 1,13 and 0,9, respectively) related to considerable hydrothermal input (Gaucher et al., 2015). Lake Superior-type NIFs commonly exhibit positive Eu and negative Ce anomalies, the latter feature ascribed to alternating oxygenated and anoxic conditions (Gaucher et al., 2015).

The LREE-depletion and HREE-enrichment obtained from the studied samples of the Dunderlandsdalen deposit correspond to the geochemical characteristics of other reported BIFs. Similar REE patterns have also been reported from numerous Archean to Paleoproterozoic BIFs. The shale-normalized Eu anomalies (from 1,08 to 1,22) obtained from the mineralized samples strongly contrast those of earlier BIFs but are, on the other hand, somewhat similar compared to the values of the Rapitan type IFs of the Urucum District, Brazil (Klein & Ladeira, 2004). Moreover, Ce/Ce* values, whether normalized to chondrite or PAAS, are always slightly negative and also resemble those reported by Klein & Ladeira (2004). Based on such REE patterns, the authors suggested that Fe, Mn, and Si were sourced from fluids of hydrothermal origin, but that – in comparison with the Archean and Paleoproterozoic occurrence – the hydrothermal signal was significantly weaker. Several authors, including Sverjensky (1984), proposed that the weakly positive Eu anomalies could also reflect low-temperature hydrothermal fluids.

5.6 Comparison to SEDEX deposits

The Dunderlandsdalen IFs have originally been characterized as SEDEX deposits (Geological Survey of Norway, 2015), which form through rift-related hydrothermal activity distant from volcanic centers (see section 3.1.2.1). Except for the presence of minor amphibolite lenses and gneisses of presumed intrusive and extrusive origin (Grenne et al., 1999), the lack of a volcanic association is a feature shared by the studied deposits. The latter is also characterized by the stratiform nature and the presence of carbonate host rocks of typical SEDEX deposits.

However, notable differences may be seen between the mineral associations of the Dunderland IFs and classic SEDEX deposits, with the former characterized by low grades of Pb and Zn. The mineralization is also generally lacking in sulfides, although locally, up to 1m thick pyrrhotite bands are present at the margins of the iron ore bodies (Bugge, 1948). Accessory amounts of pyrite have also been observed as disseminations throughout quartz veins, with pyrite occasionally accompanied by minuscule chalcopyrite grains. In addition, no regularities regarding the amount of sulfur and iron have been observed within the various samples. The trace element composition of typical SEDEX deposits is also characterized by substantial amounts of heavy metals, such as Hg, Cd, As, Sb. In contrast, lithogeochemical analyses reflected the low trace element contents of the Dunderland Formation mineralizations.

Several authors have considered the possibility of a genetic link between SEDEX deposits and other types of sediment-hosted deposits (Emsbo et al., 2016, and references therein). Moreover, Fe-Mn-P mineralizations and metalliferous black shales are often reported from the same stratigraphic horizons in which SEDEX deposits occur. In the Uppermost Allochthon, two principal types of stratabound or stratiform deposits occur as (1) metasedimentary and metavolcanic-hosted polymetallic sulfides and (2) Fe-oxide ores, respectively (Grenne et al., 1999). The former include the Zn-Pb-Cu sulfide ores of Mofjell and Bleikvassli of the Rødingsfjellet Nappe Complex, which display mineralogical and geochemical features consistent with SEDEX deposits (Skauli et al., 1992; Grenne et al., 1999). According to Grenne et al. (1999) these deposits, along with the extensive metasedimentary IFs, may be interpreted as Laurentian passive margin sequences. It would be tempting to propose a genetic link between the two types of deposits. Pb-isotope data indicate a maximum age of 1.0 Ga for the Bleikvassli deposits (Skauli et al., 1992); however, there is still considerable uncertainty linked with the age interpretation of these sulfide ores. Moreover, Melezhik et al. (2015) note that the features of the IFs do not fit well with a Laurentian origin and instead proposed deposition on the passive margin of an unknown microcontinent.

5.6.1.1 Vent-distal hydrothermal products?

Previous workers, such as Lydon (1996), have noted that hematite-magnetite mineralizations and Mn-enrichment may be the expressions of vent-distal hydrothermal SEDEX deposit products. These mineralogical assemblages are commonly accompanied by chert, barite, pyrite, Ca-Mg carbonates, and minor amounts of sphalerite, with Ba/Zn values typically increasing away from the hydrothermal vent complexes (Figure 6).

In the Dunderland Formation, the Mn-enriched zones are characterized by a prevalence of Mn-bearing carbonates and garnets. A similar mineralogical assemblage has been reported from the Cambrian

Harlech Fe-Mn-deposits of North Wales, in which kutnohorite and spessartine are important constituents of the gangue mineralogy (Bennett, 1987). Bennett (1987) also reported the presence of authigenic barite and noted that these deposits in several ways mirror the distal products from submarine hydrothermal exhalative activity. The Dunderland IFs share several features with the vent-distal products of idealized SEDEX deposits. However, Ba contents of all analyzed specimens were low, and no barite ($BaSO_4$) has been recorded. Thus, a genetic link between the studied Dunderland Formation IF and distal facies SEDEX deposits cannot confidently be inferred. Furthermore, from chemostratigraphic studies, Melezhik et al. (2018) deduced a Cryogenian deposition, contemporaneous to most IFs worldwide. The author of the present thesis thus suggests that the studied samples represent the products of geological processes on a global scale, rather than being expressions of the distal SEDEX environment.

5.6.1.2 Fault architecture

Yang et al. (2006) carried out numerical modeling to test hydrothermally sourced stratiform Zn-Pb-Ag deposition against basin morphology in the Northern Mount Isa Basin. They noted that deposition of stratiform Zn-Pb favored fluid convection by moderately crustal-penetrating faults (10-15 km). Interestingly, shallow faults (<5 km) could be linked with the formation of exhalative Fe and Mn mineralizations by the submarine venting of low-temperature hydrothermal fluids. Although being mere speculation at this point, this model could possibly explain the low Pb and Zn grades of the Dunderland IFs.

5.7 Controlling mechanisms of Fe-oxide formation

$\delta^{18}O$ and $\delta^{56}Fe$ isotope analyses of different generations of hematite, magnetite, and quartz were initially carried out to determine the sources of elements, along with the mode of transport and depositional mechanism. However, due to the finely intergrown nature of the hematite, magnetite and gangue quartz, clear isotopic signals could not be obtained. Hence, these analyses could not resolve any of the matters mentioned above. The same issue was in effect during XRD analyses of mineralized samples, yielding unsuccessful attempts at obtaining the crystallinity of two different generations of hematite.

However, based on the preceding results and discussion, the author suggests that the primary Fe-mineralization occurred under the influence of hydrothermal fluids. This is supported by REE patterns of mineralized samples as well as by the stable isotope composition of various generations of carbonate minerals. A hydrothermal, rather than hydrogenous source, is also backed by near-chondritic Y/Ho. Slightly positive Eu anomalies may suggest precipitation from low-temperature hydrothermal fluids; however, the use of REE patterns as tracers for Fe-mineralization is complicated

by the positive correlation between the REEs and aluminosilicate components. A significant supply of Fe from a continental weathering source may also not be ruled out, in accordance with Cox et al. (2013).

There were no direct indicators of the ligands involved in Fe-transport prior to deposition from the obtained geochemical data. However, the transport of Fe is predominantly governed by a low redox potential (i.e. predominance of Fe^{2+} over Fe^{3+}), low pH conditions and the ubiquitous presence of NaCl in hydrothermal solutions. Fe transport was thus probably linked with the formation of Fe-chloride complexes (Seward et al., 2014): $Fe^{2+} + 2Cl^- \rightarrow FeCl_2$ (aq).

In the studied samples of the Dunderland Formation, hematite is always the principal Fe-bearing mineral, along with lesser amounts of magnetite. Notably, the samples represent limited proportions of the ore body, and none of the samples typify ore in which magnetite is the main Fe-bearing constituent. Nonetheless, Bugge (1948) noted that the P-rich lower ore horizon is predominantly made up of magnetite in mineralogical assemblages corresponding to higher metamorphic grades. A similar link was noted in the studied samples, as magnetite often occurred in close spatial association with hornblende and epidote. Furthermore, no petrographic observations suggested the presence of early-stage magnetite, indicating that the oxidation of Fe^{2+} did not occur by biological pathways (Halverson et al., 2011). Oxidation of Fe^{2+} may instead have been coupled to an abiotic pathway by the reaction (Cox et al., 2013): $2Fe^{2+} + 0.5O_2 + 5H_2O \rightarrow 2Fe(OH)_3 + 4H^+$. Although the reaction is abiotic in a strict sense, it was probably dependent on the production of O_2 from cyanobacteria, and hence tightly linked to biological activity. The latter may be supported by the observation of organic-rich material within the studied samples (Figure 23).

Bugge (1948) suggested that the iron could originally have been deposited in the ferrous state as siderite ($FeCO_3$) and that subsequent oxidation resulted in the formation of hematite by the reaction: $2FeCO_3 + 0.5O_2 \rightarrow Fe_2O_3 + 2CO_2$. The slightly negative shale-normalized Ce anomalies could speak for an initial deposition of Fe-carbonates under reducing conditions (Lovley & Phillips, 1986). However, there are otherwise no indicators of early stage Fe-carbonates in the study area. Also, the deposition of Fe-carbonates, i.e. siderite ($FeCO_3$), is restricted to non-sulfidic and anoxic environments and does not form in equilibrium with seawater (Figure 56B).

It is instead suggested that the primary mineralizing events were characterized by fast precipitation of nano-particle Fe-oxyhydroxides, along with a chert-like SiO_2 precipitate from low-temperature hydrothermal fluids (<250° C, Sverjensky, 1984). The Fe-oxyhydroxides were further altered to hematite by thermal dehydroxylation (Cornell & Schwertmann, 2003), represented by the reaction: $2FeOOH \rightarrow Fe_2O_3 + 2H_2O$. Amorphous silica was also altered to quartz by subsequent diagenesis and

metamorphism. Further replacement of hematite by magnetite took place via reductive dissolution and reprecipitation, represented by the reaction: $2Fe_2O_3 + H_2 \rightleftharpoons 2Fe_3O_4 + H_2O$. Alternatively, replacement of hematite by magnetite may occur by non-redox reactions through the addition of Fe^{2+} from aqueous solutions. However, such transformations are accompanied by significant volume changes and are, thus, limited to unconsolidated sediments (Mücke & Cabral, 2005).

Based on the preceding paragraphs, the primary mineralizing events (as illustrated in Figure 66) and post-depositional processes responsible for the Fe-mineralization of the Dunderland Formation may be summarized as follows: (1) transport of Fe by hydrothermal solutions in chloride complexes; (2) submarine hydrothermal venting and subsequent abiotic oxidation of Fe^{2+}, resulting in precipitation and deposition of colloidal Fe-oxyhydroxides; (3) diagenesis and dehydroxylation of Fe-oxyhydroxides to hematite; (4) Fe-enrichment during the D_1- and D_2-events by formation of well-crystallized specularite and tabular hematite; and (5) replacement of hematite by magnetite through reductive dissolution and reprecipitation during the D_1/D_2-events.

5.7.1.1 Implications of glacial deposits, host rock marbles, and volcanics

The close spatial association between the Fe-mineralization and diamictites in the Dunderland Formation could, according to Melezhik et al. (2015), suggest that the initial accumulation of Fe^{2+} was directly related to glacial activity. In addition to the prerequisite of anoxic conditions, ice-capped oceans could also have accounted for an increase in Fe solubility by increasing seawater salinity (Bühn & Stanistreet, 1997). Whether or not the diamictites represent actual glacial deposits is beyond the scope of this thesis to determine. On the other hand, the presence of laterally extensive and thick marble units characterized by low Al_2O_3 and SiO_2 contents indicates a deposition on a passive margin carbonate platform, in accordance with Melezhik et al. (2015). A deposition in a continental margin back-arc extensional basin is another possibility, as supported by the contrasting Eu behavior of mineralized samples (see section 5.2.4.3).

The magnetite-rich ores of the lower horizon (see section 2.1.4.1), meanwhile, are interstratified with significant quantities of suspected volcanic amphibolites (Grenne et al., 1999). Thus, it may not be sensible to rule out the possibility of a different mode of genesis for the magnetite-rich horizon, which involves volcanic processes.

5.7.1.2 Genetic relationship between IF and Mn-enrichment

The Fe-mineralizations of the upper horizon also occur in close association with a local Mn-enriched zone (Figure 17A). Similar associations have been reported from other Precambrian IFs by several authors (e.g. Visser, 1954; Aro & Schissel, 1992; Klein & Ladeira, 2004). In contrast, no significant Phanerozoic IFs exhibit similar features (Roy, 1988). Nonetheless, the genetic link between Fe and Mn

in NIFs is still under debate. Kimberley (1989) suggested that separation of the elements could take place by differential hydrothermal dissolution rather than preferential precipitation during exhalative activity. This would further imply that Mn and Fe were precipitated from different fluids. Other workers, such as Bühn & Stanistreet (1997), noted that the metal separation predominantly occurs during precipitation and that Mn and Fe precipitate from the same source. Such a relationship is reflected by the typical gradational character between Fe- and Mn-mineralizations, suggesting a direct link between the precipitation of the metals (Bühn & Stanistreet, 1997). In the studied deposits of the Dunderland Formation, this feature is apparently evident in the local Mn-rich zone. The possibility that subsequent shearing may have affected the contact between Fe- and Mn-mineralization cannot be ruled out. However, the general notion of a contemporaneous deposition, along with the deposits closely related character requires any genetic relation to be treated together.

In the Dunderland Formation, manganese is present as Mn^{2+} in Ca-Mg-Mn carbonates and rhodonite. Furthermore, Mn controls the distribution of spessartine garnets, which make up an essential component of the metamorphic assemblage. Notably, a similar mineralogical assemblage has been reported from the aforementioned Harlech Mn deposit, Wales (Bennett, 1987), in which kutnohorite ($CaMn(CO_3)_2$) occurs in close association with spessartine (±hematite, magnetite). Bennett (1987) suggested that Mn initially precipitated as oxyhydroxides from submarine exhalative hydrothermal fluids, as indicated by REE patterns characterized by positive Ce and Eu anomalies. Further diagenesis played an important part by remobilization and formation of manganous carbonates. REE patterns of a Ca-Mn carbonate from the Dunderland Formation show relatively similar shapes like the ones reported from the Harlech deposits, though the negative Ce anomalies of the former would be suggestive of a much more dilute hydrothermal signal. Furthermore, Kuleshov (2017) noted that there is no documentation of Mn-rich carbonates precipitating directly from seawater. Rather, their formation is presumably related to post-depositional processes.

From a tectonic point of view, the Neoproterozoic Mn-IF association may hold important implications. For instance, Bühn & Stanistreet (1997) noted that the genesis of late Proterozoic Mn-IFs was associated with exhalative activity and deposition on the continental shelf setting during the early break-up of Rodinia. The interpreted depositional ages of the host rock marbles correspond to the dislocation of Rodinia – further supporting the notion that the Mn-IF association could serve as an indicator of an initial supercontinental break-up.

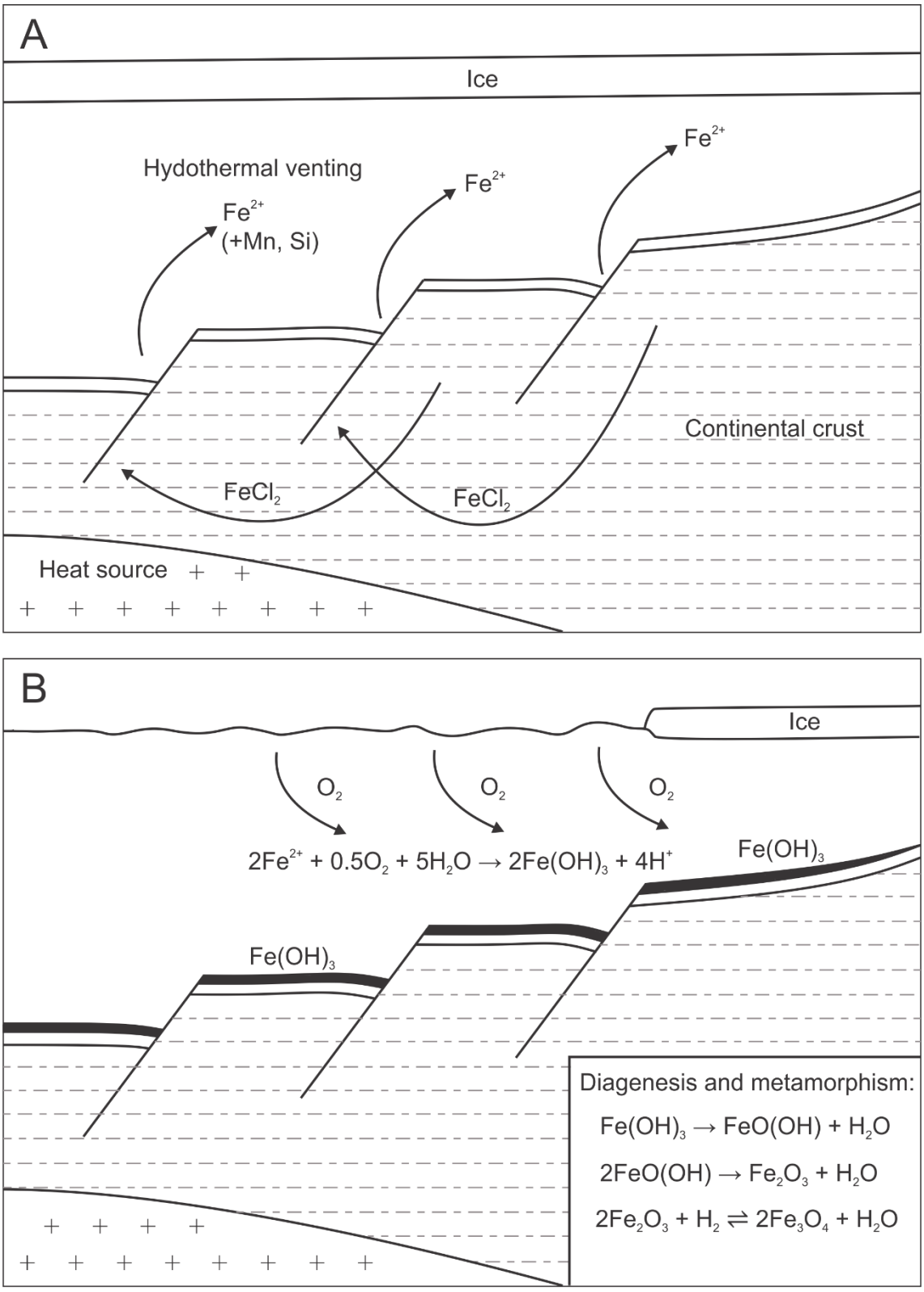

Figure 66 – Highly schematic diagrams illustrating the suggested genetic model for the Dunderland Formation iron deposits. The geochemical characteristics of the mineralization and the spatial relationship between the IFs and diamictites suggest that the primary mineralizing events took place in a glaciated, hydrothermally influenced rift-setting. (A) Although not a pre-requisite for Fe-mineralization, an ice-capped basin could have accounted for the initial buildup of dissolved Fe. (B) The subsequent interglacial period(s) could have brought oxygenation of the oceanic bottom waters, resulting in precipitation of precursor Fe-oxyhydroxides, which was ensued by the formation of various generations of Fe-oxides during diagenesis and metamorphic events.

6 Conclusions and recommendations for future research

6.1 Conclusions

This study has been part of a project aimed at resolving structural, geochemical and environmental aspects related to the complexly deformed Dunderlandsdalen iron deposit. The principal objective of this thesis was to acquire a better understanding of the controlling mechanisms of hematite and magnetite formation. The main focus was placed on investigating the geochemical characteristics of the mineralization and host rocks within a structural framework. Secondly, fluid inclusion studies provided insights into the post-ore P-T-X evolution of the studied area. In summary from the preceding chapters, the following conclusions are drawn from this study:

- Strain variations in the ore bodies and host rocks have given rise to various generations of Fe-oxides. In domains of low strain, where relict banding is preserved, diagenetic hematite occurs in fine-grained layers along the S_0/S_1-foliation. Mineralized samples that represent domains of high strain evidence syn-deformational enrichment linked with the main thrusting stage of the Caledonian Orogeny (D_1). They are characterized by the presence of euhedral specular hematite in discontinuous bands delineating a well-defined S_1-foliation. Magnetite consistently truncates syn-D_1 hematite and formed during metamorphic events, while paragenetically late hematite occurs as tabular grains oriented along the S_2-axial surfaces.

- Lithogeochemical analyses of mineralized samples revealed major element contents characterized by relative enrichment of Si, Fe, Mn, and P, and shale-like Ti, Mg, Na, and K contents. A binary major element pattern could invoke a dual-source model involving the mixing of hydrothermally sourced Si, Fe, and Mn with considerable amounts of detrital material (cf. Cox et al., 2013; Cox et al., 2015).

- Variability in the trace element contents between different generations of Fe-oxides reflects the influence of metamorphogenic fluids. Whereas syn-D_1 hematite exhibited the lowest trace element contents, syn-D_2 hematite showed a general enrichment of trace elements relative to other generations of Fe-oxides.

- Fluid-rock interaction during deformation could also possibly be inferred from a progressive decrease in the total REE contents ($\sum$REEs) from diagenetic hematite to late-stage hematite and magnetite. Although a correlation between $\sum$REEs and the Al_2O_3 contents complicated the use of REE patterns as proxies for iron formation, LREE-depleted and negative Ce anomalies reflect the composition of seawater. By contrast, slightly positive shale-normalized Eu anomalies of hematite samples, along with near-chondritic Y/Ho values, support a low

temperature (<250° C) hydrothermal source of Fe heavily diluted by seawater. Moreover, a contrasting character of PAAS- and chondrite-normalized Eu anomalies indicates that the mineralization received its original REE signature in a rift-related environment.

- $\delta^{13}C$ and $\delta^{18}O$ values of barren calcitic host rock marble overlap with the isotope composition of typical marine carbonates. Intermediate isotope signatures of carbonates in S_0/S_1-parallel veins and F_1-fold limbs suggest deposition under the influence of hydrothermal fluids. Depleted $\delta^{13}C$ values of F_1-fold hinge carbonate indicates that fold-hinges served as channelized pathways of fluid circulation and carbonate remobilization/re-precipitation during Caledonian deformation (D_1/D_2).

- Findings from fluid inclusion studies of quartz witness a complex post-mineralization tectonic evolution of the studied deposits. The composition of syn-deformational fluids indicates their metamorphic origin. Pre/syn-D_1 low salinity, aqueous inclusions may typify an early stage fluid influx during the Caledonian Orogeny. Dense CO_2-bearing fluid inclusions in recrystallized S_0/S_1-parallel quartz veins presumably embody the prograde devolatilization of carbonates during the main Caledonian thrusting stage (D_1). Highly saline fluids, as witnessed by halite-bearing inclusions in post-D_2 quartz-carbonate veins, represent retrograde rehydration of the pre-existing mineral assemblage during the late-stage Caledonian extension/exhumation. An abundance of decrepitated inclusions could reflect rapid uplift/exhumation of the same post-D_2 vein.

Geochemical data indicate that the initial Dunderlandsdalen Fe-mineralization involved mixing of hydrothermally sourced Fe-(Si-Mn) with a considerable detrital component in a rift-related environment. Although there is a scarcity of evidence suggestive of contemporaneous volcanic activity, the possibility that volcanic processes were active cannot be ruled out. A glacially influenced passive margin or back-arc basin environment (cf. Melezhik et al., 2015), in partnership with rifting and hydrothermal activity, may have accounted for the initial buildup of dissolved Fe during early stages of breakup of Rodinia. Oxidation and precipitation of iron during favorable redox conditions were followed by diagenesis and formation of early-stage hematite. The subsequent deformation processes, recrystallization, and remobilization of metals during the Caledonian Orogeny affected the textures and mineral chemistry of the ores. As witnessed by the macro- to microscopic features of mineralized samples, these processes resulted in the formation of various generations of Fe-oxides in structurally favorable sites, with a predominance of hematite over magnetite.

6.2 Recommendations for future research

The studied samples, which form the basis of the genetic model presented within this thesis, represent a relatively small proportion of the Fe-ore bodies of the Dunderland Formation. In view of the two distinct Fe-horizons present, it could be of interest to investigate the geochemical characteristics of the magnetite- and P-rich lower horizon, and to compare these with results from the studied hematite-rich horizon. Furthermore, inconsiderable previous work has been carried out on the metamorphic conditions of the Dunderland, a subject which would surely be of petrological interest in an area witnessing such complex deformation.

The post-D_2 quartz-carbonate vein contained relatively abundant sulfide minerals. Further, sulfides from hydrothermal systems may contain significant amounts of structurally bound Au (Vikentyev, 2015). While beyond the scope of this thesis, it could be worthwhile to investigate the trace element contents of these sulfides (i.e. by SEM-WDS), as such results could hold interesting implications for the future exploration of Au. Additionally, the lithogeochemical data in this study, however valuable, is represented by a relatively limited data set. In situ trace element analysis of the various generations of ore and gangue minerals could thus be beneficial in revealing any local/regional variations in the geochemistry of the studied deposits.

Certain limitations related to methodological problems were also evident. XRD analyses were performed on two different generations of hematite, in order to determine differences in their microstructural parameters, i.e. crystallinity. However, these parameters could not be resolved due to the finely intergrown nature of the hematite and gangue minerals. In order to filter out signals from sample impurities it is thus suggested that, for the determination of crystallinity of various ore minerals, spectroscopic methods are applied instead (as according to Sawaby et al., 1989).

Variations in $\delta^{18}O$ and $\delta^{56}Fe$ of different generations of hematite and magnetite could also not be resolved. This issue resulted from the isotopic effect of ubiquitous quartz intergrowths, which rendered the Fe-oxide isotopic signals of no use. Instead, an alternative method for obtaining the Fe and O isotopic signatures could be in situ secondary ion mass spectrometry (SIMS, Kita et al., 2011). Further, the obtained stable isotopes of the quartz-Fe-oxide mineral pairs could serve as valuable geothermometers for the primary mineralizing events or post-depositional processes, i.e. in combination with the constructed isochores of the fluid inclusion study.

References

Archer, D. G. (1992). Thermodynamic Properties of the NaCl+H2O System. II. Thermodynamic Properties of NaCl(aq), NaCl . 2H2(cr), and Phase Equilibria. *Journal of Physical and Chemical Reference Data, 21*(4), 793-829. doi:10.1063/1.555915

Aro, P., & Schissel, D. (1992). The major early Proterozoic sedimentary iron and manganese deposits and their tectonic setting. *Economic Geology, 87*(5), 1367-1374. doi:10.2113/gsecongeo.87.5.1367

Baldwin, G. J., Turner, E. C., & Kamber, B. S. (2012). A new depositional model for glaciogenic Neoproterozoic iron formation: insights from the chemostratigraphy and basin configuration of the Rapitan iron formation1Northwest Territories Geoscience Office Contribution 0052. *Canadian Journal of Earth Sciences, 49*(2), 455-476. doi:10.1139/e11-066

Baskaran, S. (2010). *Structure and Regulation of Yeast Glycogen Synthase*. (Doctor of Philosophy), Indiana University, Indiana. Retrieved from http://hdl.handle.net/1805/2278

Basta, F. F., Maurice, A. E., Fontboté, L., & Favarger, P. Y. (2011). Petrology and geochemistry of the banded iron formation (BIF) of Wadi Karim and Um Anab, Eastern Desert, Egypt: Implications for the origin of Neoproterozoic BIF. *Precambrian Research, 187*(3), 277-292. doi:10.1016/j.precamres.2011.03.011

Bau, M., & Dulski, P. (1999). Comparing yttrium and rare earths in hydrothermal fluids from the Mid-Atlantic Ridge: implications for Y and REE behaviour during near-vent mixing and for the Y/Ho ratio of Proterozoic seawater. *Chemical Geology, 155*(1), 77-90. doi:10.1016/S0009-2541(98)00142-9

Bau, M., Koschinsky, A., Dulski, P., & Hein, J. R. (1996). Comparison of the partitioning behaviours of yttrium, rare earth elements, and titanium between hydrogenetic marine ferromanganese crusts and seawater. *Geochimica et Cosmochimica Acta, 60*(10), 1709-1725. doi:10.1016/0016-7037(96)00063-4

Bennett, D. G., & Barker, A. J. (1992). High salinity fluids: The result of retrograde metamorphism in thrust zones. *Geochimica et Cosmochimica Acta, 56*(1), 81-95. doi:10.1016/0016-7037(92)90118-3

Bennett, M. A. (1987). Genesis and diagenesis of the Cambrian manganese deposits, Harlech, North Wales. *Geological Journal, 22*(S1), 7-18. doi:10.1002/gj.3350220503

Berg, A. E. (1996). *Dunderland Iron Ore Company, Limited i Rana: forspillet og første driftsperiode*. In *Mo i Rana-prosjektet* (pp. 117). Retrieved from https://urn.nb.no/URN:NBN:no-nb_digibok_2011010603005

Beukes, N., & Gutzmer, J. (2008). Origin and Paleoenvironmental Significance of Major Iron Formations at the Archean-Paleoproterozoic Boundary. *Society of Economic Geologists. SEG Reviews, 15*, 5-47. doi:10.5382/Rev.15.01

Bhatia, M. R. (1983). Plate Tectonics and Geochemical Composition of Sandstones. *The Journal of Geology, 91*(6), 611-627. doi:10.1086/628815

Bhatia, M. R. (1985). Rare earth element geochemistry of Australian Paleozoic graywackes and mudrocks: Provenance and tectonic control. *Sedimentary Geology, 45*(1), 97-113. doi:10.1016/0037-0738(85)90025-9

Bodnar, R. J. (1993). Revised equation and table for determining the freezing point depression of H2O-Nacl solutions. *Geochimica et Cosmochimica Acta, 57*(3), 683-684. doi:10.1016/0016-7037(93)90378-A

Bodnar, R. J. (2003a). Chapter 1. Introduction to fluid inclusions. In I. Samson, A. Anderson, & D. Marshall (Eds.), *Fluid inclusions: Analysis and Interpretation* (Vol. Short Course 32, pp. 1-8): Mineral. Assoc. Canada.

Bodnar, R. J. (2003b). Chapter 4. Introduction to Aqueous-Electrolyte Fluid Inclusions. In I. Samson, A. Anderson, & D. Marshall (Eds.), *Fluid inclusions: Analysis and Interpretation* (Vol. Short Course 32, pp. 81-99): Mineral. Assoc. Canada.

Bodnar, R. J. (2003c). Chapter 8. Reequilibration of fluid inclusions. In I. Samson, A. Anderson, & D. Marshall (Eds.), *Fluid inclusions: Analysis and Interpretation* (Vol. Short Course 32, pp. 230): Mineral. Assoc. Canada.

Bodnar, R. J., Lecumberri-Sanchez, P., Moncada, D., & Steele-MacInnis, M. (2014). Fluid Inclusions in Hydrothermal Ore Deposits. In: Holland H.D. and Turekian K.K. (eds.). *Treatise on Geochemistry, Second Edition, 13*, 119-142.

Bodnar, R. J., & Vityk, M. O. (1994). *Interpretation of Microthermometric Data for H2O-NaCl Fluid Inclusions*. Paper presented at the Short course on fluid inclusions in minerals, Pontagnino, Italy.

Bottinga, Y. (1968). Carbon isotope fractionation between graphite, diamond and carbon dioxide. *Earth and Planetary Science Letters, 5*, 301-307. doi:10.1016/S0012-821X(68)80056-1

Breitkopf, J. H. (1988). Iron formations related to mafic volcanism and ensialic rifting in the southern margin zone of the Damara Orogen, Namibia. *Precambrian Research, 38*(2), 111-130. doi:10.1016/0301-9268(88)90087-3

Brookins, D. G. (1988). *Eh-pH Diagrams for Geochemistry* (1st ed.). Berlin Heidelberg: Springer-Verlag

Browning, N. D., Chisholm, M. F., & Pennycook, S. J. (1993). Atomic-resolution chemical analysis using a scanning transmission electron microscope. *Nature, 366*(6451), 143-146. doi:10.1038/366143a0

Bucher-Nurminen, K. (1988). Metamorphism of ultramafic rocks in the Central Scandinavian Caledonides. *Special Publications, 3*, 86-95.

Bugge, J. A. W. (1948). Rana Gruber. Geologisk beskrivelse av jernmalmfeltene i Dunderlandsdalen. *Norges Geologiske Undersøkelse, 171*, 1-149.

Bunaciu, A. A., Udristioiu, E. G., & Aboul-Enein, H. Y. (2015). X-Ray Diffraction: Instrumentation and Applications. *Critical Reviews in Analytical Chemistry, 45*(4), 289-299. doi:10.1080/10408347.2014.949616

Bühn, B., & Stanistreet, I. G. (1997). Insight into the enigma of Neoproterozoic manganese and iron formations from the perspective of supercontinental break-up and glaciation. *Geological Society, London, Special Publications, 119*(1), 81. doi:10.1144/GSL.SP.1997.119.01.05

Canfield, D. E., Poulton, S. W., Knoll, A. H., Narbonne, G. M., Ross, G., Goldberg, T., & Strauss, H. (2008). Ferruginous Conditions Dominated Later Neoproterozoic Deep-Water Chemistry. *Science, 321*(5891), 949. doi:10.1126/science.1154499

Carne, R. C., & Cathro, R. J. (1982). Sedimentary exhalative (SEDEX) zinc-lead-silver deposits, Northern Canadian Cordillera. *75*, 66-78.

Chou, I. M. (1987). Phase relations in the system NaCl-KCl-H2O. III: Solubilities of halite in vapor-saturated liquids above 445°C and redetermination of phase equilibrium properties in the system NaCl-H2O to 1000°C and 1500 bars. *Geochimica et Cosmochimica Acta, 51*(7), 1965-1975. doi:10.1016/0016-7037(87)90185-2

Clayton, R. N., O'Neil, J. R., & Mayeda, T. K. (1972). Oxygen isotope exchange between quartz and water. *Journal of Geophysical Research, 77*(17), 3057-3067. doi:10.1029/JB077i017p03057

Collett, B. M. (1970). Scanning Electron Microscopy: A Review and Report of Research in Wood Science. *Wood and Fiber Science, 2*, 113-133.

Cook, N. J. (1993). Conditions of metamorphism estimated from alteration lithologies and ore at the Bleikvassli Zn-Pb-(Cu) deposit, Nordland, Norway. *Norsk Geologisk Tidsskrift, 73*(4), 226-233.

Coplen, T. B. (1995). Reporting of stable hydrogen, carbon, and oxygen isotopic abundances. *Geothermics, 24*(5), 707-712. doi:10.1016/0375-6505(95)00024-0

Coplen, T. B., Qi, H., Révész, K., Casciotti, K., & Hannon, J. E. (2006). Determination of the δ15N of Nitrate in Solids; RSIL Lab Code 2894. Stable isotope ratio methods, sec. C. In K. Révész & T. B. Coplen (Eds.), *Methods of the Reston Stable Isotope Laboratory (slightly revised from version 1.0 released in 2007)* (Vol. Book 10, pp. 35). Virginia: U.S. Geological Survey.

Cornell, R. M., & Schwertmann, U. (2003). *The Iron Oxides: Structure, Properties, Reactions, Occurences and Uses* (2nd ed.). Weinheim: Wiley.

Cox, G., Halverson, G., Poirier, A., Le Heron, D., Strauss, J., & Stevenson, R. (2015). A model for Cryogenian iron formation. *433*, 280-292. doi:10.1016/j.epsl.2015.11.003

Cox, G. M., Halverson, G. P., Minarik, W. G., Le Heron, D. P., Macdonald, F. A., Bellefroid, E. J., & Strauss, J. V. (2013). Neoproterozoic iron formation: An evaluation of its temporal, environmental and tectonic significance. *Chemical Geology, 362*(C), 232-249. doi:10.1016/j.chemgeo.2013.08.002

Craig, H. (1953). The geochemistry of the stable carbon isotopes. *Geochimica et Cosmochimica Acta, 3*(2), 53-92.

Craig, H. (1961). Isotopic Variations in Meteoric Waters. *Science, 133*(3465), 1702-1703. doi:10.1126/science.133.3465.1702

Danielson, A., Möller, P., & Dulski, P. (1992). The europium anomalies in banded iron formations and the thermal history of the oceanic crust. *Chemical Geology, 97*(1), 89-100. doi:10.1016/0009-2541(92)90137-T

Dare, S. A. S., Barnes, S.-J., Beaudoin, G., Méric, J., Boutroy, E., & Potvin-Doucet, C. (2014). Trace elements in magnetite as petrogenetic indicators. *Minera Deposita, 49*(7), 785-796. doi:doi:10.1007/s00126-014-0529-0

Darling, R. S. (1991). An extended equation to calculate NaCl contents from final clathrate melting temperatures in H2O-CO2-NaCl fluid inclusions: Implications for P-T isochore location. *Geochimica et Cosmochimica Acta, 55*(12), 3869-3871. doi:10.1016/0016-7037(91)90079-K

Das Sharma, S., Patil, D. J., & Gopalan, K. (2002). Temperature dependence of oxygen isotope fractionation of CO2 from magnesite-phosphoric acid reaction. *Geochimica et Cosmochimica Acta, 66*(1), 589-593.

Dillard, J. G., Crowther, D. L., & Murray, J. W. (1982). The oxidation states of cobalt and selected metals in Pacific ferromanganese nodules. *Geochimica et Cosmochimica Acta, 46*(5), 755-759. doi:10.1016/0016-7037(82)90027-8

Douville, E., Bienvenu, P., Charlou, J. L., Donval, J. P., Fouquet, Y., Appriou, P., & Gamo, T. (1999). Yttrium and rare earth elements in fluids from various deep-sea hydrothermal systems. *Geochimica et Cosmochimica Acta, 63*(5), 627-643. doi:10.1016/S0016-7037(99)00024-1

Dupuis, C., & Beaudoin, G. (2011). Discriminant diagrams for iron oxide trace element fingerprinting of mineral deposit types. *International Journal for Geology, Mineralogy and Geochemistry of Mineral Deposits, 46*(4), 319-335. doi:10.1007/s00126-011-0334-y

Egerton, R. F. (2005). *Physical Principles of Electron Microscopy*. New York, USA: Springer.

Elderfield, H., & Greaves, M. J. (1982). The rare earth elements in seawater. *Nature, 296*, 214-219. doi:10.1038/296214a0

Ellefmo, S. L. (2005). *A probabilistic approach to the value chain of underground iron ore mining.* (Doctor of engineering), Norwegian University of Science and Technology, Trondheim.

Emsbo, P., Seal, R. R., Breit, G. N., Diehl, S. F., & Shah, A. K. (2016). Sedimentary exhalative (sedex) zinc-lead-silver deposit model. *Scientific Investigations Report*, 72. doi:10.3133/sir20105070N

Eyles, N., & Januszczak, N. (2004). 'Zipper-rift': a tectonic model for Neoproterozoic glaciations during the breakup of Rodinia after 750 Ma. *Earth-Science Reviews, 65*(1), 1-73. doi:10.1016/S0012-8252(03)00080-1

Fall, A., Tattitch, B., & Bodnar, R. J. (2011). Combined microthermometric and Raman spectroscopic technique to determine the salinity of H2O–CO2–NaCl fluid inclusions based on clathrate melting. *Geochimica et Cosmochimica Acta, 75*, 951-964. doi:10.1016/j.gca.2010.11.021

Flanagan, F. J., & Gottfried, D. (1980). *USGS rock standards; III, Manganese-nodule reference samples USGS-Nod-A-1 and USGS-Nod-P-1* (1155). Retrieved from http://pubs.er.usgs.gov/publication/pp1155

Fossen, H., & Rykkelid, E. (1992). Postcollisional extension of the Caledonide orogen in Scandinavia: Structural expressions and tectonic significance. *Geology, 20*(8), 737-740. doi:10.1130/0091-7613(1992)020<0737:PEOTCO>2.3.CO;2

Frelinger, S. N., Ledvina, M. D., Kyle, J. R., & Zhao, D. (2015). Scanning electron microscopy cathodoluminescence of quartz: Principles, techniques and applications in ore geology. *Ore Geology Reviews, 65*, 840-852. doi:10.1016/j.oregeorev.2014.10.008

Gaucher, C., Sial, A. N., & Frei, R. (2015). Chapter 17 - Chemostratigraphy of Neoproterozoic Banded Iron Formation (BIF): Types, Age and Origin. In M. Ramkumar (Ed.), Chemostratigraphy (pp. 433-449). Oxford: Elsevier. Retrieved from http://www.sciencedirect.com/science/article/pii/B9780124199682000170. doi:10.1016/B978-0-12-419968-2.00017-0

Gee, D. G., Fossen, H., Henriksen, N., & Higgins, A. K. (2008). From the early Paleozoic platforms of Baltica and Laurentia to the Caledonide Orogen of Scandinavia and Greenland. *Episodes, 31*(1), 44-51.

Gee, D. G., & Sturt, B. A. (1985). *The Caledonide orogen : Scandinavia and related areas* (Vol. 1). Chichester: Wiley.

Geological Survey of Norway. (2015). Ørtfjell Deposit no. 40 in Rana (1833) municipality (printout).

Gjelle, S., Søvegjarto, U., & Tveiten, B. (Cartographer). (1991). Berggrunnskart DUNDERLANDSDALEN 2027 I. Norges Geologiske Undersøkelse

Goldstein, R. (2001). Fluid inclusions in sedimentary and diagenetic systems. *Lithos, 55*, 159-193. doi:doi.org/10.1016/S0024-4937(00)00044-X

Goldstein, R. (2003). Petrographic analysis of fluid inclusions. In I. Samson, A. Anderson, & D. Marshall, eds. Fluid Inclusions: Analysis and Interpretation. In *Mineral. Assoc. Canada,* (Vol. Short Course 32, 1-8, pp. 9-53).

Goldstein, R., & Reynolds, J. T. (1994). *Systematics of Fluid Inclusions in Diagenetic Minerals. SEPM Short Course* (Vol. 31).

Graf, J. L., O'Connor, E. A., & van Leeuwen, P. (1994). Rare earth element evidence of origin and depositional environment of Late Proterozoic ironstone beds and manganese-oxide deposits, SW Brazil and SE Bolivia. *Journal of South American Earth Sciences, 7*(2), 115-133. doi:10.1016/0895-9811(94)90003-5

Grenne, T., Ihlen, P., & Vokes, M. F. (1999). Scandinavian Caledonide Metallogeny in a plate tectonic perspective. *Mineralium Deposita, 34*(5), 422-471. doi:DOI: 10.1007/s001260050215

Gross, G. A. (1980). A classification of iron formations based on depositional environments. *The Canadian mineralogist, 18*(2), 215-222.

Gu, X., Schulz, O., Vavtar, F., Liu, J., Zheng, M., & Fu, S. (2007). Rare earth element geochemistry of the Woxi W–Sb–Au deposit, Hunan Province, South China. *Ore Geology Reviews, 31*(1), 319-336. doi:10.1016/j.oregeorev.2005.01.003

Gurvich, E. G. (2006). *Metalliferous sediments of the world ocean: fundamental theory of deep-sea hydrothermal sedimentation*: Springer.

Halverson, G. P., Poitrasson, F., Hoffman, P. F., Nédélec, A., Montel, J. M., & Kirby, J. (2011). Fe isotope and trace element geochemistry of the Neoproterozoic syn-glacial Rapitan iron formation. *Earth and Planetary Science Letters, 309*(1), 100-112. doi:10.1016/j.epsl.2011.06.021

Hassan, K. M. (2011). Note on the stable isotope values of vein calcite in the El-Seboah peralkaline granite (SW Egypt). *Mineralogia, 42*, 113-120. doi:10.2478/v10002-011-0010-y

Hein, J. R., Hsueh-Wen, Y., Gunn, S. H., Gibbs, A. E., & Chung-ho, W. (1994). Composition and origin of hydrothermal ironstones from central Pacific seamounts. *Geochimica et Cosmochimica Acta, 58*(1), 179-189. doi:10.1016/0016-7037(94)90455-3

Hoefs, J. (1980). *Stable Isotope Geochemistry* (2nd ed. Vol. 9). New York: Springer-Verlag.

Hoffman, P., Kaufman, A., Halverson, G., & Schrag, D. P. (1998). A Neoproterozoic Snowball Earth. *281*, 1342-1346.

Hoffmann, K. H., Condon, D. J., Crowley, J. L., & Bowring, S. A. (2004). U-Pb zircon date from the Neoproterozoic Ghaub Formation, Namibia: Constraints on Marinoan glaciation. *Geology, 32*(9), 817-820. doi:10.1130/G20519.1 %J Geology

Hoffmann, K. H., & Prave, A. R. (1996). A preliminary note on a revised subdivision and regional correlation of the Otavi Group based on glaciogenic diamictites and associated cap dolostones. *Communications of the Geological Survey of Namibia, 11*, 81-86.

Holland, H. D. (2006). The oxygenation of the atmosphere and oceans. *Philosophical Transactions of the Royal Society B, 361*, 903-915. doi:10.1098/rstb.2006.1838

Ilyin, A. V. (2009). Neoproterozoic banded iron formations. *Lithology and Mineral Resources, 44*(1), 78-86. doi:10.1134/S0024490209010064

James, H. L. (1954). Sedimentary facies of iron-formation. *Economic Geology and the Bulletin of the Society of Economic Geologists, 49*(3), 235-293. doi:10.2113/gsecongeo.49.3.235

Jefferson, C. W., Delaney, G. D., Yeo, G. M., & Young, G. M. (1979). Middle and late Proterozoic evolution of the northern Canadian Cordillera and Shield. *Geology, 7*(3), 125-128. doi:10.1130/0091-7613(1979)7<125:MALPEO>2.0.CO;2 %J Geology

Johnson, C. A., & Skinner, B. J. (2003). Geochemistry of the Furnace Magnetite Bed, Franklin, New Jersey, and the Relationship between Stratiform Iron Oxide Ores and Stratiform Zinc Oxide-Silicate Ores in the New Jersey Highlands. *Economic Geology, 98*(4), 837-854. doi:10.2113/gsecongeo.98.4.837 %J Economic Geology

Joy, D. C. (1991). The theory and practice of high-resolution scanning electron microscopy. *Ultramicroscopy, 37*(1), 216-233. doi:10.1016/0304-3991(91)90020-7

Joy, H. W., & Libby, W. F. (1960). Size Effects Among Isotopic Molecules. *Journal of Chemical Physics, 33*(1276). doi:10.1063/1.1731392

Kaufman, A. J., Klein, C., Hayes, J. M., & Beukes, N. J. (1990). Carbonate petrography, kerogen distribution, and carbon and oxygen isotope variations in an early Proterozoic transition from limestone to iron-formation deposition, Transvaal Supergroup, South Africa. *Economic Geology, 85*(4), 663-690. doi:10.2113/gsecongeo.85.4.663 %J Economic Geology

Kendall, C., & Caldwell, E. A. (1998). Fundamentals of Isotope Geochemistry. In C. Kendall & J. J. McDonnel (Eds.), *Isotope Tracers in Catchment Hydrology* (pp. 51-86). Amsterdam: Elsevier Science B. V.

Kerkhof, A., & Hein, U. (2001). Fluid inclusion petrography. *Lithos, 55*, 27-47. doi:10.1016/S0024-4937(00)00037-2

Kimberley, M. M. (1989). Exhalative Origins of Iron Formations. *Ore Geology Reviews, 5*(1-2), 13-145. doi:10.1016/0169-1368(89)90003-6

Kind, T., & Fiehn, O. (2010). Advances in structure elucidation of small molecules using mass spectrometry. *Bioanalytical Reviews, 2*(1), 23-60. doi:10.1007/s12566-010-0015-9

Kita, N. T., Huberty, J. M., Kozdon, R., Beard, B. L., & Valley, J. W. (2011). High-precision SIMS oxygen, sulfur and iron stable isotope analyses of geological materials: accuracy, surface topography and crystal orientation. *SIMS Proceedings Papers, 43*(1-2), 427-431. doi:10.1002/sia.3424

Klein, C. (2005). Some Precambrian banded iron-formations (BIFs) from around the world: Their age, geologic setting, mineralogy, metamorphism, geochemistry, and origins. *American Mineralogist, 90*(10), 1473-1499. doi:10.2138/am.2005.1871

Klein, C., & Beukes, N. J. (1993). Sedimentology and geochemistry of the glaciogenic late Proterozoic Rapitan Iron-Formation in Canada. *Economic Geology and the Bulletin of the Society of Economic Geologists, 88*(3), 542-565. doi:10.2113/gsecongeo.88.3.542

Klein, C., & Ladeira, E. A. (2004). GEOCHEMISTRY AND MINERALOGY OF NEOPROTEROZOIC BANDED IRON-FORMATIONS AND SOME SELECTED, SILICEOUS MANGANESE FORMATIONS FROM THE URUCUM DISTRICT, MATO GROSSO DO SUL, BRAZIL. *Economic Geology, 99*(6), 1233-1244. doi:10.2113/gsecongeo.99.6.1233

Klinkhammer, G. P., Elderfield, H., Edmond, J. M., & Mitra, A. (1994). Geochemical implications of rare earth element patterns in hydrothermal fluids from mid-ocean ridges. *Geochimica et Cosmochimica Acta, 58*(23), 5105-5113. doi:10.1016/0016-7037(94)90297-6

Knoll, A. H., Hayes, J. M., Kaufman, A. J., Swett, K., & Lambert, I. B. (1986). Secular variation in carbon isotope ratios from Upper Proterozoic successions of Svalbard and East Greenland. *Nature, 321*(6073), 832-838. doi:10.1038/321832a0

Konhauser, K. O., Lalonde, S. V., Amskold, L., & Holland, H. D. (2007). Was There Really an Archean Phosphate Crisis? *Science, 315*(5816), 1234. doi:10.1126/science.1136328

Konhauser, K. O., Planavsky, N. J., Hardisty, D. S., Robbins, L. J., Warchola, T. J., Haugaard, R., . . . Johnson, C. M. (2017). Iron formations: A global record of Neoarchaean to Palaeoproterozoic environmental history. *Earth-Science Reviews, 172*, 140-177. doi:10.1016/j.earscirev.2017.06.012

Konhauser, K. O., Raiswell, R., Hamade, T., Morris, R. C., Ferris, F. G., Southam, G., & Canfield, D. E. (2002). Could bacteria have formed the Precambrian banded iron formations? *Geology, 30*(12), 1079-1082. doi:10.1130/0091-7613(2002)030<1079:CBHFTP>2.0.CO;2

Kuleshov, V. (2017). Chapter 3 - Genetic Types, Classifications, and Models of Manganese-Ore Formation. In J. B. Maynard (Ed.), *Isotope Geochemistry* (pp. 63-352): Elsevier.

Kump, L. R., & Seyfried, W. E. (2005). Hydrothermal Fe fluxes during the Precambrian: Effect of low oceanic sulfate concentrations and low hydrostatic pressure on the composition of black smokers. *Earth and Planetary Science Letters, 235*(3), 654-662. doi:10.1016/j.epsl.2005.04.040

Laajoki, K. (1975). Rare-earth elements in Precambrian iron formations in Vayrylankyla, South Puolanka area, Finland. *Bulletin of the Geological Society of Finland*(47), 93-107.

Lambrecht, G., & Diamond, L. W. (2014). Morphological ripening of fluid inclusions and coupled zone-refining in quartz crystals revealed by cathodoluminescence imaging: Implications for CL-petrography, fluid inclusion analysis and trace-element geothermometry. *Geochimica et Cosmochimica Acta, 141*, 381-406. doi:10.1016/j.gca.2014.06.036

Lepp, H. (1968). The distribution of manganese in the Animikian iron formations of Minnesota. *Economic Geology, 63*(1), 61-75. doi:10.2113/gsecongeo.63.1.61 %J Economic Geology

Lindberg, M. L. (2014). *Strukturer og mineralomvandling i Stensundtjern malmfelt, og dannelse av jernmalmene i Dunderlandsformasjonen.* (Master), The Arctic University of Norway, Tromsø.

Lovley, D. R., & Phillips, E. J. P. (1986). Organic Matter Mineralization with Reduction of Ferric Iron in Anaearobic Sediments. *Appl Environ Microbiol, 51*(4), 683-689.

Lydon, J. W. (1996). Exhalative Base Metal Sulphides. In O. R. Eckstrand, W. D. Sinclair, & R. I. Thorpe (Eds.), *Geology of Canadian Mineral Deposit Types* (pp. 129-196): Geological Society of America.

Lyons, T., Gellatly, A. M., McGoldrick, P., & Kah, L. (2006). Proterozoic sedimentary exhalative (SEDEX) deposits and links to evolving global ocean chemistry. *198*, 169-1841198. doi:10.1130/2006.1198(10)

Melezhik, V. A., Gorokhov, I. M., Fallick, A. E., Roberts, D., Kuznetsov, A. B., Zwaan, K. B., & Pokrovskii or Pokrovsky, B. (2002). Isotopic stratigraphy suggests Neoproterozoic ages and Laurentian ancestry for high-grade marbles from the North- Central Norwegian Caledonides. *Geological Magazine, 139*(4). doi:10.1017/S0016756802006726

Melezhik, V. A., Ihlen, P., Bjerkgård, T., Sandstad, J. S., Raaness, A., Kuznetsov, A. B., . . . Fallick, A. E. (2018). A common mid-Neoproterozoic chemostratigraphic depositional age of marbles and associated iron formations. *Norwegian Journal of Geology, 98*(4), 405-459.

Melezhik, V. A., Ihlen, P., Kuznetsov, A. B., Gjelle, S., Solli, A., Gorokhov, I. M., . . . Bjerkgård, T. (2015). Pre-Sturtian (800–730 Ma) depositional age of carbonates in sedimentary sequences hosting stratiform iron ores in the Uppermost Allochthon of the Norwegian Caledonides: A chemostratigraphic approach. *Precambrian Research, 261*. doi:10.1016/j.precamres.2015.02.015

Melezhik, V. A., Zwaan, B. K., Motuza, G., Roberts, D., Solli, A., Fallick, A. E., . . . Kuznetsov, A. B. (2003). New insights into the geology of high-grade Caledonian marbles based on isotope chemostratigraphy. *Norwegian Journal of Geology, 83*, 209-242.

Michard, A., & Albarède, F. (1986). The REE content of some hydrothermal fluids. *Chemical Geology, 55*(1), 51-60. doi:10.1016/0009-2541(86)90127-0

Michard, A., Michard, G., Stüben, D., Stoffers, P., Cheminée, J. L., & Binard, N. (1993). Submarine thermal springs associated with young volcanoes: The Teahitia vents, Society Islands, Pacific Ocean. *Geochimica et Cosmochimica Acta, 57*(21), 4977-4986. doi:10.1016/S0016-7037(05)80003-1

Mikucki, J. A., Pearson, A., Johnston, D. T., Turchyn, A. V., Farquhar, J., Schrag, D. P., . . . Lee, P. A. (2009). A Contemporary Microbially Maintained Subglacial Ferrous "Ocean&quot. *Science, 324*(5925), 397.

Morey, G. W. (1957). The solubility of solids in gases. *Economic Geology, 51*, 225-251.

Murray, R. W. (1994). Chemical criteria to identify the depositional environment of chert: general principles and applications. *Sedimentary Geology, 90*(3), 213-232. doi:10.1016/0037-0738(94)90039-6

Mücke, A., & Cabral, R. A. (2005). Redox and nonredox reactions of magnetite and hematite in rocks. *Geochemistry, 65*(3), 271-278. doi:10.1016/j.chemer.2005.01.002

Nascimento, R. S. C., Sial, A. N., & Pimentel, M. M. (2007). C- and Sr-isotope systematics applied to Neoproterozoic marbles of the Seridó belt, northeastern Brazil. *Chemical Geology, 237*(1), 191-210. doi:10.1016/j.chemgeo.2006.06.017

Newbury, D. E., & Ritchie, N. W. M. (2013). Is Scanning Electron Microscopy/Energy Dispersive X-ray Spectrometry (SEM/EDS) Quantitative? *The Journal of Scanning Microscopies. Scanning, 35*, 141-168. doi:10.1002/sca.21041

O'Neil, J. R. (1977). Stable isotopes in mineralogy. *Physics and Chemistry of Minerals, 2*(1), 105-123. doi:10.1007/BF00307527

O'Neil, J. R. (1986). Therotical and Experimental Aspects of Isotopic Fractionation. In J. W. Valley, H. P. J. Taylor, & J. R. O'Neil (Eds.), *Stable isotopes in high temperature geological processes* (Vol. 16, pp. 1-37). Washington, D. C., USA: Mineralogical Society of America.

Olivarez, A. M., & Owen, R. M. (1989). REE/Fe variations in hydrothermal sediments: Implications for the REE content of seawater. *Geochimica et Cosmochimica Acta, 53*(3), 757-762. doi:10.1016/0016-7037(89)90019-7

Osmundsen, P. T., Braathen, A., Nordgulen, O., Roberts, D., Meyer, G., & Eide, E. (2003). The Devonian Nesna shear zone and adjacent gneiss-cored culminations, North-Central Norwegian Caledonides. *Journal of the Geological Society, 160*(1), 137-150. doi:10.1144/0016-764901-173

Pitcairn, I. K., Skelton, A. D. L., Broman, C., Arghe, F., & Boyce, A. (2010). Structurally focused fluid flow during orogenesis: the Islay Anticline, SW Highlands, Scotland. *Journal of the Geological Society, 167*(1), 659-674. doi:doi: 10.1144/0016-76492009-135

Planavsky, N. J., Rouxel, O. J., Bekker, A., Lalonde, S. V., Konhauser, K., Reinhard, C. T., & Lyons, T. (2010). The evolution of the marine phosphate reservoir. *Nature, 467*(7319), 1088. doi:10.1038/nature09485

Qureishy, T. (2012). *Synthesis and structural studies of Mg2Si1-xSnx.* (Master's Thesis in Materials, Energy and Nanotechnology), University of Oslo, Oslo.

Rabbia, O. M., & Hernández, L. B. (2012). Mineral chemistry and potential applications of natural-multi-doped hydrothermal rutile from porphyry copper deposits. In J. Low (Ed.), *Rutile: Properties, Synthesis and Applications* (pp. 209-228): Nova Science Publishers, Incorporated.

Ramdohr, P. (1969). OXIDE ORE MINERALS: CUPRITE. In P. Ramdohr (Ed.), *The Ore Minerals and their Intergrowths* (pp. 878-1074): Pergamon.

Ramos de Oliveira, L. A., Rosière, C. A., & Rios, F. J. (2015). Chemical fingerprint of iron oxides related to iron enrichment of banded iron formation from the Cauê Formation - Esperança Deposit, Quadrilátero Ferrífero, Brazil: a laser ablation ICP-MS study. *Brazilian Journal og Geology, 45*(2), 193-216. doi:10.1590/23174889201500020003

Randle, V. (2009). Electron backscatter diffraction: Strategies for reliable data acquisition and processing. *Materials Characterization, 60*(9), 913-922. doi:10.1016/j.matchar.2009.05.011

Robb, L. (2005). *Introduction to Ore-Forming Processes*. Malden: Blackwell Publishing.

Roberts, D. (1988). The terane concept and the Scandinavian Caledonides: a synthesis. *Nor. geol. unders. Bull, 413*, 93-99.

Roberts, D. (2003). The Scandinavian Caledonides: event chronology, palaeogeographic settings and likely modern analogues. *Tectonophysics, 365*(1), 283-299. doi:10.1016/S0040-1951(03)00026-X

Roberts, D., Heldal, T., & Melezhik, V. A. (2001). Tectonic structural features of the Fauske conglomerates in the Løvgavlen quarry, Nordland, Norwegian Caledonides, and regional implications. *Norsk Geologisk Tidsskrift, 81*, 245-256.

Roberts, D., Nordgulen, Ø., & Melezhik, V. A. (2007). *The Uppermost Allochthon in the Scandinavian Caledonides: From a Laurentian ancestry through Taconian orogeny to Scandian crustal growth on Baltica* (Vol. 200).

Roedder, E. (1984). *Fluid inclusions. Reviews in Mineralogy* (Vol. 12): Mineralogical Society of America.

Rosenbaum, J., & Sheppard, S. M. F. (1986). An isotopic study of siderites, dolomites and ankerites at high temperatures. *Geochimica et Cosmochimica Acta, 50*(6), 1147-1150. doi:10.1016/0016-7037(86)90396-0

Roy, S. (1988). Manganese metallogenesis: A review. *Ore Geology Reviews, 4*(1), 155-170. doi:10.1016/0169-1368(88)90011-X

Rubinson, M., & Clayton, R. N. (1969). Carbon-13 fractionation between aragonite and calcite. *Geochimica et Cosmochimica Acta, 33*(8), 997-1002. doi:10.1016/0016-7037(69)90109-4

Rudnick, R. L., & Gao, S. (2003). Composition of the Continental Crust. In H. D. Holland & K. K. Turekian (Eds.), *Treatise on Geochemistry* (Vol. 3, pp. 1-64): Elsevier.

Rusk, B., & Reed, M. (2002). Scanning electron microscope–cathodoluminescence analysis of quartz reveals complex growth histories in veins from the Butte porphyry copper deposit, Montana. *Geology, 30*(8), 727-730. doi:10.1130/0091-7613(2002)030<0727:SEMCAO>2.0.CO;2

Sawaby, A., Moharram, M. A., Shabaka, A. A., & El Saker, N. (1989). Spectroscopic method for the determination of crystallinity of hematite. *Proceedings of the Indian Academy of Sciences - Chemical Sciences, 101*(6), 529-538. doi:10.1007/bf02880819

Science/AAAS. (2015). The Scanning Electron Microscope: A Small World of Huge Possibilities Retrieved from http://poster.sciencemag.org/sem/

Seward, T. M., Williams-Jones, A. E., & Migdisov, A. A. (2014). 13.2 - The Chemistry of Metal Transport and Deposition by Ore-Forming Hydrothermal Fluids. In H. D. Holland & K. K. Turekian (Eds.), *Treatise on Geochemistry (Second Edition)* (2nd ed., pp. 29-57). Oxford: Elsevier.

Shepherd, T. J., Rankin, A. H., & Alderton, D. (1985). *A Practical Guide to Fluid Inclusion Studies*. Glasgow: Blackie & Son Limited.

Sisson, V., & Hollister, L. (1990). A fluid-inclusion study of metamorphosed pelitic and carbonate rocks, south-central Maine. *75:1-2*.

Skauli, H., Bjørlykke, A., & Thorpe, R. I. (1992). Lead-isotope study of the sulphide ore and alteration zone, Bleikvassli zinc-lead deposit, northern Norway. *Mineralium Deposita, 27*(4), 276-283. doi:10.1007/BF00193398

Smith, D. B. (1995, 16 Dec. 2016). Cody Shale, SCo-1. *U.S. Geological Survey Certificate of Analysis.* . Retrieved from https://crustal.usgs.gov/geochemical_reference_standards/codyshale.html

Spero, H. J., & Lea, D. W. (2002). The Cause of Carbon Isotope Minimum Events on Glacial Terminations. *Science, 296*(5567), 522-525. doi:10.1126/science.1069401 %J Science

Stephens, M. B., & Gee, D. G. (1989). Terranes and polyphase accretionary history in the Scandinavian Caledonides. In R. D. Dallmeyer (Ed.), *Terranes in the Circum-Atlantic Paleozoic Orogens: Geological Society of America Special Paper 230* (pp. 17-30): Geological Society of America

Sterner, S. M., Hall, D. L., & Bodnar, R. J. (1988). Synthetic fluid inclusions. V. Solubility relations in the system NaCl-KCl-H2O under vapor-saturated conditions. *Geochimica et Cosmochimica Acta, 52*(5), 989-1005. doi:10.1016/0016-7037(88)90254-2

Stevenson, J. R. (2003, 26. Nov. 2013). What is Resolution? Retrieved from https://www.cas.miamioh.edu/mbiws/microscopes/resolution.html

Sturt, B. A., & Ramsay, D. M. (1999). Early Ordovician terrane-linkages between oceanic and continental terranes in the central Norwegian Caledonides. *Terra Nova, 11*, 79-85.

Sun, J., Zhu, X., & Li, Z. (2018). Confirmation and global significance of a large-scale early Neoproterozoic banded iron formation on Hainan Island, China. *Precambrian Research, 307*, 82-92. doi:10.1016/j.precamres.2018.01.005

Sverjensky, D. A. (1984). Europium redox equilibria in aqueous solution. *Earth and Planetary Science Letters, 67*(1), 70-78. doi:10.1016/0012-821X(84)90039-6

Swanson-Hysell, N. L., Rose, C. V., Calmet, C. C., Halverson, G. P., Hurtgen, M. T., & Maloof, A. C. (2010). Cryogenian Glaciation and the Onset of Carbon-Isotope Decoupling. *Science, 328*(5978), 608.

Søvegjarto, U. (Cartographer). (1973). Dunderlandsgruppen (map). M=1:2000. Rana Gruber

Søvegjarto, U., Marker, M., & Graversen, O. (Cartographer). (1988). Berggrunnskart MO I RANA 1927. Norges Geologiske Undersøkelse

Taylor, H. P., Frechen, J., & Degens, E. T. (1967). Oxygen and carbon isotope studies of carbonatites from the Laacher See District, West Germany and the Alnö District, Sweden. *Geochimica et Cosmochimica Acta, 31*(3), 407-430. doi:10.1016/0016-7037(67)90051-8

Taylor, S. R., & McLennan, S. M. (1985). *The Continental Crust: its Composition and Evolution*. Oxford: Blackwell.

Torsvik, T. H., Smethurst, M. A., Meert, J. G., Van der Voo, R., McKerrow, W. S., Brasier, M. D., . . . Walderhaug, H. J. (1996). Continental break-up and collision in the Neoproterozoic and Palaeozoic — A tale of Baltica and Laurentia. *Earth-Science Reviews, 40*(3), 229-258. doi:10.1016/0012-8252(96)00008-6

Toth, J. R. (1980). Deposition of submarine crusts rich in manganese and iron. *GSA Bulletin, 91*(1), 44-54. doi:10.1130/0016-7606(1980)91<44:Doscri>2.0.Co;2

Valley, J. W. (1986). Stable isotope geochemistry of metamorphic rocks. In J. W. Valley, H. P. J. Taylor, & J. R. O'Neil (Eds.), *Stable isotopes in high temperature processes* (Vol. 16). Michigan, USA: Mineralogical Society of America.

Van Baalen, M. R. (1993). Titanium mobility in metamorphic systems: a review. *Chemical Geology, 110*(1), 233-249. doi:10.1016/0009-2541(93)90256-I

Veizer, J., & Hoefs, J. (1976). The nature of O18/O16 and C13/C12 secular trends in sedimentary carbonate rocks. *Geochimica et Cosmochimica Acta, 40*(11), 1387-1395. doi:10.1016/0016-7037(76)90129-0

Vikentyev, I. V. (2015). Invisible and microscopic gold in pyrite: Methods and new data for massive sulfide ores of the Urals. *Geology of Ore Deposits, 57*(4), 237-265. doi:10.1134/S1075701515040054

Visser, D. J. L. (1954). Deposits of manganese ore on rooinekke and neighbouring farms, District Hay. *South African Journal of Geology, 57*(1), 61-75.

Volkert, R., Monteverde, D., Friehauf, K., Gates, A., Dalton, R. F., & Smith Iii, R. C. (2010). Geochemistry and origin of Neoproterozoic ironstone deposits in the New Jersey Highlands and implications for the eastern Laurentian rifted margin in the north-central Appalachians, USA. *206*, 283-306. doi:10.1130/2010.1206(13)

Webb, A. D., Dickens, G. R., & Oliver, N. H. S. (2003). From banded iron-formation to iron ore: geochemical and mineralogical constraints from across the Hamersley Province, Western Australia. *Chemical Geology, 197*(1), 215-251. doi:doi:10.1016/S0009-2541(02)00352-2

White, W. M., & Klein, E. M. (2014). 4.13 - Composition of the Oceanic Crust. In H. D. Holland & K. K. Turekian (Eds.), *Treatise on Geochemistry (Second Edition)* (pp. 457-496). Oxford: Elsevier.

Whitney, D. L., & Evans, B. W. (2010). Abbreviations for names of rock-forming minerals. *American Mineralogist, 95*, 185-187. doi:10.2138/am.2010.3371

Wilkinson, J. (2014). Sediment-Hosted Zinc-Lead Mineralization: Processes and Perspectives. In H. D. Holland & K. K. Turekian (Eds.), *Treatise on Geochemistry: Second Edition* (Second ed., Vol. Chapter 13, pp. 219-249). Oxford: Elsevier.

Xu, D., Wang, Z., Cai, J., Wu, C., Bakun-Czubarow, N., Wang, L., . . . Kusiak, M. A. (2013). Geological characteristics and metallogenesis of the shilu Fe-ore deposit in Hainan Province, South China. *Ore Geology Reviews, 53*, 318-342. doi:10.1016/j.oregeorev.2013.01.015

Xuexin, S., Qingsheng, X., Yuemin, G., Xueying, M., & Hong, O. (1997). REE Geochemistry of VMS and SEDEX Ores in China. *Acta Geologica Sinica - English Edition, 71*(3), 263-272.

Yang, J., Large, R., Bull, S. W., & Scott, D. (2006). Basin-Scale Numerical Modeling to Test the Role of Buoyancy-Driven Fluid Flow and Heat Transfer in the Formation of Stratiform Zn-Pb-Ag Deposits in the Northern Mount Isa Basin. *Economic Geology, 101*(6), 1275-1292. doi:10.2113/gsecongeo.101.6.1275

Young, T. P. (1989). Phanerozoic ironstones: an introduction and review. *Geological Society, London, Special Publications, 46*, ix-xxv. doi:10.1144/GSL.SP.1989.046.01.02

Zhang, Y. G., & Frantz, J. D. (1987). Determination of the Homogenization Temperatures and Densities of Supercritical Fluids in the System NaCl-KCl-CaCl2-H2O Using Synthetic Fluid Inclusions *Chemical Geology, 64*, 335-350.

Zheng, Y.-F., & Hoefs, J. (1992). Carbon and oxygen isotopic covariations in hydrothermal calcites. Theoretical modeling on mixing processes and application to Pb-Zn deposits in the Harz Mountains, Germany. *Mineralium Deposita, 28*(1), 79-89. doi:DOI: 10.1007/BF00196332

Zwaan, K. B., Fareth, E., & Grogan, P. W. (Cartographer). (1998). Geologisk kart over Norge, Berggrunnskart Tromsø. Norges Geologiske Undersøkelse

Appendices

Appendix A: Lithogeochemistry detection limits (MDL) for all analyzed elements

Table A1 – Detection limits for major element oxides.

Analyte	SiO_2	Al_2O_3	Fe_2O_3	MgO	CaO	Na_2O	K_2O	TiO_2	P_2O_5	MnO	Cr_2O_3	LOI	TOT/C	TOT/S
Unit	%	%	%	%	%	%	%	%	%	%	%	%	%	%
MDL	0.01	0.01	0.04	0.01	0.01	0.01	0.01	0.01	0.01	0.01	0.002	-5.1	0.02	0.02

Table A2 – Detection limits for trace elements.

Analyte	Be	Sc	V	Co	Ni	Cu	Zn	Ga	As	Se	Rb	Sr	Y	Zr	Nb	Mo
Unit	PPM	PPM	PPM	PPM	PPM	PPM	PPM	PPM	PPM	PPM	PPM	PPM	PPM	PPM	PPM	PPM
MDL	1	1	8	0.2	0.1	0.1	1	0.5	0.5	0.5	0.1	0.5	0.1	0.1	0.1	0.1

Table A3 – Detection limits for trace elements.

Analyte	Ag	Cd	Sn	Sb	Cs	Ba	Hf	Ta	W	Au	Hg	Tl	Pb	Bi	Th	U
Unit	PPM	PPM	PPM	PPM	PPM	PPM	PPM	PPM	PPM	PPB	PPM	PPM	PPM	PPM	PPM	PPM
MDL	0.1	0.1	1	0.1	0.1	1	0.1	0.1	0.5	0.5	0.01	0.1	0.1	0.1	0.2	0.1

Table A4 – Detection limits for rare earth elements (REEs).

Analyte	La	Ce	Pr	Nd	Sm	Eu	Gd	Tb	Dy	Ho	Er	Tm	Yb	Lu
Unit	PPM	PPM	PPM	PPM	PPM	PPM	PPM	PPM	PPM	PPM	PPM	PPM	PPM	PPM
MDL	0.1	0.1	0.02	0.3	0.05	0.02	0.05	0.01	0.05	0.02	0.03	0.01	0.05	0.01

Appendix B: Mineral abbreviations

Mineral abbreviations according to Whitney & Evans (2010)

Symbol	Mineral Name
Alm	Almandine
Ap	Apatite
Bt	Biotite
Cb	Carbonate
Ccp	Chalcopyrite
Chl	Chlorite
Clc	Clinochlore
Cum-Gru	Cummingtonite-grunerite
Czo	Clinozoisite
Ep	Epidote
Fsp	Feldspar
Grt	Garnet
Hem	Hematite
Hbl	Hornblende
Kut	Kutnohorite
Mhs	Magnesiohastingsite
Mag	Magnetite
Ms	Muscovite
Phl	Phlogopite
Pl	Plagioclase
Py	Pyrite
Po	Pyrrhotite
Qz	Quartz
Rdn	Rhodonite
Rt	Rutile
Sps	Spessartine
Zo	Zoisite

Appendix C: SEM-EDS spot analysis results

Table C1 – SEM-EDS spot analysis results of various lithologic units from the Dunderland Formation (wt.% normalized). CHS – Calc-silicate hematite schist; Mn-M – Mn-rich metapelite; GMS – Garnet-mica schist.

Lithology	Thin s.	C	O	F	Na	Mg	Al	Si	P	K	Ca	Mn	V	Fe	Ag	Te	Ba
									Muscovite								
CHS	FL 7	-	46.65	0.05	1.04	1.75	13.85	24.15	-	5.91	2.01	0.10	-	4.50	-	-	-
									Biotite								
CHS	FL 7	-	45.06	0.00	0.93	8.40	9.31	21.88	-	5.60	1.71	0.19	-	6.93	-	-	-
Mn-M	Rana 3a	-	41.83	1.73	0.79	11.69	6.50	20.14	-	6.80	1.40	2.26	-	3.30	-	-	-
GMS	FL 1c	-	43.91	0.00	0.84	6.63	9.42	19.17	-	6.35	2.59	0.12	-	10.98	-	-	-
									Almandine								
GMS	FL1 c	-	40.46	-	-	1.39	9.77	18.69	-	-	6.13	2.01	-	21.54	-	-	-
									Spessartine								
Mn-M	Rana 13a	-	41.06	2.68	1.75	1.15	9.97	19.7	-	-	5.16	15.39	-	3.15	-	-	-
									Magnesiohastingsite (?)								
CHS	FL 8	-	43.28	-	1.45	7.31	5.41	21.66	-	-	8.47	0.59	-	10.19	-	-	-
									Cummingtonite-grünerite (?)								
Mn-M	Rana 6	-	44.43	0.69	1.35	9.97	1.29	28.17	-	-	4.82	4.29	-	5.00	-	-	-
									Rhodonite								
Mn-M	Rana 6	-	38.69	-	-	1.09	-	21.66	-	-	2.57	36.00	-	-	-	-	-
									Plagioclase								
Mn-M	Rana 13a	-	48.06	-	8.59	-	10.33	31.48	-	0.14	1.39	-	-	-	-	-	-
									Apatite								
CHS	FL 8	5.98	36.77	1.88	-	-	2.45	4.89	13.05	-	-	31.09	-	2.45	-	1.79	-
Mn-M	Rana 4b	6.50	36.15	1.67	-	-	0.16	0.14	13.23	-	-	30.27	-	10.66	-	1.21	-
									Phosphate (?)								
Mn-M	Rana 5a	6.97	43.00	3.16	4.25	-	4.09	14.3	7.90	-	-	-	4.28	-	3.43	-	8.63

Table C2 – SEM-EDS spot analysis results of various carbonates from the Dunderland Formation (wt.% normalized).

Element	C	O	F	Mg	Ca	Mn	Fe	Sr
				Ca-Mn carbonate – Thin section FL 5 – Mn-rich metapelite				
Min.	10.51	44.12	1.96	1.18	16.46	17.11	0.5	2.95
Max.	14.19	46.59	2.25	1.43	17.22	20.37	1.16	3.69
Avg.	12.35	45.355	2.105	1.305	16.84	18.74	0.83	3.32
				Ca-Mn-Mg carbonate – Thin section Rana 14 – Calc-silicate hematite schist				
Min.	10.76	48.78	1.68	7.43	19.78	7.38	1.62	0.60
Max.	10.81	49.21	1.74	7.96	19.82	9.29	2.01	1.12
Avg.	10.79	49.00	1.71	7.70	19.80	8.34	1.82	0.86
				Ca-Mg-Fe carbonate – Thin section SSP3 – Quartz-hematite schist				
Min.	10.04	46.17	0.00	6.53	19.22	2.76	5.55	0.04
Max.	12.64	49.76	0	7.41	20.76	3.94	6.18	0.38
Avg.	11.34	47.97	0.00	6.97	19.99	3.35	5.87	0.21

Table C3 – SEM-EDS spot analysis results of accessory opaque phases from the Dunderland Formation and post-D_2 quartz-carbonate vein (wt.% normalized). PD_2 – Post-D_2 Qz-Cb vein; CHS – Calc-silicate hematite schist; Mn-M – Mn-rich metapelite.

Lith.	Thin s.	O	Si	S	Ca	Ti	Fe	Cu	Zn	Se	Sn	Te	Pb
							Chalcopyrite						
PD_2	Rana 10a	11.03	-	13.44	-	-	0.77	60.29	0.62	0.78	4.88	6.56	1.63
							Rutile						
PD_2	Rana 10a	42.31	5.08	1.30	1.38	46.07	3.86	-	-	-	-	-	-
							Chalcocite (?)						
CHS	FL 8	10.49	-	14.01	-	-	15.88	56.28	0.25	0.45	0.47	0.81	1.36
CHS	FL 7	12.94	-	13.86	-	-	7.52	48.38	0.15	10.29	1.33	3.54	2.00
							Cuprite (?)						
Mn-M	Rana 3a	12.53	-	-	-	-	0.51	77.71	0.42	2.97	2.96	2.42	0.47
							Pyrite						
Mn-M	Rana 13c	9.73	-	40.64	-	-	40.98	0.05	0.26	0.47	1.93	2.82	3.13

Appendix D: XRD analysis results

Table D1 – XRD analysis results of S_1-parallel hematite sample.

Pos. [°2Th.]	Height [cts]	FWHM [°2Th.]	d-spacing [A]	Rel. Int. [%]	Tip width [°2Th.]	Matched by
20.9115	801.77	0.2362	4.24815	16.44	0.2834	01-070-3755
24.1474	2374.91	0.0984	3.68569	48.69	0.1181	01-089-2810
26.6505	2472.51	0.1771	3.34494	50.69	0.2125	01-070-3755
33.1325	4877.81	0.1574	2.70387	100.00	0.1889	01-089-2810
35.6283	4473.02	0.1574	2.51997	91.7	0.1889	01-089-2810
39.2928	328.12	0.2362	2.29299	6.73	0.2834	01-089-2810; 01-070-3755
40.8931	1289.5	0.1968	2.20688	26.44	0.2362	01-089-2810
49.4669	2581.08	0.0787	1.84259	52.91	0.0945	01-089-2810
54.0638	2034.88	0.1378	1.69628	41.72	0.1653	01-089-2810
57.5586	394.24	0.3149	1.60133	8.08	0.3779	01-089-2810
62.4268	1608.46	0.2755	1.48764	32.98	0.3306	01-089-2810
64.0153	2000.01	0.1181	1.45451	41.00	0.1417	01-089-2810; 01-070-3755
72.0176	271.6	0.6298	1.31132	5.57	0.7557	01-089-2810
75.5138	347.08	0.3149	1.25906	7.12	0.3779	01-089-2810; 01-070-3755
84.9545	334.64	0.3149	1.14163	6.86	0.3779	01-089-2810; 01-070-3755
88.5916	359.45	0.3936	1.10392	7.37	0.4723	01-089-2810
93.88	259.87	0.4723	1.05515	5.33	0.5668	
106.769	288.16	0.7872	0.96048	5.91	0.9446	
122.5106	423.65	0.288	0.87856	8.69	0.3456	

Table D2 – Compounds identified from the XRD analysis results of S_1-parallel hematite sample as presented above.

Visible	Ref. Code	Score	Compound Name	Displacement [°2Th.]	Scale Factor	Chemical Formula
*	01-089-2810	81	Iron(III) oxide - alpha	0	1.125	Fe2O3
*	01-070-3755	53	Quartz	0	0.504	SiO2

Table D3 – XRD analysis results of S_2-parallel hematite sample.

Pos. [°2Th.]	Height [cts]	FWHM [°2Th.]	d-spacing [A]	Rel. Int. [%]	Tip width [°2Th.]	Matched by
2119351.00	28280.42	0.2362	10.08291	100.00	0.2834	00-042-1437
900294,00	483.86	0.2362	7.11752	1.71	0.2834	00-029-0701
17.5569	537.25	0.3936	5.05153	1.9	0.4723	00-042-1437
20.8387	764.8	0.1968	4.26283	2.7	0.2362	01-078-2315
24.1248	1200.91	0.1574	1822987,00	4.25	0.1889	00-024-0072; 00-042-1437
25.1365	380.71	0.2362	3.54287	1.35	0.2834	00-029-0701
26.4675	20864.03	0.2362	3.36765	73.78	0.2834	01-078-2315; 00-042-1437
30.1457	167.71	0.4723	2829202,00	0.59	0.5668	01-074-2034
33.1754	2661.98	0.1181	2.70047	9.41	0.1417	00-024-0072
35.5343	4993.51	0.144	2.52433	17.66	0.1728	00-024-0072; 00-042-1437; 01-074-2034
35.6423	5055.93	0.096	2.52319	17.88	0.1152	
39.2943	4869.44	0.24	2.29101	17.22	0.288	00-024-0072; 01-078-2315; 00-042-1437
40.8488	590.67	0.24	2.20734	2.09	0.288	00-024-0072
42.4494	296.05	0.288	2.12774	1.05	0.3456	01-078-2315
44.8383	3698.53	0.144	2.01977	13.08	0.1728	00-042-1437; 00-029-0701
45.563	484.35	0.384	1.98932	1.71	0.4608	01-078-2315; 00-042-1437
49.4907	1177.34	0.24	1.84024	4.16	0.288	00-024-0072
50.168	574.82	0.288	1.81697	2.03	0.3456	01-078-2315; 00-029-0701
54.0575	1233.17	0.24	1.69506	4.36	0.288	00-024-0072
56.9689	368.94	0.288	1.61515	1.3	0.3456	01-078-2315; 01-074-2034
57.5918	725.33	0.192	1.59916	2.56	0.2304	00-024-0072
59.9714	430.26	0.288	1.54127	1.52	0.3456	01-078-2315; 00-042-1437; 00-029-0701
62.4472	873.23	0.288	1.48598	3.09	0.3456	00-024-0072; 01-074-2034
63.9967	773.78	0.336	1.45368	2.74	0.4032	00-024-0072; 01-078-2315
68.3654	165.49	0.768	1.37104	0.59	0.9216	01-078-2315; 00-042-1437
71.882	526.12	0.336	1.31237	1.86	0.4032	00-024-0072; 00-042-1437
75.2461	361.22	0.48	1.26183	1.28	0.576	00-024-0072; 00-042-1437; 01-074-2034
84.6444	257.53	0.96	1.14407	0.91	1.152	00-024-0072; 01-078-2315; 00-042-1437
88.5528	184.42	0.576	1.10339	0.65	0.6912	00-024-0072
106.991	596.52	0.288	0.95831	2.11	0.3456	00-024-0072
118.7831	160.17	1.152	0.895	0.57	702728,00	
122.6067	196.62	1.152	0.87816	0.7	702728,00	00-024-0072

Table D4 – Compounds identified from the XRD analysis results of S_2-parallel hematite sample as presented in Table D3.

Visible	Ref. Code	Score	Compound Name	Displacement [°2Th.]	Scale Factor	Chemical Formula
*	00-024-0072	71	Hematite	0	0.148	Fe2O3
	01-078-2315	43	Quartz	0	0.197	SiO2
	00-042-1437	37	Phlogopite, ferroan	0	0.874	K(Mg, Fe)3(Al, Fe)Si3O10(OH, F)2
	00-029-0701	26	Clinochlore, ferroan	0	0.02	(Mg, Fe)6(Si, Al)4O10(OH)8
*	01-074-2034	41	Iron (III) Ti, Al, Mg, Cr, V(III), Mn silicon oxide	0	0.113	(Fe4.42 Fe5.245 Ti4.72 Al0.7 Mg0.4 Cr0.3 V0.15)(Fe7.82 Mn0.114Si0.06)O32

Appendix E: Lithogeochemistry reference values

Table E1 – Major element oxides normalized to Al_2O_3 wt.% for Cody shale (SCo-1) and Mn-nodules (NOD-A-1). Values of Cody shale are from Smith (1995); values of Mn-nodules are from Flanagan & Gottfried (1980).

Reference	Al_2O_3 wt.%	SiO_2	TiO_2	Fe_2O_3T	MnO	MgO	CaO	NaO	K_2O	P_2O5
Cody shale. Sco-1	62.8	4.58	0.05	0.37	0.00	0.20	0.19	0.07	0.20	0.02
Mn-nodules. NOD-1-A	3.87	0.87	0.16	5.33	9.05	1.40	5.38	0.38	0.24	0.29

Table E2 – Trace element reference values (in ppm) of bulk continental crust (from Rudnick & Gao, 2003) and bulk oceanic crust (from White & Klein, 2014).

Reference	Sc	V	Cr	Co	Ni	Cu	Ga	Y	Zr	Zn	As	Rb	Ba	Pb
Bulk continental crust	21.9	138	135	26.6	59	27	16	19	132	72	2.5	49	456	11
Bulk oceanic crust	36.2	177	317	31.7	134	43.7	-	18.1	44.5	48.5	-	1.74	19.4	0.47

Table E3 - REE reference values (in ppm). PAAS and chondrite values are from Taylor and McLennan (1985).

Reference	La	Ce	Pr	Nd	Sm	Eu	Gd	Tb	Dy	Ho	Er	Tm	Yb	Lu
PAAS	38.00	80.00	8.90	32.00	5.60	1.10	4.70	0.77	4.40	1.00	2.90	0.40	2.80	0.43
Chondrite	0.237	0.613	0.0928	0.457	0.148	0.0563	0.199	0.0361	0.246	0.0546	0.16	0.0247	0.161	0.0246

Table E4 – REE composition of the Qinlin SEDEX deposit (from Xuexin et al.. 1997) and Rapitan IF (from Halverson et al.. 2011).

Reference	La	Ce	Pr	Nd	Sm	Eu	Gd	Tb	Dy	Ho	Er	Tm	Yb	Lu
Qinlin SEDEX	17.4	38.9	4.84	19.3	4.01	0.97	4	0.58	3.86	0.87	2.46	0.34	2.03	<0.1
Rapitan IF	5.99	15	2.31	11.3	2.9	0.92	3.24	0.52	3.23	0.65	1.89	0.27	1.74	0.26

Appendix F: Lithogeochemistry results bulk rock samples

Table F1 – Major element oxides (wt. %) of bulk rock samples from the Dunderlandsdalen deposits and Varés.

Lab sample	Mineralogy	SiO_2	Al_2O_3	Fe_2O_3	MgO	CaO	Na_2O	K_2O	TiO_2	P_2O_5	MnO	Cr_2O_3	LOI	Total	TOT/C	TOT/S
SSP47	Magnetite	18.59	3.17	62.64	6.62	0.27	0.07	n.d.	0.06	n.d.	0.57	3.097	3	99.66	0.09	n.d.
SSP48	Vares: Hematite	22.56	8.6	57.88	2.15	2.39	0.7	2.28	0.76	0.77	0.09	0.012	1.6	99.83	0.11	n.d.
SSP49	Hematite	42.04	5.69	40.95	1.59	4.92	0.78	0.53	0.44	0.45	0.24	0.005	2.2	99.86	0.6	n.d.
SSP50	Mn-rich	47.83	9.02	14.29	3.27	5.49	1.83	0.89	0.6	0.24	11.2	0.008	5.1	99.84	1.47	n.d.

n.d. = not detected

Table F2 - Trace element composition (in ppm) of bulk rock samples from the Dunderlandsdalen deposits and Varés.

Lab sample	Mineralogy	Ag	Cd	Sn	Sb	Cs	Ba	Hf	Ta	W	Au	Hg	Tl	Pb	Bi	Th	U
SSP47	Magnetite	n.d.	n.d.	n.d.	n.d.	1.7	8	0.4	0.2	0.9	n.d.	n.d.	n.d.	1.2	n.d.	0.8	0.1
SSP48	Vares: Hematite	0.1	n.d.	n.d.	n.d.	2.3	539	3.6	0.5	0.6	1	0.01	0.2	0.9	n.d.	5.3	0.5
SSP49	Hematite	n.d.	n.d.	n.d.	n.d.	0.7	140	1.7	0.3	n.d.	2.1	n.d.	0.1	1	n.d.	2.4	0.7
SSP50	Mn-rich	n.d.	n.d.	1	1	1.7	192	3.8	0.8	1.1	1.1	n.d.	0.3	3.2	n.d.	5.8	0.2

Table F3 - Trace element composition (in ppm) of bulk rock samples from the Dunderlandsdalen deposits and Varés.

Lab sample	Mineralogy	Be	Sc	V	Co	Ni	Cu	Zn	Ga	As	Se	Rb	Sr	Y	Zr	Nb	Mo
SSP47	Magnetite	n.d.	45	191	700	6395	2.1	16	1.7	1.1	n.d.	0.6	50.9	1.3	13.7	2.6	0.7
SSP48	Vares: Hematite	4	16	148	32.9	15.8	4	42	2.3	2.2	n.d.	74.2	322	39.7	119.5	6.6	n.d.
SSP49	Hematite	n.d.	10	120	6.8	8.1	133.3	20	0.7	n.d.	n.d.	18.9	406	29.5	67.2	5.6	0.2
SSP50	Mn-rich	n.d.	11	38	197.9	40.2	49.5	47	1.7	45.2	n.d.	39.5	197	31.9	138.1	14.2	0.5

Table F4 – REE composition (in ppm) of bulk rock samples from the Dunderlandsdalen deposits and Varés.

Lab sample	Mineralogy	La	Ce	Pr	Nd	Sm	Eu	Gd	Tb	Dy	Ho	Er	Tm	Yb	Lu
SSP47	Magnetite	3.2	6.5	0.7	2.5	0.4	0.03	0.39	0.05	0.25	0.17	0.18	0.04	0.21	0.06
SSP48	Vares: Hematite	23.1	45	5.79	23.4	5.06	1.17	5.53	0.93	6.06	1.3	4.02	0.58	3.83	0.6
SSP49	Hematite	15.8	30.7	3.59	15.6	3.17	0.82	3.52	0.57	3.88	0.83	2.74	0.38	2.68	0.43
SSP50	Mn-rich	30.4	56.6	6.49	26	5.06	1.21	5.58	0.91	5.48	1.11	3.2	0.46	3.11	0.49